Synthesis and thin film growth of alkaline cobaltates Na_xCoO_2 and Li_xCoO_2

TECHNISCHE UNIVERSITÄT DARMSTADT

vom Fachbereich

Material- und Geowissenschaften

genehmigte

Dissertation

zur Erlangung des akademischen Grades
eines Doktors der Ingenieurwissenschaften (Dr.-Ing.)

von

Dipl.-Ing. Sandra Hildebrandt

geb. in Zwickau

Darmstadt 2013

D17

Referent: Prof. Dr. Lambert Alff
Zweitreferent: Prof. Dr. Wolfgang Donner

Tag der Einreichung: 14.12.2012
Tag der Disputation: 18.02.2013

Die wahre Lebenskunst besteht darin,
im Alltäglichen das Wunderbare
zu sehen.

Pearl S. Buck

Acknowledgements

An dieser Stelle möchte ich allen danken, die zum Gelingen dieser Arbeit beigetragen haben.

Herr **Prof. Dr. Lambert Alff**, Leiter des Fachgebietes Dünne Schichten, möchte ich danken für die Möglichkeit der Durchführung meiner Doktorarbeit in seinem Fachgebiet.

Des Weiteren gebührt Herrn **Prof. Wolfgang Donner** , Leiter des Fachgebiets Strukturforschung, mein Dank für die Übernahme des Zweitgutachtens, sowie Herrn **Prof. Wolfgang Ensinge**r, Leiter des Fachgebiet Materialanalytik, und Frau **Prof. Barbara Albert**, Leiterin der Arbeitsgruppe Albert, anorganische Chemie, die sich freundlicherweise als Prüfer zur Verfügung stellten.

Herr **Dr. Philipp Komissinskiy** möchte ich danken für die Betreuung meiner Arbeit und seiner Unterstützung während meiner Zeit als Doktorandin.

Den Mitarbeitern des **Fachgebiet Dünne Schichten,** besonders Herrn **Jürgen Schreeck** und Frau **Marion Bracke**, möchte ich für Ihre Hilfe in technischen und organisatorischen Fragen danken.

Dank gilt ebenfalls meinen **Mitdoktoranden** und **Kollegen** des Fachgebiets Dünne Schichten für die Zusammenarbeit während der Zeit meiner Promotion, sowie den zahlreichen **Professoren, wissenschaftlichen Mitarbeitern und Doktoranden anderer Fachgebiete der Material- und Geowissenschaften**.

Herrn **Timo Kober,** Mitarbeiter des Fachgebiets Mess-und Sensortechnik, möchte ich im Besonderen danken, für die gute und erfolgreiche Zusammenarbeit, auf dem ganz unbekannten Themengebiet der Drucksensorik.

Meinen **Eltern** und **Schwiegereltern** möchte ich für Ihre Unterstützung besonders als Großeltern danken. Ohne Eure Hilfe wäre der Spagat zwischen Familie und Promotion sicherlich nicht geglückt. Vielen Dank!

Liebe **Fantti,** Danke für alles, Du fehlst!

Meinem Sohn **Matti Erwin** vielen Dank für die vielen schönen Momente des Mutterseins. Jeder Tag mit Dir ist ein Erlebnis und besonderer Dank Deiner kindlichen Ehrlichkeit!

Zu guter Letzt ein Dankeschön an meinen Mann **Erwin Hildebrandt**. Die gemeinsamen Jahre der Promotion haben unser Leben entscheidend geprägt, die Geburt unseres Sohnes **Matti** und unser Zusammenwachsen als Familie sind nur zwei wichtige Ereignisse. Es gab viele Höhen und leider auch manche Tiefen, besonders die letzten beiden Jahre haben uns viel abverlangt. Für Deine bedingungslose Unterstützung, für Deine Stärke, Deine Kraft und Deine klaren Gedanken in dieser Zeit bin ich Dir dankbar. Minun Karhuni, rakastan sinua hyvin paljon ja odotan monta onnellista vuotta yhdessä!

Eidesstattliche Erklärung

Hiermit versichere ich an Eides statt, dass ich die vorliegende Dissertation selbständig und nur mit den angegebenen Hilfsmitteln angefertigt habe.

Darmstadt, im Dezember 2012

Sandra Hildebrandt

Sandra Hildebrandt, born 10th of February in Zwickau, Germany, married, one child.

School teaching

08/1993 – 06/2002	Freiherr-vom-Stein school, secondary school, Frankfurt, Germany, Examination: Abitur
08/1989 – 07/1993	Riedhofschule, primary school, Frankfurt, Germany

University study

10/2002 – 01/2008	Study of materials science at TU Darmstadt, Germany. Engineering diploma in materials science. Title of diploma thesis: „*Supraleitende und magnetische Oxidschichten für Josephson-Kontakte*“.
01/2008 – 02/2013	Doctoral thesis at Advanced Thin Film Technology, Institute for Materials Science, TU Darmstadt, Germany. Supervisor: Prof. Dr. Lambert Alff Title of Doctoral Thesis: “*Synthesis and thin film growth of alkaline cobaltates Na_xCoO_2 and Li_xCoO_2*”.

Career history

01/2008 – 12/2012	Scientific assistant at Advanced Thin Film Technology, Institute for Materials Science, TU Darmstadt, Germany. Head of division: Prof. Dr. Lambert Alff
07/2012	Manager Applied Technology Technical materials Contact and Power Technology Materials Umicore AG & Co. KG, Hanau, Germany

Preface

The family of cobaltates plays an important role in the field of energy materials used in rechargeable batteries or thermo electrics. Sodium cobaltate (Na_xCoO_2) is a novel material with a huge variety of physical properties like thermoelectric behavior, charge and spin ordered states. Dependent on the sodium content in the composition the oxidation state of the Co ion changes from 3+ to 4+, this is the reason for the different possibilities of applications. A superconducting phase was found in water intercalated sodium cobaltate ($Na_xCoO_2 \cdot yH_2O$) with x = 0.25 - 0.33 and y = 0.9 - 1.3.[1] The pairing state is still not fully clear, but there are some indications for a spin-triplet or p-wave superconducting pairing state. Li_xCoO_2 is a representative for cathode materials in thin film Li-ion batteries, by partly substitution of Co by Ni and Mn, the battery has a high specific capacity and a long cycle life.[2]

In this study sol-gel synthesis was used to fabricate Na_xCoO_2, $LiNi_{1/2}Co_{1/2}O_2$ and $LiNi_{1/3}Mn_{1/3}Co_{1/3}O_2$. By using acetate precursors a lower process temperature was accessible, which has a positive effect on the sodium and lithium loss during synthesis. The lithium based powders were single phase and kept cation stoichiometry after sintering. A small grain size is favourable for battery applications. Sodium content was slightly reduced after temperature treatment compared to the initial cation mixture, due to the high volatility of Na. To fabricate thin films PLD was used for deposition. All films were deposited on $SrTiO_3$ substrates. The growth mechanism of Na_xCoO_2 on $SrTiO_3$ was investigated and an in-plane and out-of-plane relation between film an substrate was found. The films grow 15° and 45° rotated with respect to the *ab*-plane of the substrate. The sodium content and the crystallinity of the Na_xCoO_2 was investigated as a function of the post deposition treatment. A change of x between 0.38 and 0.84 can be achieved. The γ- phase was preserved in all films despite of the change of the sodium content. The *in-situ* variation of sodium stoichiometry, allows to tune the film properties in a wide range. This feature is an advantage compared to bulk Na_xCoO_2, in which only certain stoichiometries can be stabilized. Fabrication of superconducting thin films $Na_{0.33}CoO_2 \cdot 1.3H_2O$ was challenging, since the superconducting phase is metastable and hardly to stabilize as a thin film. $LiNi_{1/3}Mn_{1/3}Co_{1/3}O_2$ and $LiNi_{1/2}Co_{1/2}O_2$ thin films were grown by PLD in (104)-orientation. These thin film materials are promising candidates as cathode materials for the development of thin film batteries.

List of publications, conference contributions, and patents

Publications

S. Hildebrandt, A. Eva, P. Komissinskiy, C. Fasel, I. Fritsch, and L. Alff
"Sol-gel synthesis of sodium and lithium based materials"
J. Sol-Gel Sci. Technol. **63**, 2012 , Page 307-314, DOI 10.1007/s10971-012-2789-4

S. Hildebrandt, T. Kober, R. Werthschützky, and L. Alff
"Kristobalitbildung (SiO_2) im Herstellungsprozess überlastfester Differenzdrucksensoren"
Sensoren und Messsysteme 2012, 16. GMA/ITG-Fachtagung, P1.4

S. Hildebrandt, P. Komissinskiy, M. Major, W. Donner, and L. Alff
"Epitaxial growth and control of the sodium content in Na_xCoO_2 thin films"
Thin Solid Films, *submitted*

Conference contributions

S. Hildebrandt, I.Fritsch, C. Fasel, P. Komissinskiy, J. Kurian, H.-U. Habermeier, and L. Alff
"Na_xCoO_2 bulk preparation by sol-gel and solid state routes"
DPG-Spring meeting, Dresden, Germany, 22. - 27. March 2009

S. Hildebrandt, I.Fritsch, Y. Krockenberger, P. Komissinskiy, H.-U. Habermeier, and L. Alff
"Superconductivity in $Na_{1-x}CoO_2 \cdot y\ H_2O$ thin films"
EUCAS, Dresden, Germany, 13. - 17. September 2009

S. Hildebrandt, I.Fritsch, Y. Krockenberger, P. Komissinskiy, H.-U. Habermeier, and L. Alff
"Superconductivity in $Na_{1-x}CoO2 \cdot y\ H_2O$ thin films"
DPG-Spring meeting, Regensburg, Germany, 21. - 26. March 2010

S. Hildebrandt, P. Komissinskiy, M. Major, W. Donner, and L. Alff
"Epitaxial growth and control of sodium content in $Na_xCoO_2 \cdot y\ H_2O$ thin films grown by pulsed laser deposition"
DPG-Spring meeting, Berlin, Germany, 26. - 30. March 2012

Patents

S.Hildebrandt, L. Alff, T.Kober, R. Taipen, A.T. Tham, and R. Werthschützky, *„Gegenkörper für Druckmesszelle, Druckmesszelle mit solchen Gegenkörper und Verfahren zu dessen Herstellung"* Endress + Hauser GmBH+Co.KG. No.:12184039.1-1236 (Date 12.09.2012), Pr.: DE/13.10.11/DEA102011084457

Contents

1 Introduction

1.1 Motivation

Thin films in general and thin films of complex oxides in particular are nowadays established in science as well as in industrial applications as the leading edge of technology. Many modern comforts like solar cells, light emitting diodes, and protection films on several instrumentations guarantee chemical stability to the environmental impacts and would not be possible without thin films as an advanced tool for modern lifestyle. Additional examples for thin film applications are optical data storage, semiconductors, wire protection or simply decorative coatings. We live in an age of innovation and mechanization, in which thin films play a central role for the development of new ways of fabrication and scaling down process of devices. Thin film studies are import especially for materials, which are metastable and cannot be synthesized as bulk materials. In the case of Na_xCoO_2, phase formation of several stoichiometries, which are not stable as bulk Na_xCoO_2 is possible. Usually an advantage of thin film technology is the reproducibility of the thin film properties and the possibility to specifically change the properties of the thin film by changing the process control.

Since the discovery of high-temperature superconductors (HTSCs) in the 1980's thin films of these materials got more and more into the focus of society.[3] The story of superconductivity starts in 1911, when Heike Kamerlingh Onnes discovered the effect of superconductivity in his studies on Hg. He found that mercury looses its electrical resistance below a temperature of 4.2 K. Metals which are in the superconducting state are perfect diamagnets. Many scientists discovered a lot of effects in superconductivity, like Fritz and Heinz London described the interaction between an electromagnetic field and superconductors. Lew Schubnikow discovered Type II superconductors, whereas Lew Landau and Vitaly Ginzburg gave a phenomenological description of the superconducting phase transition. In the history of superconductors there was always one goal in the minds of all scientists developing new superconductors: The discovery of a room temperature superconductor, which would revolutionize the whole story of electronics and energy market.

Energy materials as storage materials for rechargeable batteries or photovoltaics play a distinct role in this context since the finite nature and instability of resources on the world get more and more important. Na_xCoO_2 as a material which adheres a non-conventional superconducting phase and $LiCoO_2$ as a representative material for energy industry meet the actual high demands of our time.

1.2 Objects of this study

The aim of this thesis can be divided into two main goals in conjunction with the two materials as representatives of the alkaline cobaltates. For the Na_xCoO_2 these are

- synthesis and optimization of Na_xCoO_2 as bulk material
- growth study and optimization of thin film growth as well as the establishment of a reproducible way of depositing Na_xCoO_2 thin films with pulsed laser deposition (PLD).
- optimization of post deposition treatment of the thin films to produce stable superconducting thin films in a reproducible way to study the mechanism of superconductivity of an unconventional superconductor.

For Li_xCoO_2 these goals are

- influence of the substrate orientation on the film growth of Li_xCoO_2 thin films by PLD
- substitution of Co in Li_xCoO_2 by doping with Ni and Mn to reduce the cobalt amount utilizing the sol-gel technique to achieve small grain sizes for better ionic transport properties in batteries.
- fabrication of thin films of $LiNi_{1/2}Co_{1/2}O_2$ and $LiNi_{1/3}Mn_{1/3}Co_{1/3}O_2$ with PLD, so use in a thin film battery.

2 Fundamentals

2.1 Sodium cobaltate Na_xCoO_2

Since 1943, when Woltersdorf *et al.* first report on the formation of Na_xCoO_2 as a member of the chemical group of ortho salts, Na_xCoO_2 has drawn a lot of attention of the scientific community.[4] Ortho salts are compounds with the highest sodium oxide content available in chemistry. Woltersdorf *et al.* investigated reactions between sodium oxide, Na_2O, and the oxides of zinc, copper, cobalt, and nickel to find out whether these heavy metal oxides, having little acidic properties, are able to form sodium salts. For that purpose, Woltersdorf *et al.* synthesized ortho salts of these elements. It was possible to prepare violet, crystalline Na_2CoO_2 by using 1 mol of CoO and 2 to 2.4 mol of Na_2O. Na_2CoO_2 tends to incorporate oxygen in a highly humid atmosphere and forms black Na_2CoO_4, whereas it sustains in dry atmosphere. Fouassier *et al.* investigated in 1973 the sodium-cobalt-oxygen system in detail, four bronze types of Na_xCoO_2 with $x < 1$ were found.[5] The structure of Na_xCoO_2 consists of octahedral sheets of CoO_2 in between sodium ions. Depending on the amount of sodium, the structure is either octahedrally or trigonal prismatically coordinated. From this investigation, four phases $\alpha, \alpha', \beta, and\ \gamma$ depending on the amount of sodium, can be distinguished, as shown in Fig. 2.2 (a). The four phases are named H1, H2, H3 and O1, as shown in the phase diagram, which was first presented by Huang *et al.* in 2004. In addition, physical properties of the four phases were investigated, which will be discussed later.[6] Sodium cobaltate crystallizes in the α-phase (H3) with $0.9 \leq x \leq 1$, it is rhombohedral with $a = 2.88$ Å and $c = 15.58$ Å, the oxygen atoms along c-axis are stacked ABCABC. The α'- or H2- phase occurs at a sodium amount of $x = 0.75$, which has a monoclinic structure with $a = 4.89$ Å, $b = 2.86$ Å, $c = 5.77$ Å, and $\beta = 111°$. When $0.55 \leq x \leq 0.60$, the system has an orthorhombic lattice with $a = 2.83$ Å, $b = 4.89$ Å, and $c = 16.53$ Å, this phase is named β or O1, the oxygen stacking in this unit cell is AABBCC. All other compounds with a different x stabilize in the γ- or the H1-phase, which is hexagonal with $a = 2.83$ Å and a c-axis, which is very sensitive to the amount of Na or Co in the unit cell. Here, the oxygen stacking is AABB. The different stacking of oxygen, cobalt, and sodium in the unit cell, depending on the crystalline phase, is shown in Fig. 2.2 (b).

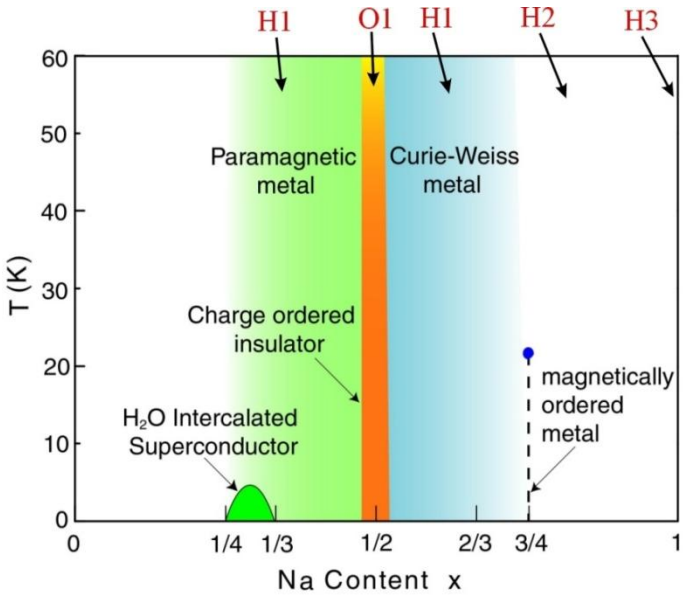

Fig. 2.1: Phase diagram of Na_xCoO_2. After Foo *et al.*[7]

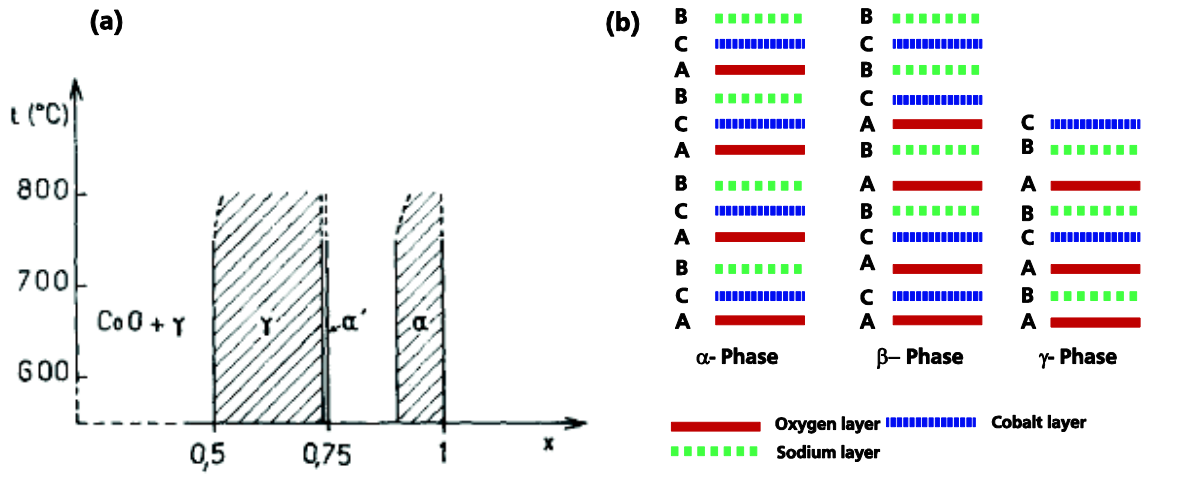

Fig. 2.2: (a) Phase diagram of the cobalt-oxygen-sodium system, where x displays the sodium content.[5] (b) Stacking of oxygen, cobalt, and sodium layers in the unit cell, depending on α, β, and γ.

The sensitivity of the c-axis length to the amount of Na in the unit cell is demonstrated in Fig. 2.3. Between $x = 0.85$ and 0.95 there is a symmetry change of the crystal structure from point group 194 to 165. In the doping range from $x = 0.25$ to $x = 0.85$ c-axis varies linearly with doping. The a-axis varies only about 20 pm throughout the whole doping range.

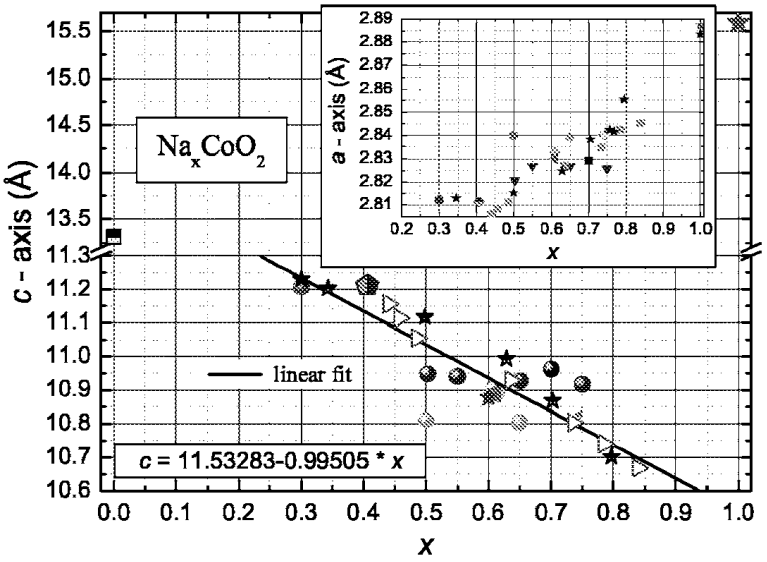

Fig. 2.3: Lattice parameters from literature for independently refined diffraction and ICP-AES measurements for different x in Na_xCoO_2, taken from Krockenberger *et al.*[8]

In 1974, Jansen *et al.* continued the investigation of sodium oxocobaltate Na_xCoO_2.[9] Compared to other cobaltates containing elements of the fourth period of the transition metals, the a-axis is comparably small, which can be attributed to the presence of additional Co^{4+} ions in the lattice. They have performed first measurements concerning magnetic properties of Na_xCoO_2 and showed that Na_xCoO_2 is weakly paramagnetic in a temperature range between 73 and 297 K. The spin configuration was predicted to be t^6_{2g} and the weak paramagnetism was attributed to the non-diagonal terms of the spin moment, comparable to $AgCoO_2$. The result of the magnetic characterization is shown in Fig. 2.4.

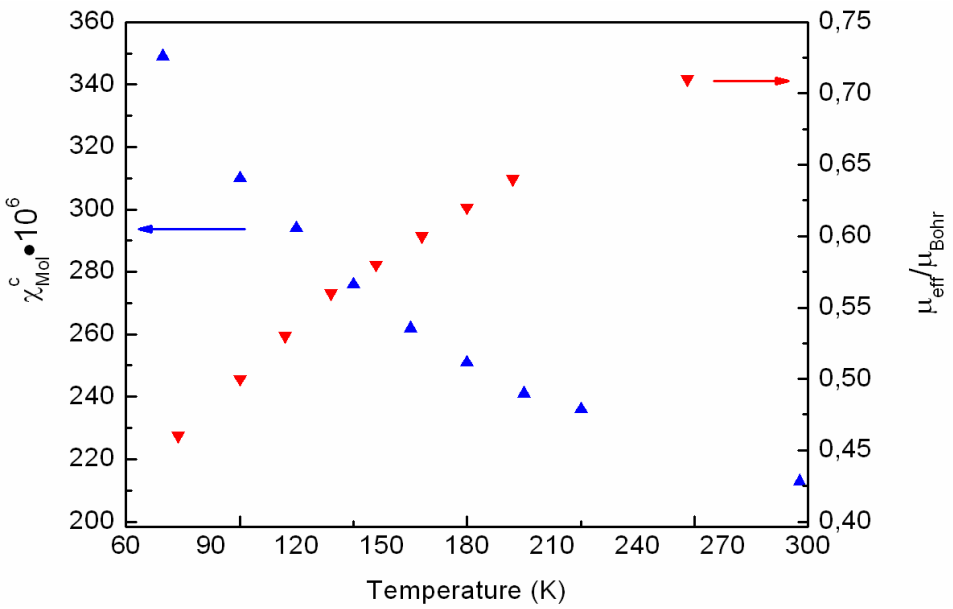

Fig. 2.4: Results of magnetic characterization of $NaCoO_2$ by Jansen *et al.*[9]

In the late 1980's, Molenda *et al.* were interested in ionic transport properties of Na_xCoO_{2-y}.[10] An electrochemical cell was used utilizing a sodium anode, a Na_xCoO_{2-y} cathode, and $NaClO_4$ in propylene carbonate as an electrolyte. The cell was cycled with various current densities. Previous studies led to the assumption, that the resulting voltage vs. sodium content is strongly dependent on the oxygen content in the material. They produced $Na_{0.7}CoO_{2-y}$ by direct synthesis of Na_2O and Co_3O_4. In $NaCoO_2$, the trivalent cobalt ions are in the low-spin state t_{2g}^6, as Jansen *et al.* postulated in 1974.[9] Since the resulting band is completely filled, the cobalt ions are formally tetravalent, when sodium ions are removed from the interlayer of the unit cell. In the obtained $Na_{0.7}CoO_2$, holes are introduced in the t_{2g} band from the sodium non-stoichiometry. This was proven by electrical characterization of the conductivity vs. oxygen pressure, where a positive *Hall*-exponent describes holes as the charge carrier majority. The variation of conductivity with temperature shows a metallic character and a high value of thermoelectric power at room temperature. Until 2004, a lot of scientific efforts by many groups were spent to investigate Na_xCoO_2 in detail, which finally resulted in the phase diagram shown in Fig. 2.1. It was found that sodium cobaltate has a huge variety of physical properties depending on the sodium content. One of the most studied properties is its huge thermoelectric power. As Na_xCoO_2 is an ionic conductor it can be used as a bulk battery material. In this context it is worth to optimize the bulk Na_xCoO_2 by for example reducing the grain size to achieve a better ionic transport.

In 1997, Terasaki *et al.* continued the thermoelectric characterization, which was started by Molenda *et al.* earlier.[10, 11] They have studied transport properties of $NaCo_2O_4$ single crystals and found the highest thermoelectric power to be $S = 100\ \mu V/K$ at room temperature and a comparably low resistivity of 200 $\mu\Omega$cm.[11] Furthermore, it was found that the mobility is $\mu = 13 cm^2/Vs$, which is rather low compared to metals. The results of their measurements are shown Fig. 2.5.

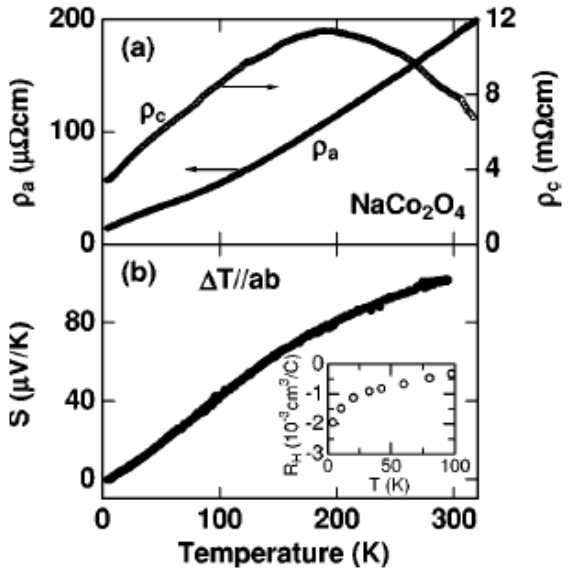

Fig. 2.5: (a) In-plane (ρ_a) and out-of –plane (ρ_c) resistivity of $NaCo_2O_4$. (b) In –plane thermoelectric power (S) of $NaCo_2O_4$ single crystals. The inset shows the in-plane Hall coefficient (R_H).[11]

The resistivity was found to be anisotropic in magnitude and in temperature dependence. The ratio of ρ_c/ρ_a is 200 at 4.2 K, which is comparable to that of $La_{2-x}Sr_xCuO_4$[12] and Sr_2RuO_4.[13] The electronic states of layered sodium cobaltate can be considered as quasi 2-dimensional. It shows out-of-plane resistivity with transition from metallic to semiconducting behavior around 190 K with increasing temperature, similar to Sr_2RuO_4. In Fig. 2.5 (b) the in-plane thermoelectric power is shown. The magnitude of S is ten times larger than typically expected for metals or high-temperature superconductors[14] and its sign of the Hall coefficient is opposite to the Hall coefficient shown in the inset of Fig. 2.5 (b).This means that the simple free-electron picture is inapplicable. Since S is large and ρ_a is low, sodium cobaltate is a good candidate for thermoelectric applications. Terasaki *et al.* compared their data with those of Bi_2Te_3, a typical thermoelectric material.[15] The results are shown in Table 2.1.

Table 2.1: Thermoelectrical properties for Na_xCoO_2 and Bi_2Te_3 at 300 K. ρ, S, and m represent in-plane resistivity, in-plane thermoelectric power, and mobility, respectively.

Parameter	Unit	$NaCo_2O_4$	Bi_2Te_3
ρ	mWcm	0.2	1
$\lvert S \rvert$	μV/K	100	200
S^2/ρ	mW/K^2cm	50	40
μ	cm^2/Vs	13	150

The thermoelectric power S of $NaCo_2O_4$ is only half of that of Bi_2Te_3. Since ρ is only one fifth of that of Bi_2Te_3, the power factor S^2/ρ is still comparable. However, the mobility μ is more than ten times smaller compared to Bi_2Te_3. This means $NaCo_2O_4$ has a much larger number of charge carriers n. In conclusion it was stated that a dirty conductor can be as efficient as other thermoelectric materials with better conductivity, but still the origin of this large $|S|$ is unclear. In 2003, Wang *et al.* explained the enhanced thermopower.[16] They started a theoretical investigation on how electron-electron interaction may enhance the thermo

power of materials, especially in the case of transition-metal oxides. The movement of electrons in a solid under electric field produces an entropy current in addition to the charge current, this is called *Peltier* effect. The interesting point of this theory is the electronic spin entropy, which is dominated by the entropy current. Wang *et al.* report on the complete suppression of the spin entropy term in a longitudinal magnetic field.[16] In conventional metals, the movement of electrons by a $-\nabla T$ is cancelled by parallel movement of holes in such a way that S is reduced by a factor T/T_F from its natural value k_B/e, here T_F, k_B, and e are the Fermi temperature, Boltzmann constant, and the electron charge, respectively. Furthermore, a longitudinal magnetic field $H \| -\nabla T$ should have no effect to S, due to the fact that the currents are indifferent to spins. For a material with a strong electron-electron interaction, the spin degrees have a large contribution to S, see Eq. 2.1.

Eq. 2.1
$$S = \frac{\mu}{eT} = -\frac{\sigma}{e}$$

in this formula, μ represents the chemical potential and σ the entropy per electron. The entropy per electron equals $k_B \ln(g_s g_c)$; with g_s and g_c as the spin and configuration degeneracies. When the spin degeneracy is lifted in a magnetic field ($g_s \rightarrow 1$), the enhancement to S is suppressed, which is usually of the order of k_B/e. By investigation the thermopower and magnetization in longitudinal and transversal magnetic fields, it was demonstrated that $NaCo_2O_4$ is a strongly correlated system in which the spin entropy is solely determinant for S at 2 K and dominant for S at 300 K. At moderate temperatures (30 K), S decreases under an applied field of 14 T ($H||-\nabla T$). This effect is more pronounced by lowering the temperature further. At 4 K the sign of S is changed from positive to negative and saturates at a field of 12 T to -0.25 μVK^{-1}. By further decreasing T, the thermo power decreases monotonically to zero. The results are shown below in Fig. 2.6.

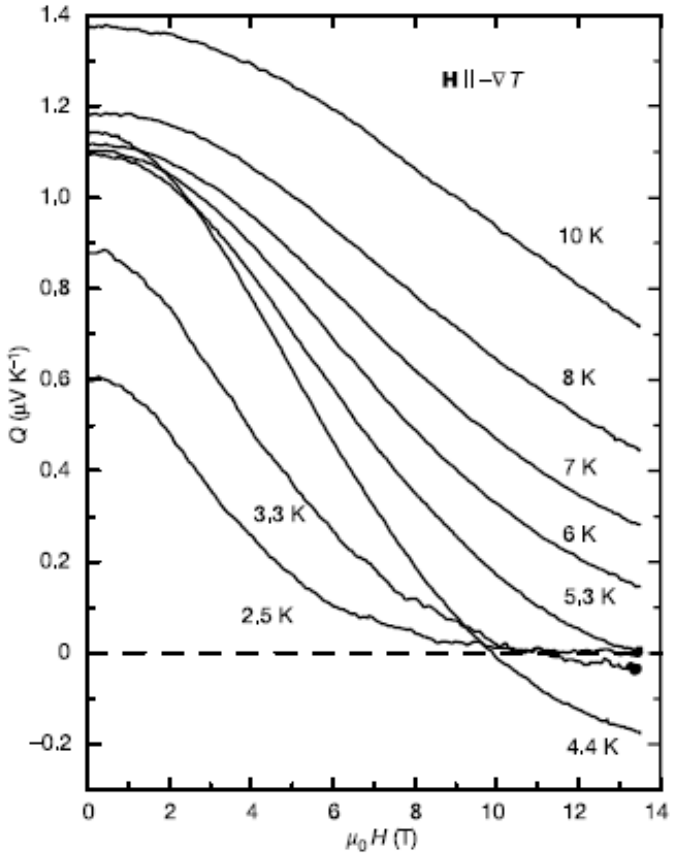

Fig. 2.6: In-plane thermo power, S vs. in-plane field $H||-\nabla T$.[16]

The strong impact of magnetic field on S is also observed with H parallel to c. The complete suppression is not explainable by the conventional band picture for metals, in which an applied field changes the amount of spin-up and spin-down electrons without altering the entropy current. Wang *et al.* suggest that the entropy currents derive from the spin-half excitations, which occur due to the difference in valency of $Co^{4+}(s = 1/2)$ and $Co^{3+}(s = 0)$. The charge transport mechanism is hole hopping from Co^{4+} to Co^{3+} ions. During this transport spin-half is transferred in background of Co^{3+} ions, which are magnetically inert (diamagnetic). This transfer can be understood as the transfer of the spin entropy. Here, the Co ions are always in their low-spin configuration. From calculations and fitting Wang *et al.* conclude that the entropy current observed in the thermo power is dependent of the spin-half excitations. The complete suppression of S represents the removal of the spin degeneracy by an applied field. By changing the sodium content in the material, thus the concentration of Co^{4+} is changed too, the thermo power is drastically enhanced by increasing sodium content.[17] This turns Na_xCoO_2 to be a promising candidate for the search for improved thermoelectric materials.

In the region of $x > 0.5$, Na_xCoO_2 is a so-called *Curie-Weiss* metal. The *Curie law* describes the behavior of the susceptibility χ_m, as a function of temperature (see Eq. 2.3) in the case of perfect spin-paramagnetism.[18]

Eq. 2.2
$$\chi_m = \frac{C}{T}$$

Here, C is a material specific constant. In 1907, *Pierre-Ernest Weiss* extended the *Curie* law with magnetic cooperating effects, which lead to ferromagnetism, antiferromagnetism or ferrimagnetism. The *Curie-Weiss* law describes actually the susceptibility of a ferromagnet in the paramagnetic phase, by introducing the *Curie-temperature* T_c in the *Curie*-law.

Eq. 2.3
$$\chi_m = \frac{C}{T - T_c}$$

Eq. 2.3 has to be extended for temperatures near T_c. Calculations from Domb *et al.* describe the susceptibility by following formula.[19]

Eq. 2.4
$$\chi_m \propto -\frac{C}{(T - T_c)^{1.33}}$$

In sodium cobaltate, the *Curie-Weiss* susceptibility is much larger than what is expected for weakly interacting metals (*Curie-Weiss* metals). Na_xCoO_2 combines an unusual mix of behaviors that are a hybrid of those between a good metal and of insulators.[20] Haerter *et al.* showed in 2006 that strong electron correlations, along with a geometrically frustrated lattice, could explain such a behavior. They applied the *t-J* model, which describes strongly correlated electron systems by forbidding double occupancy of lattice sites.[21-23] It was derived from the *Hubbard* model,[24] which is a simple model to study the interaction of kinetic energy, considering *Pauli* principle and Coulomb repulsion in one system.

Unusual transport and unconventional magnetic behavior was found in the α'- or H2 phase of Na_xCoO_2 (x = 0.75). Takeuchi *et al.* first reported on magnetic anomalies in $Na_{0.75}CoO_2$ in 2002.[25] They characterized powder samples regarding temperature dependence of the susceptibility, field cooled (FC) and zero-field cooled (ZFC) magnetic measurements. The result of their study is shown in Fig. 2.7.

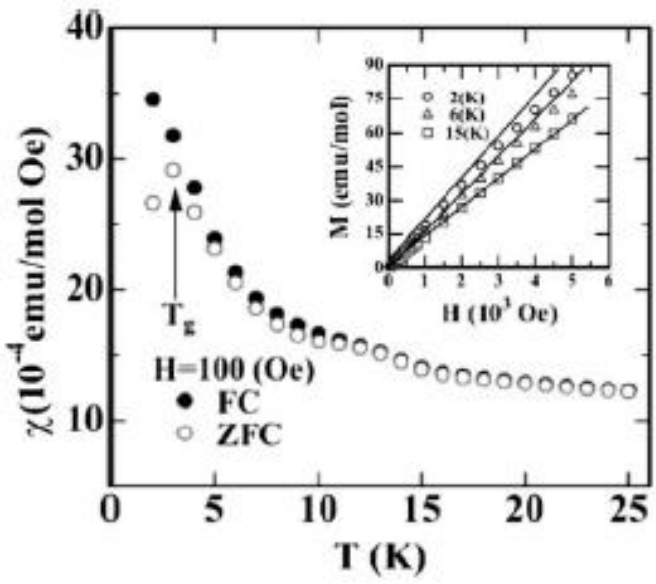

Fig. 2.7: Magnetic susceptibility of $Na_{0.75}CoO_2$ measured under FC and ZFC conditions. The magnetization as a function of magnetic field, is given as an inset.[25]

At low temperatures, a divergence between χ_{FC} and χ_{ZFC} is observed. The inset of Fig. 2.7 shows a linear relation between magnetization and magnetic field at 15 K. The small

deviation at 2 K and 6 K suggests a short-range ferromagnetic coupling. Near T_g = 3 K, a cusp transition can be observed for ZFC conditions similar to spin glasses. Further temperature-dependent susceptibility measurements under different magnetic fields (near T_g) prove the existence of a short range ordering. Takeuchi *et al.* found $Na_{0.75}CoO_2$ not to be a conventional itinerant paramagnet.[25] This result was confirmed by Toyohashi *et al.* in 2003.[26] They found a second order magnetic transition at 22 K, accompanied with a large jump in specific-heat, a weak spontaneous magnetization (M_s = 1.2·10^{-4} μ_B/Co site at 2 K), a rapid resistivity drop to ~15 μΩcm, and a large positive magnetoresistance effect (MR) with $\Delta\rho_{7T}/\rho_0$ ~0.3 at 2 K. This strongly indicates the presence of an unconventional electronic state of strongly correlated electrons. Toyohashi *et al.* suggested a spin-density wave (SDW) or a charge-density wave (CDW) as the possible order state, coexisting below T_m. This feature was in good agreement with the results of positive muon spin rotation (μ^+SR) measurements performed by Sugiyama *et al.* in the same year.[27] At temperatures below 22 K, zero-field μ^+SR exhibit clear oscillations due to static internal magnetic fields. It has to be denoted that the volume fraction of the magnetically ordered phase was only ~21% at 2.5 K. The results of Sugiyama's measurements are displayed in Fig. 2.8.

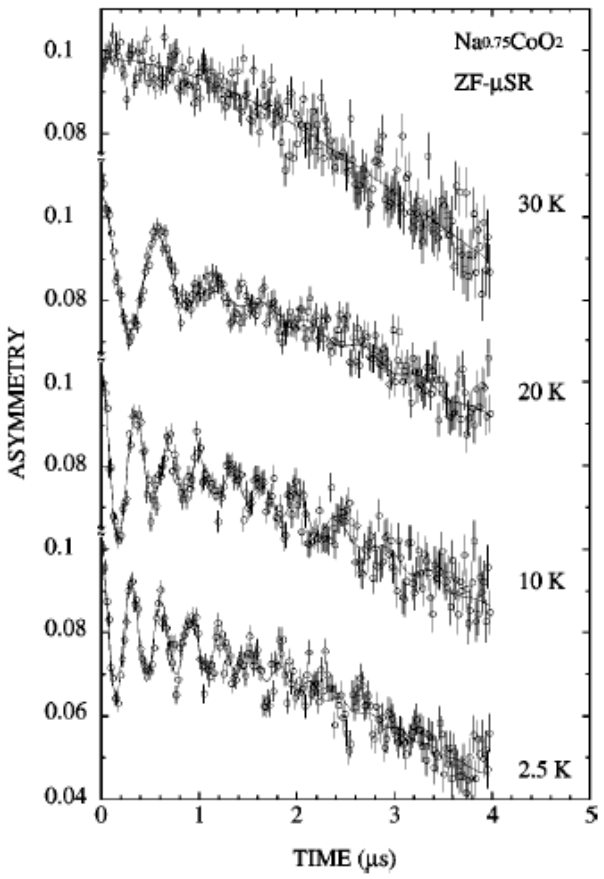

Fig. 2.8: Zero-field μ^+SR time spectra of $Na_{0.75}CoO_2$ obtained at 30, 20, 10, and 2,5 K. Solid lines represent results of fitting using a Gaussian Kubo-Toyabe function taken from reference.[27]

The transition is induced by the ordering of Co spins in CoO_2 planes. If the muons, which are in an ordered field, are bound to oxygen, an estimation of the ordered Co moment would be possible. At 2.5 K it is ~0.18 μ_B ($\nu_{\mu,1}$ = 3.3 MHz and $d_{Co\text{-}O}$ = 1.914 Å). This moment at the cobalt site is 100 times larger than that estimated by magnetic characterization Motohashi

et al. ($1.2 \cdot 10^{-4}$ μ_B) made.[26] Sugiyama *et al.* suggested a commensurate SDW state, as it would drastically decrease bulk magnetization.[27] The cobalt moments are likely to couple ferromagnetically in the CoO_2 plane, but antiferromagnetically along *c*-axis. In 2004, Sakurai *et al.* continued magnetic characterization of Na_xCoO_2 in a very small range of x between 0.70 and 0.84.[28] They found for $Na_{0.78}CoO_2$ T_m to be completely independent from H as shown in Fig. 2.9. The transition and the hysteresis between ZFC and FC is prominent for $x = 0.78$ and less pronounced for further decreasing in x. Nevertheless it is independent from x that means the magnetic phase diagram has not a dome shape, as suggested by Sugiyama *et al.*[29, 30] Furthermore, it is a trace of the phase being responsible for the transition. To explain this phenomena Sakurai *et al.* suggested a phase separation into Na-rich and Na-poor domains.[28] The transition at T_m takes place only in the Na-rich domain, whose fraction increases with x. This idea is consistent with specific heat measurements and μ-SR data.

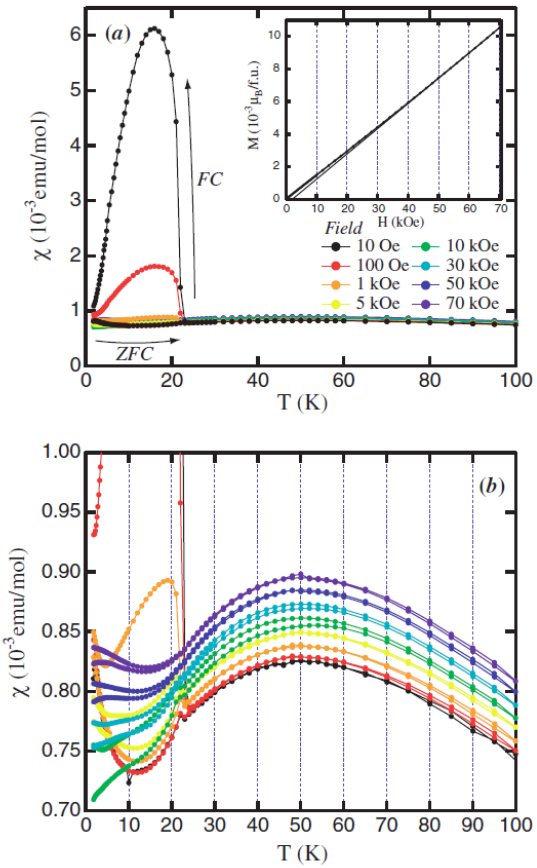

Fig. 2.9: (a)Temperature dependency of the susceptibility of $Na_{0.78}CoO_2$ measured under various magnetic fields by Sakurai *et al.*[28] (b) Expanded graph of (a) for better clarity.

Many research groups concentrated on the formation of a SDW in Na_xCoO_2, results are discussed controversially for $x > 0.5$. It is clear that characterizations on samples with exact stoichiometry as well as characterizations on the same batch of samples to unify the picture for a single doping level, is a necessity. For that reason, Wooldridge *et al.* focused on magnetic susceptibility, specific heat capacity, and transport measurements of single-crystal samples with $x = 0.71$.[31] They found an antiferromagnetic SDW ground state below 22 K in consistency with previous work. In addition, they found the reduction in electron-electron scattering to be a result of SDW formation, which leads to an increase of the conductivity along *ab*,

although the number of carriers is reduced. They found, that a significant part of the SDW state is pinned below 7 K, which results in a glassy ground state.

By reducing the sodium content down to $x = 0.5$, another interesting region in the phase diagram of sodium cobaltate is reached. There are almost sharp borders at which the material shows a charge-ordered insulating behavior. In 2004, Huang *et al.* focused on $Na_{0.5}CoO_2$ and found a low temperature phase transition.[32] In the same year, Foo *et al.* investigated unusual properties of Na_xCoO_2 with x=0.5.[7] In both studies two cusps at $T_{c1} = 88$ K and $T_{c2} = 53$ K were found for specific heat measurements and the magnetic characterization, respectively. The results are shown in Fig. 2.10.

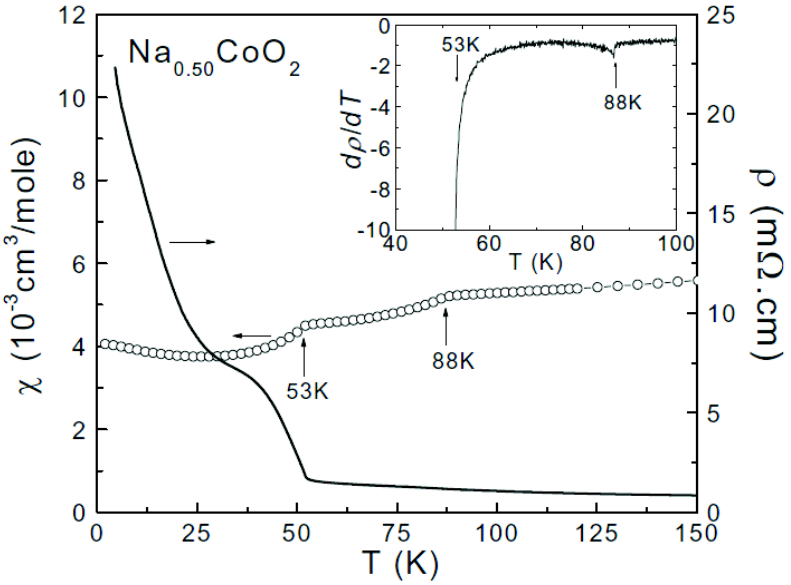

Fig. 2.10: Magnetic and resistive characterization of $Na_{0.5}CoO_2$ below 100 K by Huang *et al.*[32] Resistivity data was obtained with a single crystal, whereas susceptibility data was obtained with a polycrystalline sample.

The resistivity was measured in the CoO_2 plane and shows the two previously mentioned cusps. Below 53 K, the resistivity settles until 25 K, below ρ is increasing again, indicating another possible phase transition. The magnetic susceptibility shows only two transitions at 53 K and 88 K. Structural characterizations show, that T_{c1} is probably related to a structural change of $Na_{0.5}CoO_2$, in which *a*- and *b*-axis of the orthorhombic cell are tripled by a structural distortion. Additional diffraction spots in the electron diffraction pattern taken by Huang *et al.* is evidence supporting that theory.[32] From structure refinement and neutron diffraction data the superstructure was attributed to be *Pnmm* (SG 59). Interestingly, Na is ordered in this structure. Due to the presence of two types of Co-atoms, which are found to be ordered in chains and cause charge ordering, Na^+ tends to form zigzag chains being as far apart as possible from each minimizing the Na^+-Na^+ coulombic repulsion. Temperature dependent transmission electron microscope (TEM) studies performed by Yang *et al.* demonstrated a series of phase transitions between 300 and 1000 K, possibly due to Na^+ ordering. The result is depicted in Fig. 2.1. The material has an incommensurate modulated structure at 300 K which transforms in a hexagonal superstructure phase with double cell parameters in *a* and *b* when heating. This superstructure is stable in a temperature range between 410 and 470 K, see Fig. 2.11 (b), whereas at 470 K the material transforms into another high-temperature hexagonal structure, see Fig. 2.11(a). During cool down the material transforms at ~200 K in an

orthorhombic structure, as previously mentioned. The high-temperature structure is similar to that of conventional hexagonal phases with no ordered states. This more or less ideal structural homogeneity is connected to high Na^+ mobility at high temperatures. Upon 850 K, a degradation of the thin TEM samples into polycrystalline samples take place. The superstructure presented in Fig. 2.11 (b) arises from Na^+-ordering between the CoO_2 layers in the unit cell. In this arrangement the sodium ions can occupy two possible trigonal prismatic positions in the lattice, Na(1) and Na(2). These positions are limited by the space between two adjacent oxygen planes. The Na(1) trigonal prism shares faces with the CoO_6 octahedral, whereas the other Na(2) trigonal prism shares edges with the octahedron.[32] The described structure is shown in Fig. 2.12 as a structure model based on symmetric occupation of a fraction of the Na(2) sites.

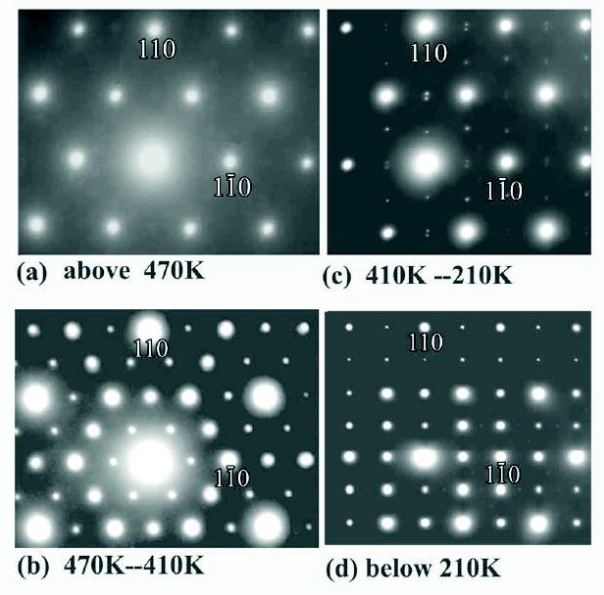

Fig. 2.11: Electron diffraction patterns from $Na_{0.5}CoO_2$ taken by Yang *et al.* at temperatures of (a) 500 K, (b) 420 K, (c) 300 K, and (d) 100 K.[33]

Structural data obtained between 200 and 410 K, see Fig. 2.11 (c), shows a complex ordered structure corresponding to different Na-ordered states. It is most likely that $Na_{0.5}CoO_2$ has a meta stable structure within this large temperature range.[34]

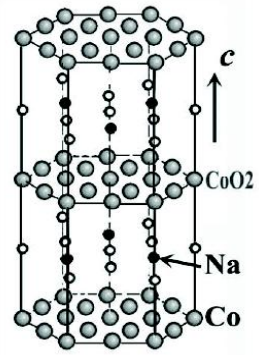

Fig. 2.12: Structural model from Yang *et al.* for the superstructure phase observed between 410 and 470 K. The black circles indicate occupied Na sites.[33]

The low temperature structural phase transition represented in Fig. 2.11 (d) is attributed to the incommensurate structural modulation, leading to changes in wavelength, intensity, and incommensurability. The intensity of the satellite reflections above 200 K increases when *in situ* cooling below 200 K. In summary, it is remarkable that $Na_{0.5}CoO_2$ as a part of the Na_x-CoO_2 phase diagram has several phases arising from sodium ordering. Below a sodium content of $x = 0.5$, Na_xCoO_2 is a paramagnetic metal, including the region of superconductivity. Between $x = 0.25$ and $x = 0.33$ the superconducting phase exists, provided a certain amount of water molecules is intercalated in the structure (y=1.3). This was found in 2003 by Takada *et al.* and attracted a lot of scientific interest to this material.[1] Since the discovery of HTSCs in layered copper oxides like Ba-La-Cu-O by Bednorz and Müller in 1986, many groups were searching for similar behavior in other layered metal oxides, involving 3*d*- transition metals.[3] It was believed a long time, that the copper oxide planes are a necessity for superconductivity in such layered materials. This assumption was altered by Takada *et al.* presenting Na_x-$CoO_2{\cdot}yH_2O$ ($x = 0.35$, $y = 1.3$) to be superconducting with a T_c of about 5 K.[1] This compound consisted of two-dimensional, electronically active CoO_2 layers separated by Na^+-ions and H_2O molecules acting as charge reservoirs, shown in Fig. 2.13.

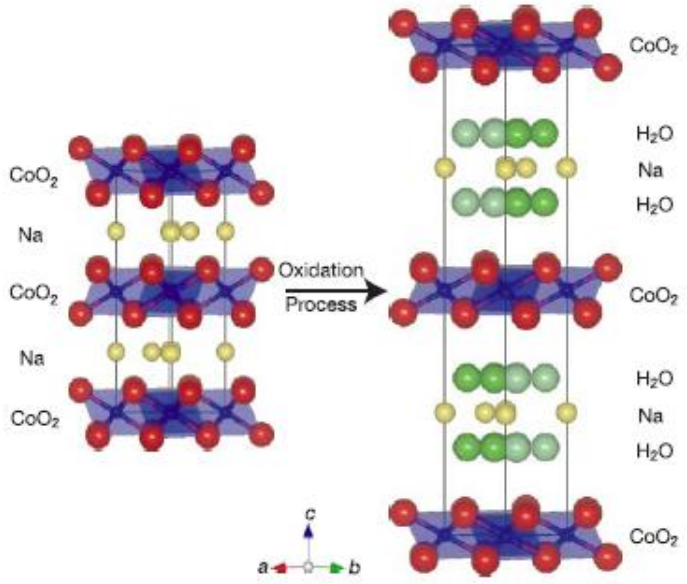

Fig. 2.13: Scheme of the crystal structure of Na_xCoO_2 changing to $Na_xCoO_2{\cdot}yH_2O$. Taken from Takada *et al.*[1]

To observe superconductivity it was necessary to reduce the sodium content of a host material, e.g. $Na_{0.7}CoO_2$, by using an oxidizing agent like Br_2. In a second step the material was immersed in H_2O to intercalate water molecules. All reflections in the X-ray diffraction pattern were indexed based on the space group $P6_3/mmc$, and a huge increase of the *c*-axis was observed. This supports the theory, that water molecules are intercalated in the structure by an oxidation process. The magnetic susceptibility and resistivity are plotted in Fig. 2.14 (a) and (b).

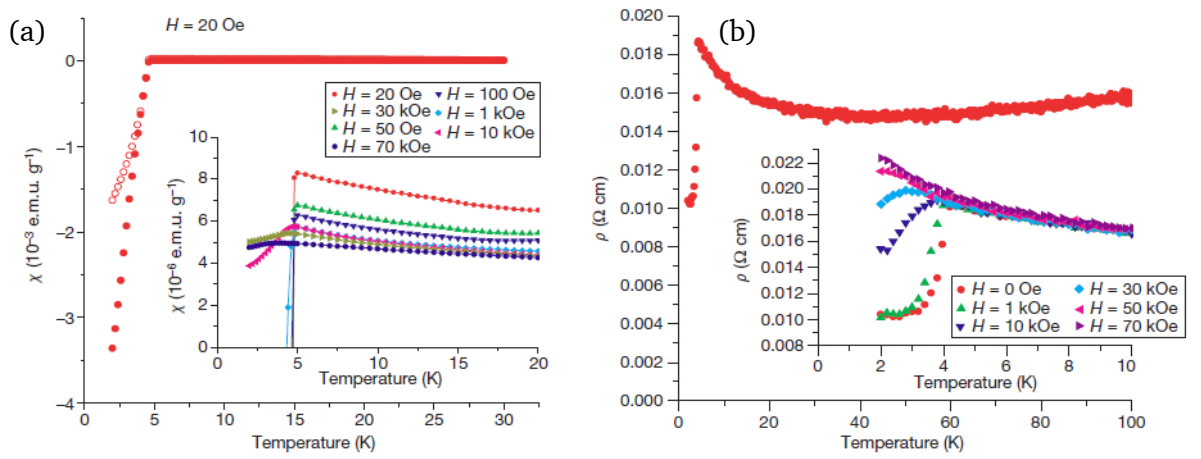

Fig. 2.14: (a) Magnetic susceptibility of $Na_xCoO_2{\cdot}yH_2O$. Filled circles obtained for ZFC; open circles for FC. (b) Resistivity of $Na_xCoO_2{\cdot}yH_2O$, measured on a compressed powder sample by standard four-probe method. Taken from Takada *et al.* [1]

Under a magnetic field of 20 Oe at about 5 K, a steep decrease of χ was observed under ZFC and FC conditions. The FC susceptibility at 2 K was $-1.6{\cdot}10^{-3}$ emu/g. This is 6.5% of the theoretical value known for perfect diamagnetism. Twice as large diamagnetism was observed for ZFC. The *M-H* curve at 2 K indicates a type II superconductor with a critical field around 100 Oe. The resistivity data (Fig. 2.14 (b)) show a sharp decrease at around 4 K, which supports the observation of a superconducting transition. The difference in onset temperatures for both measurements is probably due to a variation of water content in the sample, which is very sensitive to environmental humidity. Takada *et al.* found a similarity between cobalt oxide systems and high-T_c copper oxide systems.[1] In high-T_c copper oxides, superconductivity occurs in CuO_2 planes, where Cu^{2+} (S= 1/2) moments couple antiferromagnetically. Antiferromagnetism is suppressed by a low level of charge carrier doping and is metallic. The present material can be described in the same way as electron doped systems for low-spin Co^{4+}(S = 1/2) with an electron density of around x = 0.35 per Co atom. As shown in Fig. 2.14, the increasing magnetic field broadened the superconducting transition, but did not lower T_c onset, which is similarly found for high-T_c cuprate. The large separation of CoO_2 layers by water molecules is essential for inducing superconductivity. The main difference between these two systems is the formation of a magnetically frustrated lattice formed by Co ions, in contrast to the square geometry of CuO_2 planes. Schaak *et al.* reported on the superconducting phase diagram of $Na_xCoO_2{\cdot}1.3H_2O$, which cleared the picture of the triangular cobalt-oxygen lattice and the relation to CuO_2.[35] They showed that the compound displays similar behavior on chemical doping than what is observed in cuprates. Superconductivity only occurs in a very narrow range of sodium concentration and decreases for both, over- and underdoped materials. On the other hand, the triangular lattice is completely different to that of cuprates, coupled charges and spin dynamics play an essential role in superconductivity. Schaak *et al.* found that by introducing water into the compound, the *c*-axis is elongated to 19.43 Å with x = 0.45 and 19.77 Å with x = 0.26.[35] Magnetic characterizations of the samples with different sodium content showed a significant dependence of T_c from x as displayed in Fig. 2.15.

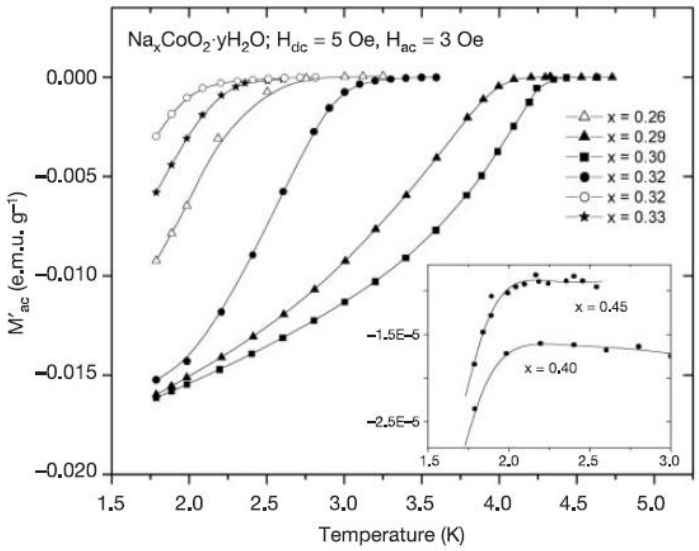

Fig. 2.15: Zero field cooled AC magnetization (H_{dc} = 3 Oe, H_{ac} = 5 Oe, f = 10 Hz), obtained by Schaak *et al.*[35]

From the measured data it was possible to plot a phase diagram of $Na_xCoO_2 \cdot 1.3H_2O$ as presented in Fig. 2.16. For $x = 0$ the formal Co oxidation state is 4+, with a t^5_{2g} electron configuration in the low spin state. For $x = 1$ Co is formally 3+ with the configuration t^6_{2g}, also in the low spin state.

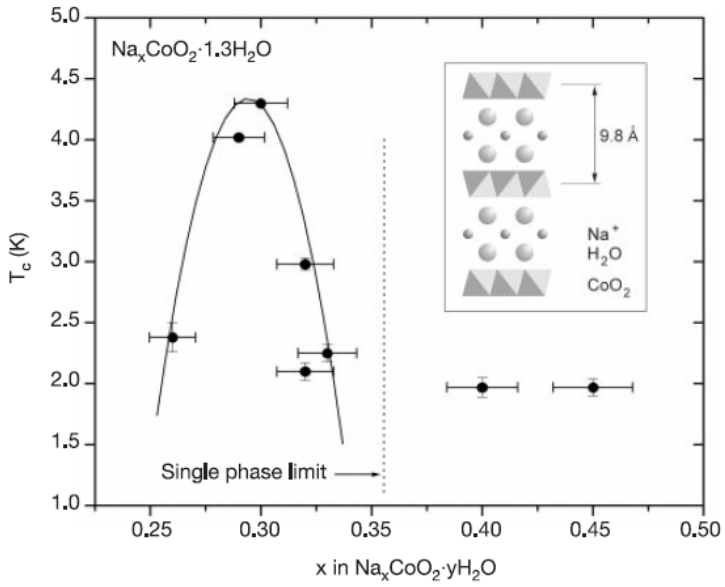

Fig. 2.16: Phase diagram of $Na_xCoO_2 \cdot 1.3H_2O$ superconductivity based on Schaak *et al.* The right inset shows the schematic representation of the layered crystal structure.[35]

Electronic structure calculations for $Na_{0.5}CoO_2$ by Singh *et al.*[36] indicate that the t_{2g} band would be completely filled if $x = 0.5$, which is similar to that of semiconductors. The trigonal distortion of the CoO_6 octahedra in this structure will presumably lead to a splitting of the t_{2g} band, resulting in a fully filled four-electron band and a half filled two-electron band for $x = 0$. This is a Mott-Hubbard insulator, as known for cuprates. In this picture, each added Na atom results doping of one electron per cobalt atom into the half-filled band, the optimal chemical doping level for superconductivity in cobaltates would then be 0.3, compared to

+0.15 electrons in the cuprates, like the experimental data shows. Observations of the previously mentioned unusual transport properties at higher doping levels gives evidence to the idea, that coupled spin and charge dynamic implicated in superconductivity. More details about the electronic state of the triangular lattice will be needed to get a full picture of the superconducting mechanism, which takes place. Further studies about chemical composition and structure of hydrated phases using Raman spectroscopy and inductively coupled plasma emission spectroscopy (ICP-AES) were done by Takada *et al.*[37] It was found, that the Na content changes from $x = 0.406$ to $x = 0.337$ by the immersion process in water. This suggests a second mechanism besides the intercalation process. The decrease in the Na content can be explained by partial ion-exchange of Na^+ ions in the cobalt oxide with protons or H_3O^+ ions from water, as described by the following relation.

Eq. 2.5 $$Na_{0.406}CoO_2 + (0.140 + n)H_2O \rightarrow Na_{0.337}(H_3O)_{0.070}CoO_2 \cdot nH_2O + 0.070Na^+ + 0.070OH^-$$

Comparing to $LiMn_2O_4$, the reduction process of Co atom takes place during the immersion process meanwhile oxygen is liberated.[38] By intercalating Na^+ ions, pH value of the solution decreases because of the limited amount of Na^+ ions in the solvent. The lower the pH, the higher the potential of oxygen liberation is. Based on this a possible second reaction was formulated.

Eq. 2.6 $$Na_{0.337}(H_3O)_{0.070}CoO_2 \cdot nH_2O + 0.246H_2O \rightarrow Na_{0.337}(H_3O)_{0.234}CoO_2 \cdot nH_2O + 0.041O_2$$

It is not yet clear, whether the reactions (Eq. 2.5 and Eq. 2.6) take place separately or simultaneously. Moreover, the results from Raman spectroscopy presented in Fig. 2.1 indicate H_3O^+ substituting Na^+ ions rather than protons.

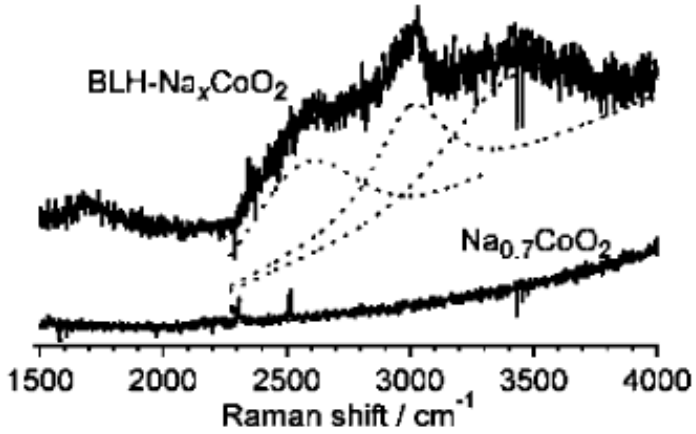

Fig. 2.17: Raman spectra for $Na_{0.7}CoO_2$ and the hydrated material (BHL-Na_xCO_2). Data from Takada *et al.*[37]

The Raman peak at 1700 cm^{-1} for BHL-Na_xCoO_2 can be ascribed to the bending mode of an H_3O^+ ion,[39] it can be distinguished from the bending mode of H_2O,[40] which occurs at 1,600 cm^{-1}. The broad band between 2,300 cm^{-1} and 3,800 cm^{-1} can be deconvoluted into several peaks, attributed to stretching vibrations from OH groups. The most distinct peak at 2,995 cm^{-1} is attributed to the stretching mode of H_3O^+ions.[40] Since peak intensity is high enough, the amount of H_3O^+ ions in BHL-Na_xCoO_2 is significant. Based on this study, the intercalating species in the structure has to be extended by the presence of H_3O^+ ions, in addition to Na^+ ions and H_2O. Nevertheless, structure refinements provided no structural changes down to 12.5 K. A work of Milne *et al.* demonstrates, that superconductivity is obtained over a

wide range of Co valency, 3.24 - 3.35.[41] Measurements of the *c/a* ratio of the lattice constants suggest that the separation of the CoO_2 sheets increases when the Co valence is tuned to the ideal region for superconductivity. At this point the interlayer coupling between CoO_2 shows 2D like behavior, so dimensionality plays a key role for the superconducting phase. However, the interesting thing about superconductivity in this compound is its relation to water molecules stretching the crystal structure. Lin *et al.* studied the intercalation and deintercalation process of water in single crystals of sodium cobaltate.[42] In Fig. 2.18, the possible structures of hydrated phases corresponding to the number of water molecules, *n,* in one formula unit are depicted. It was found that $y = 0$, 0.3, 0.6, 0.9, 1.3, or 1.8., but only the compound with $y = 1.3$ leads to superconductivity. The similarity of all hydrated compounds is the collapse or decomposition into Na_2O and Co_3O_4.Unfortunately, the most instable, hydrated phase is the one, which hosts superconductivity.

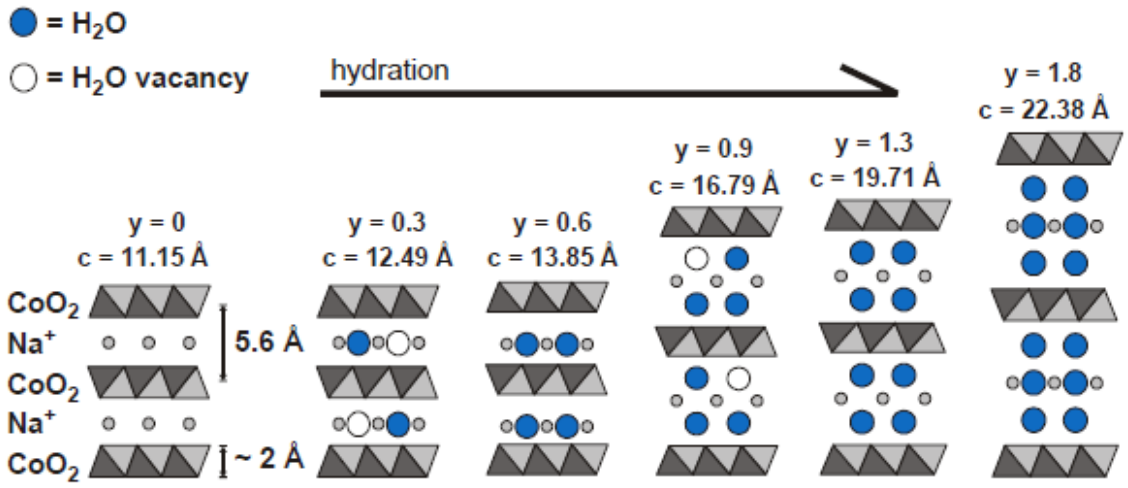

Fig. 2.18: Schematic representation of possible structures of ordered phases of $Na_{0.3}CoO_2{\cdot}yH_2O$, $y = 0$, 0.3, 0.6, 0.9, 1.3, and 1.8. Taken from Lin *et al.*[42]

As a function of hydration, two coexisting phases, $y = 0$ and $y = 0.6$, were observed in the XRD pattern. The dry sample was stored in air and absorbed water forming partially a hydrate. As hydration continues, the phase at $y = 0.6$ is stable for 10 days. The phase of $y = 1.3$ is formed after 1h of hydration. When the diffusion path of water molecules is along Na-planes filling partially occupied sites, the process does not stop until water saturation occurs in these planes. During the different stages of the intercalation process, two water molecules are inserted in each Na-site and form a cluster of $Na(H_2O)_2$, the resulting phase is $Na_{0.3}CoO_2$ $0.3H_2O$. Adding two more water molecules to the lower hydrate $Na_{0.3}CoO_2{\cdot}0.6H_2O$ is formed. This phase is metastable and forms only under ambient and humid conditions, it decomposes after long hydration times of 10 days. The phase at $y = 1.3$ is formed after 10 days, accompanied by decomposing of both other phases ($y = 0$ and $y = 0.6$). This leads to the conclusion, that the sample is fully hydrated after four water molecules are intercalated. The time dependence of the formation of the three phases ($y = 0$, $y = 0.6$, and $y = 1.3$) is deduced from the intensity of the (002) reflection as shown in Fig. 2.19. During the hydration process, there was no evidence for the formation of other possible phases (y = 0.3, 0.9, or 1.8) as shown in Fig. 2.18. This supports the theory that the initial intercalation process takes place with two water molecules, followed by another two water molecules forming an additional layer of H_2O between Na and CoO_2 planes.

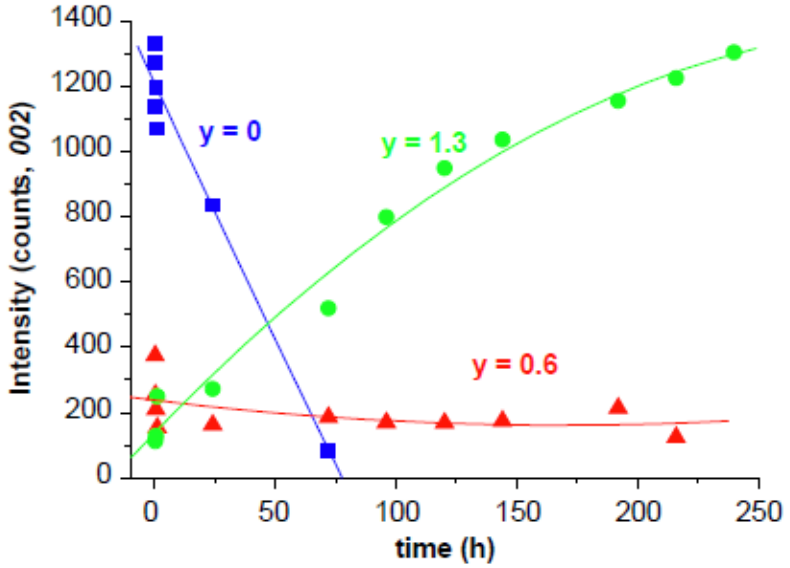

Fig. 2.19: Time dependency of the (002) intensity for y = 0, 0.6, and 1.3. Taken from Lin *et al.*[42]

After 15 days of hydration it is possible to stabilize the over-hydrated phase with $y = 1.8$. With thermogravimetric measurements (TG), the step-wise deintercalation process from the over-hydrated phase was monitored. Clearly, 5 steps of dehydration could be distinguished. The corresponding TG curve is presented in Fig. 2.20.

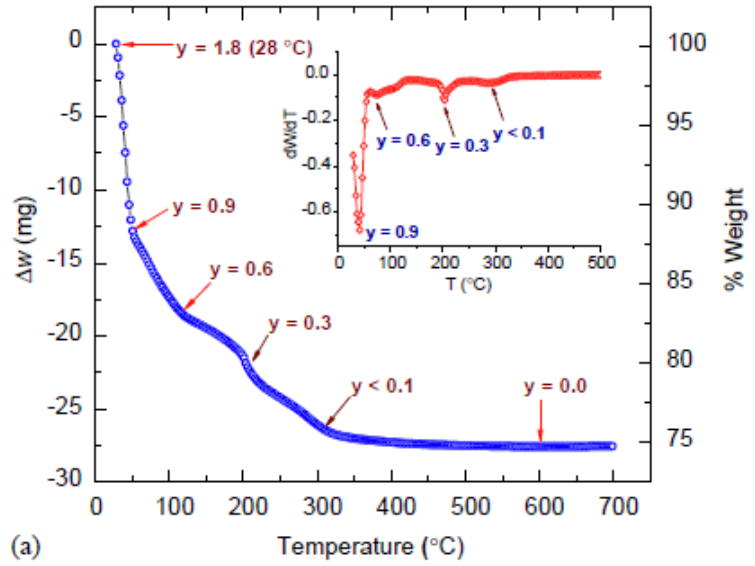

Fig. 2.20: TG curve of the over-hydrated $Na_{0.3}CoO_2 \cdot 1.8H_2O$ showing temperature dependency of the weight loss for the compound heated in 0.3 K/min in flowing oxygen. The inset shows the derivation of the curve. Taken from Lin *et al.*[42]

Each plateau corresponds to a dehydrated phase with different water content, the y values were calculated from the measured weight loss. Turning points between every plateau can be clearly seen in the derivative curve of the weight loss curve and can be attributed to phase transitions. The deintercalation process from $y = 1.3$ to lower y takes place stepwise. At temperatures of approximately 50, 100, 200, and 300 °C, water loss is estimated to be one

molecule per formula unit, corresponding to y = 0.9, 0.6, 0.3, and 0. The entire removal of water from the crystal lattice occurs around 600 °C.

The crystal stability of the superconducting compound is a major topic for investigating the mechanism of superconductivity. Barnes *et al.* focussed on the study of the deintercalation reaction of sodium using Br_2/H_2O and found that the complete reaction to $Na_{0.33}CoO_2 \cdot 1.3H_2O$ is finished after 1 to 2 hours.[43] With additional time, there is a further, but slow decrease of sodium. After long reaction times or large Br_2 concentration, a secondary phase is formed as shown in Fig: 2.21. A broad reflection develops at around 18-19° in 2θ near the (004) reflection of $Na_{0.33}CoO_2 \cdot 1.3H_2O$.

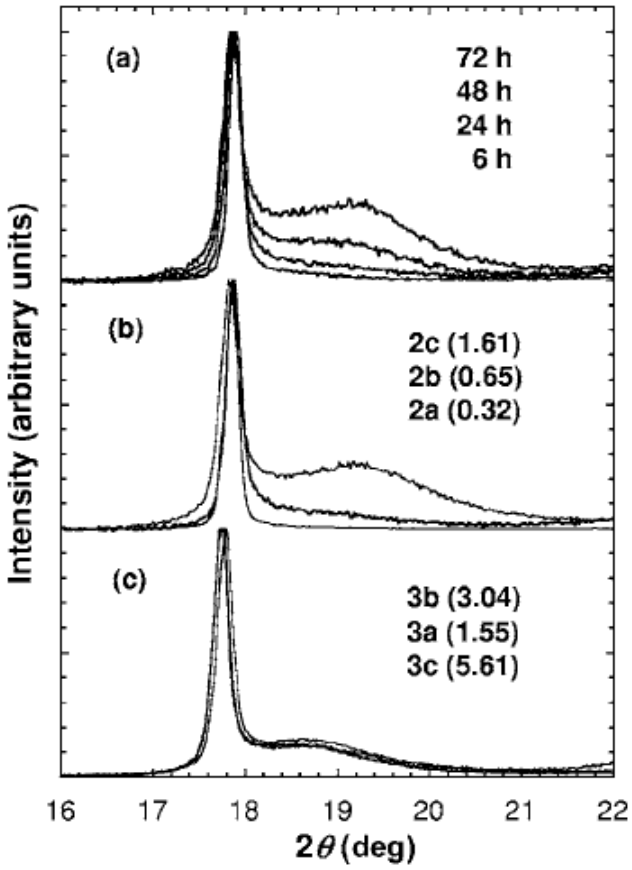

Fig: 2.21. (004) reflection (a) as function of reaction time, (b) as a function of Br_2 concentration, and (c) showing the effect of added Br_2 above the point of saturation. Taken from Barnes *et al.*[43]

The intensity of the (004) reflection increases with increasing reaction time. After treating a sample for two weeks with Br_2/H_2O it was possible to determine impurity phases $Na_{0.33}CoO_2 \cdot 0.6H_2O$ and CoOOH. The broad reflection around 18-19° in 2θ corresponds to the (002) reflection of CoOOH. It crystallizes in two different polymorphs, either hexagonal or rhombohedral.[44] X-ray data obtained by Barnes *et al.* denotes to the hexagonal CoOOH, which has the same structure like $Na_{0.33}CoO_2 \cdot 1.3H_2O$, but H^+ as separating species between CoO_2 planes. A possible reaction with intercalated water is presented in Eq. 2.7

Eq. 2.7 $$2Na_xCoO_2 \cdot yH_2O \rightarrow 2CoOOH + 2xNa^+ + 2xOH^- + (2y - x - 1)H_2O + (1 - x)/2O_2$$

According to this reaction a slow formation of oxygen vacancies in the CoO_2 layers occur, which continually reduce the oxidation state of Co. It was found that T_c is highest for the cobalt oxidation state +3.5. The formation of CoOOH affects superconductivity in Na_xCoO_2 in a negative way, so there is a narrow time gap, in which the formation of the hydrated compound takes place without forming impurity phases. The origin of the pairing mechanism for the observed superconductivity is not yet clear. There are two theories followed by scientific community; (i) spin-singlet (*d*-wave) pairing, and (ii) spin-triplet (*p*-wave) pairing on the other hand. Common to all theories of unconventional superconductivity is, that the Cooper pairs are not in spin-singlet states with *s*-wave symmetry known for conventional superconductors. According to the Pauli exclusion principle, pairs with a singlet or triplet spin part have a corresponding even or odd spatial part, denoted by *s*-, *p*-,*d*-, or *f*- wave pairing, according to the pair angular momentum of $L = 0$, 1, 2, or 3, respectively. High-T_c superconductors are also unconventional superconductors, but with singlet pairs and *s*-wave or *d*-wave symmetry.[45] Matano *et al.* reported about this evidence for *d*-wave pairing from ^{59}Co Knight Shift[a] measurements. It has been found that this shift decreases as a function of temperature below T_c along *a* and *c* axis. The field dependence of the Knight shift K_a and K_c, as well as the decrease of it is ceased above a $H_{c2} = 7$ T, which is an evidence for line nodes in the gap function. In node less state superconductors, all quasi-particles are localized in vortex cores and the Knight shift originating from nuclei outside the vortex cores will have no dependence of the magnetic field.[46] If there are nodes in the gap function, the quasi-particles will be emerged of the vortex core along the nodal directions and the density of states will be proportional to $H^{1/2}$. Such a feature has been observed in typical *d*-wave superconductors. The reduction of K_a and K_c below T_c is due to the reduction of spin susceptibility which is an indication for Cooper pairs in the singlet state. The same result was published by Kuroki *et al.*, who postulate an inner Fermi surface in addition to the outer Fermi surface for a high Fermi level, which results in two disconnected Fermi surfaces.[47] This inner Fermi surface occurs due to local minimum structure of the a_{1g} band at the Γ point. From their calculations, superconductivity has a *s*-wave symmetry gap with a change of sign between the inner and the outer Fermi surface. The presented theories are two examples for the controversial discussion about pairing symmetry in Na_xCoO_2. Mazin *et al.* have reported a critical estimation of pairing symmetry and derive a 2*D* order parameter in $Na_xCoO_2{\cdot}yH_2O$.[48] They consider 26 possible symmetries compatible with the hexagonal structure. Some of these symmetries can be excluded due to their nonconformity with the electronic structure of Na_xCoO_2, others can be excluded due to the absence of characteristic effects, which are associated with them. In total six out of 26 possible symmetries match with physical properties and the observed effects in $Na_xCoO_2{\cdot}yH_2O$. In these six symmetries, three different pairing symmetries are present, *p*, *d* and *f*. After refinement of the stabilization criteria by pairing energy, four additional symmetries can be excluded, since they would imply a remarkable loss in pairing energy. The two remaining states are $x(x^2\text{-}3y^2)z$ and $y(y^2\text{-}3x^2)z$. For these states the most likely superconducting symmetry is the *f*-state. The *f*-wave states correspond to Cooper pairs with spins in the *xy* planes and thus to a constant Knight shift. The superconducting state of $Na_xCoO_2{\cdot}yH_2O$ cannot be identified unambiguously, but the number of possibilities can be reduced by studies of that kind. For further

[a] The Knight shift is the shift in the nuclear magnetic resonance frequency of paramagnetic materials. It refers to the shift *K* of element in a metal environment due to conducting electrons in the metal, compared to the same element in a non-metal environment.[18] W. D. Knight, Physical Review **76**, 1259 (1949).

investigating the superconducting gap symmetry, tunneling spectroscopy on superconducting thin films would be required to settle the controversial discussion on the superconducting mechanism in $Na_xCoO_2 \cdot yH_2O$.

2.1.1 Na_xCoO_2 thin films

Thin films of Na_xCoO_2 have been grown using different deposition techniques, PLD,[49-53] reactive solid phase epitaxy (R-SPE),[54] and sol-gel spin coating.[55] Table 2.2 gives an overview of various Na_xCoO_2 thin films grown with different techniques. The sodium content in the films is between 0.5 and 0.83, depending on the deposition method. All kinds of possible phases of Na_xCoO_2 were grown, whereas most films are γ- phase. A very promising deposition method for film with high sodium content is R-SPE used by Ohta *et al.*[54] They deposited a CoO epitaxial layer with PLD on a *a*-cut sapphire substrate, capped by an yttria stabilized zirconia single crystal plate to avoid surface contamination. In the next step $NaHCO_3$ powder was added to the stack and put together in a furnace at 700 °C for one hour. During heat treatment, two phase changes occurred, which are illustrated in Fig. 2.22. In a temperature range between 300 and 600 °C, first thermal oxidation of CoO to Co_3O_4 takes place, in the second step between 600 and 700 °C Na_xCoO_2 is formed by diffusion of Na^+ ions into the Co_3O_4 layer. The grown films are epitaxial after heat treatment. There are two important features for the Na^+ diffusion used by Ohta *et al.*[54] First, the insertion of Na^+ is limited to lateral directions, the insertion of the top layer is not sufficient since as it was observed that only the periphery of the Co_3O_4 film has been transformed into Na_xCoO_2. Second, the epitaxial film is retained after the diffusion of Na^+ is finished, instead of breaking the film due to intercalation. It is considered that cracking due to Na^+ diffusion and healing by solid-state sintering is very well-balanced at this temperature range. The thermoelectric properties of these films were comparable to those obtained for bulk single crystals.

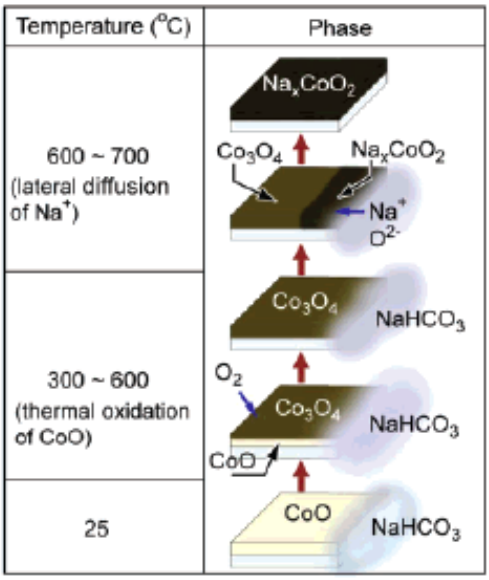

Fig. 2.22: Schematic illustration of the growth mechanism of Na_xCoO_2 epitaxial layers by R-SPE.[54]

Table 2.2: Overview of different Na_xCoO_2 thin films grown by various deposition techniques.

Author	*x* (Na)	Phase	Orientation	Method	Substrate/ (Orientation)	Year
H. Ohta *et al.*	0.83	γ	11-20	R-SPE	*a* -cut sapphire	2004
X.P.Zhang *et al.*	0.71,0.75	α' , γ	001	PLD	$LaAlO_3$(001)	2005
J.Y.Son *et al.*	0.6, 0.7	β, γ	001	PLD	*c* -cut sapphire	2005
Y. Krockenberger *et al* .	0.58	γ	001	PLD	$SrTiO_3$(001) MgO (001) $NdGaO_3$(001) $SrLaGaO_4$(100) *r*- cut sapphire	2005
H. Zhou *et al.*	~0.6	β	001	PLD	LaAlO3(001) $SrTiO_3$(001) MgO (001)	2005
W.J. Chang *et al.*	~0.68	γ	001	PLD+Na lateral diffusion	c-cut sapphire	2006
L.Yu *et al.*	0.51,0.54, 0.59	γ	001	PLD	$SrTiO_3$(001)/ 5°[010]	2007
J.Y.Son *et al.*	0.5, 0.7	γ	001	PLD+ deinter calation	*c* -cut sapphire	2008
J.Y.Son *et al.*	0.7	*g*	001	PLD	*c* -cut sapphire $SrTiO_3$(111) MgO(111)	2007 2008
K. Sugiura *et al.*	0.78	*g*	11-20	R-SPE	*c* -cut sapphire	2009
C.-J. Liu *et al.*	0.7	*g*	001	Sol-Gel spin coating	*c* -cut sapphire	2009
L.Yu *et al.*	0.5-0.7	*g*	001	PLD	$SrTiO_3$ (100), $SrTiO_3$(110), $LaAlO_3$(100) *c* -cut sapphire	2011

Most of the publications on film growth of Na_xCoO_2 were in 2005. Different authors used PLD to fabricate epitaxial films of Na_xCoO_2 on different substrates. Therefore a target is prepared commonly by solid state sintering of Na_2CO_3 and Co_3O_4 stoichiometrically mixed. The sodium content in the resulting targets vary from $x = 0.75$ (Zhang *et al.*[50]), over $x = 0.8$ (Son *et al.*,[51, 56, 57] Zhou *et al.*[49]), to $x = 0.86$ (Yu *et al.*[58]). Depending on the deposition parameters used, sodium content and crystal phase of the films could be controlled as well as surface morphology. Son *et al.* demonstrated a kinetic dependence of thin film growth.[51] With a low deposition rate of 0.02 Å/pulse resulting in layer-by -layer growth only γ-Na_xCoO_2 could be stabilized, whereas an increase of the deposition rate lead to mixed phases of β and γ. At the higher side, for 0.2 Å/pulse only the β-phase is stable. The growth mode is also influenced by

the deposition rate, β-phase films show according to *Vollmer-Weber,* whereas γ-phase films grow according to *Frank-van-der Merwe* growth mode. From Table 2.2 is can be seen, that not all Na stoichiometries can be made as thin films, since the Na_xCoO_2 has metastable phases. By optimization the growth and annealing conditions during film deposition it might be possible to stabilize films with $x < 0.5$. In this context the epitaxial relation between substrate and film is interesting to understand the growth mode of Na_xCoO_2.

The surface roughness of the γ-phase was 8 Å in RMS. The film surface show large terraces with terraces heights of nearly half of the *c*-axis. The large width of the terraces represent that the surface diffusion of ad-atoms along the surface is long enough and the kinetics of the steps is widespread due to the low deposition rate inhibiting from frequent nucleation of ad-atoms, like in the growth of the β- phase.[59] A very important deposition parameter for PLD in general is substrate temperature. Deposition temperatures available in literature differ between 200 and 750 °C. It has to be mentioned, that high deposition temperatures above 650 °C do not favor the formation of Na_xCoO_2 due to the high volatility of Na, while low temperatures below 500 °C lead to the formation of impurity phases, such as $Na_2(CoO_3)$, Na_3CoO_2, and Co_3O_4.[49]

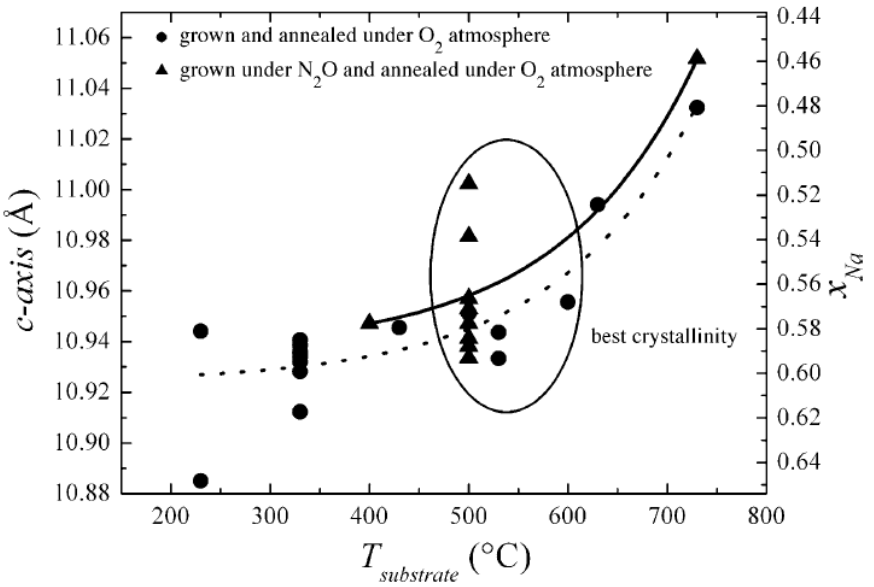

Fig. 2.23: Temperature dependency of the *c*-axis of thin films of Na_xCoO_2 grown on STO (001), taken from Krockenberger *et al.*[53]

Krockenberger *et al.* analyzed the temperature dependency of the *c*-axis, Na-content, and film crystallinity of films grown on $SrTiO_3$ (STO) oriented in (100), results are shown in Fig. 2.23.[53] The higher the deposition temperature, the lower the sodium content in the films. Best crystallinity is achieved at intermediate temperatures in the range of 480 - 600 °C. However, it is necessary to post-anneal the films to achieve good crystallinity. It is worth to mention, that with sodium content in the target below $x = 0.65$, pure Co_3O_4 is obtained in the resulting films. Son *et al.* investigated the dependence of sodium content and (002) peak position, compairing films with $x = 0.5$ and $x = 0.7$, results are shown in Fig. 2.24.[60]

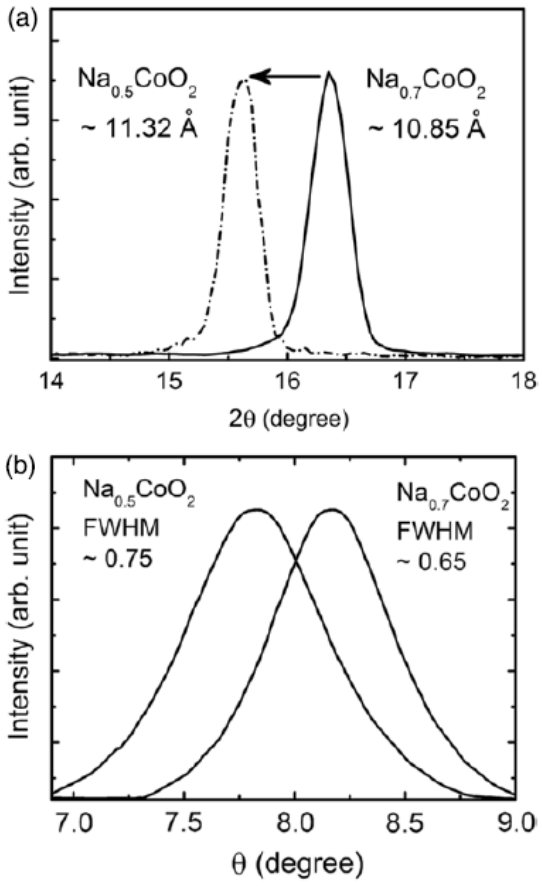

Fig. 2.24: (a) (002) reflection of Na_xCoO_2 thin film with $x = 0.5$ and 0.7. (b) Rocking curves of the (002) reflection of $Na_{0.5}CoO_2$ and $Na_{0.7}CoO_2$ thin films.

To reduce the sodium content from $x = 0.7$ to $x = 0.5$, an iodine solution was used, in which the film has been dipped in intervals of 30 min. As Krockenberger *et al.*, Son *et al.* found a six-fold symmetry of the (104) reflection, which corresponds to a the hexagonal structure of the films.[53] The full width at half maximum (FWHM) of the (104) reflections determined for $Na_{0.7}CoO_2$, differ from the FWHM found for $Na_{0.5}CoO_2$, probably in-plane crystallinity is influenced by deintercalation of sodium. From the (104) reflections, the *a*-axis lattice constants were determined to be 2.81 Å for $Na_{0.5}CoO_2$ and 2.82 Å for $Na_{0.7}CoO_2$, respectively. These values are slightly lower compared to the value of a single crystal of $Na_{0.7}CoO_2$. This small change in *a* is attributed to the relatively high change in *c* (11.32 Å for $x = 0.5$ and 10.85 Å or $x = 0.7$) compared to *c* for bulk Na_xCoO_2 (11.11 Å for $x = 0.5$ and 10.97 Å or $x = 0.7$).[7] This confirms the high Young's modulus of the CoO_2 layers. The surface morphology of the thin films observed with SEM and AFM in Fig. 2.25 show spiral patterns with multi-terraces, which indicate epitaxial film grown with atomically flat surfaces.

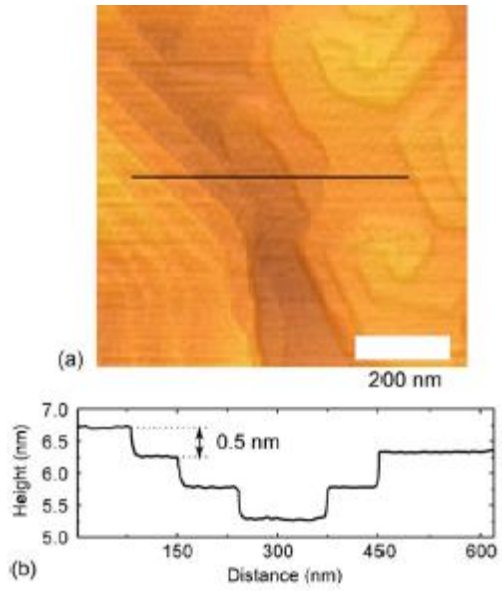

Fig. 2.25: (a) AFM image of an epitaxial $Na_{0.5}CoO_2$ thin film fabricated by Son *et al.*[60] (b) Sectional contour graph of the line shown in the AFM image in (a).

The resistivities for the thin films grown by Son *et al.* show two different behaviors.[61] The $Na_{0.5}CoO_2$ thin film exhibits an insulating transport behavior with three weak anomalies known for charge-ordered insulators below 100 K, similar to single crystals.[7] The resistivity of the $Na_{0.7}CoO_2$ films follows metallic behavior, as observed for bulk single crystals. Corresponding data is presented in Fig. 2.26.

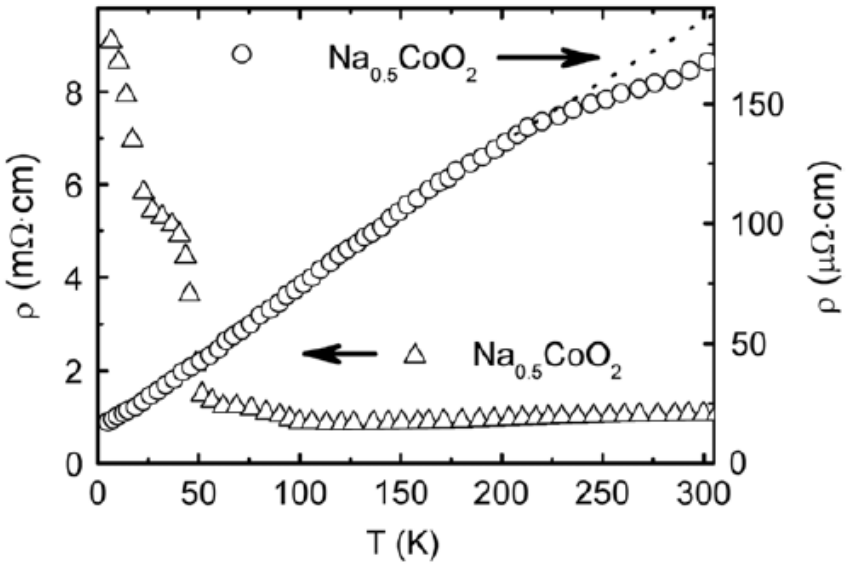

Fig. 2.26: Resistivities of $Na_{0.5}CoO_2$ and $Na_{0.7}CoO_2$ thin films, taken from Son *et al.*[61]

In Na_xCoO_2 the Co ion has a two-dimensional triangular lattice and low spin states of Co^{3+}or Co^{4+} ions, the oxygen 2*p* states are lower in energy than the cobalt 3*d* states. The ratio of $Co^{3+}$to Co^{4+} is affected by the amount of sodium acting as a donor changing Co^{4+} with S=1/2 to Co^{3+} with S = 0. The current transport mechanism can be described by hole hopping (spin S = -1/2) at Co^{4+} ions to Co^{3+} ions in a diamagnetic matrix. Up to 200 K, the temperature dependence of the resistivity shows a linear increase indicating the presence of a

strongly-correlated system. The resistivity is ~177 μΩcm at 300 K, which is lower as for bulk single crystals. Depending on the substrate type (Fig. 2.27), the behavior of resistivity as a function of temperature changes. This was proven by Krockenberger *et al.* by comparing $Na_{0.58}CoO_2$ films grown on $SrTiO_3$ (001)with $Na_{0.58}CoO_2$ films grown on $SrLaGaO_4$ (100).[53]

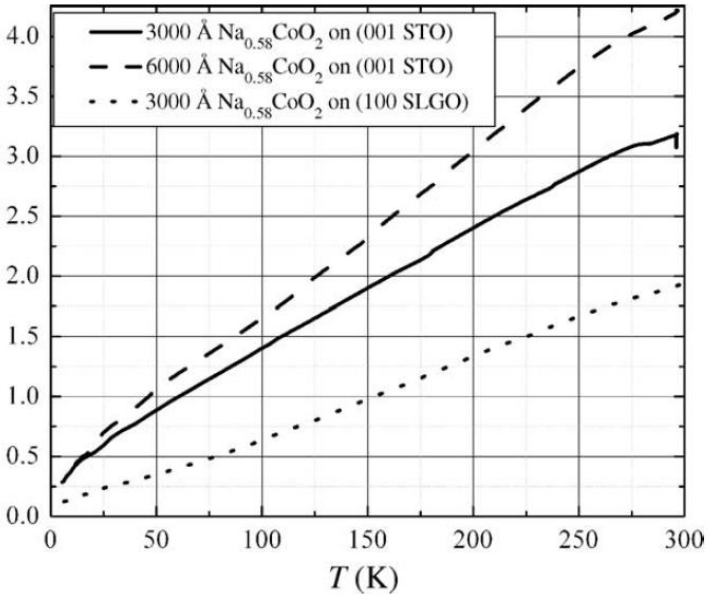

Fig. 2.27: Resistivity as a function of temperature of $Na_{0.58}CoO_2$ thin films grown on STO (001) and SLGO (100). Taken from Krockenberger *et al.*[53]

The films grown on different substrates show qualitatively similar resistivity behavior, but the absolute resistivity values are lowest for the film grown on (100) $SrLaGaO_4$. This could be due to a lower lattice mismatch for this substrate. For $Na_{0.58}CoO_2$ thin films, a metallic behavior was found by Krockenberger *et al*. over the hole temperature range, which is contradictionary to findings in literature. Okabe *et al*. associated an upturn in resistivity around 50 K with an t onset of the charge ordering phase.[62] The choice of substrate has a huge impact on film growth, physical properties, and film morphology. Depending on the amount of epitaxial stress, the growth mode changes. The comparison of *c*-cut sapphire, MgO (111), and $SrTiO_3$ (111) substrates published by Son *et al.,* emphasize the importance of strain for the growth of Na_xCoO_2.[56] Especially surface morphology is affected by the used substrate type.

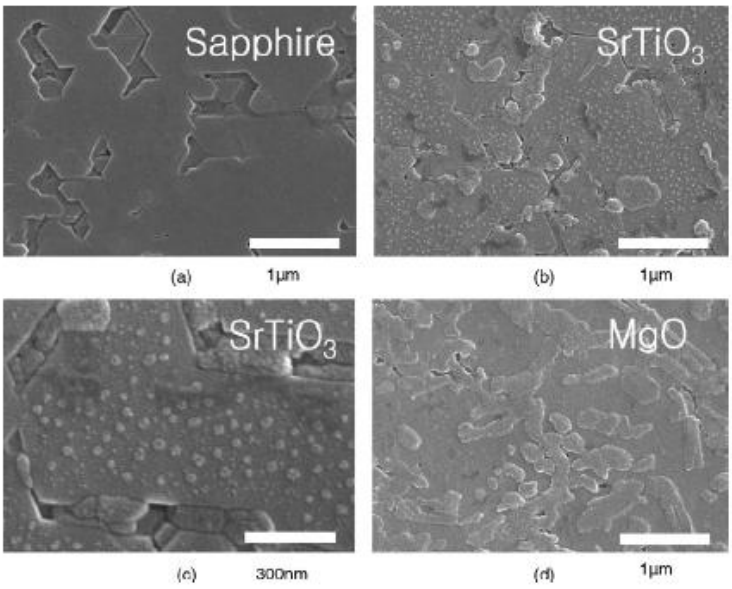

Fig. 2.28: Surface morphologies of $Na_{0.7}CoO_2$ thin films grown on (a) *c*-cut sapphire, (b) and (c) $SrTiO_3$ (111), and (d) MgO (111) substrates. Taken from Son *et al.*[56]

On *c*-cut sapphire, large hexagonal grains of Na_xCoO_2 are observed. The film grows in step-flow mode resulting due to low deposition rate of 0.02 Å/per pulse used during ablation. The films grown on (111) $SrTiO_3$ show similar hexagonal grains, but with additional nano-islands of around 30 nm diameter. These nano islands are formed as a result of the release of elastic strain energy during relaxation as the lattice misfit is 2.4%. This implies a change in growth mode from step-flow to Stranski-Krastanow growth mode. On (111) MgO, large grains are formed by excess ad-atoms covering an aperture between hexagonal grains. The lattice misfit of 5.4% for (111) MgO leads to tensile stress. Under these conditions and a critical thickness of step-flow growth mode, the grains are formed by ad-atom diffusion into grain boundaries resulting from an increasing chemical potential on the surface of hexagonal grains. The comparison of the AFM images (Fig. 2.29) of the film surface grown on *c*-cut sapphire and (111) $SrTiO_3$ shows a spiral feature with 100 - 200 nm multi-terraces and nano-islands with a height of 6.2 nm, respectively. On the (111) MgO substrate, terrace width is smaller than for terraces on *c*-cut sapphire, which indicate a lower diffusion coefficient for step-flow growth on MgO.

Another physical property, which is dependent on substrate type was found by Yu *et al.*[58] They investigated *c*-axis oriented, 200 nm thick $Na_{0.54}CoO_2$ thin films grown on (100) $SrTiO_3$ with a 5° vicinal cut towards [010]. The vicinal cut of the substrate results in a step-and-terrace structure with typical step heights of 0.39 nm, and a terrace width of 4.4 nm. Resistivity was obtained along [100] and [010] directions, Fig. 2.30 (a) and (b).

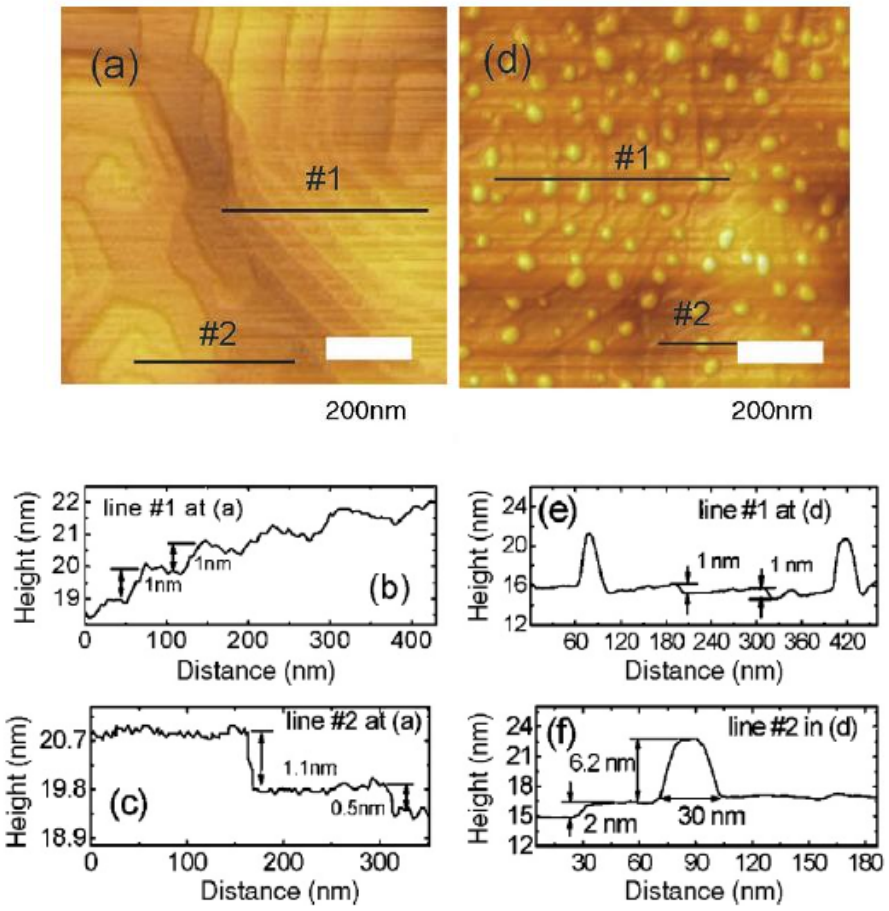

Fig. 2.29: AFM images of $Na_{0.7}CoO_2$ thin films grown on (a) *c*-cut sapphire and (d) (111) $SrTiO_3$. (b-f) Sectional contour graphs of the corresponding lines #1 and #2 in (a) and (d). Taken from Son *et al.*[56]

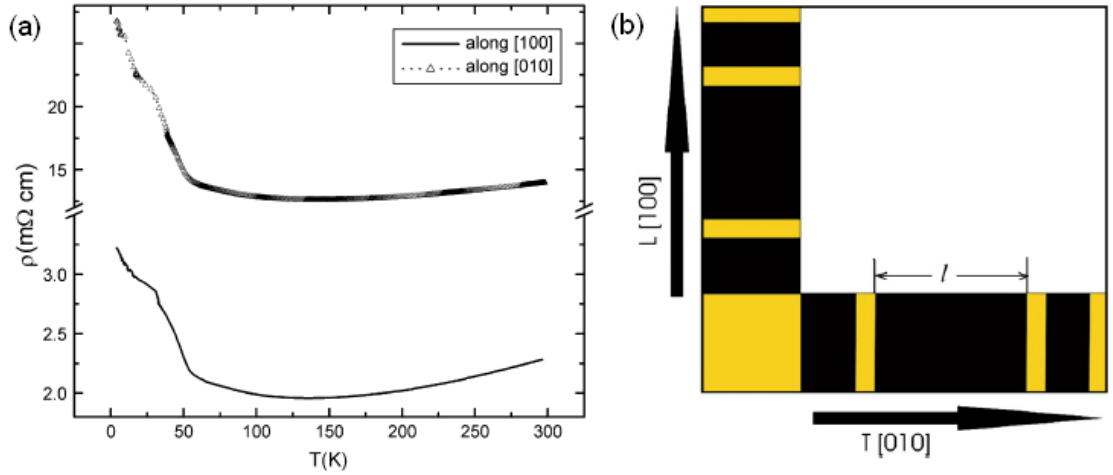

Fig. 2.30: (a) Resistivity vs. temperature of a $Na_{0.54}CoO_2$ film grown on (100) $SrTiO_3$ with 5° vicinal along [100] and [010]. (b) Scheme of a pattern $Na_{0.54}CoO_2$ film with the directions longitudinal (L) and transversal (T) to the step edges. Taken from Yu *et al.*[58]

Along [100] direction, a weak temperature dependency of the resistivity ρ_L between 50 K and 300 K is observered. It is followed by a strong increase of ρ_L to a charge ordered state, which is in good agreement with the data published on $Na_{0.5}CoO_2$ single crystals.[7] Quantitative analysis of ρ_L shows that it is enhanced by a factor of 8 due to grain boundary scattering and crystallographic disorder in the film. The ρ_T curve shows similar temperature

dependence, but having a 6.2 times larger resistivity at room temperature along [010]. This increase of resistivity can be explained by a combination of in-plane and *c*-axis current transport according to Eq. 2.8, derived by Haage *et al.* for YBCO system.[63]

Eq. 2.8
$$\rho_T(T) = \rho_c(T)\sin^2\theta + \rho_a(T)\cos^2\theta$$

In Eq. 2.8, θ is the tilt angle of the substrate. In YBCO a similar anisotropy of the resistivity along different directions was found. Along *T* there is a zigzag current path, perpendicular to CuO_2 planes and parallel to the CuO chains as basis of the current transport theory. A modeled macroscopic current flowing through a network of resistors linked in series represents the in- and out-of-plane contributions to the current path. A similar anisotropy of resistivity (ρ) and Seebeck coefficient (S) was found for 180 nm thick $Na_{0.7}CoO_2$ thin films grown on *m*-cut sapphire by R-SPE by Sugiura *et al.,* see Fig. 2.31.[64] Resistivity and Seebeck coefficient were measured below 300 K by standard four-probe technique and conventional steady state method along three directions, parallel (*x*), perpendicular (*y*) to [1120], and along *c*. ρ_c and S_c were comparable to those measured *in-plane* in single crystals. Along the [*x*], ρ_x and S_x display metallic hole conduction with values similar to ρ_c and S_c suggesting that the conductivity along [*x*] is controlled by hole transport within CoO_2 planes. The slight difference of ρ_x to ρ_c is probably due to defects in the film in the *m*-plane. In contrast, ρ_y and S_y show anisotropic behavior. As for ρ_x, resistivity steeply increases, however, the values for ρ_y are five to ten times higher than for ρ_x. S_y increases almost linearly with temperature, compared to S_x the values are ½ times S_x. The behavior of ρ_y as a function of temperature differs from that for out-of-plane resistivity reported for thin single crystals,[11] which show a crossover at ~200 K likely due to a change in dimensionality or due to sodium rearrangement.[65, 66] This implies that hole transport properties along [*y*] do not perfectly coincide with *c*-axis transport, as assumed from the tilted crystallographic orientation of the film. Summarizing the results, a higher thermoelectric performance can be achieved within the CoO_2 plane. This kind of anisotropy is consistent with other layered cobaltates, including Ca_xCoO_2, Sr_xCoO_2,[67] and $Ca_3Co_4O_9$.[68] One of the most important features in the layered cobaltates is a rather large in-plane Seebeck coefficient compared to the out-of-plane Seebeck coefficient, despite the lower in-plane resistivity.

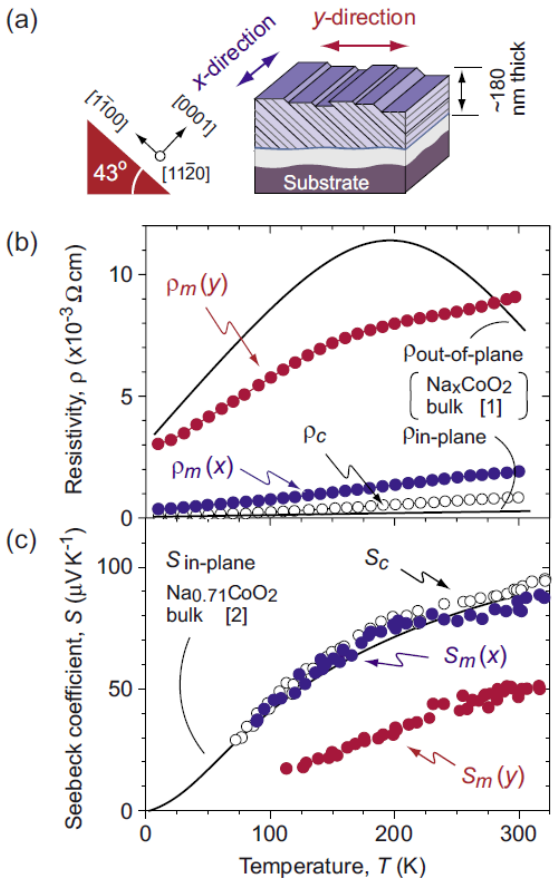

Fig. 2.31: (a) Scheme of a 180 nm thick $Na_{0.7}CoO_2$ thin film on *m*-cut sapphire, [*x*] and [*y*] are parallel and perpendicular to [11-20].(b) resistivity vs. temperature dependence along *x*, *y*, and *c*. (c) *S*-*T* dependence along *x*, *y*, and *c*. Reference data [1] and [2] for single crystals are included as well. Taken from Sugiura *et al.*[64]

Within a variety of anisotropic thermoelectric compounds, like Bi_2Te_3[69] or other oxides,[70] *S* along the direction of the lower ρ is small or similar to that along the direction of the higher ρ, mainly due to difference of the band dispersion. The large Seebeck coefficient in cobaltates may be due to the highly reduced valence band width within the CoO_2 plane, caused by strong coulomb repulsion between charge carriers on triangular Co sites.

2.1.2 Superconducting Na_xCoO_2 thin films

Since superconductivity was reported for bulk Na_xCoO_2 in 2003, only two authors , Krockenberger *et al.*[8] and Liu *et al.*,[55] reported on superconducting thin films grown by PLD and sol-gel spin coating. In order to obtain superconducting $Na_xCoO_2{\cdot}yH_2O$ thin films by PLD, it is necessary to intercalate water into films with a sodium content of $x \approx 0.3$. This was achieved by first stabilizing $Na_{0.6}CoO_2$ films on (100) STO substrates and subsequently deintercalating Na^+ ions by the use of a strong oxidizing agent like a bromine solution to achieve the desired composition. More critical is the intercalation of water into the thin films. In contrast to bulk materials, thin films have to be handled with care to avoid peeling off the substrate. Krockenberger *et al.* used 100% humidity supplied by a D_2O bath at a well-defined temperature of 19 °C for up to 196 h.[8] After this treatment, $Na_{0.3}CoO_2{\cdot}1.3D_2O$ films were obtained with a clean and smooth surface. In the corresponding ρ–*T* curve, as well as in the magnetization curve, both presented in Fig. 2.32, the films show a superconducting transition

at T_{c0} = 4.2 K with a flux expulsion effect at the critical temperature in the magnetization curve. The transition width (1.5 K) is relatively sharp, confirming high film quality. Above T_c films show metallic behavior up to room temperature, similar to HTSC's.

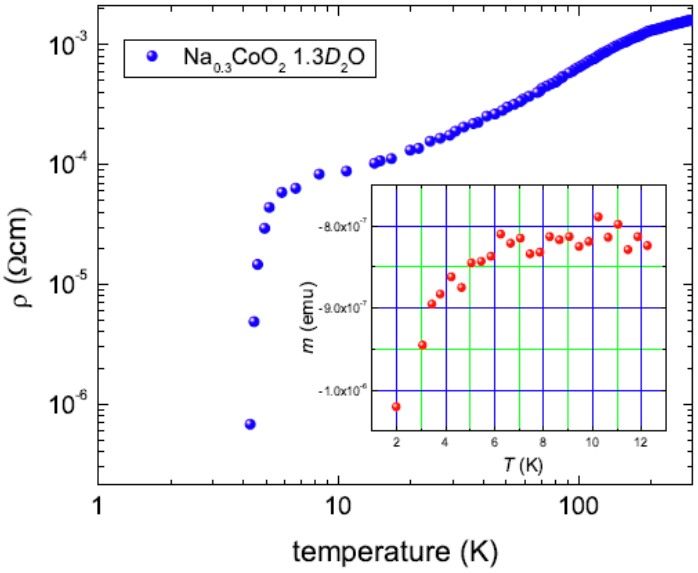

Fig. 2.32: Resistivity vs. temperature for a $Na_{0.3}CoO_2 \cdot 1.3D_2O$ thin film grown on STO (100). The inset shows the corresponding magnetization vs. temperature curve. Taken from Krockenberger *et al.*[8]

The second reported superconducting 700 nm thick $Na_{0.7}CoO_2$ thin film was deposited by sol-gel spin coating on *c*-cut sapphire substrates with subsequent treatments of $NaMnO_4$ solution as a deintercalation and oxidizing agent and afterwards stored in a wet desiccator for 4-7 days to obtain the superconducting phase.[55]

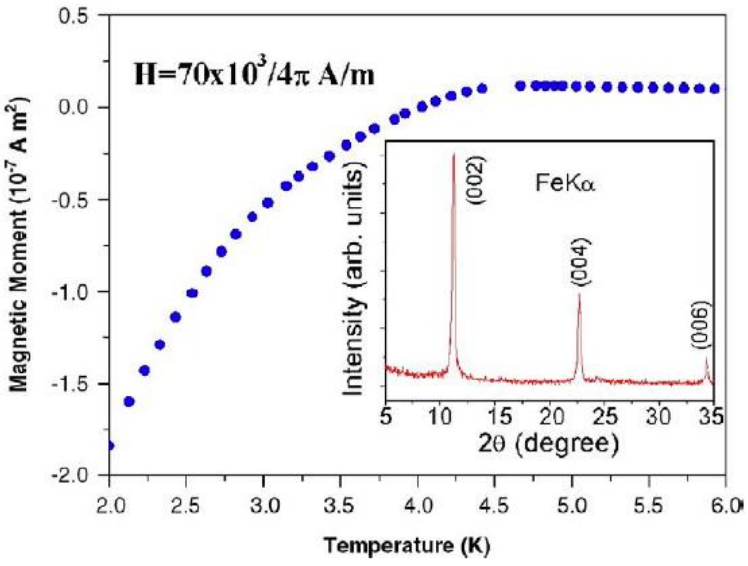

Fig. 2.33: Temperature dependency of the magnetic moment of a water-intercalated film prepared by sol-gel spin coating and sintered at 800 °C. The inset shows the corresponding XRD pattern of the film using Fe K_α radiation, Taken from Liu *et al.*[55]

In contrast to films made by Krockenberger *et al.*, the onset temperature of the superconducting transition is T_{onset} = 4.12 K, probably quality of the sol-gel spin coated films is lower

than that of films grown by PLD. Additionally impurity phases such as Co_3O_4 are present in most films and the spin-coated films are not epitaxially grown, as besides to the (00*l*) reflections, (101) and (104) reflections could be indexed in the XRD pattern shown in Fig. 2.34.

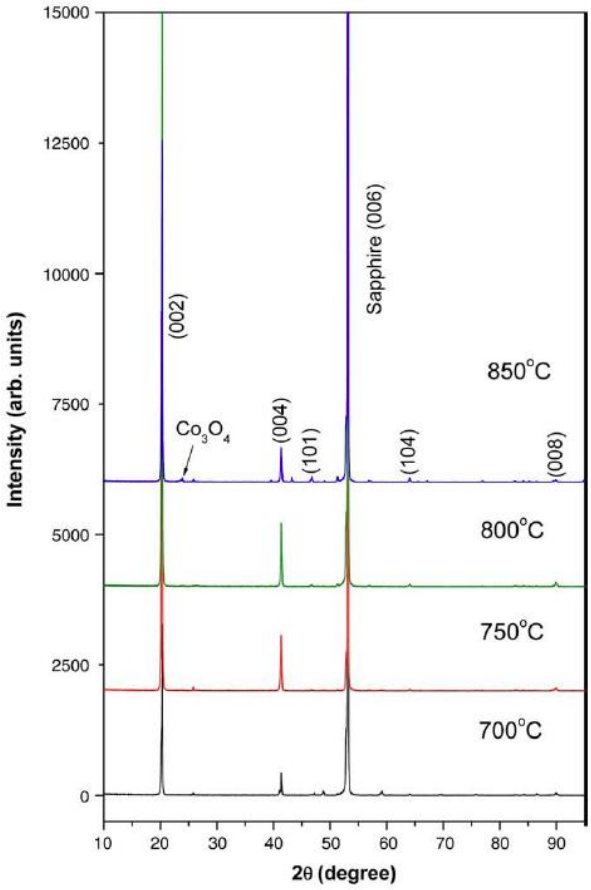

Fig. 2.34: XRD pattern of γ-Na_xCoO_2 films at different sintering temperatures. Taken from Liu *et al.*[55]

2.2 Lithium cobaltate (Li_xCoO_2) and other oxides

$LiCoO_2$ as a layered compound has drawn a lot of attention from scientific community focusing on rechargeable Li-ion batteries. Li-ion cells have been realized commercially in the early 1990s. Li-ion batteries provide higher energy density compared to other rechargeable batteries such, as lead-acid, nickel-cadmium, and nickel-metal hydrate. The basic principles of batteries are described elsewhere.[71, 72] Due to their higher cell voltage (open-circuit voltage V_{OC}) of ~4 V, the very light-weight lithium, and Li having the highest oxidation potential of all elements, battery cells have high volumetric and gravimetric energy densities. This is achievable by the use of non-aqueous electrolytes, which allow a wider range of operation temperatures. Modern lithium batteries are made from intercalation compounds of both electrodes, such as $LiCoO_2$ as cathode material and lithiated graphite (LiC_6) as anode material. Rechargeable lithium batteries in general involve a reversible insertion and extraction of lithium ions into and out of the electrode materials. This process is a redox reaction of electrode materials represented by moving ions through the electrolyte in one direction and by an electronic current flowing through an external circuit in the opposite direction. During the lithium insertion and extraction processes, the layered structure is maintained, which results in good

reversibility. One very important characteristic of a cell is the difference in chemical potential (V_{OC})between cathode, $\mu_{Li(c)}$, and anode, $\mu_{Li(a)}$, which is defined as follows.

Eq. 2.9
$$\frac{\mu_{Li(c)} - \mu_{Li(a)}}{F}$$

F represents the Faraday constant (96,485 C/mol). The open-circuit voltage is determined by the chemical potentials of lithium involved in the transport reactions at the electrodes. These transport mechanisms are a function of the work functions of anode and cathode. The energy diagram of a lithium cell is illustrated in Fig. 2.35.

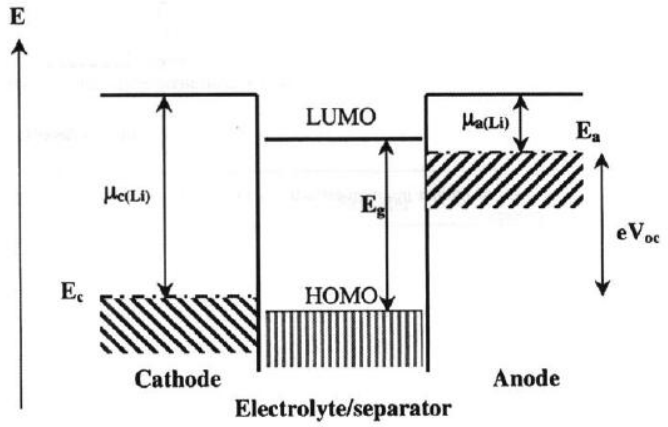

Fig. 2.35: Schematic energy diagram of a lithium cell with open contacts. HOMO represents the highest occupied molecular orbital and LUMO the lowest unoccupied molecular orbital in the electrolyte. Taken from Nazri *et al.*[71]

For thermodynamic stability, the redox energy levels of the cathode (E_c) and the anode (E_a) should be located within the band gap (E_g) of the electrolyte. This inhibits an unwanted reduction or oxidation of the electrolyte during charging and discharging. These processes are the reason why electrochemical stability limits cell voltage according to the criteria shown in Eq. 2.10.

Eq. 2.10
$$eV_{OC} = \mu_{Li(c)} - \mu_{Li(a)} < E_g$$

To successfully build a cathode in a rechargeable lithium cell, the insertion compound $Li_xM_yX_z$ has to fulfill at least six criteria:

1. Possibility to insert and extract huge amounts (x) of lithium maximizing cell capacity.
2. Reversibility of the insertion and extraction process without major changes in structure providing good cycling stability.
3. The insertion compound should exhibit electronic (σ_e) and ionic conductivity (σ_{Li}) to minimize polarization losses during charging and discharging.
4. Chemical inertness of the insertion compound with respect to the electrolyte.
5. The redox energy level of the electrodes should be located in between the band gap of the electrolyte preventing their oxidation or reduction.
6. The insertion compound has to be cheap, eco-friendly, and light-weight, so the M^{n+} ions should be 3*d*-transition metals.

Possible candidates for the insertion compound are shown in Fig. 2.36, sorted by their electrochemical potential vs. Li metal. This work concentrates on cathode compounds of

formula $LiCoO_2$, $LiNi_{1/2}Co_{1/2}O_2$ (LNCO), and $LiNi_{1/3}Mn_{1/3}Co_{1/3}O_2$ (LNMCO). Nowadays, the most commonly used cathode material nowadays is $LiCoO_2$ due to its high cell voltage, electrochemical properties, and stable structure during charging and discharging. $LiCoO_2$ stabilizes in rock salt structure, in which Li^+ and Co^{3+} occupy alternating (111) planes, so that stacking along *c*-axis is –(O-Li-O-Co-O)-. The oxygen stacking herein is ABCABC. This structure similarly named as the *O*3 structure, as the Li ions occupy octahedral sites and in total there are three CoO_2 layers per unit cell, see Fig. 2.37.

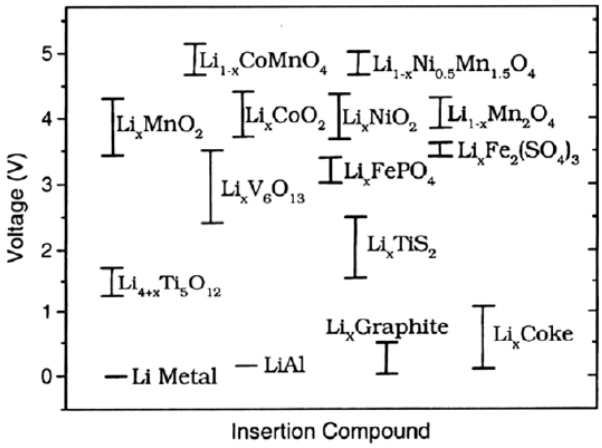

Fig. 2.36: Electrochemical potential vs. Li metal for possible insertion compound candidates. Taken from Nazri *et al.*[71]

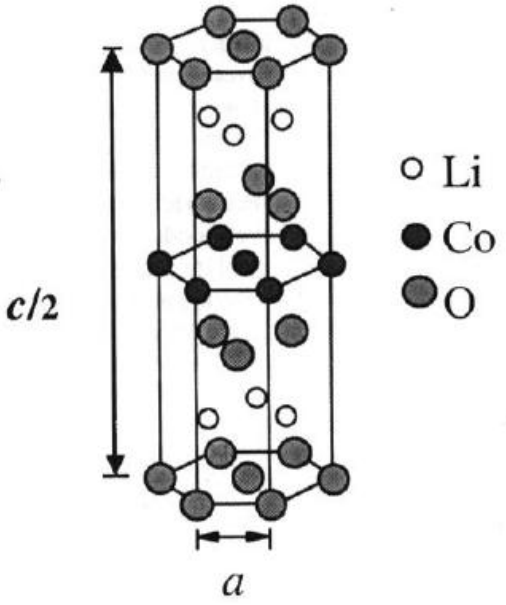

Fig. 2.37: Schematic of the crystal structure of layered O3 $LiCoO_2$. Taken from Nazri *et al.*[71]

The $LiCoO_2$ structure with strongly correlated CoO_2 planes allows reversible Li^+ insertion and extraction into and out-of the Li planes. Hereby, a fast two-dimensional flow of Li ions in between CoO_2 is possible due to the edge-shared LiO_6 octahedrals. This is the reason for a high ionic conductivity. A high electronic conductivity in this structure is guaranteed by the edge-shared CoO_6 arrangement with a direct connection between the Co atoms. The reason for that is the direct Co-Co interaction with a partly filled t^{6-x}_{2g} band, depending on whether if the cobalt ion is in 3^+ or 4^+. Superior structural stability is provided by the strong preference of low-spin Co^{3+} ($t^6_{2g}e^0_g$) and Co^{4+}($t^5_{2g}e^0_g$) on the octahedral sites, which enable a migration of

$Co^{3+/4+}$ ions from these sites to octahedral sites of lithium planes. However, only half of the lithium ions per formula unit can be reversibly inserted and extracted, leading to a limitation of capacity of 50% (theoretical capacity: 280 mAh/g). The energy diagram of $Li_{0.5}CoO_2$ is illustrated in Fig. 2.38 (a).

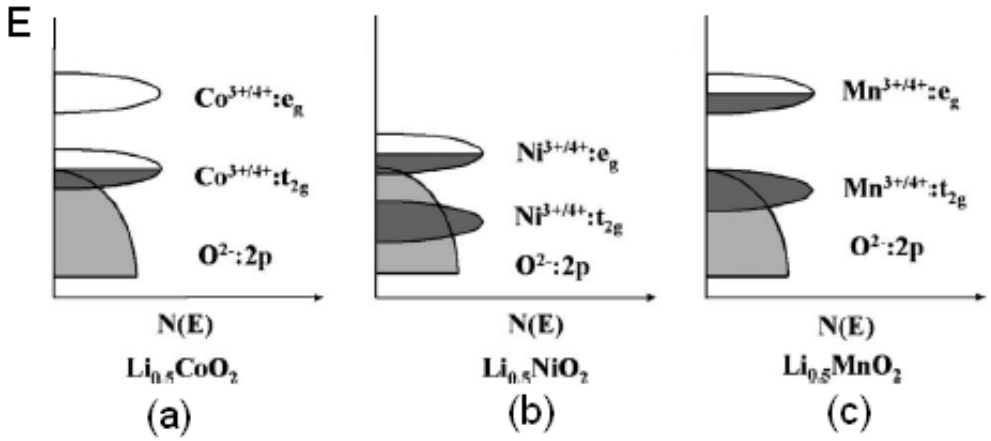

Fig. 2.38: Schematic band diagrams for (a) $Li_{0.5}CoO_2$, (b) $Li_{0.5}NiO_2$, and (c) $Li_{0.5}MnO_2$. Taken from Manthiram *et al.*[73]

In the case of $LiCoO_2$ with a Co^{3+} $3d^6$ configuration, the t_{2g} band is completely filled whereas the e_g band is completely empty. When Li is extracted from $LiCoO_2$, Co^{3+} is oxidized to Co^{4+} resulting in the removal of electrons from the t_{2g} band. Since the t_{2g} band is overlapping with the O^{2-} $2p$ band, an extraction of Li ions ($x < 0.5$) leads to the removal of electrons in the O^{2-} $2p$ as well, itself resulting in an oxidation of O^{2-} ions to molecular O_2. The loss of molecular oxygen destabilizes the crystal structure. Compared to compounds, having Ni or Mn instead of Co, bands are filled differently, see Fig. 2.38 (b) and (c). Since the Ni^{3+} ion has $3d^7$ configuration and the Mn^{3+} ion has $3d^4$ configuration, so the t_{2g} bands are completely filled, electrons will be removed from e_g bands. This slightly overlaps with the oxygen $2p$ band in the case of nickel, but does not overlap with the oxygen $2p$ band in the case of manganese. Therefore, $LiNiO_2$ and $LiMnO_2$ have a better chemical stability compared to $Li_{0.5}CoO_2$. It has been reported by Ohzuku *et al.*[74] and Lu *et al.*[75], that exemplarily the mixed oxides $LiNi_{1/3}Mn_{1/3}Co_{1/3}O_2$ and $LiNi_{1/2}Co_{1/2}O_2$ offer higher reversible capacities compared to $LiCoO_2$ of about 160-200 mAh/g, which is 60 - 70% of their theoretical capacity. The better chemical stability of these compounds results from partly substitution of Co by Ni and Mn, which is the reason for their higher capacities compared to $LiCoO_2$.[73] It has to be mentioned that although LNCO and LNMCO have higher capacity, they have lower rate capability compared to $LiCoO_2$ as shown in Fig. 2.39 (a). $LiCoO_2$ retains almost 90% of its capacity when changing the discharge rate from $C/10$ to $4C$, whereas LNMCO only retains 75%. The monotonic decrease in rate capability with decreasing Co content is due to increasing cation disorder (Fig. 2.39(b)) and, thus, the decrease in lithium extraction rate. Yoshizawa *et al.* investigated thermal characteristics of charged LNMCO and $LiCoO_2$ by mass spectrometry.[76] For $LiCoO_2$ two oxygen signals are identifiable in the mass spectrum at 240 °C and 280 °C, whereas two signals appear for LNMCO at 260 °C and 480 °C, respectively. The oxygen signals are evidence for thermal degradation of $LiCoO_2$, and show the superiority of LNMCO compared to $LiCoO_2$. The reason for the degradation is a phase change from a layered to a spinel structure during degradation, hindering oxygen loss from the structure. This has been observed in high-temperature XRD measurements of LNMCO. Although the ionic distribution of lithium and the

transition metals in a cubic closed package of oxygen is not clear, cation mobility seems to play an important role for the suppression of oxygen loss in lithium nickel oxides.[77, 78] In this case, the mobile species could be manganese cations.

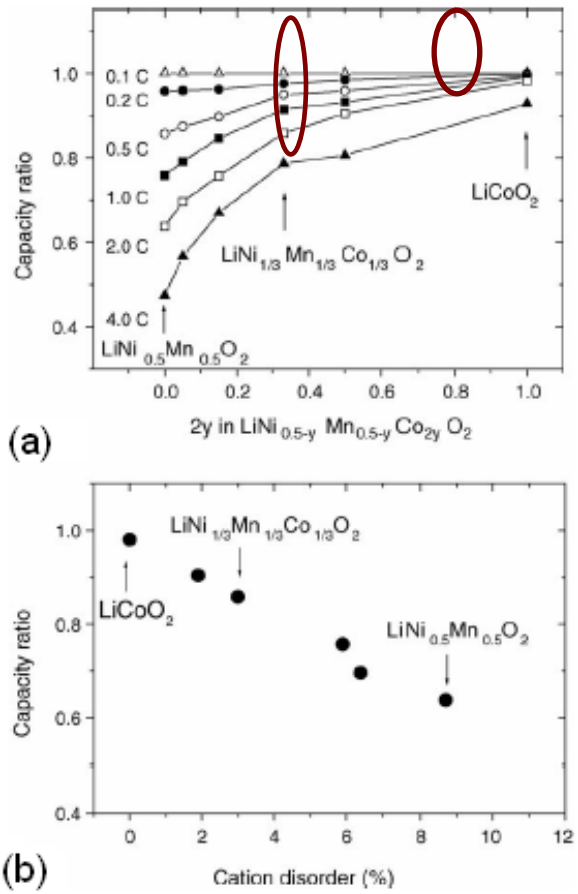

Fig. 2.39: (a) Comparison of the rate capabilities of $LiNi_{0.5-y}Mn_{0.5-y}Co_{2y}O_2$ cathodes with various Co contents. (b) Correlation of rate capability to cation disorder in $LiNi_{0.5-y}Mn_{0.5-y}Co_{2y}O_2$. Taken from Manthiram *et al.*[73]

Similar to Na_xCoO_2, lithium cobaltate undergoes several phase transitions by delithiation. In a lithium range from $0.5 < x < 1$ the *O*3 type structure is favored, below $x = 0.45$ a *P*3 type structure for CoO_2 forms, and for $x < 0.45$ a coexistence of *O*3 and *P*3 type structure is observed.[71] This is in contrast to other publications, which report on the existence of an *O*1 structure for electrochemically synthesized samples.[79-81] However, the *P*3 structure is metastable and transforms slowly into *O*1 structure. The oxygen stacking along *c* in *O*3 structure is -(ABCABC)-, in *P*3 structure –(AABBCC)-, and in *O*1 structure –(ABABAB)-, as illustrated in Fig. 2.40.

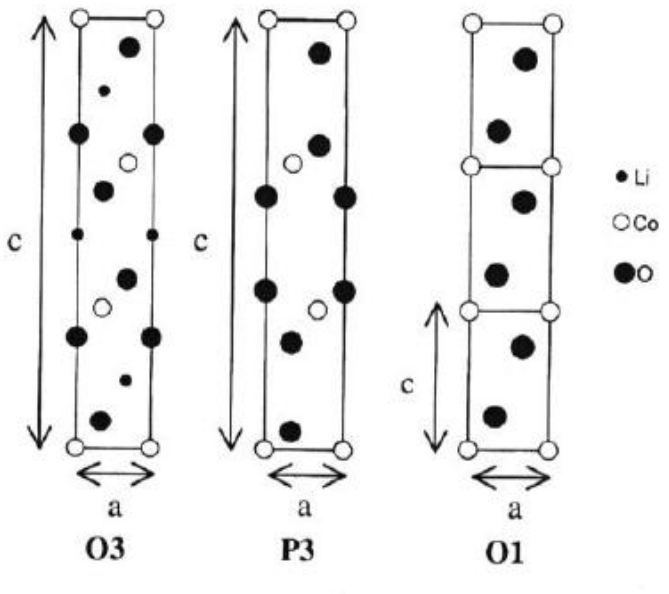

Fig. 2.40: Crystal structures of O3, P3, and O1, view along [010], taken from Nazri *et al.*[71]

The *P*3 and *O*1 structures are formed by sliding some CoO_2 planes, without breaking any Co-O bonds, resulting in 3 or 1 CoO_2 sheet in the unit cell depending on the phase. Lithium is coordinated hereby either octahedrally (O) or prismatically (P). The oxidation state of Co increases linearly with x from +3 to +3.8, while the oxygen content remains 2 for $0.5 < x < 1.0$. Below $x = 0.5$ the oxidation state is constant and charge compensation is achieved by a

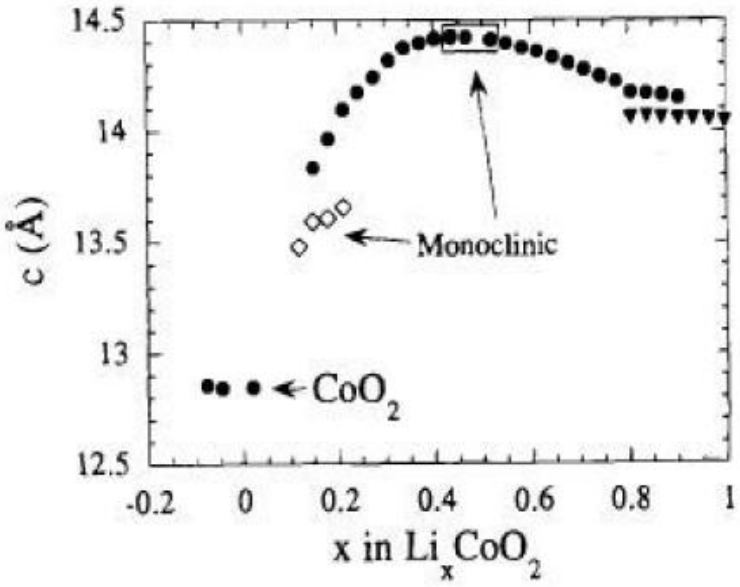

Fig. 2.41: Variation of the *c* as a function of lithium extraction from Li_xCoO2. Taken from Amatucci *et al.*[79]

loss of molecular oxygen with $\delta = 0.28$ for $CoO_{2-\delta}$. The lithium stoichiometry at which the oxygen loss starts is similar to the lithium stoichiometry at which the *P*3 structure begins to form. This indicates that the *P*3 structure is oxygen deficient with shorter O-O distances across the Van-der-Waals gap between the CoO_2 sheets. As for sodium cobaltate, there is a correlation of the Li content in $LiCoO_2$ and *c*-axis length of the, as reported by Amatucci *et al.*[79] In contrast to the almost linear dependence of the *c*-axis length in Na_xCoO_2, the *c*-axis in Li_xCoO_2 has a maximum at $x \sim 0.5$ and a sharp decrease for $0.4 > x > 0.2$.

2.2.1 Li*M*O_2 thin films

Thin films of $LiCoO_2$, LNMCO, and LNCO are usually deposited by RF magnetron sputtering[82, 83] or PLD[84] on various substrates. The substrate has to be conductive when using the thin film as cathode material. Due to that, platinum, silicon, and gold coated alumina are often used as substrate materials. Depending on the deposition method and deposition conditions, films have different orientation and physical properties. Xie *et al.* deposited thin films of $LiCoO_2$ by RF sputtering on sapphire substrates, yielding thicknesses from 310 to 1350 nm. The films had mixed orientation of (003) and (104), depending on the thickness.[83] Thicker films tended to be (104)-oriented, whereas thinner films were (003)-oriented. This is in good agreement with similar dependency reported by Wang *et al.*, they found that films with a thickness greater 1 μm tend to be (101)- and (104)-oriented, minimizing volume strain energy.[82] For film thicknesses below 500 nm, preferred orientation is (003) minimizing surface strain energy, which is a result of the annealing process during film fabrication. The higher the portion of (104) orientation, the higher is the Li-ion diffusion coefficient is. The improved diffusion kinetics compared to film with a higher portion of (003) orientation, could be explained by the crystal structure of $LiCoO_2$, in which Li-layers are parallelly arranged to the Li diffusion path in the case of (104) orientation, and perpendicularly to it in the case of (003) orientation. Xia *et al.* report on (00*l*)-oriented films with thicknesses of 300 nm deposited, by PLD on Si with buffer layers of Pt/Ti/SiO_2 using a $LiCoO_2$ target. Their intension was to measure the chemical diffusion coefficient, D_{Li}.[85] The results showed that D_{Li} ranges from $3.15 \cdot 10^{-12}$ to $1.47\ 10^{-11}$ cm^2/s in the potential range of 3.94 to 4.18 V. It has to be mentioned that by changing the amount of Li in the films (similar to Na_xCoO_2), structure changes as depicted in Fig. 2.42. This in turn influences D_{Li}. For example, for $0.5 < x < 0.75$, *c* increases a little with decreasing Li content, and the activation barrier does not change significantly. Therefore, the diffusion coefficient is mainly determined by the increasing concentration of Li vacancies. For low Li concentrations ($x < 0.4$), *c* decreases and the oxidation state of the Co ions increase with decreasing Li content, resulting in a significant increase of the activation barrier energy.

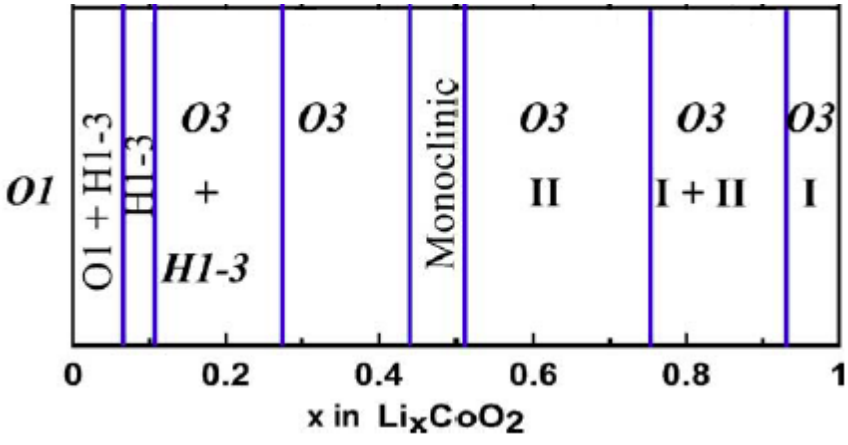

Fig. 2.42: Phase diagram of Li_xCoO_2 derived from differential capacity data and *in situ* XRD measurements. *H*1-3 structure is comparable to the previously described *P*3 structure. Taken from Chen *et al.*[86]

2.3 Fundamentals of thin film growth

Thin films in general have a thickness in the micrometer or nanometer range, because of that characteristic length scale they might exhibit different physical and chemical properties as compared to bulk. Since the surface/volume ratio is huge, surface and interface have great impact influence on film characteristics. The film-substrate misfit can cause stress, strain, and can introduce defects in the film. Thin film properties can be used for novel applications, in which, for example, electrical, magnetic, optical, and thermal properties can be combined. Thin film growth is divided in three subsequent steps. First, atoms, molecules, or clusters are emitted a source, second, the species reach to the substrate, and third, after initial nucleation, film growth takes place. The process of deposition is subject to both, thermodynamics and kinetics. Thermodynamics do influence film structure, film nucleation, and film growth mode. The film growth mode is dependent on surface and interface energies. Kinetic aspects are reflected in adsorption and desorption rates, which also do influence the growth mode and film nucleation on the substrate. Thermodynamics of film nucleation is illustrated in Fig. 2.43 (a).

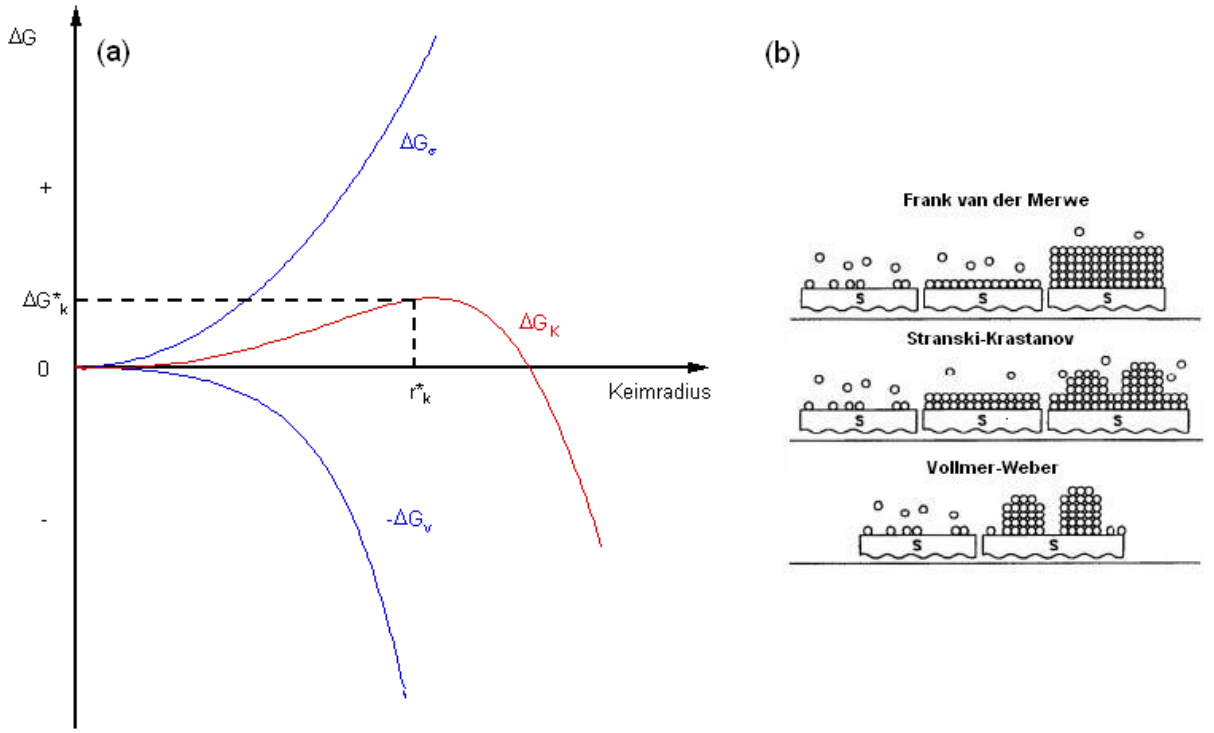

Fig. 2.43: (a) Nucleation as a function of nucleus radius and the surface (ΔG_σ), volume enthalpy (ΔG_V), nucleation enthalpy (ΔG_K), and the critical radius r^*_k of the nucleus.[87] (b) The three types of thin film growth modes.[88]

For nuclei $\leq r^*_k$ surface energy ΔG_σ predominates, free enthalpy increases for nucleation. Has a nucleus reached a critical radius r^*_k, the free enthalpy of the system decreases for $r > r^*_k$. For $r \geq r^*_k$, nuclei are stable, for $r < r^*_k$ they are unstable and their decomposition is thermodynamically favorable. From the thermodynamic, point of view there are mainly three different growth modes: *Frank van der Merwe* (layer-by-layer), *Vollmer-Weber* (island) and *Stranski-Krastanow* (layer-island) growth mode. Film growth mode, depends on the corresponding surface energies and surface stress/strain. The thermodynamic equilibrium of surface energies is described by *Young's* formula, see Eq. 2.11, with solid -vapor interfacial tension, γ_{SV}, film-vapor interfacial tension, γ_{fv}, film-solid interfacial tension, γ_{fs} and the contact angle

θ, illustrated in Fig. 2.44. Different growth modes lead to different relations of tensions and contact angle, which are described in the following.

Eq. 2.11 $$\gamma_{SV} = \gamma_{fs} + \gamma_{fv} \cos\theta$$

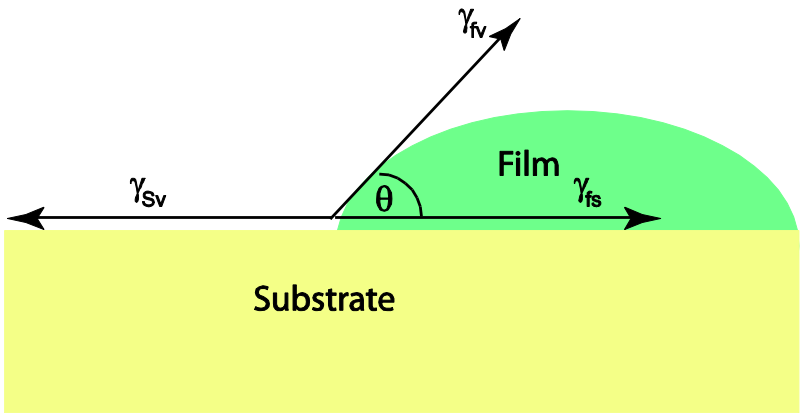

Fig. 2.44: Surface and interface tension illustrating *Young's* formula.

The three growth modes are:

Frank van der Merwe $\gamma_{SV} \approx \gamma_{fs} + \gamma_{fv}$ and $\theta \approx 0$

Films grow two-dimensionally and have a smooth surface, adhesion is greater than cohesion.

"Step-flow" special type of Frank van der Merwe

In this case the mean free path of the adsorbed atoms at the surface is even higher than for *Frank van der Merwe* growth. Atoms can directly diffuse to an existing step and get incorporated there, which leads to step growth.[89]

Vollmer-Weber $\gamma_{SV} < \gamma_{fs} + \gamma_{fv}$ and $\theta > 0$

Films grow three-dimensionally and have a rough surface, cohesion is greater than adhesion.

Stranski-Krastanow: $\gamma_{SV} > \gamma_{fs} + \gamma_{fv}$ and $\theta \approx 0$ (for the first monolayers)

$\gamma_{SV} < \gamma_{fs} + \gamma_{fv} + \gamma_{strain}$ (for subsequent layers)

The adhesion forces change during the growth, due to a large misfit of lattice parameters of substrate and film.

2.3.1 Thin film growth techniques

The deposition methods of thin films can be divided into two main categories: physical techniques like physical vapor deposition (PVD) and chemical techniques like chemical vapor deposition (CVD).[90] CVD is a reaction of gaseous species, where a solid product is formed on a suitable substrate. The hot filament chemical vapor deposition (HFCVD) is one example for

CVD. Here, the reaction is supported by resistive heating. Advantages of CVD are precise control of composition and deposition rates, and the possibility to coat very large areas. Unfortunately not all materials can be deposited via CVD. Further details on CVD are very well-described in literature. PVD itself can be divided in mainly four prominent subgroups, depending on the deposition process.[91]

- Resistive heating
- Sputtering
- Pulsed laser deposition (ablation)
- Molecular beam epitaxy (MBE)

The main difference between resistive heating and ablation is the higher energy density during of PLD during deposition. During thermal evaporation a resistively heated crucible is used for indirect evaporation of the desired evaporant. The crucible material is usually made of tantalum, molybdenum, tungsten or niobium. There are many types of crucibles with different geometries and shapes, such as boat, coil, and cage. There is a huge variety of materials, such as metals and organic compounds, which can be evaporated utilizing this deposition method. However, material flux is angle dependent, due to the nonlinear irradiation, which is the major disadvantage of this method. This can be overcome by using a shield over the crucible with a defined hole or mesh to get a constant evaporation rate. A special type of thermal evaporation is MBE based on electron-beam evaporation. Here, an electron beam hits the evaporant directly. This allows the evaporation of materials with very high melting points, e.g., hafnium, iridium, and rhenium. MBE allows to precisely grow single monolayer for highly epitaxial thin films. By introducing gaseous reactants, such as ozone and radicals MBE can be extended to reactive MBE (R-MBE). This R-MBE offers the possibility to grow complex oxide thin films by using the ability of *in-situ* feedback-looped rate control. R-MBE allows to grow compounds with complex stoichiometry consisting of several elements. Another deposition technique is sputtering, by which a target material (cathode) is hit by high energy gas ions, which, after transferring their kinetic energy into the target material by a collision cascade in the material eject atoms/clusters from the cathode. To eject atoms from the cathode, the surface ions need to have a minimum energy to start a collision cascade in the target material. Depending on ion energy and mass, the number of atoms ejected per incident ion varies. There are special types of sputtering, such as magnetron sputtering, and DC sputtering, which are described in details by Chopra *et al.*[91] The major advantage of sputtering is relatively high deposition rates, the possibility of large area coating, and the possibility of utilizing a huge variety of target materials. Poor control of film composition and the non-epitaxial growth have to be mentioned as major disadvantages of this technique.

Since PLD is the deposition method of choice for this thesis, it will be described in more detail. One major advantage to all other deposition techniques is the huge spectrum of target materials, which can be used for deposition, e.g., metals, oxides, magnets, conductors, insulators, as well as semiconductors.[92] By PLD, high depositions rates up to 10,000 Å/s are possible. Even the deposition of polymers or biological materials is accessible by PLD. Another major advantage is the direct transfer of stoichiometry from target to substrate. This is possible due to pulsed laser ablation, which is a non-equilibrium process, in which very high laser energies are absorbed at very small target areas. For low laser energies, the target would just be heated without ablation. The basic principles of PLD will be described based on the custom-made PLD system used for this thesis, see Fig. 2.45.

Fig. 2.45: Custom-made, quartz glass PLD chamber. The laser beam enters the chamber through a quartz-glass window at the bottom, and is focused on the target at the top (target rotation), and the plasma plume is directed down to the substrate, which is fixed onto a stainless steel plate, on top of a heating system.

The used laser is an excimer laser, type LEXtra (KrF, 248 nm) from Lambda Physics. Excimer is the abbreviation for excited dimer, which is an excited molecule consisting of two atoms, such as Xe_2. An excimer laser is a member of the group of gas lasers, which are able to emit radiation in a wide wave length range from 126 - 600 nm, depending on the used gas mixture, see Fig. 2.46.

The customized deposition chamber shown in Fig. 2.45 is made of quartz glass and can be easily cleaned by HCl. Especially for 'dirty' materials, such as PZT or alkaline elements this type of deposition chamber is favorable compared to commonly used stainless steel chambers. For each material a substrate plate was made, which can be changed very quickly, so many different materials can be deposited without the risk of contamination by the previous deposition material. For the heating system a bulb heater was designed. Temperatures up to 800 °C can be reached. The chamber can be flushed with oxygen, nitrogen or argon.

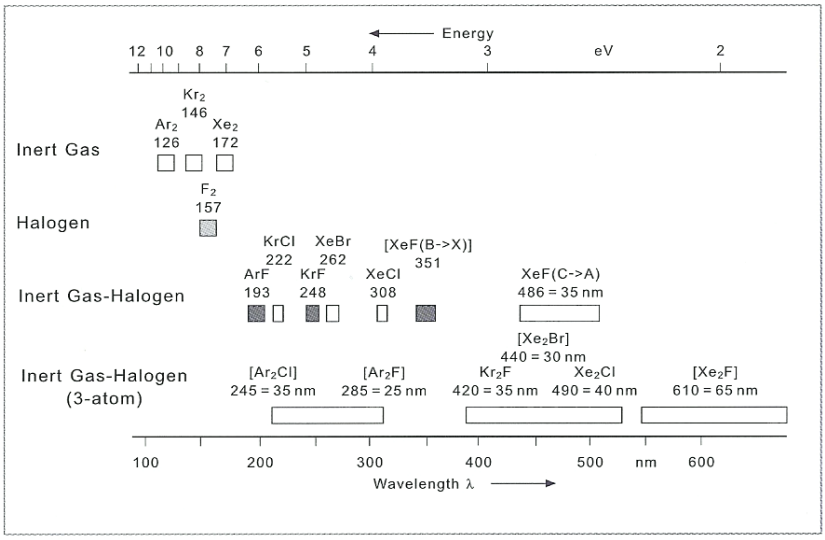

Fig. 2.46: Emission bands of different laser gases, taken from Basting *et al.*[93]

The laser principle is based on stimulated emission. When an atom in its ground state absorbs electromagnetical radiation $h \cdot \nu$, it is excited from its ground state, E_1, into an excited state, E_2. Is the atom falling back to ground state (spontaneous emission), radiation is emitted with an energy of E= E_2 - E_1, which is called spontaneous emission. A system in its excited state, which is stimulated by a phonon of the energy $h \cdot \nu_{12}$, *KrF** the activated molecule is formed. Different reaction processes take place to create the excited dimer, which are shown in Fig. 2.47 and described by Eq. 2.12.

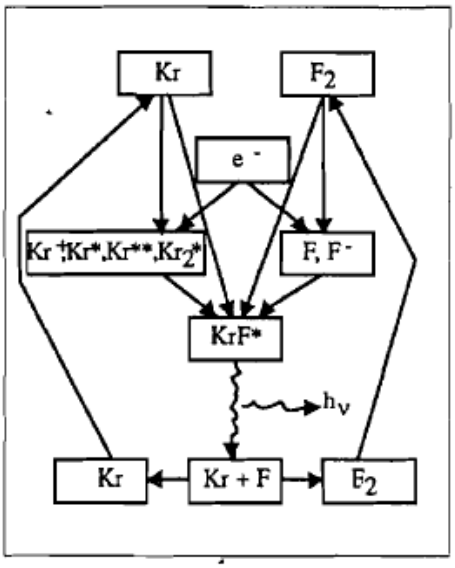

Fig. 2.47: Different types of reactions forming *KrF**, taken from Basting *et al.*[93]

Eq. 2.12 $$KrF^* + h \cdot \nu \rightarrow Kr + F + 2h \cdot \nu(248nm)$$

During the laser process losses occur due to deactivation of KrF* (spontaneous emission). This happens due to a collision with a third collision partner *M*, or by forming Kr_2F due to

impurities in the laser gas. In the following equations, the most important reactions which take place in the KrF laser gas mixture are described.

Pumping

Eq. 2.13	$e^- + Kr \rightarrow Kr^+ + 2e^-$	positive inert gas ion production
Eq. 2.14	$e^- + Kr \rightarrow Kr^* + e^-$	inert gas metastable production
Eq. 2.15	$e^- + F_2 \rightarrow F^- + F$	negative halogen ion production
Eq. 2.16	$Kr^+ + F^- + M \rightarrow KrF^* + M$	KrF* production
Eq. 2.17	$Kr^+ + F_2 \rightarrow KrF^* + F$	KrF* production

Losses

Eq. 2.18	$KrF^* \rightarrow Kr + F + 2h \cdot \nu(248\text{nm})$	spontaneous emission
Eq. 2.19	$KrF^* + M \rightarrow Kr + F + M$	collisional deactivation
Eq. 2.20	$KrF^* + M + Kr \rightarrow Kr_2F + M$	collisional deact. producing Kr_2F
Eq. 2.21	$X + 2h \cdot \nu(248nm) \rightarrow X^*$	laser photon absorption

The potential curve and the laser transition of the so-called “ionic-channel” (Eq. 2.12, Eq. 2.16 and Eq. 2.17) are shown in Fig. 2.48.

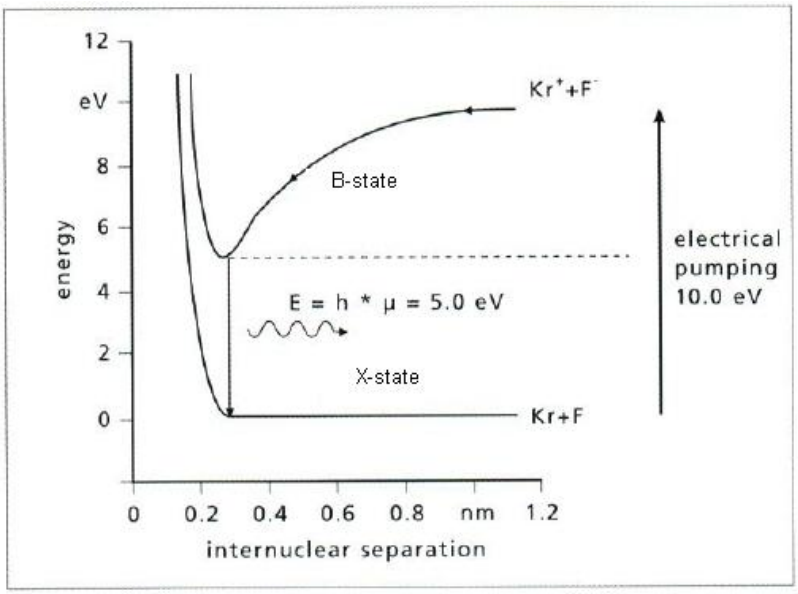

Fig. 2.48: Potential curve diagram for the KrF excimer laser process, taken from Basting *et al.*[93]

In contrast to other laser types, the excitation of active media by an excimer laser is per driven by kinetic processes, involving a collision partner (buffer gas Ne). The buffer gas is require to absorb a portion of the kinetic energy of the KrF collision which otherwise would

excite atoms here at 0.3 nm. The threefold collision of Kr^* and F^- ions and the buffer gas results in the formation of the upper laser level (B-state). Although the potential energy of the excited molecule is low, it is unstable and decays after less than 10 ns to its ground state (X-state). This B → X transition corresponds to laser radiation in inert gas halogen excimer lasers. After the decay of the excited molecules, the components are ready for a subsequent excitation cycle. For halogen molecules, there is no ground state, so the emission of the UV photon from the ionic B-state occurs over a wide wavelength range. Typical emission spectra of KrF excimer lasers cover a band width of more than 0.4 nm. Another consequence of the non-existing lower X-state, a single excited molecule already meets the condition for population inversion. This makes the excimer laser gas to be an ideal laser medium.

The deposition process is located in a vacuum chamber, in which the laser beam is focused through a quartz glass window onto the target. When using an excimer laser, a precise control of laser energy is necessary to achieve a uniform ablation. For that reason, the beam has to pass an optical system consisting of several lenses, mirrors and apertures before it enters the deposition chamber. The deposition process can be divided into four steps, which are the adsorption, melting of surface, ionization and ablation, and emission of plasma ("laser plume"), see Fig. 2.49.

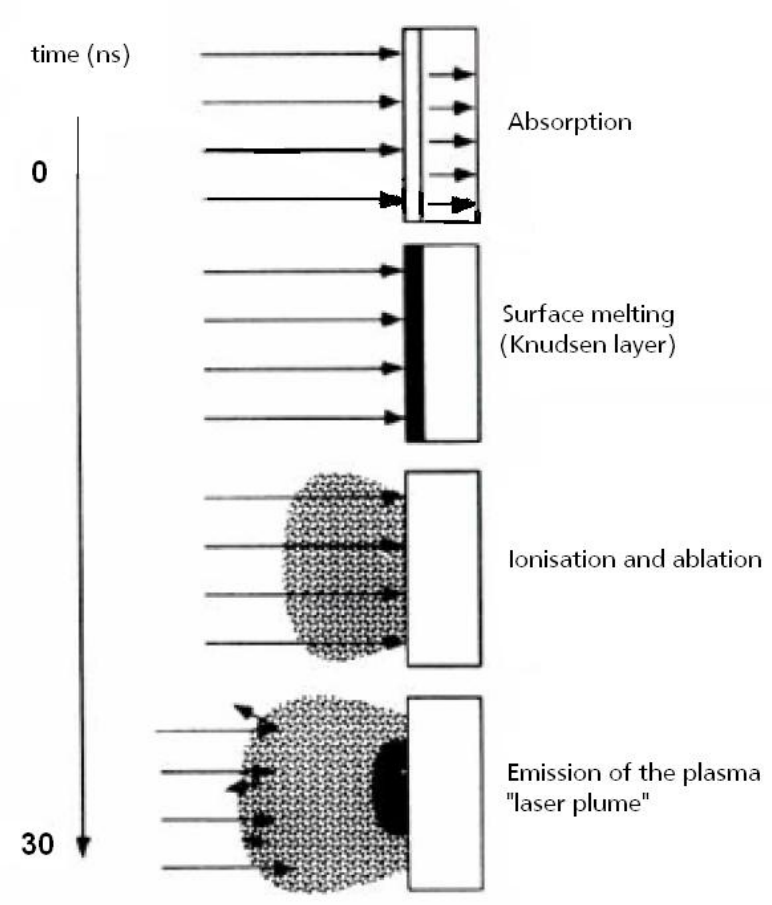

Fig. 2.49: Interaction of a laser pulse with target material.

The energy of a laser pulse incident on target surface, is absorbed and a thin layer of the target material starts to melt, the so called *Knudsen layer*.[94] Target material starts to boil-off and transforms into the gas phase. This causes phase transitions and introduces stress waves of high amplitude in the solid target. Material ejection takes place within a picosecond

timescale. The subsequent laser pulses ionize the evaporated material and leading to a formation plasma plume perpendicular to the target surface. The plasma plume consists of an ensemble of neutral and charged particles. In addition to that, several working gases can be introduced into the chamber, which influence the dynamics of the plasma plume, and film formation. First, a detailed description of processes taking place at the target is necessary. The mechanisms that contribute to the ablation of a target material can be divided into primary and secondary processes.[95] They include thermal, electronic, and macroscopic sputtering. The relative importance of the latter one depends on the nature of the target material and on laser excitation wavelength, as well as pulse duration. Material interaction with a laser pulse involves rapid excitation of electrons in the target material. This leads to an immediate increase of the electron temperature, and thus a heating of the crystal lattice. Electronic contributions are large when using very short pulse durations in the sub-picosecond range and can be used to have large ion yields and/or supra-thermal propagation velocities in the plasma plume. Thermal contributions dominate when using longer laser pulses in the nanosecond range. Here photon coupling with electronic and vibrational modes of the target material takes place. This is favorable in target materials having low reflectivities, large absorption coefficients, low thermal diffusion coefficients, and comparatively low boiling points (T_b). The material ejection and the integral flux can be changed dramatically by increasing the fluence introducing explosive boiling of the target material. This process is referred to as phase explosion around the critical thermodynamic temperature (T_c), which is the most efficient mechanism of thermodynamic ablation besides normal vaporization and boiling.[95] Normal vaporization (sublimation and evaporation) occurs for metals and insulators at any laser fluence and pulse length, there is no temperature threshold. Normally 100 ns is sufficient for vaporization, whereas 1 ps is too small for the possibility of vaporization. Normal boiling involves heterogeneous nucleation. Here, vapor bubbles (from liquids) initiate heterogeneously from a variety of gas or solid impurities or defects in the liquid. These bubbles tend to diffuse and for $T > T_b$ to escape from the surface of the liquid. They may form either in solids or liquids and may on the surface of the liquid (surface diffusion mechanism), in the bulk of the liquid (volume diffusion mechanism), or at an underlying or enclosing solid surface (vaporization-condensation mechanism).[95] The normal boiling occurs at time scales of 1-100 ns laser pulse durations and does not occur at short-time scales such as femtoseconds. Summarizing the three mechanisms, the following dependency of diffusion coefficients are valid.

Eq. 2.22 $$D_b^s = (\frac{3}{2}\pi r^4) D_s$$ bubble surface diffusion

Eq. 2.23 $$D_b^{vol} = (\frac{3}{2}\pi r^3) D_{vol}$$ bubble volume diffusion

Eq. 2.24 $$D_b^{vap} \propto r^{-2}$$ bubble vapor-condensation

Here, D_s represents the surface diffusion coefficient, D_{vol} the volume diffusion coefficient, and r the bubble radius. For normal boiling, the heterogeneous nucleation takes place at a temperature slightly higher than the boiling temperature. In contrast, when superheating occurs at temperatures near T_{Tc}, phase explosion or explosive boiling takes place connected with homogeneous nucleation. The consequence is a hot region near the surface which breaks down in a very short time into vapor and liquid droplets. The plasma plume consists of an intense “white” continuum emission, which is observed close to the target, and is named

Bremsstrahlung. After an expansion of the plume of some mm, it usually yields to several atomic and ionic lines in wavelength-dispersed plume emission spectra.[96] Electrons are much lighter and have greater mobility than ions and neutrals, but are hindered from escaping from the dense plasma by strong *Coulomb* forces. Optical emission spectroscopy, ion probe and mass spectroscopy studies have confirmed that the distribution of ejected material is favoured along the surface normal and decreases with $cos\theta$, where θ is the angle between surface normal and surface parallel. An example is shown in Fig. 2.50, where i-CCD images from the C^+ and C^{+*} emissions of a graphite target in vacuum are shown.

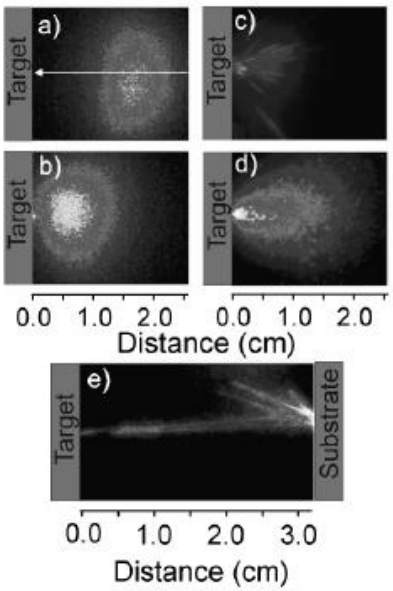

Fig. 2.50: i-CCD images of C^+ and C^{+*} emissions of a graphite target in vacuum.(a) Axis of incident beam, (c)-(e) i-CCD images of total emission from particles formed in the plume using 450 fs laser pulses. Following gate times were used: (c) Δt = 50 µs , t = 60 µs; (d) Δt= 1 µs , t= 130 µs and (e) Δt = 500 µs, t = 50 µs. (a), (b), and (d) are accumulated images of 200 laser pulses, whereas (c) and (e) are single-pulse events. Taken from Ashfold *et al.*[96]

It has to be mentioned that this type of analysis is not exact, since it only shows a two-dimensional projection of the three-dimensional cloud of emitted particles. However, it gives a very good qualitative impression of the direction in which the particles propagate. The ejected particle density from any given material is dependent on several factors, such as laser fluence and pulse duration. When using nano-second pulses, material ejection is likely due to thermal processes. The degree of ionization in a gas at local thermodynamic equilibrium can be estimated by using the *Saha* equation.

Eq. 2.25
$$n_i = \sqrt{2.4\times10^{15}\cdot T^{3/2}\cdot n_n\cdot e^{-E_i/kT}}$$

Here, n_i and n_n are the amount of single charge ions and neutrals, and E_i is the ionization potential. In the case of metal targets, the ionization fraction n_i/n_n is estimated to be greater than 0.1. From a the theoretical point of view, the value of the ionization fraction should be smaller that 10^{-5} known for graphite.[96] The process of the ionization includes *i.e.* laser induced multiphotonic ionization of the ejected material, which is a source for a chain reaction of sub-sequent ionization and plasma formation. In contrast to that electrons, which are much lighter and are more mobile than ions and neutrals, cannot escape from the plasma, as strong *Coulomb* interactions occur. These *Coulomb* interactions form the basis for the space charge

acceleration model, which is used to explain why ions propagate faster than neutrals in ablation plumes. The electrons located at the surface of the expanding plasma plume attract and thus accelerate ions, hereby the electrons increase the localized charge separation. The formation of excited particles in the plasma plume can be attributed to two mechanisms, (i) electron impact excitation (EIE) and, (ii) electron ion recombination (EIR). Both mechanisms have less effect with increasing target-substrate distance, *d*, as the plume density and the collision probability decrease.

In summary, PLD is a simple and versatile method to deposit films consisting of a very wide range of material like metals, carbon, and complex oxide ceramics. Deposition is possible on a rich variety of substrates within a wide temperature range under various background gases. The stoichiometric transfer of material from target to substrate can be tuned for example, by changing gas pressure during deposition. *In situ* multilayer fabrication by using a target carousel is possible and offers the possibility of automated deposition processes. In case the film material has involatile components, it is possible to use a so called 'mosaic target', which hosts a close mixture of the desired film components. As examples, a mixture of carbon and phosphorous is used to deposit CP_x, or a mixture of Al_2O_3 and ZnO is used to deposit Al-doped ZnO films. Deposition temperature is a crucial deposition parameter, as it has a huge influence on film morphology and microstructure. Films deposited at room temperature are usually amorphous, crystallinity can be obtained by increasing substrate temperature. The substrate is exposed to a flux of ablated ions and neutrals for subsequent short periods (~1 ms)each followed by a pause of ~ 100 ms (f = 10 Hz). During substrate bombardment by incident neutrals and ions adsorption and resorption take place. Aspects of kinetics and thermodynamics of film nucleation and growth have to be taken into account. For the previously described growth modes, it was assumed that adsorption and nucleation occurs randomly all over substrate surface. In reality this is not the case, since the substrate surface has defects, such as steps, dislocations, and point defects. These defects act as energy sinks for the incoming species. Epitaxial growth is possible, when lattice mismatch with respect to the substrate is small enough. One example for influence of the deposition parameters on film properties is given by Ashfold *et al*.[96] They investigated the ZnO system, ablated from a ZnO target under vacuum and low O_2 partial pressure. ZnO crystallizes in the wurtzit[b] structure. It exhibits piezoelectric characteristics and, therefore, is a very interesting thin film material for e.g., in acoustic wave devices. The results of Ashfold *et al.* are shown in Fig. 2.51.

[b] Many binary systems crystallize in the hexagonal wurtzit structure, e.g. ZnS, CdS, GaN. The two elements form two individual superlattices with hexagonal-closed package. The atomic positions of all atoms are very similar to those of hexagonal diamond structure, in which every atom is tetragonally coordinated. It is non-centrosymmetric (no inversion symmetry), because of that most materials, crystallizing in wurtzit structure exhibit piezo- and pyroelectric properties.

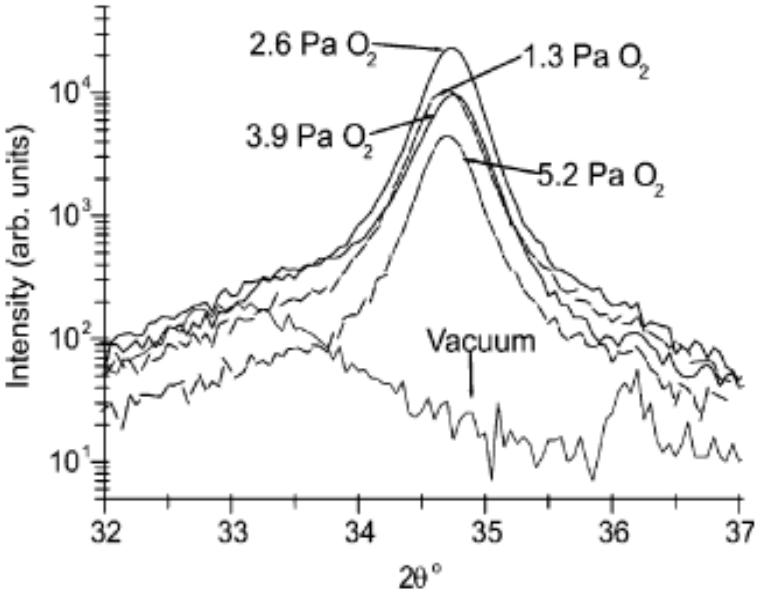

Fig. 2.51: 2θ–scans of the (0002) reflection of ZnO in ZnO:Ga, grown under different oxygen background pressures on sapphire substrates, taken from Ashfold *et al*.[96]

XRD characterization reveal low crystallinity of films deposited in pure vacuum. The optimal oxygen partial pressure for film growth is 2.6 Pa. X-ray photoelectron spectroscopy (XPS) showed that films deposited in vacuum are Zn-rich, thus oxygen deficient. Introducing oxygen during the deposition process results in films having improved crystallinity and transparency compared to films deposited in pure vacuum. The Zn-rich films can be explained by the Zn-rich nature of post-ablated target surfaces caused by preferential re-condensation and back scattered Zn atoms from the ablation plume.[97] The XPS spectra of the Zn 2*p* emission of a target surface (Fig. 2.52) show different intensities for ablated and unablated target surfaces. This result proves the theory of Zn enrichment of target surface after ablation, which then leads to Zn enriched films.

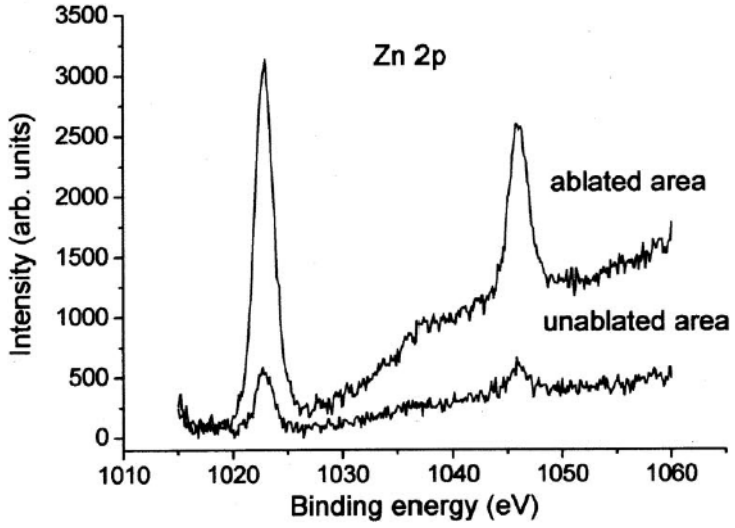

Fig. 2.52: XPS emission spectra of ZnO 2*p* recorded from ablated and unablated surfaces of a ZnO target. Taken from Claeyssens *et al*.[97]

The addition of background gases enables to influence stoichiometry, as seen for ZnO. Similar dependence is known for the growth $YBa_2Cu_3O_{7-\delta}$ or other high-T_c superconductors, in which oxygen partial pressure and the substrate temperature, play an important role for correct oxygen stoichiometry in deposited thin films. The stoichiometry is preserved in the PLD process but difficult to control for volatile species like sodium. The target composition is affected by ablation especially for materials, which have a low partial pressure. In conclusion, PLD is among the 'ideal' deposition methods for the deposition of a very broad variety of materials and compounds.[98]

3 Experimental

3.1 Target fabrication: Ceramic processing

Processing of target materials involve the preparation of high-purity and single phase powders of the desired material in the stoichiometric mixture. Here, a very brief introduction into ceramics will be given. The word 'ceramic' has is Greek and comes from 'keramos', which can be translated as 'tile', or 'burnt clay'. In science the definition by Kingery *et al.* has been for long time *the* definition of a ceramic, which was inorganic nonmetallic.[99] This definition fails for distinguishing between ceramics, organics, and metals. But what about salts and intermetallics? An unambigous definition for ceramic is hard to find, as too many aspects have to be taken into account. It is important to get a fundamental understanding of the relationship between materials properties and its chemical composition, atomic bonding, and crystal structure. This is much more important than finding a proper exact definition. Many authors have dealt with this definition topic and it can be found in corresponding literature.[99, 100]

The material's microstructure, as well as its physical and chemical properties strongly depend on the synthesis route. Mainly three types of synthesis methods for ceramics exist, solid-state synthesis, a liquid-phase synthesis (sol-gel synthesis), and gas-phase synthesis. A very detailed description of these three synthesis methods is given in literature.[99-102] The solid-state reaction is a very simple method of powder mixing with several heating cycles to obtain the desired crystal phase. Adverse to other synthesis techniques, agglomeration of powder can lead to high porosity or bad homogeneity of the sintered target, which allows additional phase formation. Purity, particle size, and reactivity affect the final physical and chemical properties of the material, and must be taken into the account already from the beginning of the target synthesis. Powder purity strongly influences high-temperature properties, such as strength, stress rapture life, and oxidation resistance. The effect of an impurity strongly depends on its chemical and physical properties in comparison to the matrix material. In some cases impurities are introduced on purposely to obtain certain material properties, as done for materials doping. Concerning electrical, optical, and magnetic properties, impurities can have an even bigger effect. Slight variations of dopant concentration and distribution can lead to entirely different behavior. The particle size is important depending on the subsequent shaping and densification processes. In most cases, 100% dense-sintered targets are targeted. It can be said that a range of different particle sizes is necessary to achieve dense-sintered targets, particles with similar size result in more than 30% porosity.[100] To avoid the disadvantages of solid-state target fabrication, the liquid-phase target fabrication, which leads to high purity powders with controlled particle size, can be used. Here the liquid mixing (sol-gel technique) has to be mentioned. Liquid mixing names all processes starting with a homogeneous solution containing the desired cations. Additives (linking agents) are added in many cases, which results in a cross-linked polymer and (after heating) in a homogeneous oxide powder. A very famous pioneer of this technique is *Pechini,* after whom this method has been named.[103] To obtain a dense-sintered target, the powder has to be densified a useful target in a second step of both production processes, which is done by sintering the powders in pellets. Sintering describes different diffusion processes, which lead to the reduction of pores, and the growth of large particles (grains) for the sake of small particles (Ostwald riping). The densification requires two aspects, (i) material transport mechanism pathways and (ii) an thermal energy source

activating and sustaining the transport. Sintering can be divided in different stages, which are presented in Fig. 3.1.

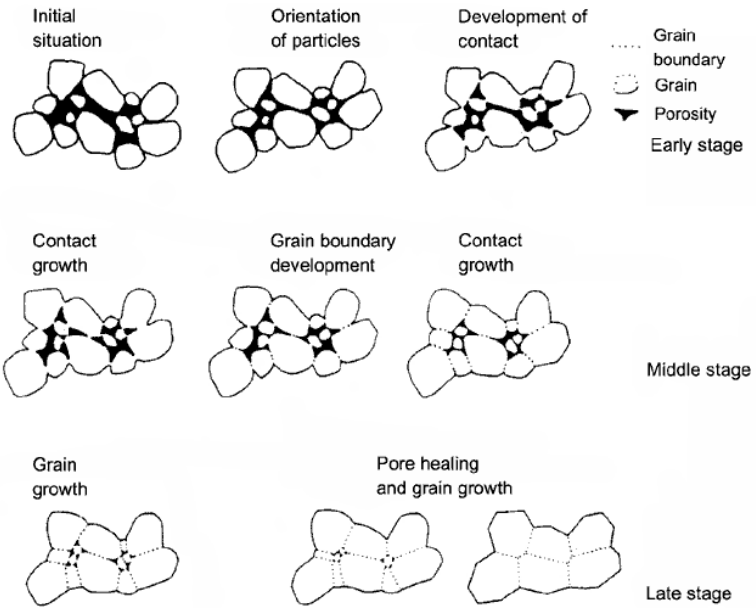

Fig. 3.1: Different stages during sintering of ceramic materials.[104]

In the early stage, a rearrangement of particles takes place and initial neck formation starts at the particle contact points. The rearrangement can be understood as a slight movement or rotation of neighbored particles to increase the points of contact. Here, surface energy is highest and due to material transport processes bonding occurs at these points. In the intermediate stage, sintering necks grow, porosity decreases, and a shrinkage of the green body is the result. A movement of grain boundaries begins, so that large particles (grains) grow for the sake of smaller grains. Geometrical change is attributed to accommodate further neck growth and decreasing porosity. This stage of sintering ends, when pores become isolated in the bulk and no interconnecting channels are existing anymore. Green body shrinkage is largest during the intermediate sintering stage. The late sintering stage represents the final densification. The underlying mechanism is vacancy diffusion along grain boundaries. Pore reduction and vacancy diffusion are assisted by the movement of grain boundaries and grain growth.[105, 106] In the case of fast grain growth, grain boundaries may move faster than pores thus leaving them isolated within grains. To achieve maximum density, grain growth has to be controlled properly. Depending on the mechanism the origin of the material transport and its driving energy is different. More details on that can be found in literature.[100]

The targets for the deposition of Na_xCoO_2 thin films via PLD as well as for $LiCoO_2$ thin films were fabricated according to, (i) solid state synthesis and (ii) sol-gel synthesis, which has been established for Na_xCoO_2 for the first time for this thesis. In addition, $LiNi_{1/2}Co_{1/2}O_2$ and $LiNi_{1/3}Mn_{1/3}Co1_{/3}O_2$ were synthesized by the sol-gel technique.

3.1.1 Solid state synthesis of Na_xCoO_2 and $LiCoO_2$

For the solid-state synthesis of Na_xCoO_2, cobalt oxide (Co_3O_4, 99.998%, *Sigma Aldrich*) and sodium carbonate(Na_2CO_3, 99.99% *Alfa Aesar)* were used.

Co_3O_4

Cobalt oxide is a black odourless, and incombustible powder with a molecular weight of 240.795 g/mol, with a density of 6.07 g/cm^3 @ 20 °C. It is almost not soluble in water and has a decomposition temperature of 900 °C, where it decomposes to several cobalt compounds.[107] It crystallizes in spinel structure[c], in which Co^{2+} ions are tetrahedrally coordinated and Co^{3+} ions are octahedrally coordinated.

Na_2CO_3

Sodium carbonate is a white, flint-like, and odourless powder, also known as soda ash. The molecular weight of the anhydrous compound is 105.99 g/mol with a density of 2.53 g/cm^3 @ 20 °C. It is soluble in water and has a decomposition temperature of 400 °C, at which the compound decomposes to sodium oxide. Na_2CO_3 is very hygroscopic and usually appears in its hydrated form. The decahydrate of Na_2CO_3 loses water at a temperature of 34 °C , whereas the monohydrated form loses water at a temperature of 100 °C.[107] It crystallizes in several structures, which there are monoclinic, hexagonal, and orthorhombic, depending on the amount of water hydrated in Na_2CO_3.[108]

Both powders were carefully preheated in a furnace at 100 °C to keep them water-free. To fabricate a target of $Na_{0.75}CoO_2$, it is necessary to mix the powders in a molar ratio of Na : Co = 1.8 : 1. Excess of sodium is crucial to obtain the sodium cobaltate phase, since the volatility of Na would lead to the formation of Na_xCoO_2 and unreacted Co_3O_4 for lower Na : Co ratios. For 12 g of mixed powder, 5.48 g of Co_3O_4 and 6.53 g of Na_2CO_3 were weighted and carefully mixed in an agate mortar for 30 min until the powder mixture has a homogeneous, dark grey color. The powder mixture was filled to an Al_2O_3-crucible an heated in a muffle furnace (*Nabertherm*, LT 3/12) for calcination. The powder mixture was heated three times for 12 h in the muffles furnace to temperatures of 760, 820, and 860 °C, respectively with subsequent grinding. Phase formation was monitored by X-ray diffraction after every calcination step. Before pressing the powder into pellets with a diameter of 18 mm, 1 g of Na_2CO_3 was added to the final $Na_{0.75}CoO_2$ powder to increase the amount of sodium in the target before sintering. Six grams of powder were used per target. Before uniaxially pressing with 400 MPa (cold press), 1 ml of polyvinyl alcohol (PVA) was added as a binder, and stearic acid was used as a lubricant for the die surfaces. Since PVA was provided in a watery solution, the powder had to be dried again in a furnace at 100 °C for 30 min prior pressing. The sintering temperature program is illustrated in Fig. 3.2.

[c] The spinel structure is a cubic, closed packed lattice with one octahedral and two tetrahedral sites per unit cell. The tetrahedral sites are usually smaller than the octahedral sites. The general formula for spinel structure is $A^{2+}B_2^{3+}O_4^{2-}$, examples for spinells are $MgAl_2O_4$ and $CuFe_2O_4$.

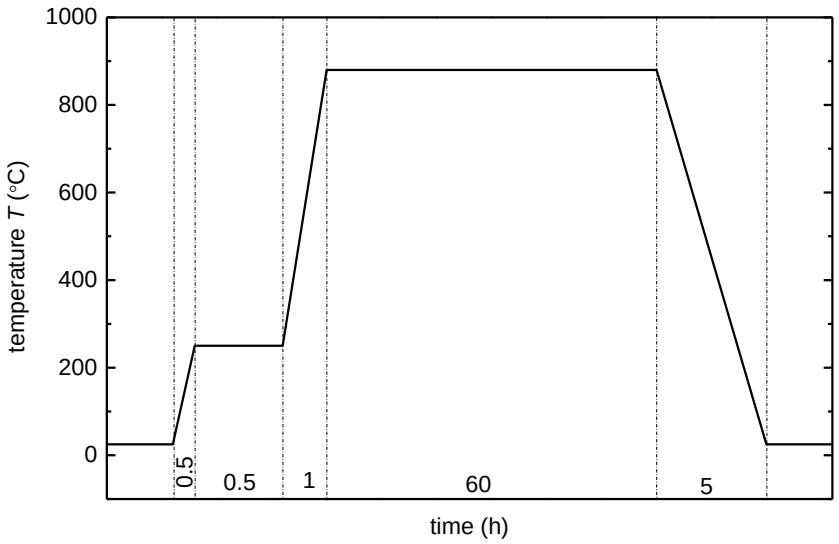

Fig. 3.2: Temperature sequence for final sintering of $Na_{0.75}CoO_2$ target.

The resulting target had a tap density of 72%, which has been calculated after sintering as the ratio of mass and volume of the pellet. The surface of the target shows platelet-shaped and needle-shaped crystals, see Fig. 3.3

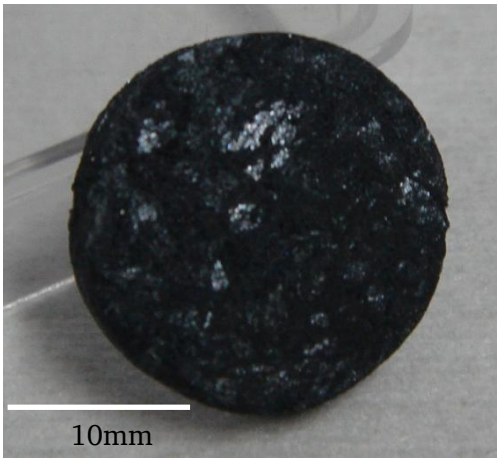

Fig. 3.3: Photograph of the Na_xCoO_2 target prepared by solid-state route.

3.1.2 Sol-gel synthesis of Na_xCoO_2, $LiNi_{1/3}Mn_{1/3}Co_{1/3}O_2$ and $LiNi_{1/2}Co_{1/2}O_2$ targets

When using the sol-gel technique, one has to take into account several parameters for choosing the starting materials. For Na_xCoO_2, the pristine powders containing sodium and cobalt have to be first all soluble in water-based media. For this synthesis route, other precursor powders are needed than for solid state reaction. The chosen materials were sodium acetate ($NaCH_3COO$, 99.997%, *Alfa Aesar*), cobalt acetate tetrahydrate $(CoCH_3COO)_2{\cdot}4H_2O$, 98%, *Sigma Aldrich*), lithium acetate ($LiCH_3COO$, 99.95%, *Sigma Aldrich*), nickel acetate tetrahydrate $(Ni(CH_3COO)_2{\cdot}4H_2O$, 99.998%, *Sigma Aldrich*), and manganese acetate ($Mn(CH_3COO)_2$, 98%, *Sigma Aldrich*). Here a short introduction to these five organic materials is given in the following.

$Co(CH_3COO)_2 \cdot 4H_2O$

Cobalt acetate tetrahydrate is a red-purple, crystalline powder, which is not combustible and well soluble in water. The molecular mass of the anhydrate is 177,02 g/mol with a density of 1.7 g/cm^3. At a temperature of 140 °C, the crystal water is evaporated from the compound.[107] Mu *et al.*[109] and Mohamed *et al.*[110] investigated the thermal decomposition of cobalt acetate tetrahydrate. The tetrahydrate is dehydrated in two steps by losing two water molecules at each step at temperatures of 58 °C and 115 °C, respectively. At a temperature of 260 °C, cobalt acetyl is formed, further heating above 500 °C leads to the formation of Co_3O_4.

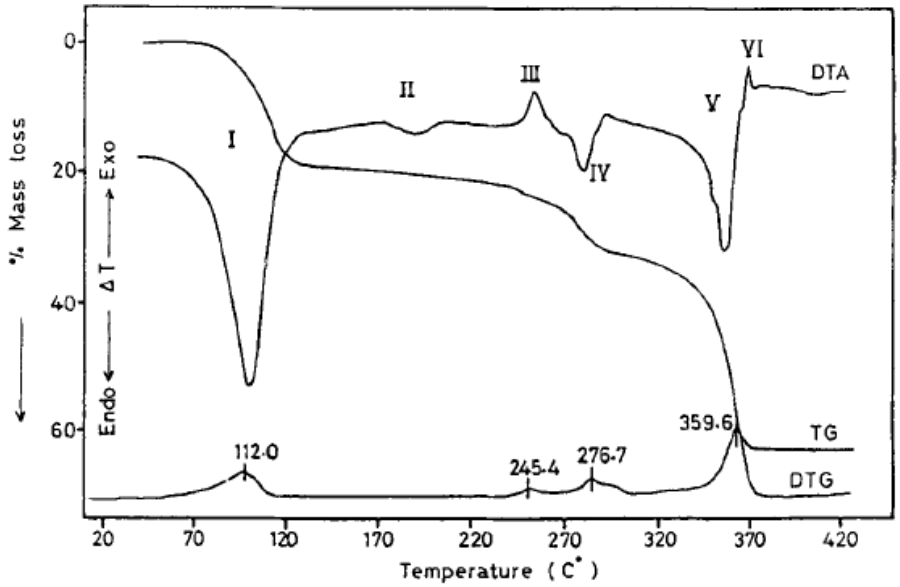

Fig. 3.4: TG, DTA, and DTG curves of cobalt acetate tetrahydrate in N_2.Taken from Mohamed *et al.*[110]

In Fig. 3.4 the relevant events are marked with roman numbers I-VI. The endothermic signal (I) is attributed to the dehydration of the tetrahydrate to a monohydrate. The second signal (II) is exothermic when using air instead of N_2 and is possibly due to the oxidation of decomposition products, or the formation of a stable compounds (e.g. oxides). The second endothermic signal (III) denotes to the formation of an intermediate product of acetyl cobalt acetate. An subsequent endothermic process (IV) was confirmed by IR spectroscopy to be a formation of cobalt acetate hydroxide due to the evaporation of CH_3CHO from acetyl cobalt acetate. The major loss in mass of 31% is accompanied by the fourth endothermic event (V) and related to an autocatalytic decomposition of adsorbed acetates or other compounds on cobalt oxide surface. The second exothermic signal (VI) indicates no loss in mass, suggesting the recrystallization of CoO. Compared to the two-step model of Mu *et al.*, the results of Mohamed *et al.* describe a one-step model of dehydration. It has to be mentioned, that the explanation of the dehydration process is very complex and not fully understood, yet.

$NaCH_3COO$

Sodium acetate is a colorless and odourless powder, which is highly hygroscopic. The molecular weight of the anhydrous compound is 82.03 g/mol with a density of 1.52 g/cm^3. It decomposes to sodium oxide at a temperature of 324 °C, has a flashing point of 250 °C, and

an ignition point of 607 °C.[107] Its crystal structure is monoclinic. A detailed description of the thermal decomposition is difficult due its high hygroscopy. Kemper *et al.*[111] and Judd *et al.*[112] studied the thermal decomposition of sodium acetate. It was found that the dehydration depends on the amount of material and takes place stepwise. The dehydration process corresponds to a loss in mass of ~40% (see Fig. 3.5(a)) and two endothermic signals in the DTA curve. In a temperature range from 160 to 385 °C, no changes in mass occur, the endothermic signal at 335 °C (feature III in Fig. 3.5 (b)) can be attributed to melting of anhydrous sodium acetate, which denotes to change in phase, without change in mass. The major loss of mass of 70% takes place above 385 °C and is connected to the formation of sodium carbonate.

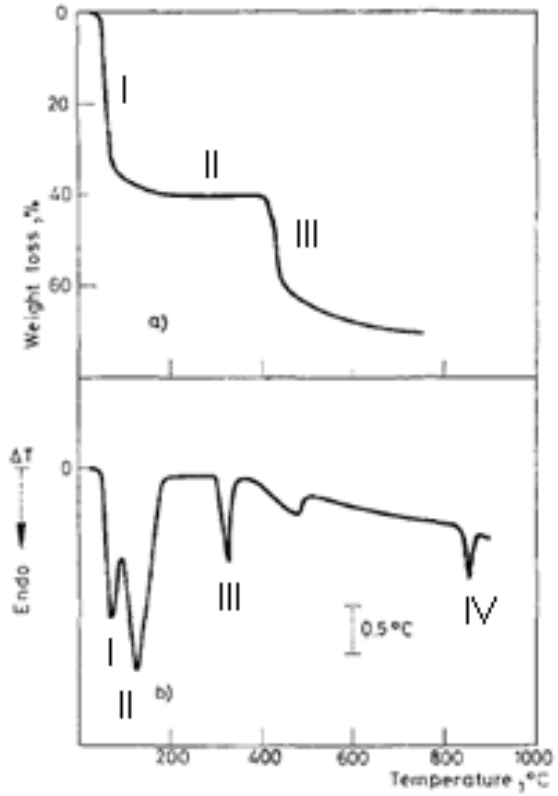

Fig. 3.5: (a) TG and (b) DTA curves for sodium acetate trihydrate in N_2, taken from Judd *et al.*[112]

Judd *et al.*[112] postulate a temperature interval of 170 to 300°C, in between dehydrated sodium acetate is stable. This was confirmed by Kemper *et al.*[111], who found stable powders of dried sodium acetate within a temperature range of 30 to 300 °C. In contrast to the results of Judd *et al.,* Kemper *et al*. found, that the starting temperature for the transformation of dehydrated sodium acetate to sodium carbonate is within a lower temperature interval of 300 to 325 °C. Hydrated sodium acetate has a melting point of 58 °C, loses its water within a temperature range of 77 to 127 °C, and recrystallizes subsequently, this leads to various signals in the DTA curve.

$LiCH_3COO$

Anhydrous lithium acetate is a crystalline, white powder with a molecular mass of 65.99 g/mol and a density of 1.26 g/cm^3. It is soluble in water and has a melting point of 286 °C. It has an orthorhombic structure.[113] Krönig investigated the thermal decomposition of some pure metal acetates and lithium acetate, see Table 3.1 and Table 3.2.[114] The thermal decomposition of lithium acetate starts at a temperature of 330 °C, at which it decomposes into lithium carbonate, lithium oxide, and acetone under the release of hydrocarbons and hydrogen.

Table 3.1: Thermal decomposition of some metal acetates, taken from Krönig.[114]

		Acetate					
Metals	Initial weight (g)	calc. (%)	meas. (%)	Start of gas formation (°C)	Start of vapor formation (°C)	Duration of vapor formation (°C)	Time of vapor formation (min)
Li	13.20	10.06	10.31	330	345	45	50
Na	16.40	39.85	39.85	390	410	40	75
K	19.60	28.04	28.04	390	420	20	120
Cu	18.16	35.0	35.0	250	250	25	15

Table 3.2: Decomposition products of some metal acetates, taken from Krönig.[114]

Metals	Total mass (g)	Metal (%)	Metal oxide (%)	Metal carbonate (%)	Carbon (%)
Li	7.3	/	0.25	99.35	0.4
Na	10.1	/	/	99.62	0.39
K	13.75	/	0.75	95.52	3.73
Cu	6.73	81.44	11.955	0.68	5.94

$Ni(CH_3COO)_2 \cdot 4H_2O$

Nickel acetate tetrahydrate is a green odourless and hygroscopic powder with a molar mass of 248,84 g/mol and a density of 1.744 g/cm^3. It has a monoclinic crystal structure. The crystal water of the tetrahydrate is splitted off within a temperature range of 50 to 110 °C, and the material decomposes at 250 °C.[107] Several authors investigated the thermal decomposition of nickel acetate tetrahydrate in detail.[115-118]

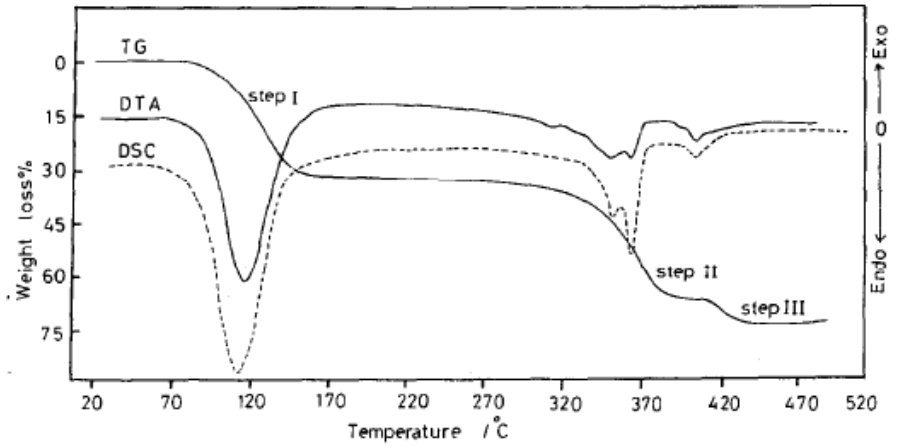

Fig. 3.6: TG, DSC, and DTA curves of the thermal decomposition of nickel acetate tetrahydrate in N_2, taken from Mohamed *et al.*[116]

Nickel acetate tetrahydrate decomposes in three steps, between 80 and 170 °C it loses its crystal water, with further heating a transformation to nickel acetate (0,86 $Ni(CH_3COO)_2 \cdot 0{,}14\ Ni(OH)_2$) takes place.[117] At a temperature of 250 °C, a fraction of the basic nickel acetate decomposes to nickel carbide,[118] the other fraction to nickel carbonate,[115] which final leads to the formation of metallic nickel and nickel oxide.[115, 116] It has to be mentioned that the atmosphere in which the material is heated is crucial for the formation of the decomposition products. In the case of hydrogen present during the measurement, only elementary nickel is formed, in contrast to the formation of nickel and nickel oxide in inert atmosphere.

$Mn(CH_3COO)_2$

Manganese acetate is a crystalline powder with a light red color, with a molecular mass of 173.03 g/mol, a density of 1.6 g/cm^3, and a melting point of 80 °C. It is soluble in water and decomposes at a temperature of 323 °C.[107] The crystal structure of manganese acetate is monoclinic.[119] The decomposition of anhydrous manganese acetate starts at a temperature of 300 °C and decomposes into acetone, carbon dioxide and manganese oxide. In Fig. 3.7, the experimental results of thermogravimetric measurements on manganese acetate tetrahydrate by Newkirk *et al.* is shown.[120] The two features below 300 °C occur due to the subsequent loss of two water molecules from the tetrahydrate per formula unit. In addition to the results of Newkirk *et al.,* Nohman *et al*. found Mn_3O_4 and Mn_2O_3 to be present after decomposition of manganese acetate.[121]

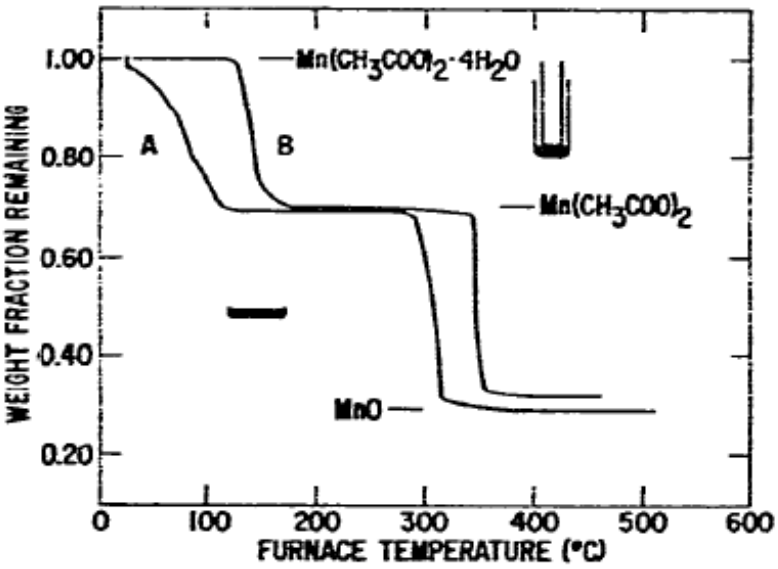

Fig. 3.7: TG curve of manganese acetate tetrahydrate. (a) In an open crucible in air, and (b) in a shallow dish in N_2, taken from Newkirk *et al.*[120]

Prior to sol-gel synthesis, the acetates are dried at temperatures between 85 and 120 °C for up to 24 h obtaining water-free compounds. The process was monitored by independent thermogravimetric analyses and differential scanning calorimetry measurements. The corresponding acetates were separately dissolved in distilled water, 20 ml of each solution were mixed together with 2 to 3 ml of tartaric acid as complexing agent. The concentration of each solution is given in Table 3.3.

Table 3.3: Acetates, nominal cation stoichiometry of the precursors, and concentration of the water solutions used for the synthesis of Na_xCoO_2, $Li(Ni_{1/2}Co_{1/2})O_2$, and $Li(Ni_{1/3}Mn_{1/3}Co_{1/3})O_2$. The chemicals were supplied by Alfa Aesar (AA) and Sigma-Aldrich (SA).

Compound	Na_xCoO_2	$Li(Ni_{1/2}Co_{1/2})O_2$	$Li(Ni_{1/3}Mn_{1/3}Co_{1/3})O_2$
Acetates	Sodium acetate $Na(CH_3CO)$ AA 99.97% 1.22 mol/l	Lithium acetate $LiCH_3COO$ SA 99.95% 0.62 mol/l	Lithium acetate $LiCH_3COO$ SA 99.95% 1.04 mol/l
	Cobalt acetate $Co(CH_3COO)_2$ AA 99% 0.57 mol/l	Cobalt acetate tetrahydrate $(Co(CH_3COO)_2)\cdot 4H_2O$ SA 98.0% 0.31 mol/l	Cobalt acetate tetrahydrate $(Co(CH_3COO)_2)\cdot 4H_2O$ SA 98.0% 0.46 mol/l
		Nickel acetate tetrahydrate $(Ni(CH_3COO)_2)\cdot 4H_2O$ SA 99.998% 0.31 mol/l	Nickel acetate tetrahydrate $(Ni(CH_3COO)_2)\cdot 4H_2O$ SA 99.998% 0.49 mol/l
			Manganese acetate $Mn(CH_3COO)_2$ SA 98% 0.35 mol/l
Nominal cation stoichiometry	Na:Co = 1:1	Li:Ni:Co = 1:1/2:1/2	Li:Ni:Mn:Co= 1:1/3:1/3/:1/3
Calcination	6 h at 500 C, 600 C and 700 C	600 C for 6 + 12 h	600 C for 6 + 12 h

The solutions were heated up to 75 °C under continuous stirring, until they boiled to gels. The gels were dried in a furnace at 70 to 80 °C for 12 to 24 h evaporating, residual solvents, followed by grinding of the extracted powders in an agate mortar to obtain a well-mixed powder with uniform particle size. Subsequently, the powders were carefully preheated up to 400 to 500 °C for 6 h with low heating rates of 0.8 - 1.1 K/min, which is essential to avoid the combustion of organic residuals. The obtained powders were calcined several times at different temperatures to form the desired compounds (see Table 3.3). In order to ensure uniform oxidation conditions only a few grams of the powders were calcined at once. In between the calcination steps, the powder was grinded in an agate mortar to improve homogeneity. For preparation of dense, bulk materials after the last calcination step, six grams of the powder was pressed into a cylindrical pellet using an uniaxial cold press at 400 MPa. Prior pressing, 1 ml of PVA was added as a binder, and stearic acid was used as a lubricant for the die surfaces. Since PVA was provided in a watery solution the powder had to be dried again in a furnace at 100 °C for 30 min prior to pressing. The sintering sequence for the sol-gel synthesized targets is illustrated in Fig. 3.8. A photograph of the ready to use target after sintering is shown in Fig. 3.9.

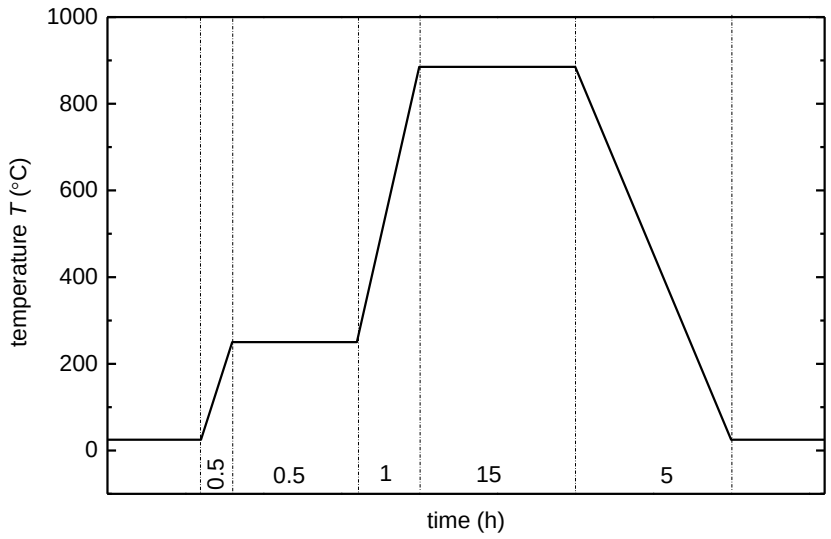

Fig. 3.8: Temperature sequence for the final sintering of Na_xCoO_2, $LiNi_{1/2}Co_{1/2}O_2$ and $LiNi_{1/3}Mn_{1/3}Co_{1/3}O_2$ after sol-gel synthesis.

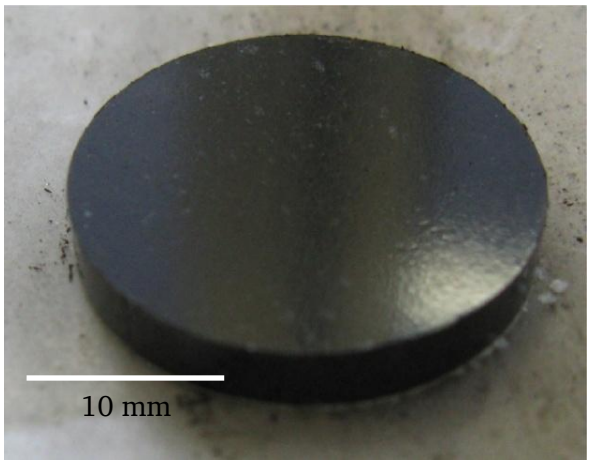

Fig. 3.9: Photograph of the $LiNi_{1/3}Mn_{1/3}Co_{1/3}O_2$ target prepared by sol-gel technique.

3.2 Substrate: strontium titanate $SrTiO_3$ (STO)

For the growth of high quality thin films, the choice of suitable substrates is very crucial. There are several demands to be met by the substrate material, such as chemical inertia, matching thermal expansion, and small lattice mismatch (*lm)*. The film thermal expansion coefficient, α,[d] which differs to thermal expansion coefficient of the substrate, leads to reduced adhesion of the film, which in turn can result in film delamination. To avoid film delamination due to stress and strain, the lattice mismatch should be as small as possible. The lattice mismatch (l*m*), the lattice constants a_f and a_s of film and substrate follow Eq. 3.1.

[d] $\alpha = \frac{1}{L}\frac{dL}{dT}$ in [K^{-1}], with L as length and dT as change of temperature. The thermal expansion coefficient is specific to materials.

Eq. 3.1

$$lm = \frac{(a_f - a_s)}{a_s}$$

The larger lm, the higher the accumulated strain in the film is. The thicker the film, the more elastic energy is stored in it. When a critical film thickness is reached, the energy is reduced by the formation of dislocations. Furthermore, surface quality, film purity, film homogeneity, as well as thermal stability of the substrate have major influence on film quality. Phillips et al. investigated the substrate selection in detail with respect to the influence on the thin film growth.[122] In Table 3.4, seven substrate properties and their effect on film properties are summarized. It visualizes how important the choice of a suitable substrate can be, for the example of superconductivity. From previous studies it is known that on (001)-oriented SrTiO3, NaxCoO2 can be grown epitaxially and with high quality, so STO was the substrate of choice for this thesis.[8, 49, 58] SrTiO3 has a perovskitee structure with alternating TiO2 and SrO planes in c-axis direction. Some material parameters of SrTiO3 are listed in Table 3.5.

Table 3.4: Global issues on substrate selection and the effect on film properties, taken from Phillips *et al.*[122]

	Issue						
Effect	Chemical compatibility	Thermal exp. Match	Surface quality	Substrate cleanliness	Substrate homogeneity	Substrate therm. Stability	Buffer layers
Max. processing temperature	x	x				x	x
Reacted layer at interface	x			x			x
Impurity in film	x			x			x
Impurity in substrate	x						x
Film adhesion	x	x			x		x
Film cracking		x					
Film microstructure			x	x	x	x	x
Film composition	x						x
Film morphology			x	x	x	x	x
Film uniformity			x	x	x	x	x
Superconductivity properties	x	x	x	x	x	x	

[e] The perovskite structure is a member of the cubic structures and has the general formula ABO_3 with the oxidation states A^{+II}, B^{+IV}, and O^{-II}. *A* and *B* are cations of different sizes, whereas *A* is usually bigger than *B* and 12-fold cubooctahedrally coordinated. *B* has a 6-fold coordination. The positions in the unit cell are A (000), B (½½ ½) and O (½½0). Some prominent representatives of this structural class are $CaTiO_3$, $MgSiO_3$, and $SrTiO_3$.

Table 3.5: Material parameters of $SrTiO_3$.

Properties	$SrTiO_3$
a (Å)	3.905
b (Å)	3.905
c (Å)	3.905
density r (g/cm^3)	5.12
melting point T_m (°C)	2080
specific heat c (kJ/kg·K)	0.632
thermal expansion α (10^{-6}/K)	10.4
moh's hardness	6.0-6.5
dielectric constant e (300K)	320

STO is a quantum paraelectric material[123] with a structural phase transition from cubic to tetragonal in a temperature range between 105 K[124, 125] to 110 K.[126] This phase transition is driven by a condensation of a zone corner phonon and includes an oxygen octahedral rotation.[126] The change of the lattice parameters as a function of temperature is shown in Fig. 3.10. The order parameter of this transition increases drastically close to the surface.[127, 128] It leads to the formation of twin domains with different *c*-axis orientations and to the formation of so-called 'anti phase' domains. As a result a complex microstructure with 90° and 180° domain walls occurs, the schematic *a*-*c* 90° domain structure is shown in Fig. 3.11.[129]

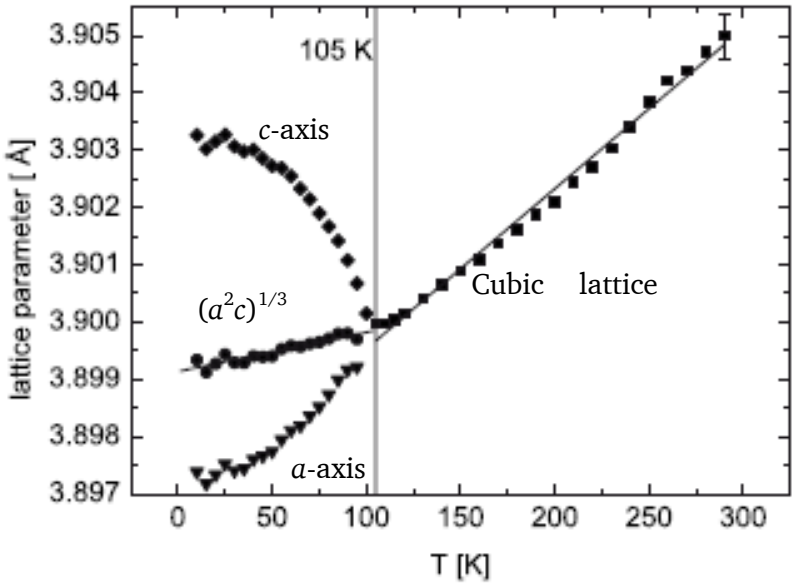

Fig. 3.10: Lattice parameter of a STO single crystal substrate (5 x 10 x 1 mm^3)as a function of temperature from 300 to 10 K, determined from the (002) reflection, lines are linear fits to the volume parameters $(a^2c)^{1/3}$. Taken from Loetzsch *et al.*[125]

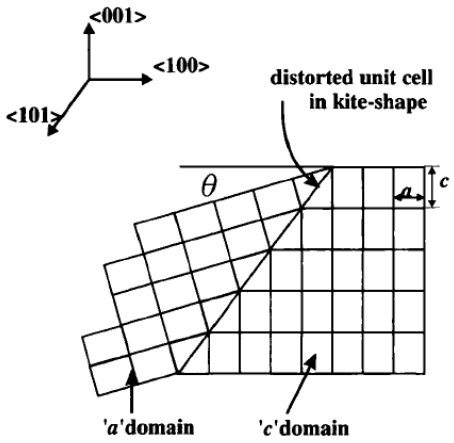

Fig. 3.11: *a-c* 90° domain structure of STO, taken from Doi *et al.*[130]

The cubic lattice is elongated along [*c*] (rotation axis), and compressed along the [*a*] in the tetragonal phase. The *a*- domain is tilted from the surface plane by an angle θ_x, because of matching the *c*-domain at the (101) plane. It has to mentioned that in the near surface region this tetragonal relaxation can be suppressed by the growth of a film on top which induces strain compensating residual strain due to surface defects (e.g. by YBCO[125]). Since Na_xCoO_2 has a hexagonal symmetry, one would expect the formation of a thin buffer to get an epitaxial relation between the substrate and the film. In the case of Na_xCoO_2 on STO the formation of a buffer layer is not the case, as discovered within this thesis. The substrates were supplied by *CrysTec* with the dimension of 5 x 5 x 0.5 mm^3 and 5 x 5 x5 1.0 mm^3.

3.3 Growth of Na_xCoO_2, $LiCoO_2$, $LiNi_{1/3}Mn_{1/3}Co_{1/3}O_2$, and $LiNi_{1/2}Co_{1/2}O_2$ thin films

For the growth of Na_xCoO_2, $LiCoO_2$, $LiNi_{1/3}Mn_{1/3}Co_{1/3}O_2$, and $LiNi_{1/2}Co_{1/2}O_2$ thin films, STO substrates with different orientations were used. To investigate thin film properties of the mentioned materials, first thin film growth has to be optimized concerning substrate temperature, annealing temperature, gas flow and gas partial pressure during and after deposition. The used STO substrates had to be handled with care and cleaned well to avoid contaminations of the surface with dust or other unwanted species. The cleaning procedure was done prior to each deposition for every single substrate, following the cleaning procedure mentioned next:

1. 10 min in ultra-sonic cleaner in acetone (> *99.9% GC Ultra Grade, Carl Roth)*
2. 10 min in ultra-sonic cleaner in ethanol (> *99.8% p.a., Carl Roth)*

After substrate cleaning, it was directly fixed onto the substrate holder, which is put on top of the bulb heater. Then the chamber was locked, flushed with nitrogen, and pumped down with the pre-pump to a pressure of 10^{-2} mbar. This procedure was repeated two times before evacuating the chamber with a turbo molecular pump until a base pressure of 10^{-5} mbar was reached. Afterwards, the main valve to the turbo molecular pump was closed, and a bypass was opened to reduce the pumping speed. At the same time a working gas (e.g. O_2) was introduced into the chamber using a mass flow controller. The flow has been changed until the desired pressure deposition pressure was reached. After the chamber pressure was stabilized, substrate was heated using an individual heating sequence for every material to be

deposited. During substrate heating, the shutter between substrate and target was closed to avoid (i) heating of the target material and (ii) deposition on the substrate due to pre-ablation of the target with a frequency of 5 Hz and 1000 pulses. For the deposition process, a KrF Excimer Laser (*Coherent Inc*.) with a wavelength of 248 nm was used. After the deposition temperature was reached, a settling time of 3 min was given before the deposition was started to have a homogenous temperature distribution in the substrate. The distance between target and substrate, $d_{T\text{-}S}$, was kept at 36 mm.

3.3.1 Growth of Na_xCoO_2 thin films

For the growth of Na_xCoO_2, substrates of STO with different orientations have been used, (100), (110), and (111). To grow Na_xCoO_2 thin films oxygen has been introduced as background gas during growth and during annealing procedure to get an oxygen stoichiometry of 2 in the films. To optimize thin film growth, several parameters, such as substrate temperature during growth (T_{sub}), substrate temperature during annealing (T_a), annealing time (t_a), gas pressure during deposition (p_d), and laser fluence (E_f) were investigated. E_f was changed by changing high voltage with an attenuator between 1; 1.2; 1.5; 1.8, and 2 J/cm^2, keeping the spot size of the laser constantly at 3.8 mm^2. The energy of one laser pulse was measured in front of the entrance window to the chamber, using an energy meter (*FieldMax II, Coherent Inc.*) and an energy detector (*Excimer Laser EnergyMax Sensor J-25MUV-248, Coherent Inc*.). The energy loss due to the window was determined to be ~10%, for a clean window. T_a was varied from 720 to 760 °C with steps of ΔT = 20 K, t_a was varied from 10 to 30 min. The deposition temperature itself was varied from 300 up to 700 °C to find the optimum growth temperature. To find the optimum oxygen partial pressure, the pressure was changed in a wide range from $1 \cdot 10^{-3}$ to $2.5 \cdot 10^{-1}$ mbar. It has to be mentioned that the chamber pressure was measured spartially below the heater. The deposition rate at a fluence of 1.2 J/cm^2 was ~0.33 Å/pulse, so for 3,600 pulses an average film thickness of ~120 nm was reached. This was measured by a profilometer (*DekTak* 8000, *Veeco*) after the step was formed by lithography. In Fig. 2.1, an example for a height scan on a film deposited with 4,600 pulses is shown.

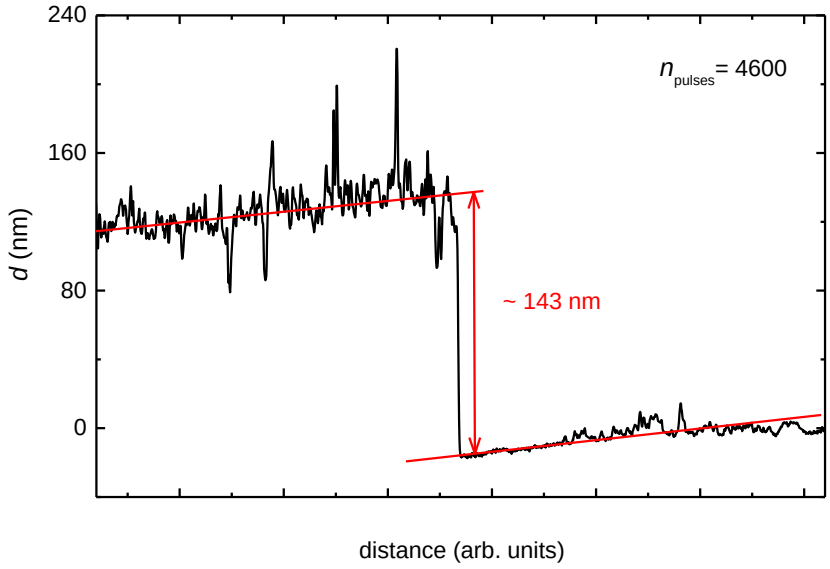

Fig. 3.12: Height scan of a Na_xCoO_2 thin film deposited with 4,600 pulses on STO (100). Half of the film was covered with photoresist to remove the uncovered portion by concentrated HCL-solution. Afterwards, the photoresist was removed using acetone.

In order to investigate the growth behavior on STO (100) and to check for a buffer layers formed between Na_xCoO_2 and STO, a series of thin films with 3 to 9 monolayers were fabricated. Since the films were very thin, they were not annealed avoiding the evaporation of sodium. In addition, interval deposition of Na_xCoO_2 was tested.[131] This technique is based on a periodic sequence of high-frequency depositions of an amount of material just enough to form one monolayer. The deposition is interrupted subsequently allowing film reorganization. This principally allows growing films according to *Frank-van-der-Merwe* growth mode instead of *Vollmer-Weber* growth mode. A sequence of five times 40 pulses at f = 30 Hz with 30 sec pause between each interval was applied.

3.3.2 Growth of $LiCoO_2$ thin films

The $LiCoO_2$ films were grown on STO (100), STO (110), and STO (111) substrates. In contrast to sodium cobaltate, the optimum oxygen pressure during the deposition was 1 mbar ,and the used laser fluence was 2 J/cm^2 at 5 Hz and 3600 pulses duration. A substrate temperature of 550 °C was adopted from the Na_xCoO_2 deposition. For most of the $LiCoO_2$ films no annealing was performed, but films were cooled down after deposition in 1 bar of oxygen.

3.3.3 $LiNi_{1/3}Mn_{1/3}Co_{1/3}O_2$ and $LiNi_{1/2}Co_{1/2}O_2$

For the growth of $LiNi_{1/3}Mn_{1/3}Co_{1/3}O_2$ and $LiNi_{1/2}Co_{1/2}O_2$, STO (111) and STO (100) were used as substrate material. Substrate temperature was 550 °C and annealing temperature was tuned between 600 and 630 °C. The deposition was performed in 1 mbar of oxygen background pressure, whereas the oxygen background pressure during 10 min of annealing was kept at 1 bar. The laser fluence was 1.2 J/cm^2 with f = 5 Hz and the number of pulses were varied between 3,600 and 5,000.

3.4 Superconducting $Na_xCoO_2{\cdot}yH_2O$ thin films

For obtaining superconducting thin films of $Na_xCoO_2{\cdot}yH_2O$ the sodium content has to be balanced between $x \approx 0.25$ and $x \approx 0.33$, at a very exact amount of water ($y = 1.3$), inserted in between the sodium and CoO layers. Realizing superconducting $Na_xCoO_2{\cdot}yH_2O$, several methods available in the case of bulk sodium cobaltate, as described in chapter 2.1.1. For bulk synthesis of superconducting sodium cobaltate, usually a Br_2/CH_3CN (1.06 eV) solution is used. Also solutions of I_2(0.54 eV), F_2(2.87 eV), and $KMnO_4$ (1.15 eV) are capable of oxidizing sodium. By using a bromine/acetonitrile solution to deintercalate sodium from the crystal lattice, the following reaction (Eq. 3.2) takes place.

Eq. 3.2
$$Na_xCoO_2 + \frac{\delta}{2} Br_2 \rightarrow Na_{x-\delta}CoO_2 + yNaBr$$

By forming NaBr, the amount of sodium in the film is reduced about a factor of δ due to the diffusion of Na in the *ab*-plane out of the unit cell. Due to strong repulsive forces between the CoO_6 layers, the diffusion path is restricted to the *ab*-plane between the oxygen layers, as shown schematically in Fig. 3.13.

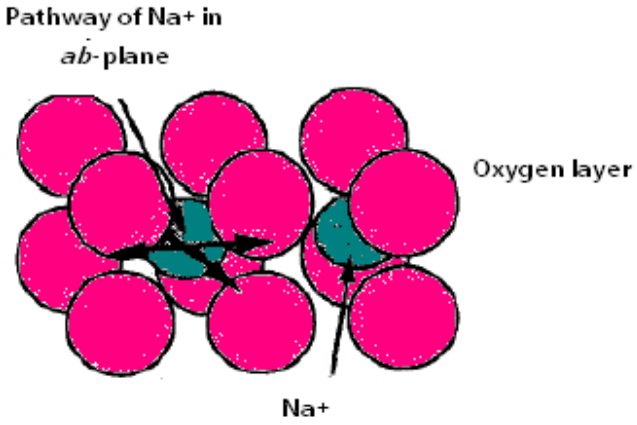

Fig. 3.13: Diffusion path of the Na^+ ions along *ab*-plane of the unit cell of Na_xCoO_2. Taken from Krockenberger *et al.*[132]

In this study, the deintercalation of sodium was accomplished by either *ex-situ* deintercalation by using 0.02 and 0.03 mol/l bromine acetonitrile solution, *in-situ* by choosing specific annealing conditions during thin film growth. Films were kept in the oxidative solution for 5 to 15 min, before they were cleaned using first pure acetonitrile and second water. To intercalate the desired amount of water molecules in the structure several methods were tested, including the ones described in literature. The tested intercalation techniques are based on different kinetics and thermodynamics. The first intercalation attempt was to put the films directly in cold, distilled water for a defined time. The second attempt was to use a green-house chamber, see Fig. 3.14 with a humidity of 99 to 100% at room temperature. To avoid direct contact of the films with condensed water in the green house chamber, a small sample holder including a roof (see inset of Fig. 3.14) for protection was designed. The green-house chamber was tempered and humidified by a warm water vapor flow with N_2 supplied by a heated reservoir of distilled water. The experimental setup is given in Fig. 3.15. The green

house was regularly flushed with N_2 to reduce CO_2 and CO partial pressures. The presence of CO_2 can lead to the formation of Na_2CO_3 and Co_3O_4, thus decomposing the film. Utilizing the warm water vapor a temperature of 85 °C at a relative humidity of 80% was stabilized. The third technique to quickly incorporate water was to use a pressured hot environment. This was realized by putting the films in a commonly, available pressure cooker. With the relief valve on top of the pressure cooker, three pressure settings were adjustable, 1 bar (relief valve completely open), 1.2 and 1.8 bar. These pressures correspond to water vapor temperatures of 100 °C, 103 °C, and 115 °C, respectively. Films treated with this method were stored in the water vapor of boiling water for several hours after flushing the chamber with N_2 and closing the lid. In addition to the three above mentioned techniques, the deintercalation of Na and the intercalation of water were combined. Therefore, a 0.02 mol/l acetonitrile solution was mixed with an equal amount of H_2O to reduce the time gap between the two steps. The idea was to incorporate water molecules at the same time when Na ions diffuse are deintercalated.. The challenge was to prevent of the oxidation of Na_xCoO_2 and, at the same time, to offer enough water for intercalation. To face this challenge the bromine solution was neutralized with an aqueous sodium hydroxide solution after the deintercalation time was finished. The sodium ions in a NaOH solution react with the excess active bromine ions, so H_2O can intercalate right at the same time, when the deintercalation process is stopped.

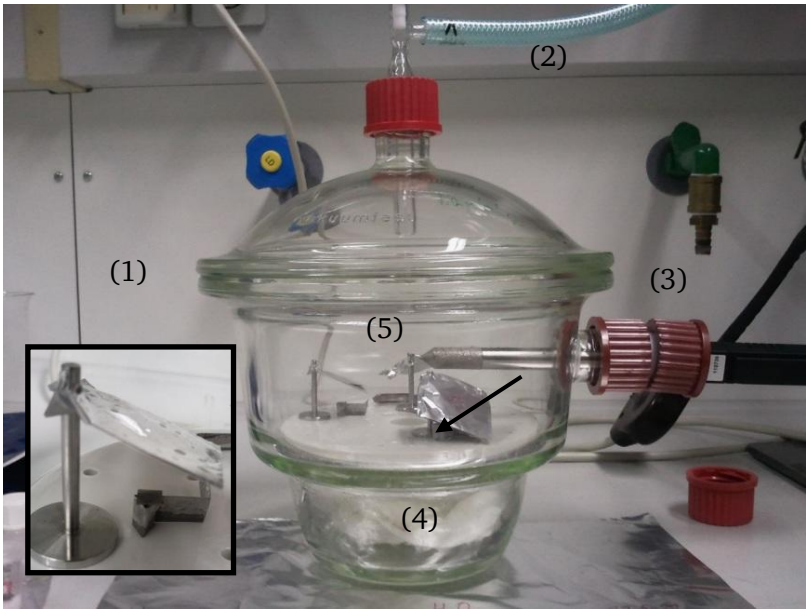

Fig. 3.14: Green-house chamber (1) used for water intercalation into Na_xCoO_2 thin films. (2) Gas inlet, (3) inlet flange for hygrometer, (4) moistured cotton to provide a humid atmosphere in the chamber, and (5) sample stage, Inset bottom left corner shows the sample holder.

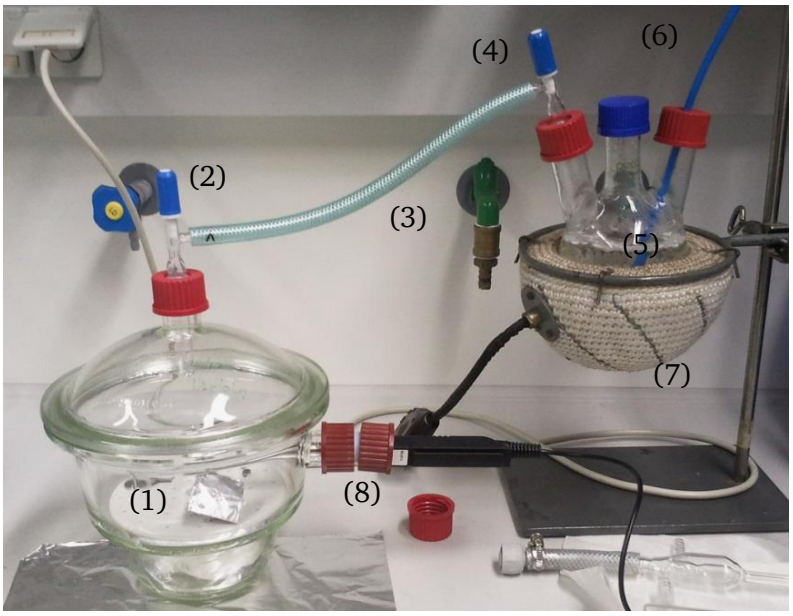

Fig. 3.15: Experimental setup for the humidification of the green-house chamber: (1) green-house chamber; (2) water vapor nitrogen inlet valve; (3) tube to water reservoir; (4) outlet valve of water reservoir,; (5) water reservoir, (6) nitrogen tube; (7) heating mantle, (8) inlet flange for hygrometer.

The following sample nomenclature was established: cnc XX t P, here *XX* represents sample number, *t* treatment duration, and *P* type of treatment after deposition. The following list gives an overview on the abbreviations for the different treatments:

2BA/W or A: sodium deintercalation with 0.02 mol/l Br_2-CH_3CN and rinsed with water or CH_3CN

3BA/W or A: sodium deintercalation with 0.03 mol/l Br_2-CH_3CN and rinsed with water or CH_3CN.

2BA + 1N: sodium deintercalation with 0.02mol/l Br_2-CH_3CN and neutralization with 1 mol/l NaOH solution.

2 or 3 BA+ cN: sodium deintercalation with 0.02 mol/l or 0.03 mol/l Br_2-CH_3CN and neutralization with concentrated NaOH solution.

1B(A+W)/W: sodium deintercalation with 0.01 mol/l Br_2-CH_3CN/H_2O and rinsed with water

For the water intercalation the following abbreviations were used:

W(T): intercalation in water at *T* (°C)

GH(T): intercalation in the green-house chamber at a starting temperature of *T* (°C) and then cooling down to room temperature

GHN(T): intercalation in the green-house chamber with nitrogen flow, a starting temperature *T* (°C) and then cooling down to room temperature

1N: sample in 1 mol/l NaOH solution after neutralization of the Br_2 solution

cN: sample in concentrated NaOH after neutralization of the Br_2 solution

PC(p): intercalation in the pressure cooker of pressure p (bar)

As deposited films are only named by *cnc*, followed by a number.

3.5 Characterization methods

In the following, a brief description of the used characterization methods for bulk targets, powders, as well as thin films is given.

3.5.1 X-ray diffraction

In 1912, X-ray diffraction at a lattice was discovered by *Max von Laue.*[133] As the wavelength of X-ray radiation has the same order of magnitude as crystal lattices, diffraction occurs, which can be used to investigate the structure of a material. After passing several lenses slits and monochromators on the primary arm of a diffractometer, the X-ray radiation strike the sample surface, one portion is elastically scattered and the other portion is diffracted, which is detected by a scintillation counter on the secondary arm of a diffractometer. The generation of X-rays is explained by the functionality of an X-ray tube. An X-ray tube consists of a cathode and an anode. The cathode filament is heated, thus free electrons are emitted from the filament. A voltage of 30 to 50 kV is applied between cathode and anode, which accelerates the electrons to the anode with high energy $E = U \cdot e$, where U is the voltage an e[f] the elementary charge of an electron. Hot electrons incident on the anode material transfer kinetic energy via collision cascades with electrons from the anode material atoms, exciting inner and outer shell electrons and phonons (dissipating heat). A decay of excited inner shell electrons result in the emittance of specific and unspecific radiation. The radiation consists of the continuous radiation (Bremsstrahlung) and characteristic monochromatic radiation, which depends on the anode material. A schematic X-ray pattern of a molybdenum target is shown in Fig. 3.16.

[f] $e = 1.6021 \cdot 10^{-19}$ C

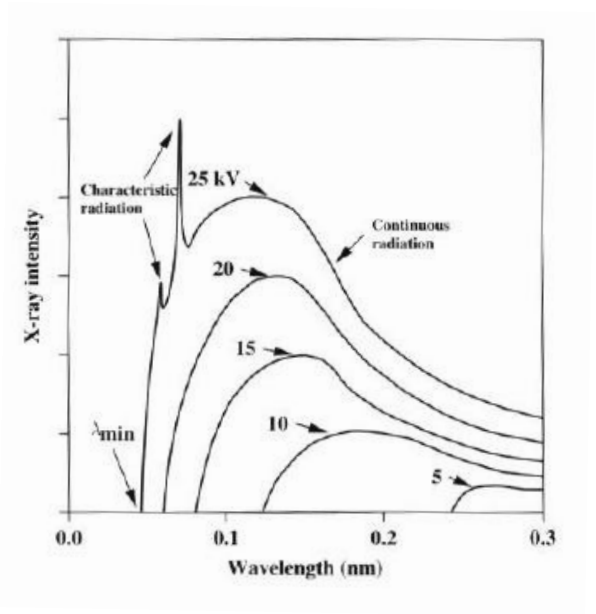

Fig. 3.16: Schematic X-ray pattern for a molybdenum target as a function of voltage and wavelength. Taken from De Graef *et al.*[134]

The maximum energy of the resulting radiation depends on the applied high-voltage and is defined in Eq. 3.3, with m[g] as the electron mass, v as velocity, h[h] as *Planck's* constant, c as speed of light, and λ as the wavelength.

Eq. 3.3
$$E_{\max} = e \cdot U = \frac{1}{2} m \cdot v^2 = \frac{h \cdot c}{\lambda}$$

The minimum wavelength of an X-ray tube is given in Eq. 3.4

Eq. 3.4
$$\lambda_{\min} = \frac{h \cdot c}{e \cdot U} \approx \frac{12.4}{U}$$

X-ray intensity is calculated by integrating over one of the curves shown in Fig. 3.16. It is proportional to the emission current, the atomic number and the used voltage. As already mentioned, characteristic radiation has its origin in electron transitions to inner shells of anode atoms. Usually these shells are fully occupied. Impinging electrons of a sufficient energy excite electrons out of the inner shells into vacuum levels. Subsequently, electrons from higher occupied states fall relax to these empty inner shell by emitting a photon with an energy equal to the energy difference between the two states. The energy difference is element specific and can be described by *Moseley's* law (Eq. 3.5)

Eq. 3.5
$$\nu_{K_\varepsilon} = \frac{3}{4} R_\infty (Z-1)^2$$

Here R_∞[i] is the *Rydberg* constant, and Z the atomic number. The energy levels of an atom and corresponding transitions are shown exemplarily in Fig. 3.17

[g] m=9.109·10^{-31} kg

[h] h= 6.626·10^{-34} Js

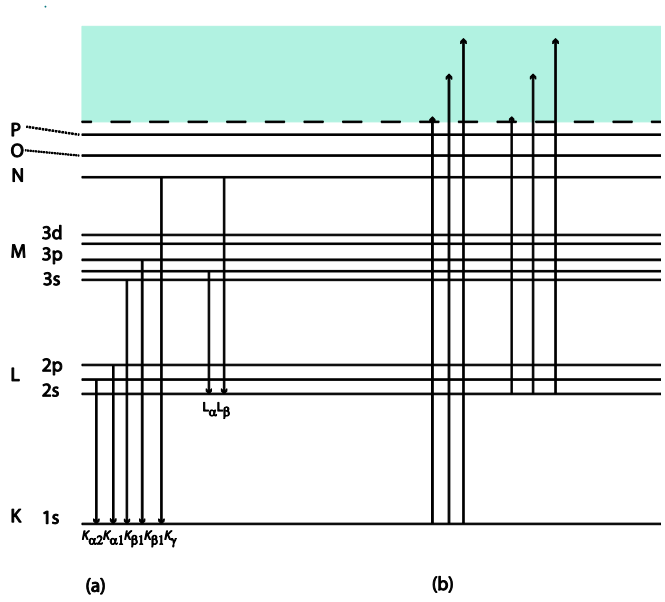

Fig. 3.17: Schematic view of energy levels in an atom. (a) Characteristic radiation resulting from different transitions. (b) Absorption of X-ray radiation and excitation off inner shell electrons.

The characteristic radiation lines are labeled as follows. The capital letter (*K, L, M*) names the energetic level *in* which the atom relaxes, the subscripted Greek letter (α, β, γ) specifies the level *from* which the atom relaxes, and the subscripted number (1, 2) the splitted energy levels of the excited state can be distinguished, compare to Fig. 3.17. Selected *K* wavelengths are given in Table 3.6.

Table 3.6: List of common target materials with their characteristic wavelengths.

Target	K_α (Å)	$K_{\alpha 1}$ (Å)	$K_{\alpha 2}$ (Å)	$K_{\beta 1}$(Å)
Cr	2.2910	2.2936	2.2897	2.0849
Fe	1.9374	1.9399	1.9360	1.7566
Co	1.7903	1.7929	1.7889	1.6308
Cu	1.5418	1.5444	1.5406	1.3922
Mo	0.7107	0.7136	0.7093	0.6323

As evident from Table 3.6, $K_{\alpha 1}$ and $K_{\alpha 2}$ are very close to each other. Due to this fact, often an average of both is calculated (K_α) by the sum of 2/3 $K_{\alpha 1}$ and 1/3 $K\alpha_2$. Nevertheless it is possible to distinguish between $K_{\alpha 1}$ and $K_{\alpha 2}$, only has been used for the measurement conducted for this thesis.

The physical background of diffraction is described by the interaction of electromagnetic waves with local electronic potentials of periodic crystal lattices. By using coherent radiation, all electrons of all atoms in one crystal layer oscillate with in phase, consequently concentrically waves are emitted, forming a complex interference pattern. Hereby, constructive interference will only occur in certain directions, depending on atomic spaces radiation wavelength. In periodic crystal lattice, many parallel planes of atoms, as shown in Fig. 3.18, exist

[i] R_∞= 1 09,6 77,5 84·10 ^{7} m^{-1}

and interact with the incident radiation. The geometric relation of incident radiation and crystal lattice was given by *Bragg*, see Eq. 3.6, and is visualized in Fig. 3.18.

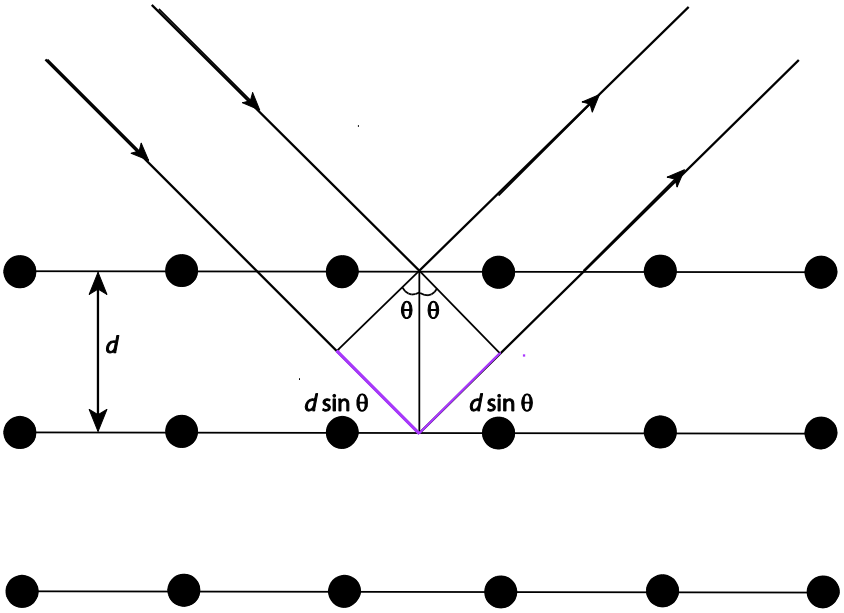

Fig. 3.18: Scheme of diffraction the lattice diffraction at a periodic lattice with periodicity I (Bragg's law).

Famous *Bragg's* law is connecting radiation wavelength (λ) with atomic distance (d), and diffraction angle (θ),

Eq. 3.6
$$2d \sin\theta = n \cdot \lambda$$

Knowing the diffraction angle θ and the wavelength λ of the used X-rays, d-spacings and thus crystal structure and indexing of the reflections with corresponding *Miller's indices hkl* is possible. By applying reciprocal metric tensors it is possible to find for all seven crystal systems the dependence of d_{hkl}, *hkl*, and the lattice constants *a*, *b*, and *c* and corresponding angles α, β, γ, to the calculated *d*-spacings from *Bragg's* law.

Table 3.7: Relation of $1/d_{hkl}$ to h,k,l and a,b,c, and α,β,γ.[134]

System	g	Expression
Cubic		$1/a\{h^2+k^2+l^2\}$
Hexagonal	^{h}g	$\{4/3a^2(h^2+k^2+hk)+l^2/c^2\}^{1/2}$

For the hexagonal lattice of Na_xCoO_2 the follow dependency (Eq. 3.7) between *hkl,* the *d*-value and the lattice constants *a*, *b*, and *c* can be derived from Table 3.7.

Eq. 3.7
$$d_{hkl} = \frac{a_0}{\sqrt{\frac{4}{3}(h^2 + hk + k^2) + \left(\frac{a_0}{c_0}\right)^2 l^2}}$$

Several measurement setups are possible to investigate crystal structure, crystallinity, symmetry, and atomic positions. In addition this method can be used to determine stress,

strains, and texturing of a thin film on a substrate. The structural investigation of all thin films and bulk materials, was done with a four-circle diffractometer (*SmartLab*, *Rigaku*) in parallel beam geometry. The optical path was the following:

Radiation source (rotating anode)→shutter→Göbel-mirror→automatic variable scattering slit PSA 0.5°→manual hight limiting slit (2mm) →incident slit box→**sample**→receiving slit box I→PSA open→automatic variable scattering slit PSA 0.5°→receiving slit box II→ attenuator→graphite monochromator→BBM slit for K_β→detector (scintillation counter with LiF crystal at 700 V)

3.5.2 High resolution scanning electron microscope

With the use of a high resolution scanning electron microscope (HRSEM) it is possible to get a very detailed view on surfaces of bulk materials, as well as thin films. An electron beam strikes the sample and is scanned over the sample surface. There are two main interactions between the incoming electrons and the sample material, which there are elastic and inelastic scattering. Because of scattering, primary electrons (incident electrons) change their impulse and energy. Due to energy transfer of primary electrons to the sample material's electrons, secondary electrons are emitted and can be detected. The following scheme (Fig. 3.19) shows the different occurring interaction between primary electrons and sample material.

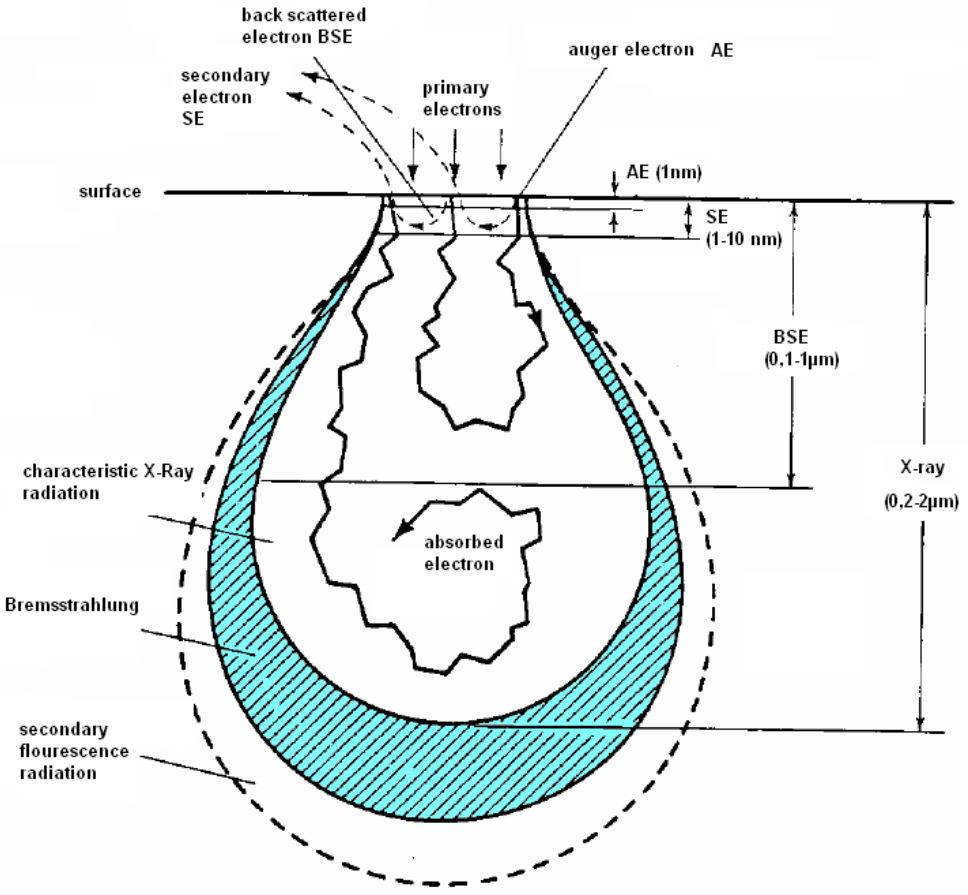

Fig. 3.19: Interaction of primary electrons with sample material and depth profile of the resulting signals. Redrawn from Eastmen *et al.*[135]

Secondary electrons can be used to get information about sample surface, as they originate only from the very first top layers. For a materials contrast and for gathering information from areas deeper inside the sample, back scattered electrons (BSE) are used, as they originate from elastic scattering with electrons and atoms within a sample material depth of 0.1 - 1 µm. In addition to emitted particles (BSE, AE) characteristic and continuous X-ray radiation is evoked due to the interaction of primary electrons and sample material's electrons. By exciting electrons from the inner shells to the vacuum energy and subsequent relaxing of electrons from outer atomic shells, element-specific X-ray radiation is evoked. Characteristic X-rays are used for qualitative and quantitative analysis of the chemical composition of the sample material. For that reason, most of the common microscopes are equipped with an energy-dispersive X-ray detector (EDS). For this study, a microscope XL 30 FEG (*Philips*) was used, equipped with an EDS-CDU LEAP detector. Since the diameter of the electron beam is very small, a lateral resolution of ~2 nm is possible. The energetic resolution of the EDS detector is 135 eV.

3.5.3 Thermogravimetric analyses

The thermo gravimetric analysis and the differentional scanning calorimetry are methods of thermal analyses, which are used to determine characteristic properties of a substance or a compound related to temperature. Thermal analysis is defined in DIN 51005 as follows.

"*A thermal analysis is the generic term of all methods used to determine chemical or physical properties of a substance or a compound as a function of temperature or time, where the sample is treated with a defined temperature program*."

This definition is very broad and includes all kinds of methods, which are related to temperature treatments. TG is a very useful tool for investigating reactions taking place, for example, for the synthesis of ceramics. In the TG the sample coupled to a balance, is heated continuously in a furnace. The change of mass vs. temperature is monitored. For reproducibility it is very important that the heat treatment takes place in a defined atmosphere. The temperature range of commercially available thermo-balances ranges from room temperature to 1,500 °C. The change of mass during heat treatment can originate due to different types of reactions such as oxidation, burning, decomposition, and desorption of molecules like H_2O.

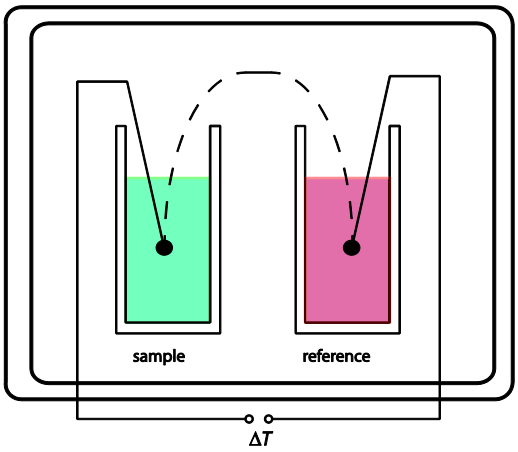

Fig. 3.20: Scheme of the measurement setup for thermogravimetry and differential thermo analysis.

3.5.4 Secondary ion mass spectrometry

Secondary ion mass spectrometry (SIMS) is a highly surface sensitive way of characterization using, an ion beam in combination with a mass spectrometer. A sample is bombarded with ions with intermediate energies of 1 to 25 keV, whereas secondary ions excessing from the sample are detected in the mass spectrometer. During measurement, primary ions ablate the sample surface continuously. By this procedure neutrals, as well as charged species are ejected (sputtered). The amount of charged atoms, molecules, and clusters depends on the type of primary ions, their energy, and their incident angle. The majority of emitted particles originate from the first 3 monolayers (~1 nm), so SIMS has a very high surface sensitivity. As a drawback, mixing due to sputtering samples specimen materials within 15 nm in depth. Mass spectrometric analysis allows quantitative analysis and chemical investigation of the ejected species. All elements can be detected, even very light elements, such as helium or hydrogen.[136] The detection limits of almost all elements are low, as there is low continuum background in the mass spectrometer. Typical detection limits of some elements in GaAs and Si are shown exemplarily in Table 3.8. Sputtering rate depends on several factors, such as type of primary ion (Cs^+, O_2^+, Ar^+), energy and angle of incidence of primary ions, binding characteristics of the elements, chemical composition of the matrix, and surface morphology. With SIMS, three types of measurements are possible, qualitative analysis, line scans, and depth profiling. For qualitative analysis, the ion beam hits a selected area of the sample and is scanned to receive a mass spectrum from that selected area. With SIMS, also semi-quantitative analyses are possible, an example is given in Fig. 3.21.

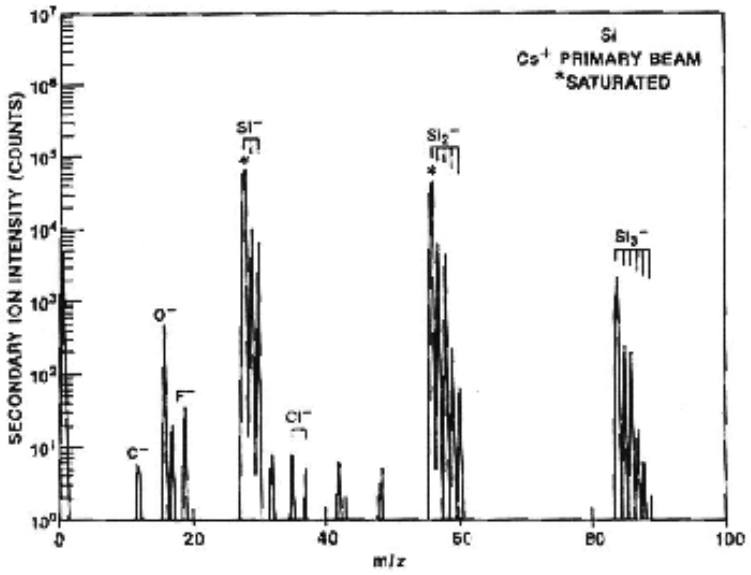

Fig. 3.21: Mass spectrum of a pure silicon wafer with Cs^+ primary ions. Taken from Ortner *et al.*[137]

Here, the Si matrix ions are present as atoms as well as clusters. In addition, C, O, F, and Cl are detected as electro-negative impurities. For a quantitative, one-dimensional analysis, a line-scan is the method of choice. The ion beam is scanned across the surface of the sample following an exactly defined line. The mass spectrometer is fixed to one or several masses, allowing to detect elements line-resolved. An example for a line-scan is given in Fig. 3.22. Here, the ^{27}Al signal was monitored and the amount of Al in the film was estimated to be 17.5 at%.

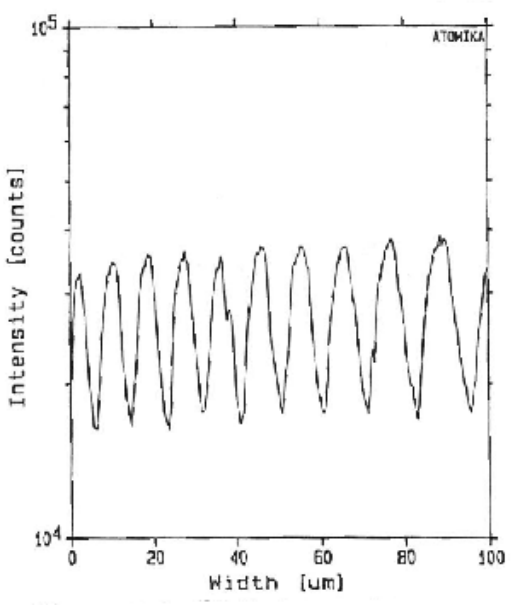

Fig. 3.22: Line-scan of an AlGaAs/GaAs film stack with Ga^+ primary ions. Taken from Ortner *et al.*[137]

A depth profile is the most common SIMS measurement. The longer the sample is bombarded by primary ions, the deeper the measurement carter in the material. For constant measurement conditions, crater depth and measurement time are linearly correlated and a depth profile (concentration of an element as a function of sputtering time) can be obtained. An example for a depth profile of scan is shown in Fig. 3.23.

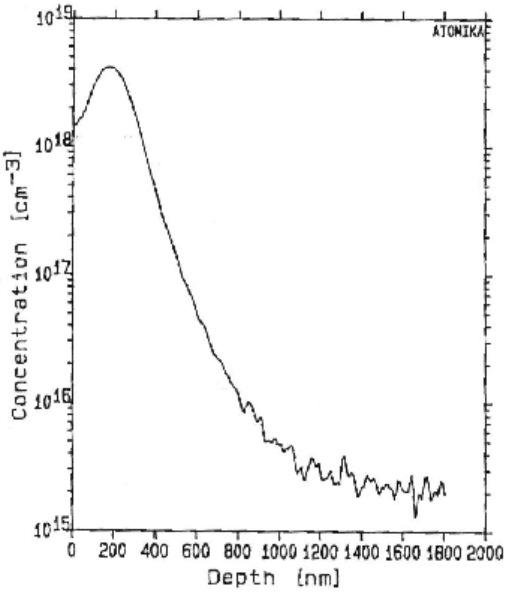

Fig. 3.23: Depth profile of ^{30}Si in a GaAs sample. Taken from Ortner *et al.*[137]

Table 3.8: Detection limits of selected elements by SIMS. Taken from Williams *et al.*[136]

Element	Substrate	Detected species	[ppma]	[atom cm^{-3}]
H	Si	H^+,H^-	20.0	1,00E+18
Be	GaAs	Be^+	0.002	8,00E+13
B	GaAs	B^+	0.01	5,00E+14
B	Si	B^+	0.002	1,00E+14
C	Si	C^-	1.0	5,00E+16
Ge	Si	O^-	2.0	1,00E+17
Al	GaAs	Al^+	0.001	4,00E+14
P	Si	P^-	0.1	5,00E+15
Si	GaAs	Si^+	0.01	4,00E+14
cr	GaAs	Cr^+	0.001	4,00E+13
Mn	GaAs	Mn^+	0.001	4,00E+13
Fe	GaAs	Fe^+	0.002	7,00E+13
Cu	GaAs	Cu^+	0.02	1,00E+15
Zn	GaAs	Zn^+	0.1	5,00E+15
Ge	GaAs	Ge^+	0.2	1,00E+16
As	Si	$AsSi^-$	0.06	3,00E+15
Sn	GaAs	Sn^+	0.1	5,00E+15

The lateral resolution of this micro probe is limited by the primary beam size and the primary ion source brightness.[138] A bright source using liquid metal field ionization can yield to a beam size down to ~200 nm, without a mass analysis system attached, even a beam size of ~50 nm is possible.[137, 138] In general, the resolution in SIMS is defined as the ratio of the extraction field strength and the energy spread of the sputtered ions. For a typical field strength of 10^6 V/m and an energy spread limited to 0.5 to 1.0 eV, a resolution of ~0.5 to 1.0 μm is achievable. For the quantification of SIMS profiles complex matrix effects have to be taken into account, which are usually done by using relative sensitivity factors (RSF). The RSF have to be defined separately for every analyzed element according to the following formula.

Eq. 3.8
$$\frac{c_A}{c_M} = s_{A/M}\frac{I_A}{I_M}$$

Here, c_A and c_M are the concentrations of the analyzed element and the matrix, respectively, and I_A and I_M are the intensities of the analyzed element and matrix, respectively. More details on quantitative analysis via SIMS can be found in literature.[136]

3.5.5 Atomic force microscope

Atomic force microscope (AFM) is very surface-sensitive on atomic scale. It is a combination of a scanning tunneling microscope and a stylus profilometer. The surface is scanned by very small stylus, which experiences different forces (sub-nano Newton), depending on the scanned surface. These forces move the cantilever, this movement detected via a laser, in reflection geometry. In contact-mode, the AFM tip is always touching the surface, which evokes repulsive, short range forces at the contact area due to the interaction of the electronic poten-

tials of the cantilever with electronic potentials of the surface atoms of the sample. In addition to that, long-range forces, e.g. *coulomb-coulomb* interaction between charges, dipole-dipole interactions, and polarization forces can occur. These types of forces can be either attractive or repulsive, as shown in Fig. 3.24.

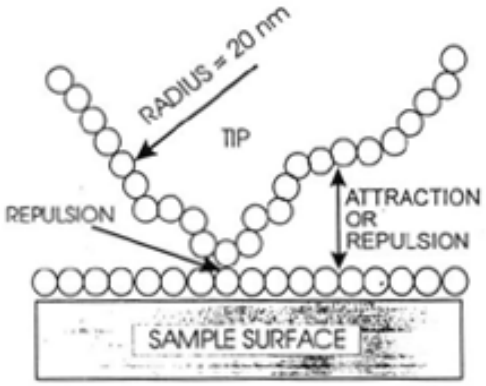

Fig. 3.24: Scheme of forces when the tip of an AFM touches sample surface. Balls represent surface atoms and tip atoms. Taken from Ortner *et al.*[137]

Both types of forces contribute to the net force acting on the stylus, but only repulsive forces allow to obtain a high-resolution image of the sample surface. Long-range attractive forces pull the tip towards the sample surface and give rise to an increase of local repulsive forces. This has an influence on measurement conditions and has to be taken into account during experiment. This is a very important fact, especially when characterizing very soft material, which can be easily altered by the tip. The interaction of tip and sample surface can be described by so-called force-distance curves. A schematic example is given in Fig. 3.25.[139-142]

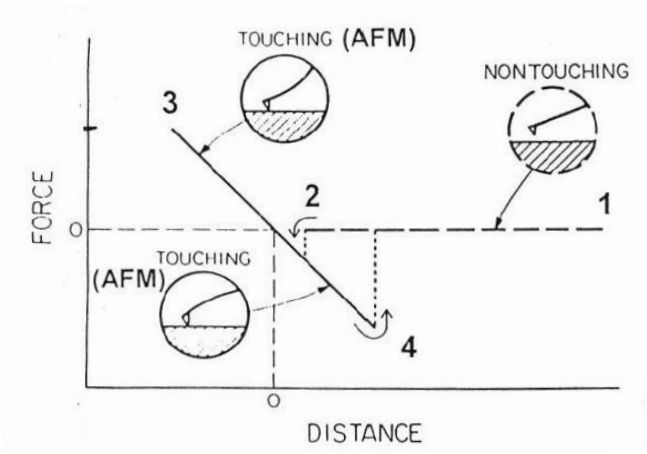

Fig. 3.25: Force-distance curve showing the interaction of a cantilever with sample surface. Taken from Ortner *et al.*[137]

For large distances between AFM tip and sample surface, there is no interaction and the force is zero (point 1 to 2 in Fig. 3.25). At point 2 in Fig. 3.25, the tip starts interacting and getting into contact with the sample surface due to attractive van-der-Waals forces. When moving the sample further towards the tip, attractive forces change to repulsive forces and by pulling back the tip, again forces are reduced along the line from point 3 to 4 in Fig. 3.25. Below the zero-force line, forces are attractive due to surface adhesion acting on the tip. In

point 4, the load of the cantilever and the adhesion force are balanced, the tip tends to flip-off the surface when retracting the sample even further. For the AFM measurements, the force can be set to values on the line between point 3 and 4. When moving the AFM tip nearer than to point 4, the contact force is minimized. A detailed description of force interactions between tip and sample surface is given in literature.[140] The analytical potential of AFM is huge since the imaging capabilities reach from micrometer scale down to atomic scale. A direct depth information is included in the images, insulators as well as conducting materials can be analyzed without coating, and *in situ* characterization under liquids and in air are possible. This allows to detect surface processes directly. For this study, a *3D Stand Alone* AFM from *Asylum Research* was used.

4 Results and Discussion

4.1 Target preparation

In this chapter, the results of the target preparation of Na_xCoO_2 by classical solid state-synthesis and by a novel sol-gel route will be presented. In addition, result of target preparation of LNMCO and LNCO will be described.

4.1.1 Na_xCoO_2 target via solid-state preparation

In the case of volatile elements like Na, which have a very high vapor pressure the formation of Na_2O, Na_2O_2, and NaO_2 has to be taken into account when preparing targets of Na_xCoO_2 at temperatures above 700 °C. Na_2O itself decomposes to Na and NaO_2 under heating conditions.[143] Due to that the sodium content is reduced in the target, during preparation of Na_xCoO_2, and can be compensated by providing excess Na_2CO_3 in the target. For the fabrication of thin films from a Na_xCoO_2 target, this fact has to be taken into account as well. For the first attempt to produce a target for thin film deposition, the classical solid-state synthesis route, as described in chapter 3.1.1, was utilized. The produced target had a diameter of 16.89 mm, a height of 5.51 mm, and a mass of 3.403 g. The geometrical density ρ was calculated by $\rho = m/V$, where m is the mass in g, and V the volume in cm^3, to 2.757 g/cm^3, which is 58% of the theoretical density of $Na_{0.75}CoO_2$ (ρ_{th}= 4.738g/cm^3). Fig. 4.1 shows a photograph of the produced target. After the sintering process plate- and needle- shaped crystals were identifiable on target surface. Sintering of Na_xCoO_2 at high temperatures (above 960 °C) has been recently reported by Yamakawa *et al.* resulting in a target density of up to 95%.[144]Disadvantage of this high density target, fabricated at higher sintering temperatures is the loss of sodium, and because of that an admixture of the very stable Co_3O_4 occurs.

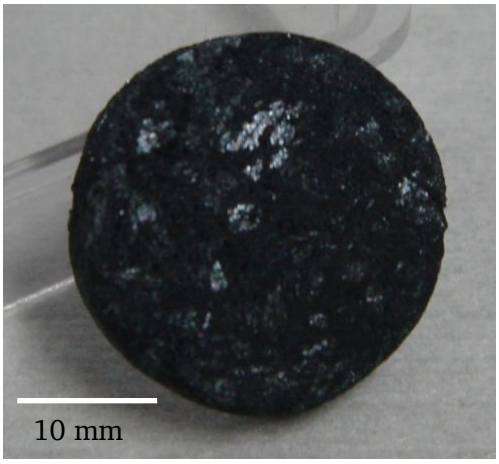

Fig. 4.1: Photograph of aγ-$Na_{0.75}CoO_2$ target produced by the classical solid-state synthesis route after sintering for 60 h at 880 °C. Plate-and needle-shaped crystals are identifiable.

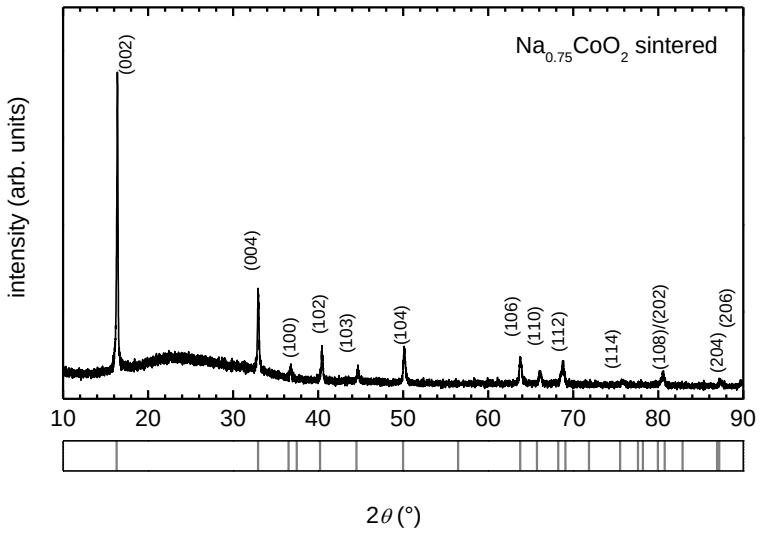

Fig. 4.2: XRD pattern of classical solid-state prepared target powder, $Na_{0.75}CoO_2$, after sintering at 880 °C in air. Reference ICDD data (PDF 04-012-5637) of $Na_{0.75}CoO_2$ is shown below.

This first attempt was successful in producing first single-phase powders and then targets of γ-$Na_{0.75}CoO_2$. All reflections can be attributed to γ-$Na_{0.75}CoO_2$. From peak positions, lattice constants can be calculated by using linear least-squares method in the hexagonal setting. For the $Na_{0.75}CoO_2$ target powder $c = 10.876$ Å and $a = 2.832$ Å. With Vergard's law[j] it is possible to determine the corresponding sodium content in the material, since a decrease of the c follows a linear dependency of increasing sodium content due to the accumulation of positive charges between the CoO2 planes in the unit cell.[8, 146] Such a linear dependence can generally be written as $c = c_0\text{-}kx$. Krockenberger *et al.* have determined $c_0 \approx 11.5328$ Å and $k \approx 0.99505$.[8] In this thesis this formula was used to determine the sodium content of Na_xCoO_2 in the target material as well as in the films. The particles of the classical solid-state fabricated target have a smooth and round shape, their size is determined to be between 7 and 20 μm. Particle size distribution is broad, probably due to the initial particle distribution before sintering of the target powder. Sintering necks of particles are depicted in Fig. 4.4 (a) and (b,) marked by red circles and arrows. As evident from Fig. 4.4 not all grains show sintering necks, a lot of pores between particles are visible, which is one reason for the obtained low target density. An explanation could be a relatively low sintering temperature of 880 °C, which was applied to keep sodium depletion as low as possible. The target material reached an intermediate sintering stage as explained in Fig. 3.1. A very interesting feature can be seen in Fig. 4.4 (b). Here different types of crystals have been formed in the grains. A zoom-out is given in Fig. 4.5.

[j] *Vegard*'s law is an approximate empiric rule, which says that an linear relation exists between the lattice constants of an alloy and the concentrations of the constituent elements at a constant temperature.[145] A. R. Denton and N. W. Ashcroft, Physical Review A **43**, 3161 (1991).

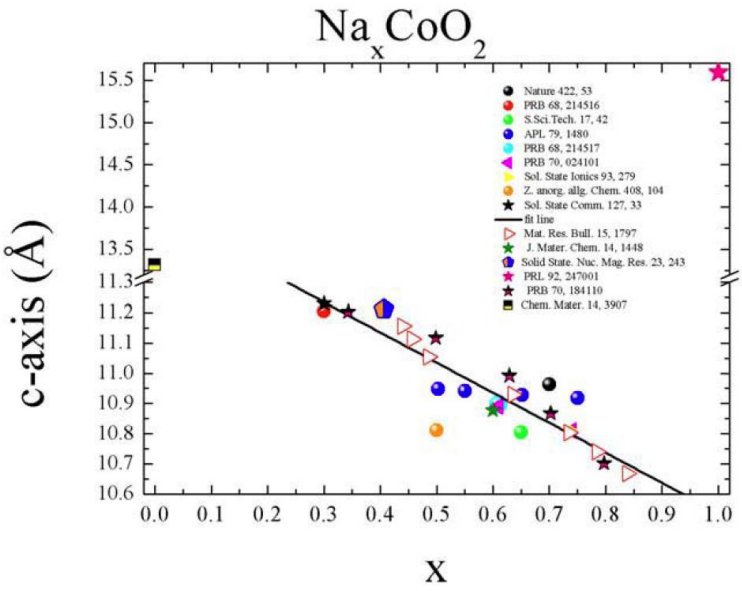

Fig. 4.3: *c*-axis length vs. sodium content. Data points have been taken from literature, where single crystals and powders were investigated by ICP and EDS analyses. Taken from Krockenberger *et al.*[8]

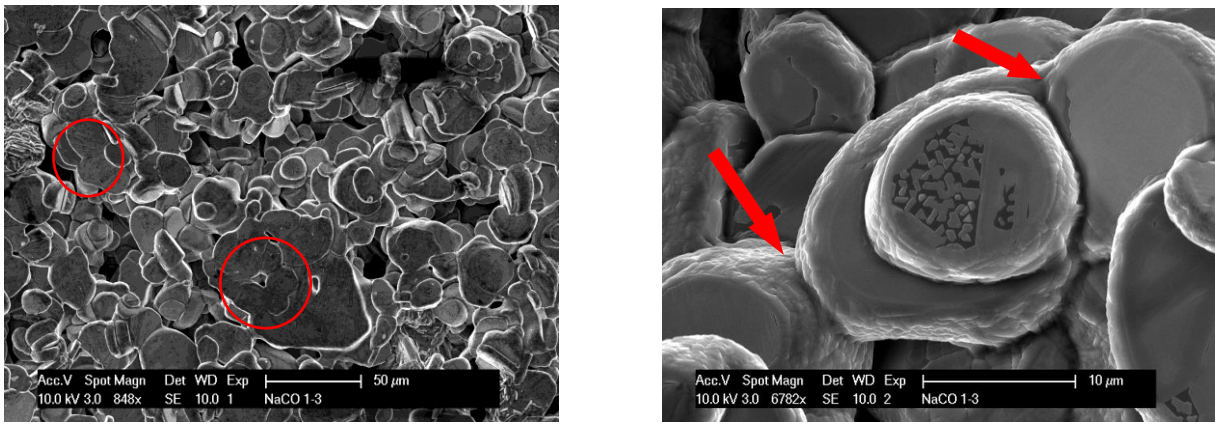

Fig. 4.4: (a) Particles of the γ-$Na_{0.75}CoO_2$ classical solid-state target surface. Particle size distribution is between 7 and 20 µm. (b) In the particle small crystals are formed about one micro and below. The red circles and arrows respectively mark some places, where the particles of the target have been connected due to sintering.

EDS measurements proved the absence of impurity phases containing other elements than Na, Co, and O within the detection limit. The EDS spectrum is shown in Fig. 4.6, all expected characteristic signals corresponding to K and L transitions of the elements Na (K_α = 1.041 keV), Co (K_α = 6.93 keV, K_β = 7.64 keV, L_α = 0.776 keV, L_l = 0.678 keV) and O (K_α = 0.525 keV) were identified. The K_α - signal of carbon at 0.277 keV is present due to residual surface carbon or carbon parts, on which the sample is attached.

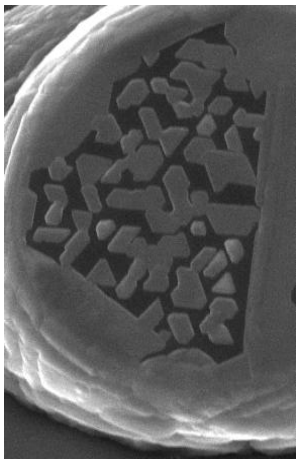

Fig. 4.5: Detailed view of a particle of γ-$Na_{0.75}CoO_2$ from Fig. 4.4 (b). Many crystals of different shape have grown in the particle; most of them show the hexagonal symmetry or the trigonal analogon.

The presence of hexagonal or trigonal crystals in the target particles is a hint for the presence of the hexagonal γ–phase. Although the γ–phase of sodium cobaltate crystallizes in hexagonal symmetry the morphology of the crystals may show a trigonal shape, since trigonal symmetry can be deduced from a dihexagonal dipyramid, which is the symmetry of the highest symmetric hexagonal point group 6/m2/m2/m.[147]

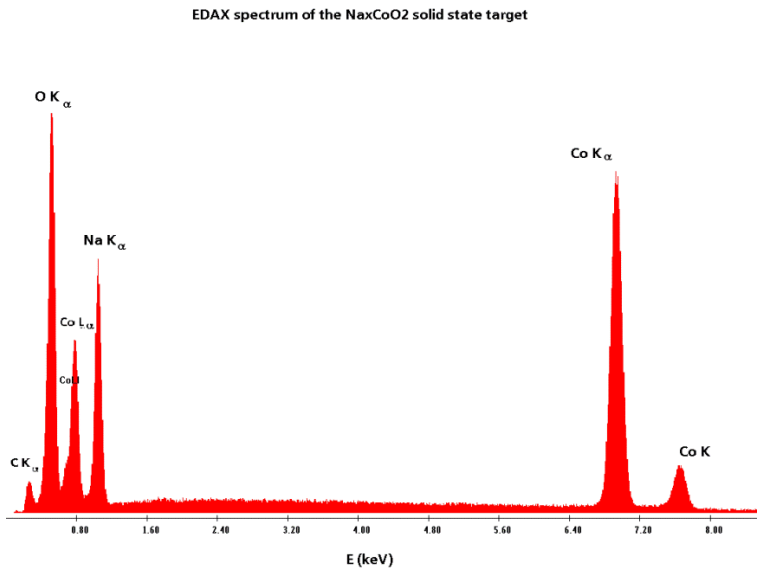

Fig. 4.6: EDS spectrum of the $Na_{0.75}CoO_2$ target fabricated using the classical solid-state synthesis route after sintering at 880 °C for 60 h.

Due to the volatility of Na, a target with a sodium content of $x = 0.75$ used for depositing thin films will lead to a mixture of Co_3O_4 and CoO as impurity phases in the film. Therefore, additional Na_2CO_3 was added to the target powder, which resulted in a Na to Co ratio of 3 to 1, as determined by EDS. After depositing several films from the same target, it usually becomes inhomogeneous. The distance from the substrate heater to the target is approximately 36 mm and, therefore the target is heated due to heat radiation from the substrate. The substrate itself is heated during ablation and annealing of up to a temperature up to 760 °C.

4.1.2 Na_xCoO_2 target via sol-gel preparation

For the sol-gel fabrication of Na_xCoO_2 targets first a thermal analyses of the precursor acetates was performed, the results of the TG and DSC analyses are shown in Fig. 4.7. In the TG curve, a two-step loss in mass took place. The first loss in mass of 10% between 100 °C and 200 °C can be explained by vaporization of residual water, and decomposition of organic acetic acid, and its subsequent combustion. The loss in mass in this temperature range corresponds to small endothermic and exothermic signals in the DSC curve. The second major loss in mass of 40% occurred between 200 °C and 270 °C with a corresponding exothermic signal at 252 °C in the DSC curve. Here, the ligands decompose and Na_xCoO_2 is gradually formed. Since the thermal analyses were performed in air, burning of organic components lead to an aggregate exothermic signal, which manifested in a strong minimum of the DSC curve.

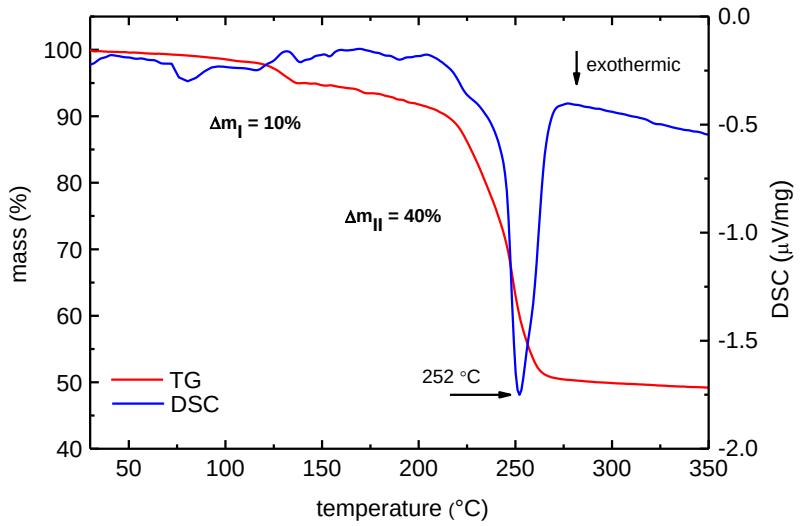

Fig. 4.7: TG and DSC of Na_xCoO_2 sol-gel precursor mixture. The maxima and minima in the DSC curve correspond to endothermic and exothermic reactions, respectively.

After the reaction to Na_xCoO_2 is completed after surpassing 270 °C, a continuous loss in mass of ~2.5% as a function of temperature between 270 °C and 600 °C is observed, which could be attributed to evaporation of volatile sodium. The loss of sodium is enhanced at higher temperatures. The XRD patterns of calcined and sintered Na_xCoO_2 powders are presented in Fig. 4.8. The comparison of the XRD pattern of calcined Na_xCoO_2 to ICDD reference data of (PDF 04-011-2274) suggests phase-pure $Na_{0.75}CoO_2$.[148] From the XRD peak positions lattice constants were calculated to be a = 2.831 Å and c = 10.929 Å for the calcined powder and a = 2.828 Å and c = 10.955 Å for the sintered powder. The obtained value for c corresponding to x = 0.75 is within the measurement uncertainty of the reported constants c_0 and k in the *Vergard's* law. The Na to Co ration of 1 to 1 in the initial acetate mixture has been reduced to 0.75 to 1 in the final product of the sol-gel synthesis. A separate sol-gel synthesis of Na_xCoO_2 with a reduced ratio of Na to Co = 0.75 to 1 under identical conditions yielded to powders of x = 0.59, as determined from XRD measurements (not shown). It seems to be that a significant sodium evaporation occurs below 500 °C, and the sodium evaporation rate increases with

initial sodium content in the precursor mixture. The oxidative evaporation of sodium follows Eq. 4.1.

Eq. 4.1
$$Na_xCoO_2 + \frac{y}{4}O_2 \rightarrow Na_{x-y}CoO_2 + \frac{y}{2}Na_2O$$

The necessary energy of several hundred millielectronvolt per mole of Na_2O in this endothermic reaction is provided by heating and increases with decreasing x.[52] This effect is also observed in electrochemical cells, in which Na_xCoO_2 has a higher oxidation potential at lower sodium contents.[149, 150]

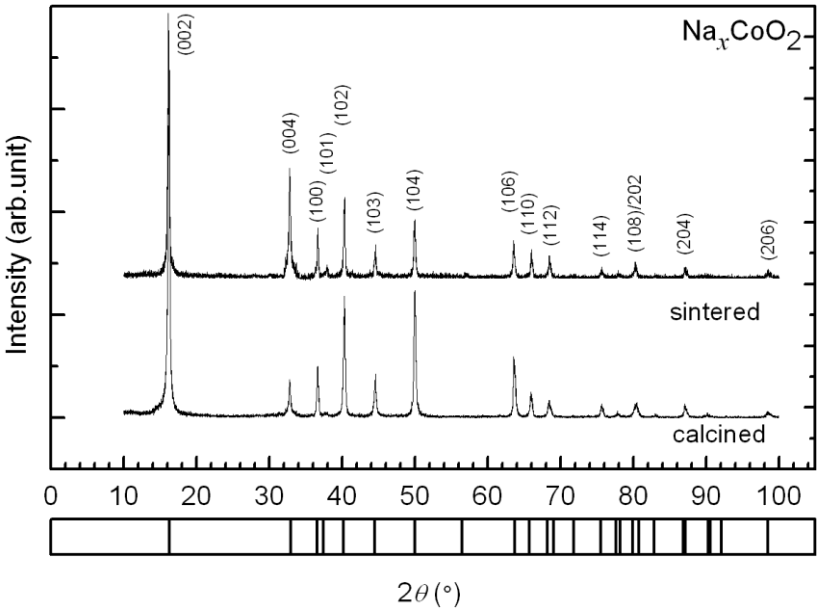

Fig. 4.8: XRD patterns of the sol-gel prepared Na_xCoO_2 powders after calcination and sintering in comparison with ICDD reference data (PDF 04-011-2274 for $x = 0.75$).[148] Sodium stoichiometry of $x \approx 0.75$ was calculated based on $c = 10.929$ Å for the calcined powder using *Vegard's* law.[8, 146] An increase of $c = 10.955$ Å of the sintered powders indicate a sodium reduction of ~ 2% compared with the calcined one.

The bulk density of the target sintered from sol-gel Na_xCoO_2 powder is determined to be 3.35 g/cm^3, which is 72% of the theoretical density of $Na_{0.75}CoO_2$(4.67g/cm^3).[148] Higher sintering temperatures above 960 °C, recently reported by Yamakawa *et al.,* resulted in a bulk density of 95%.[144] On the other hand as already mentioned, high sintering temperatures enhance, sodium evaporation which results in the admixture of Co_3O_4.[144] Additional loss of sodium at higher temperatures is verified by the elongation of *c*. The particle size of the calcined powder is determined to be between 0.2 and 1 μm, which is 5 to 10 times smaller than the particle size obtained for the classical solid-state synthesized Na_xCoO_2 powder. A SEM image of the calcined powder is shown in Fig. 4.9. Generally powders with smaller grain sizes are a candidates for producing solids with high bulk density.

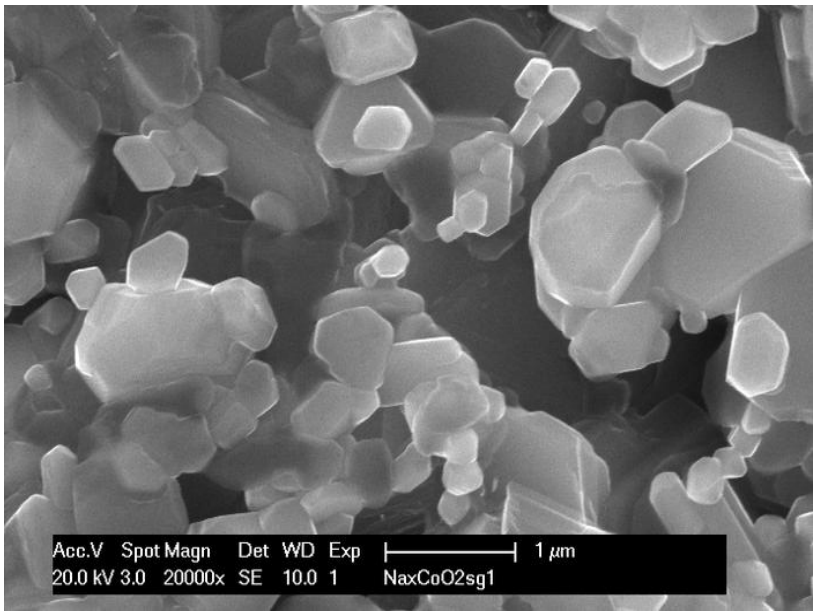

Fig. 4.9: SEM image of $Na_{0.75}CoO_2$ powder calcined at 500 °C showing grain sizes of 0.2 to 1 μm.

The temperature dependent magnetic susceptibility χ of the sol-gel prepared powder, which is proportional to *M/H,* is shown in Fig. 4.10. For temperatures above 50 K the susceptibility follows the Curie-Weiss law of $\chi = C/(T-\theta)$ with $C = 0.0273$ emu K/mol and a Weiss constant of $\theta = -165$ K. Since the transition between Curie-Weiss behavior and Pauli paramagnetism is reported to be at $x = 0.61$,[146] the observed behavior suggests a sodium stoichiometry of $x = 0.75$. The negative Weiss constant is a hint for antiferromagnetic spin interactions, which is verified by a broad feature at 37 K, the antiferromagnetic transition temperature. A similar behavior was previously observed for $Na_{0.8}CoO_2$ single crystals by Igarashi *et al.*[146] and Bayrakci *et al.*[151], which was attributed to short-range *Ising*-type[k], quasitwo-dimensional antiferromagnetic correlations.

[k] The *Ising* model describes especially the ferromagnetism of matter and is derived from the Heisenberg model by the reduction of the spin component down to 1 ($s_i^{\approx} = \pm 1$) and has the following form: $\hat{H} = -\frac{1}{2}\sum_{ij} J_{ij} s_i^{\approx} s_j^{\approx} - H_z \sum_{i=1}^{N} s_i^{\approx}$.

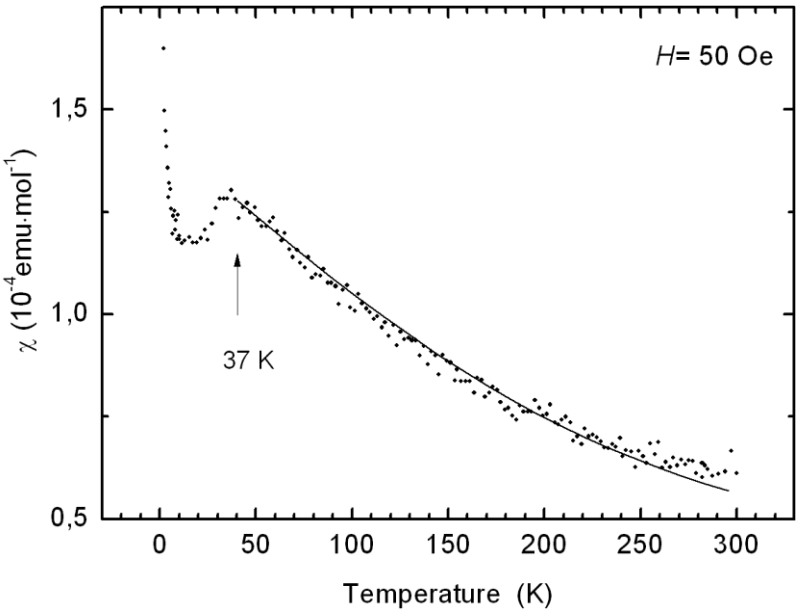

Fig. 4.10: Magnetic susceptibility as a function of temperature of the calcined $Na_{0.75}CoO_2$ powder measured at 50 Oe. The χ vs. T dependence shows Curie-Weiss behavior.

4.1.3 $LiCoO_2$ target via solid-state preparation

For the $LiCoO_2$ target fabrication a ready-to-use $LiCoO_2$ powder was supplied by *Sigma-Aldrich* (99.8%). To fabricate a target, only homogeneousing and subsequent sintering of the powder had to be done. Prior to this, the powder was tested regarding the evaporation behavior of Li during heating. As experienced with sodium, which showed huge volatility, it is necessary to know, how much of Li will be lost during sintering. For that reason powders of $LiCoO_2$ before and after a temperature treatment of 800 °C were investigated using X-ray diffraction of molybdenum radiation. The results are shown in Fig. 4.11.

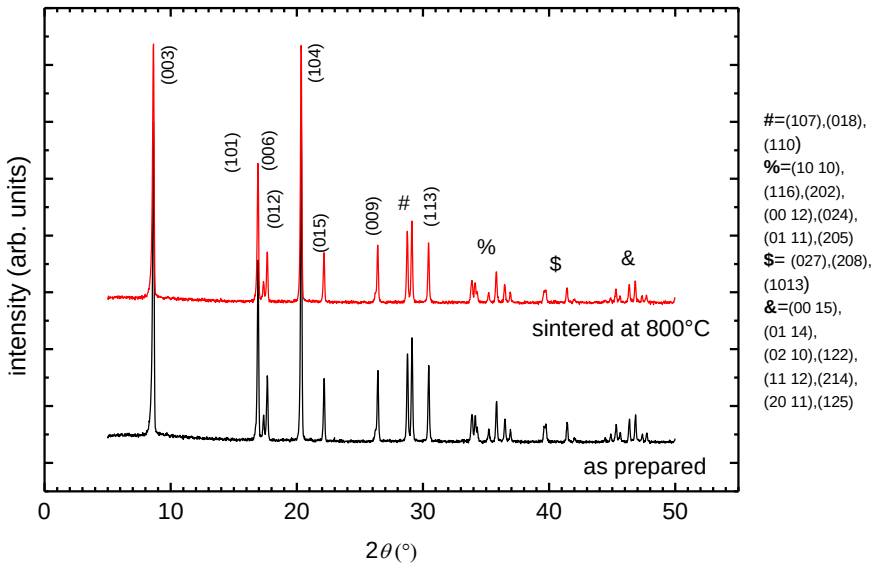

Fig. 4.11: X-ray diffraction pattern of the $LiCoO_2$ powder as prepared and sintered at 800 °C. The reflections are indexed using ICDD reference data PDF 01-076-3172[152] and PDF 00-044-0145.[153] For this measurement MoK_α (λ=0.7093 Å) was used.

The space group of $LiCoO_2$ is 166 ($R\bar{3}m$) and in both cases $LiCoO_2$ can be indexed in this space group. $LiCoO_2$ powder (as prepared) could be used as a reference referring to a lithium content of 1. Even a temperature treatment of 800 °C did not change peak positions, which means that the Li content remains constant. For better clarity, this is depicted in Fig. 4.12 showing a zoom-in of the reflections (003) and (104). In comparison to Na_xCoO_2 powders this is an interesting result, as sodium evaporates at such temperatures, although the sodium atom is larger than the lithium atom. One would expect that the tendency of evaporation is more prominent in the case of lithium, compared to sodium, which is obviously not the case. The atomic radius of lithium is 167 pm, whereas the atomic radius of sodium is 190 pm, which is slightly larger than that of lithium. At least from size considerations the lithium atom should be more volatile and, therefore, could deplete more easily. Taking physical and chemical properties of these two elements into account, this phenomenon could be explained. For that reason, selected properties of sodium and lithium are listed in Table 4.1

The temperature difference of 1 Pa vapor pressure is 243 K. This could be one explanation why the sodium depletes at a temperature of 800 °C, since 1 Pa is reached already at 554 °C. For Lithium 1 Pa vapor pressure is just reached at 797 °C, which is very close to the sintering temperature of 800 °C. Ionization energy of lithium is higher, so Na is more reactive.

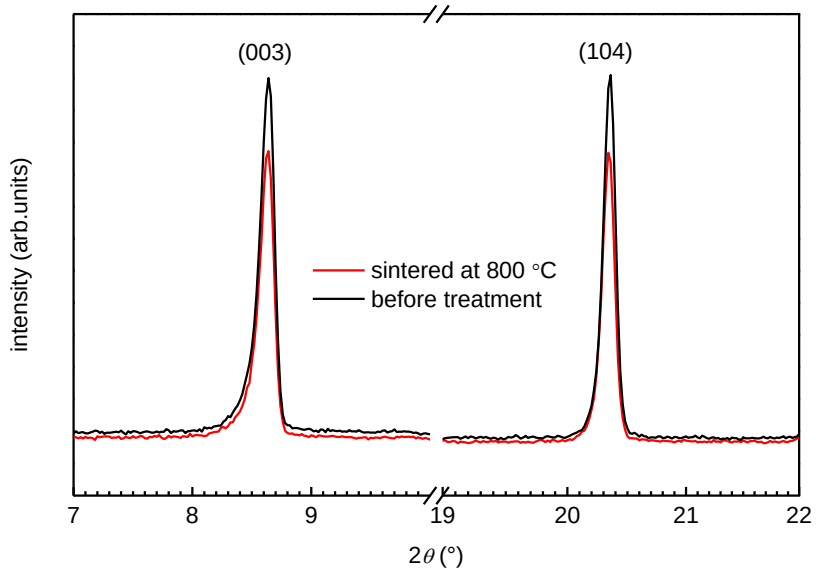

Fig. 4.12: Zoom-in of the (003) and (104) reflections of $LiCoO_2$ before (black curve) and after (red curve). Heat treatment at 800 °C Within the resolution of the diffractometer, there is no shift of peak positions observable.

Table 4.1: Comparison of physical and chemical properties of sodium and lithium

Element	Sodium	Lithium
Atomic radius (pm)	190[154]	167[154]
First Ionization energy (kJ/mol)	495.8[154]	520.2[154]
Vapor pressure of 1Pa (K)	554[155]	797[155]
Electron affinity (eV)	2.75[156]	2.9[156]
Melting point (°C)	97.72[157]	180.54[154]

This result is in good agreement with former measurements by Miyazaki *et al.* showing that temperatures above 1000 °C are needed to remove Li from $LiCoO_2$ by forming Li_2O.[149] The remaining powder would then consist of $Li_{1-x}Co_{1-y}O_2$ and $y \cdot Co_3O_4$. X-ray diffraction studies were performed by Antolini *et al.* to investigate the stability of $LiCoO_2$ and to check for impurity phases. The patterns were obtained after isothermal treatment of the powders (between 850 °C and 1100 °C).[158] Above 900 °C the Co_3O_4 starts to form. In both $LiCoO_2$ powders, before and after sintering, the splitting of the (006)/(012) and the (018)/(110) reflections is clearly observed and indicates a good layered structure in the unit cell with no cation mixing at lithium and cobalt metal sites.[159] The cation mixing in the lattice can be evaluated by integrating the intensity ratio of $I(003)$ to $I(104)$. A value of $I(003)/I(104) > 1.2$ is known for low cation mixing.[74, 160] In the case of the as prepared powder, the ratio is 2.5 and after temperature treatment the ratio is 2. This is a very good result and draws upon the very low cation mixing in both powders. This is supported by the missing super lattice reflection at $2\theta \approx 14.5°$, which is a weak and broad reflection ascribed to a short-range super lattice order of lithium and cobalt (α-$NaFeO_2$ type). This is observed when cation mixing occurs.[159] Since no loss of lithium occurred during sintering, the powder was directly used to fabricate a target for thin film deposition.

4.1.4 $Li(Ni_{1/3}Mn_{1/3}Co_{1/3})O_2$ and $Li(Ni_{1/2}Co_{1/2})O_2$ sol-gel powder fabrication

Since in this study a new attempt to fabricate LNMCO and LNCO targets by sol-gel synthesis was developed, several considerations had to be made concerning thermal properties of the starting materials. A thermal analysis of the pristine powders and their mixtures was performed. The results of the TG and DSC measurements of each powder are shown in Fig. 4.13 to Fig. 4.16.

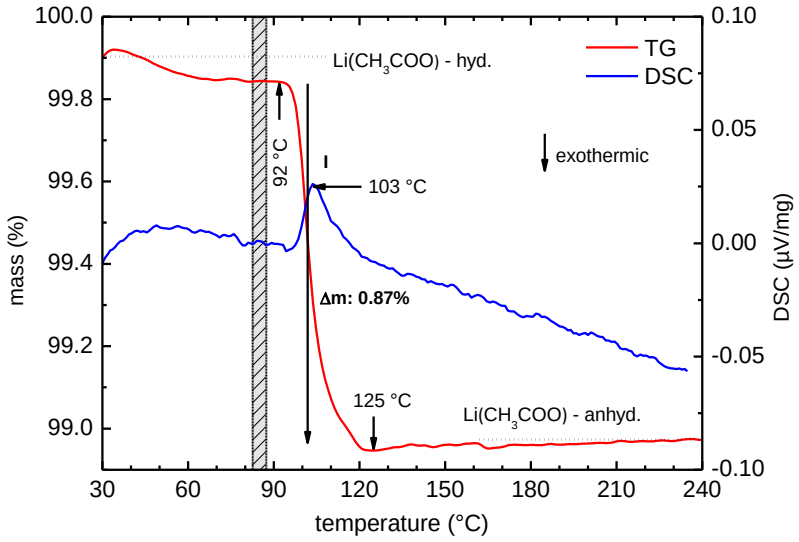

Fig. 4.13: TG and DSC curves of lithium acetate powder (mass= 95.57 mg) obtained at a heating rate of 1.7 °C/min in synthetic air (mixture of 20% O_2 and 80% N_2). The grey shaded area marks the temperature range at which the powder was dried in the furnace.

For lithium acetate a major loss in mass of ~0.87% occurred in a temperature range between 92 and 125 °C. The corresponding signal in the DSC curve is endothermic and has its maximum at a temperature of 103 °C (see step I in Fig. 4.13). The loss in mass can be attributed to the desorption of adsorbed water. One would expect that the desorption of water would start already at lower temperatures, since during powder drying in the furnace at 85 °C a loss in mass of 1.4% was observed. Since the degradation of anhydrous lithium starts above 300 °C, no additional signal was detected in the TG and DSC curve.[161]

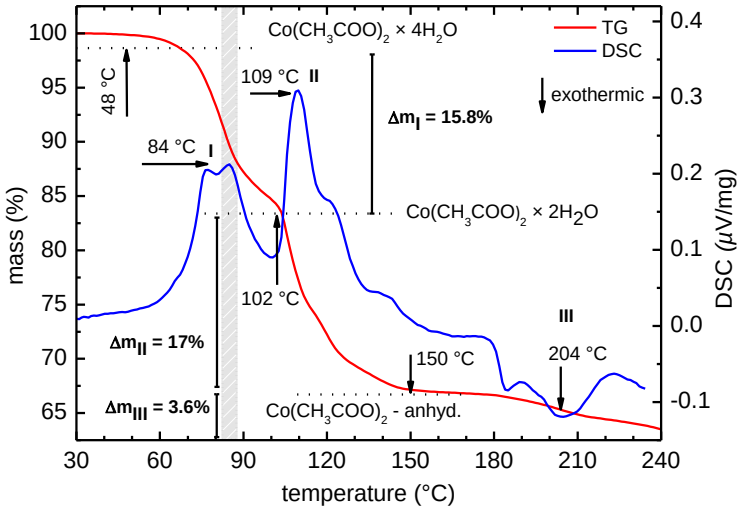

Fig. 4.14: TG and DSC curves of cobalt acetate tetra hydrate powder (mass = 95.57 mg) obtained at a heating rate of 2 °C/min in synthetic air. The grey shaded area marks the temperature range at which the powder was dried in the furnace.

The TG and DSC curve of cobalt acetate tetra hydrate can be divided into three parts, I, II, and III. Within the first region between 48 and 102 °C, the material loses around ~15.8%

of its mass. This loss in mass corresponds to an endothermic doublet in the DSC. Subsequent to this region, a second loss in mass of ~17% occurs between 102 and 150 °C with one corresponding endothermic signal in the DSC curve at 109 °C. These two losses in mass can be explained by a two-step loss of tetra hydrate with two water molecules each. This behavior is consisting with findings of Mu *et al.*; they found the first dehydration step to be in a temperature range between 58 and 104 °C, and the second dehydration step to be between 115 °C and 260 °C.[109] Whereas the first temperature range is in good agreement with the results of Mu *et al.* the second temperature range differs a lot to the temperature range obtained in this study. An explanation for this can be found in the different definitions of starting and end point of dehydration, which Mu *et al.* give in their study but do not explain it further.[109] In their study no DTA or DSC curves are given. The loss of two water molecules should result in theoretical loss in mass of ~14.5%, which is less than obtained for the TG analysis. This additional mass can be explained by adsorbed water molecules, which desorb under these conditions, since the cobalt acetate tetra hydrate is hygroscopic.[107] Finally, in region III a third loss in mass between 150 and 240 °C of ~3.4% takes place, connected to an exothermic DSC signal with its maximum at 204 °C. This is equivalent with event III from measurements of Mohamed *et al.* (see Fig. 3.4), and can be explained by the formation of an intermediate phase.[110] From mass spectrometry measurements the intermediate phase was found to contain an acetyl group (CH_3-CO) and therefore can be identified to be acetyl cobalt acetate. For the pristine powder mixture, the formation of such an intermediate compound is negligible, as powder drying takes place only at 85 °C. For mass calculations it has to be taken into account that at the temperature of 85 °C only two water molecules desorbed. Nevertheless, the loss in mass after TG and DSC analysis is 32.8% and after drying in the furnace 32.5%, which is almost identical. It can be assumed that anhydrous cobalt acetate is formed after pretreatment of the cobalt acetate tetra hydrate in the furnace at 85 °C. An isothermal heat treatment over a long time in the temperature range of dehydration (30 to 140 °C, see chapter 3.1.2) leads to water-free compounds similar to short heat treatments at higher temperatures, or continues heating up to 200 °C.

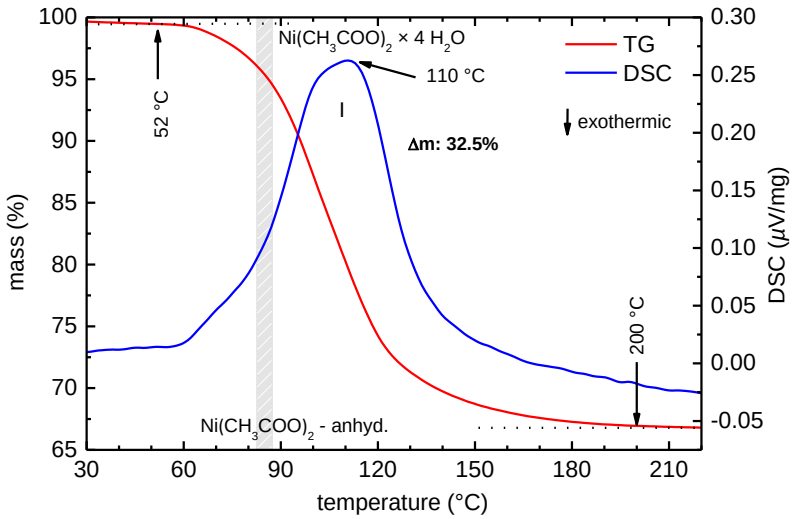

Fig. 4.15: TG and DSC curve of nickel acetate tetra hydrate powder (mass = 95.57 mg) obtained at a heating rate of 2 °C/min in synthetic air. The grey shaded area marks the temperature range, at which the powder was dried in the furnace.

The thermal analysis of nickel acetate tetra hydrate is shown in Fig. 4.15. A significant loss in mass in a temperature range between 52 and 200 °C of 32.5% corresponds to an endothermic signal at 110 °C in the DSC curve. This result is in good agreement with findings in literature, where a single-stage dehydration of nickel acetate tetra hydrate is described in a temperature range between 80 and 170 °C.[116] The difference in the temperature ranges can be explained by different heating rates used for both experiments. In this study, the heating rate was 2 °C/min, whereas the heating rate used by Mohamed *et al.* was 10 °C/min and by De Jesus *et al.* was 30 °C/min.[117] After a pretreatment at 85 °C in the furnace, the loss in mass of the nickel acetate tetra hydrate is 35%. The theoretic loss of four water molecules would result in a mass loss of ~29%, which is 6% less than the measured loss of mass after drying, and 3.5% lesser compared to the thermal analysis. A reason for the additional loss in mass is adsorbed water, as nickel acetate tetra hydrate is hygroscopic. As in the case of cobalt acetate tetra hydrate, after drying the powders for 48 h at an isothermal temperature of 85 °C, the powders are afterwards anhydrous.

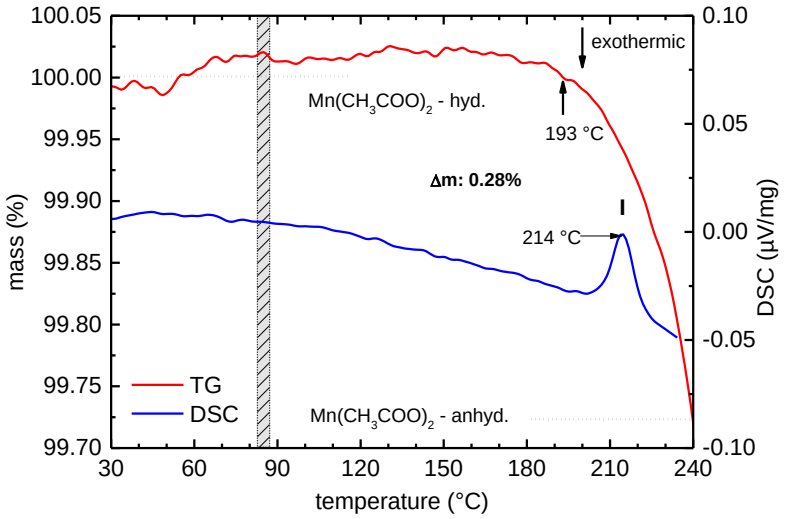

Fig. 4.16: TG and DSC curve of manganese acetate powder (mass = 95.57 mg) obtained at a heating rate of 1.9 °C/min in synthetic air. The grey shaded area marks the temperature range, at which the powder was dried in the furnace.

The results of the thermal analyses of manganese acetate are shown in Fig. 4.16. Similar to lithium acetate and nickel acetate tetra hydrate, only one significant endothermic signal is observered in the DSC curve at 214 °C. The endothermic reaction is denoted to a loss in mass of 0.28% in a temperature range between 193 and 240 °C. This loss in mass is very small and can be attributed to a loss of adsorbed water. It is worth to mention that the measured mass exceeds 100% in a temperature range between 60 and 190 °C. This is due to a measurement error in the measurement setup used for the TG measurement. Following the thermal analyses of single acetate educts, a mixture of acetates for LCMNO was exemplarily analyzed next. The results are shown in Fig. 4.17.

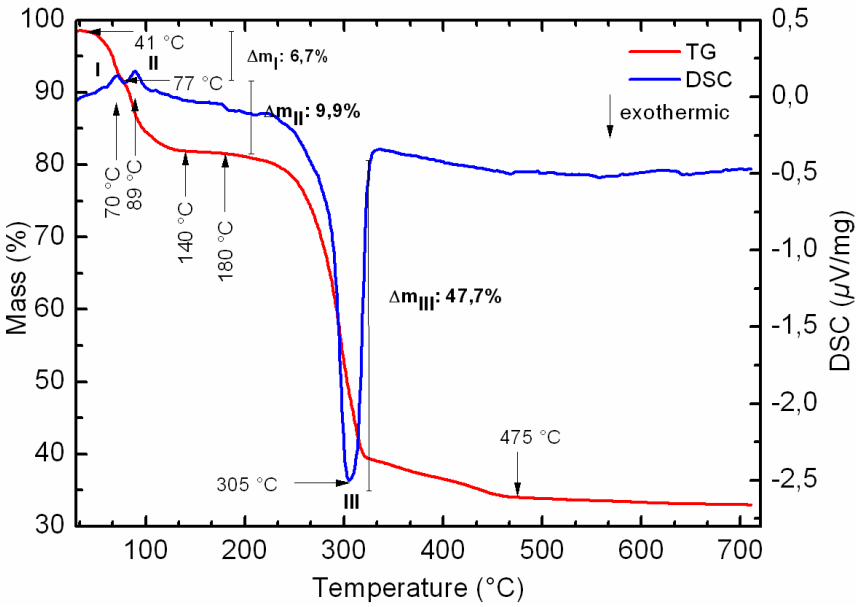

Fig. 4.17: TG and DSC curves of a mixture of acetate powders (mass = 27.76 mg) obtained at a heating rate of 1.9 °C/min in synthetic air.

The curves can be splitted in three regions, I, II, and III. The first region between 41 and 77 °C denotes to a loss in mass of 6.7% and an endothermic signal in the DSC curve at 70 °C. In region II between 77 and 140 °C, a second loss in mass of 9.9% and an endothermic signal in the DSC curve at 89 °C is identified. Both losses in mass add up to 16.6%, corresponding to a two-step dehydration of the tetra hydrated acetates and desorption of adsorbed water. In the third region between 180 and 475 °C, the loss in mass is 47.7% and refers to a strong exothermic signal in the DSC curve at 305 °C. Here, the thermal decomposition of the acetates starts with its combustion. The exothermic signal can be attributed to an intermediate oxidation process of metals to metal oxides, similar to the case cobalt acetate, in which an exothermic DSC signal at 300 °C corresponds to an oxidation of cobalt to cobalt oxide.[110] The desired phase LNMCO is formed below 600 °C, which is comparable to the lowest synthesis temperature found for the hydroxide co-precipitation route and 200 to 300 °C lower compared to other synthesis methods.[162] No loss in mass occurs above 600 °C, which is in agreement with previously discussed measurements of $LiCoO_2$ (chapter 4.1.3).[149]

After mixing the pristine powders in stoichiometric ratio 1 to 1/3 to 1/3 to 1/3, later calcination as well as sintering the resulting compound was analyzed with X-ray diffraction. The results for LNMCO are given in Fig. 4.18.

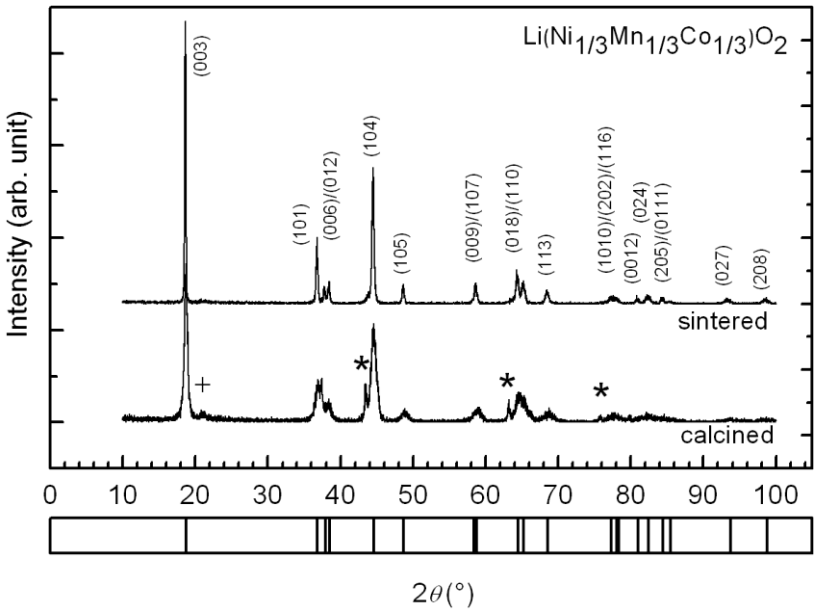

Fig. 4.18: X-ray diffraction patterns of LNMCO powder after the first calcination step and for the sintered ceramic in comparison with reference ICDD data PDF 04-013-4379.[163] NiO peaks (impurities) are denoted by (*) in the calcined pattern. A broad reflection at 21° denoted by (+) can be ascribed to a short-range super lattice order of Li and the transition metals.[164]

The LNMCO powder crystallizes in a trigonal structure (SG 166 $R\bar{3}m$). After calcination at 600 °C NiO peaks (impurities) occur in the diffraction pattern. At the beginning of the chemical reaction, one part of the supplied nickel forms LMNCO, the other part is oxidized to NiO. The increased reactivity of manganese compared to nickel results in different chemical reaction kinetics of these two cations and is the reason for the NiO formation.[165] No NiO reflections occur after sintering at 900 °C, a pure LMNCO phase is formed. For the calcined and sintered LNMCO powders a relative cation ratio of Ni:Mn:Co = 1:1:1 ± 0.03 was obtained by EDS analysis. The lattice constants are a = 2.857 Å, and c = 14.197 Å, and a = 2.862 Å, and c = 14.252 Å for the calcined and sintered powders, respectively. The lattice constants of the sintered powder correspond well to reference data for stoichiometric $LiNi_{1/3}Mn_{1/3}Co_{1/3}O_2$, [159, 163] [159, 163] thus the nominal cation stoichiometry is preserved and no Li loss occurs during sintering.[164, 168] The slightly smaller lattice constants of the calcined powder compared to the lattice constants of the sintered powder can be explained of cation mixing. The broad reflection at 2θ= 21° of the calcined powder can be ascribed to a short-range super lattice order of Li and the transition metals, like described in chapter 3.1.1. The cation mixing in the powder can be evaluated from the integrated intensity ratio of the (003) and (104) reflections. For the calcined powder this ratio is 1.11 and increases for the sintered powder to 1.2, which indicates a negligible cation mixing in the sintered powder.[160] A bulk density of 2.81 g/cm^3 was obtained for the cylindrical LNMCO target. This value corresponds to 58% of the theoretical density, which is comparable to values of below 70% reported for lithium cobaltates synthesized by other methods.[159, 166-168] Sintering of the powder at a higher temperature of 1050 °C for 12 h leads to a higher bulk density of 3.5 g/cm^3, which is 73% of the theoretical density and the highest value so far reported in literature for $LiNi_{1/3}Mn_{1/3}Co_{1/3}O_2$. However, a higher sintering temperature may result in the decomposition of the compound, as suggested by impurity reflections occurring in the XRD pattern of the LNMCO powder. The HSEM picture of the calcined powder is shown in Fig. 4.19. Smooth grains of 0.2 to 1µm size with sharp edges are observed. This is comparable with grain sizes of LNMCO powder produced by direct metal

acetate decomposition.[162] Small and smooth grains are very important to obtain good electrochemical discharge rate capability, which is required for high-power batteries.[169]

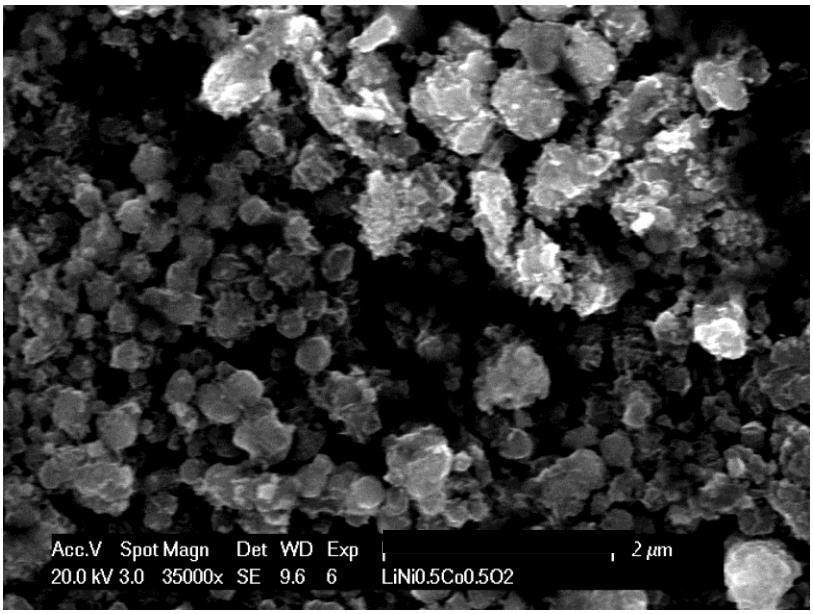

Fig. 4.19: SEM image of the sol-gel synthesized $LiNi_{1/3}Mn_{1/3}Co_{1/3}O_2$ powder calcined at 600 °C with grain sizes of 0.2 to 1 µm.

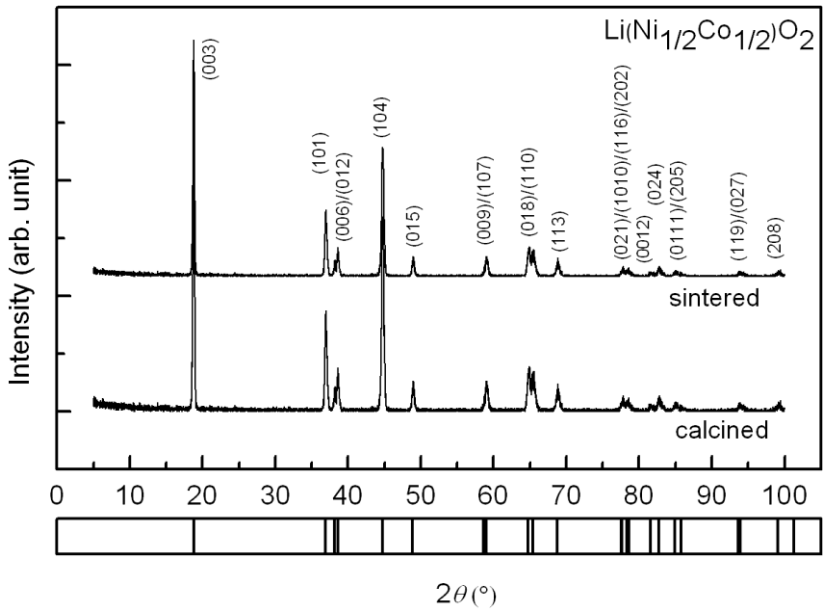

Fig. 4.20: X-ray diffraction patterns of LNCO powder after the first calcination step and for the sintered ceramic in comparison with reference ICDD data (PDF 04-013-4382).[163]

For the LNCO compound the XRD patterns after powder calcination and sintering are given in Fig. 4.20. The powder crystallizes in the trigonal structure (SG 166 $R\bar{3}m$), similar to LNMCO, and both patterns show no impurity phases other than $LiNi_{1/2}Co_{1/2}O_2$. The calculated lattice constants of the calcined and the sintered compounds are $a = 2.849$ Å and $c = 14.151$ Å, which matches very well with values reported in literature.[163, 170] As the relative ratio of Ni:Co = 1:1 (±0.03) was independently confirmed by EDS analyses, it can be concluded that no Li loss occurs in the synthesis process up to a temperature of 900 °C. The $I_{(003)}/I_{(104)}$ ratio for this compound equals 1.17, which is approaching the threshold value of 1.2 and was

calculated for the calcined and sintered powders. Since no super lattice peak at $2\theta = 21°$ is observed and a splitting of the (006)/(102) reflections and (108)/(110) reflections is evident, a LNCO powder with layered structure and small cation mixing can be synthesized at low temperatures of 600 °C. The bulk density of the LNCO target was calculated to be 3.51 g/cm^3, which is 72% of the theoretical density of LNCO. This is comparable with bulk densities reported for LNCO in literature.[160, 162, 166, 167] A SEM image of the LNCO powder after calcination is shown in Fig. 4.21. Compared to LNMCO, the grains are smoother, of similar size and are comparable to those produced by other synthesis routes.[162]

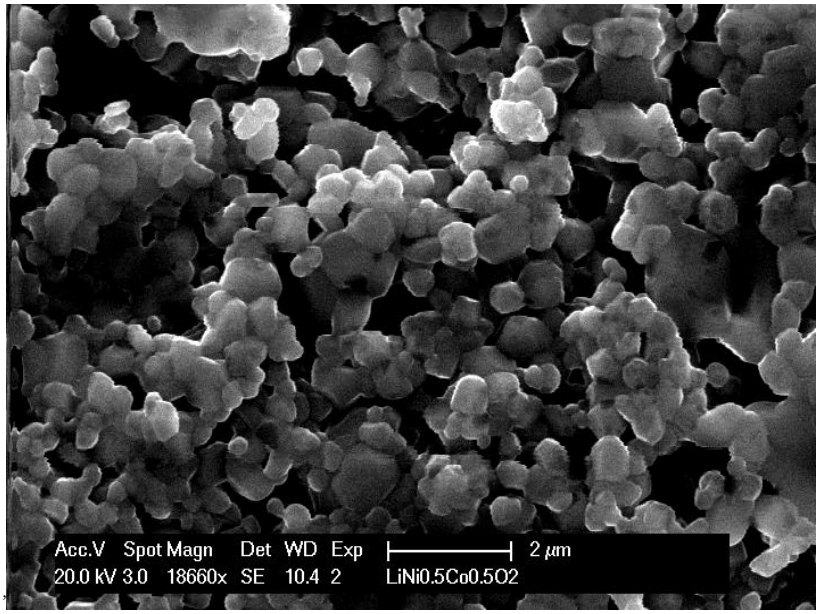

Fig. 4.21: SEM image of the sol-gel fabricated $LiNi_{1/2}Co_{1/2}O_2$ powder calcined at 600 °C yielding to grain sizes of 0.2 - 1 μm.

4.2 Thin film preparation

In this chapter the results of thin film preparation and characterization of Na_xCoO_2, $LiCoO_2$, $LiNi_{1/3}Mn_{1/3}Co_{1/3}$ and $LiNi_{1/2}Co_{1/2}O_2$ are presented and discussed. Further results of the deintercalation and intercalation experiments of Na_xCoO_2 films are presented in a separate chapter.

4.2.1 Na_xCoO_2 thin films

4.2.1.1 Optimization of growth parameters

The growth of thin films requires a very precise control and thus optimization of the growth parameters substrate temperature, T_s, laser energy density, E, and gas pressure, p. In the following, some results of the optimization process will be presented. All films were deposited with 3600 laser pulses at 5 Hz and a target-substrate distance of 38 mm. First, T_s was varied from 530 to 600 °C to find the optimum growth temperature. For that reason no annealing step after deposition was applied. The 2θ–θ scans of the (003) reflection of the films are given in Fig. 4.22. There is almost no difference of intensity as a function of substrate

temperature, a slightly higher intensity is observed for films grown at 550 °C (Fig. 4.22 (b)). As the (003) peak intensity was highest for 550 °C, this temperature was chosen for further film growth. The second optimization parameter was energy density on the target, which has been varied from 1.0 to 1.4 J/cm^2. For comparison, again the (003) reflection intensity was used.

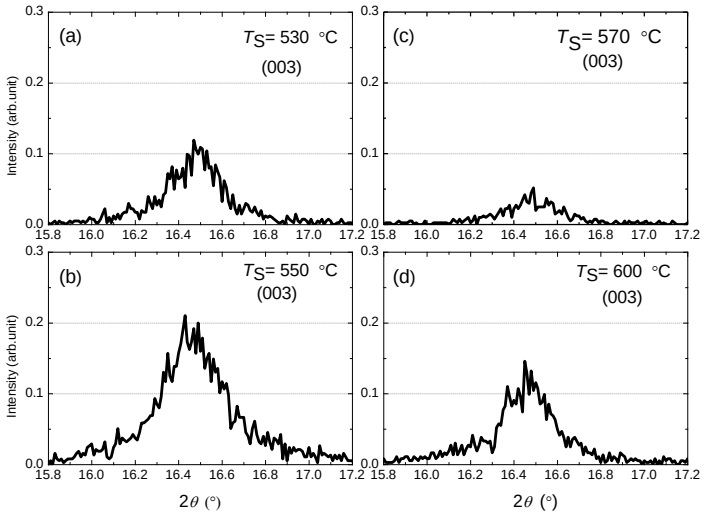

Fig. 4.22: Comparison of the (003) reflection intensity for different growth temperatures (a) 530 °C, (b) 550 °C, (c) 570 °C, and (d) 600 °C. the oxygen partial pressure was kept at 0.25 mbar and the laser fluence was 1.2 J/cm^2.

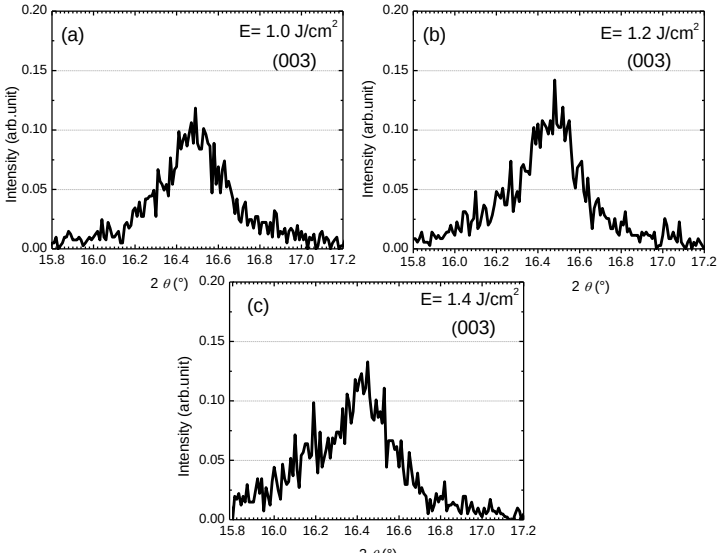

Fig. 4.23: Comparison of the (003) reflection intensity for different laser energies (a) 1.0 J/cm^2, (b) 1.2 J/cm^2, and (c) 1.4 J/cm^2. The temperature was kept at 550 °C and the oxygen partial pressure was 0.25 mbar.

Similar to the case substrate temperature, the intensity of the (003) reflection is almost independent from laser energy density, so 1.2 J/cm^2 was chosen for further experiments. In contrast to substrate temperature and laser energy density, oxygen pressure during deposition has a tremendous effect on the film growth with respect to peak intensities and peak positions of film reflections, and, thus greatly influences the sodium content in the films. The oxygen

pressure was varied from $1.0 \cdot 10^{-1}$ mbar to $3.5 \cdot 10^{-1}$ mbar. In Fig. 4.23 the (003) reflection of the thin films as a function of oxygen pressure is shown. The peak intensity varies with pressure, highest intensity is observed for a background oxygen pressure of 0.1 mbar, lowest for 0.35 mbar. The difference in peak intensity is around one order of magnitude. The intensity of the (003) reflection grown under an oxygen pressure of 0.2 mbar and 0.25 mbar is almost constant. The (003) reflection shifts from 16.18° for 0.1 mbar to 16.07 ° for 0.35 mbar, which denotes to a change of sodium content of $\Delta x \approx 0.075$. For better visibility, the four reflections of Fig. 4.24 are plotted in one graph (see Fig. 4.25). A clear peak shift towards smaller 2θ values with increasing oxygen pressure can be observed. Smaller 2θ represent increasing c, which in turn correlates to decreasing sodium content in the films. The formation of Na_2O is favored due to a higher oxygen pressure, so sodium easily reacts with oxygen atoms on its way from target to substrate and is therefore, not available for incorporation into the film. in In this study films were grown with an oxygen pressure of 0.25 mbar due to better surface smoothness. The results of AFM characterization of the thin films are shown in Fig. 4.26 - Fig. 4.29.

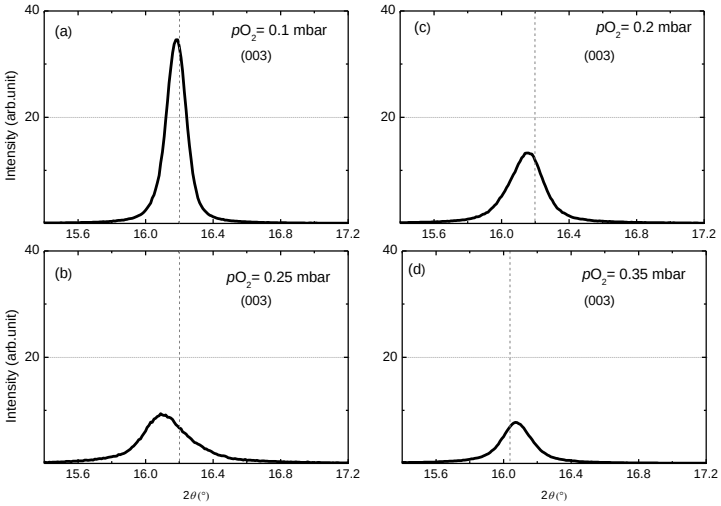

Fig. 4.24: Comparison of (003) reflections of Na_xCoO_2 films grown under different oxygen pressures. (a) 0.1 mbar, (b) 0.2 mbar, (c) 0.25 mbar, and (d) 0.35 mbar. The dashed grey lines at $2\theta = 16.2$ ° denotes to c equals 10.948 Å and thus a sodium content of $x = 0.59$.

The film with the lowest root mean square (RMS) roughness of 11 nm in an area of 3 x 3 µm is the film grown under 0.25 mbar oxygen pressure (Fig. 4.26). The 2*D* and 3*D* image of the surface shows flat hexagonal crystals, laying on top of each other, covering the steps of the substrate surface. In contrast to that, the film with the highest intensity of the (003) reflection has a rough conformable surface with a RMS roughness of 21 nm in an area of 3 x 3 µm. A hexagonal crystal with a diameter of approximately 2.2 μm and a height of ~120 nm is identifiable. This crystal could be an explanation for the high intensity of the (003) reflection shown in Fig. 4.24. The film grown under an oxygen pressure of 0.2 mbar (Fig. 4.28) has a heavily jointed surface with a RMS roughness of 44 nm in an area of 3 x 3 µm. Some areas of the substrate are not covered by the film at all. In the 2*D* scan hexagonal and trigonal crystal shapes can be identified. The film grown under the highest oxygen pressure of 0.35 mbar exhibits the highest RMS roughness (52 nm) of all investigated films. On the surface many

small, trigonally shaped crystals (diameter ≤ 1μm) are observable. Judging from the results of X-ray diffraction and AFM characterization, the oxygen pressure was set to 0.25 mbar to receive films with high surface smoothness. For water intercalation and deintercalation rougher films are preferable, since the diffusion paths of Na and H_2O are in *ab*-planes of the unit cells. On the other hand, films have to be dense and smooth for e.g., the fabrication of tunneling junctions or for electrical characterization.

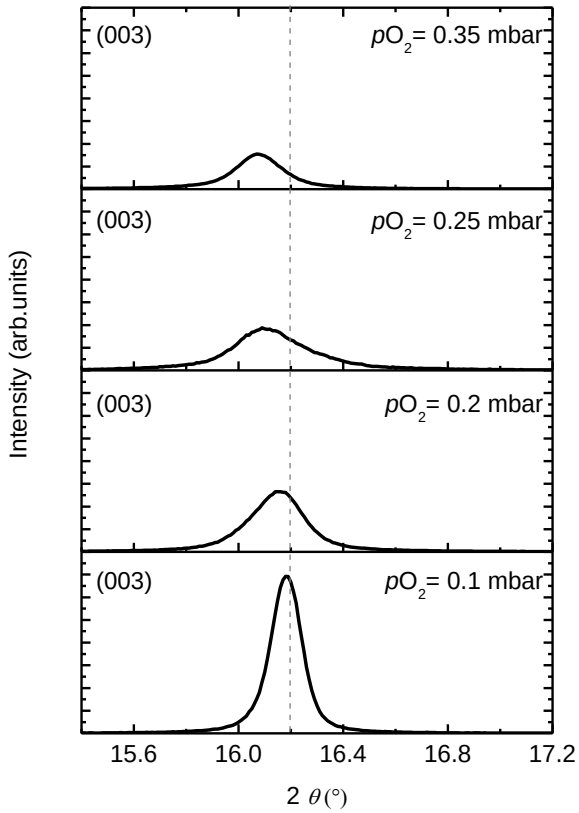

Fig. 4.25: Comparison of (003) peak positions as a function of oxygen pressure during deposition. The peak is shifted towards smaller diffraction angles with increasing oxygen pressure. The deposition temperature was kept at 550 °C and the laser fluence was 1.2 J/cm^2.

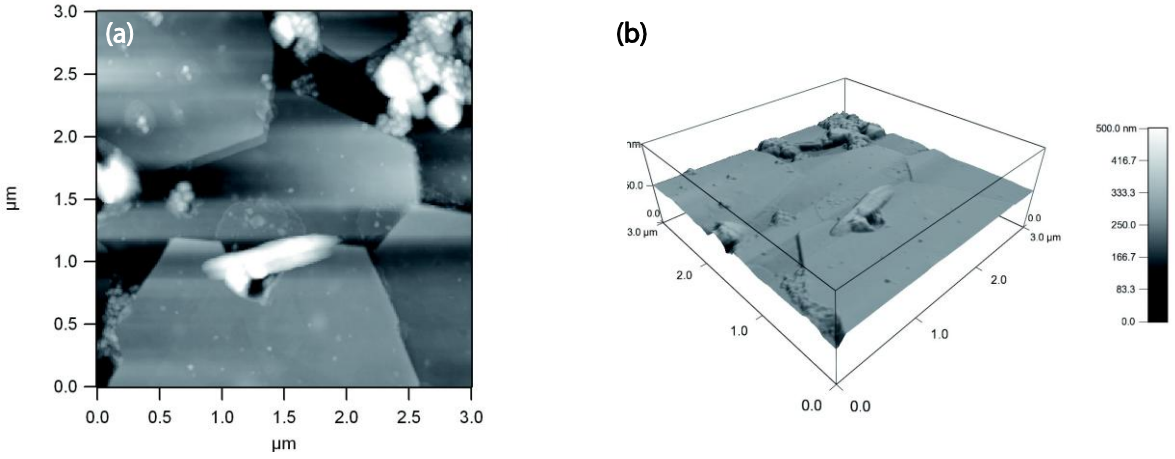

Fig. 4.26: AFM images of the Na_xCoO_2 film grown under 0.25 mbar oxygen pressure, (a) 2*D* – image, (b) 3*D* - image. The RMS roughness is 11 nm. Crystals with hexagonal symmetry are identifiable on the film surface.

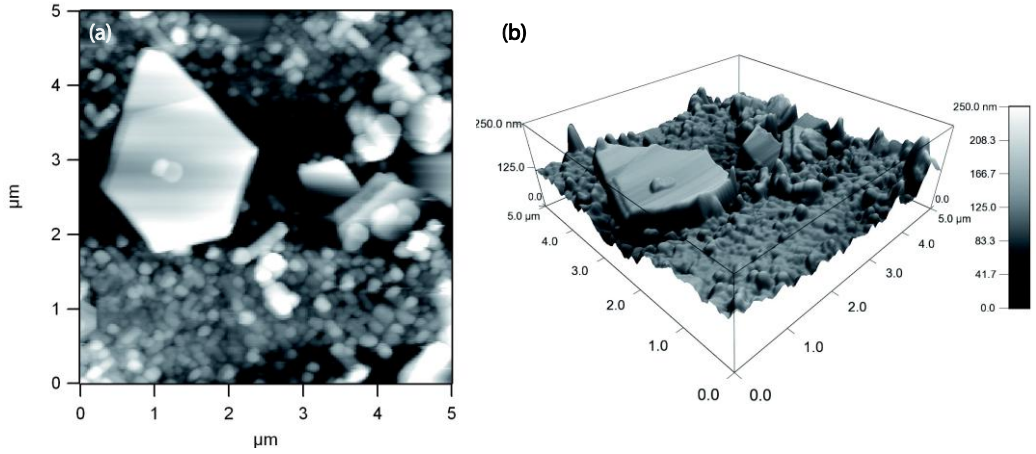

Fig. 4.27: AFM images of the Na_xCoO_2 film grown under 0.1 mbar oxygen pressure, (a) 2*D* – image, (b) 3*D* - image. The RMS roughness is 21 nm.

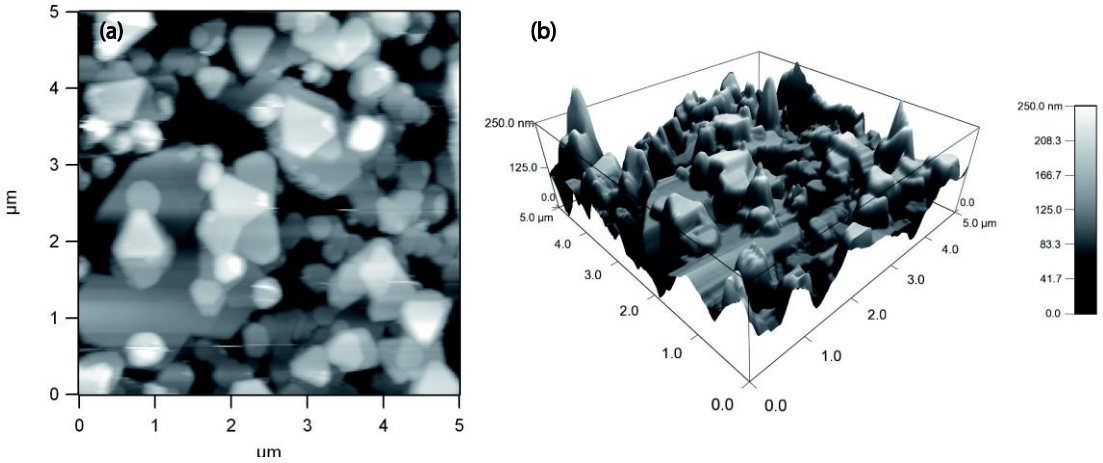

Fig. 4.28: AFM images of the Na_xCoO_2 film grown under 0.2 mbar oxygen pressure, (a) 2*D* – image, (b) 3*D* - image. The RMS roughness is 44 nm.

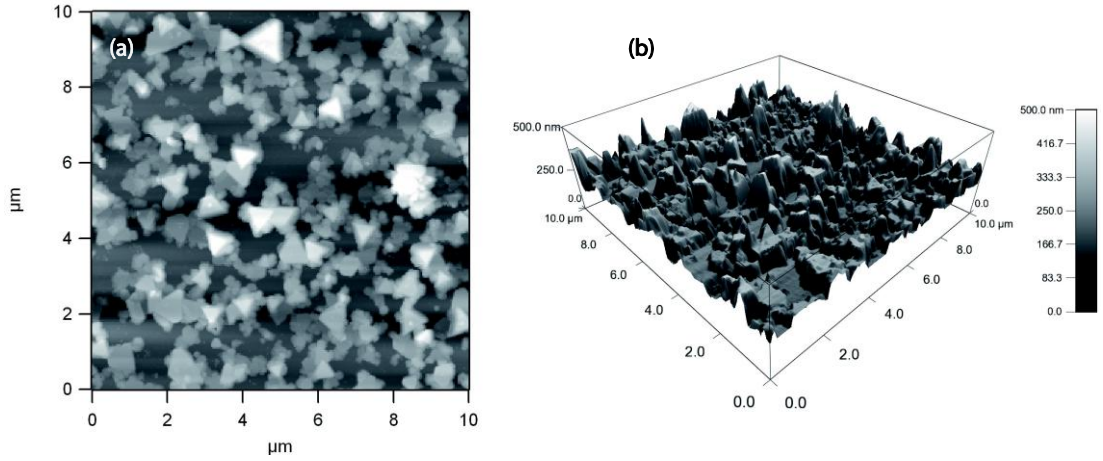

Fig. 4.29: AFM images of the Na_xCoO_2 film grown under 0.35 mbar oxygen pressure, (a) 2*D* – image, (b) 3*D* - image. The RMS roughness is 52 nm.

4.2.1.2 Epitaxial growth of Na_xCoO_2 films and control of sodium content

The growth of high-quality, epitaxial Na_xCoO_2 films by PLD has been reported on various single crystalline substrates, such as STO, MgO, $LaAlO_3$ etc. Son *et al.* reported kinetically controlled Na_xCoO_2 growth of the β-phase (x = 0.6) in island growth mode and of the γ-phase (x = 0.7) in layer-by-layer growth mode, as a function of the deposition rate.[51] Furthermore it was shown that the growth dynamics of the γ–phase are strongly affected by stress due to lattice mismatch between substrate and film resulting in different thermoelectric properties.[56] A precise control of the sodium content in the films is difficult, due to the high sodium vapor pressure of $\sim 10^4$ Pa at typically used growth temperatures of around 700 °C. Usually films deposited by PLD have a sodium content of x = 0.7. Films with lower sodium content are typically achieved by chemical deintercalation using an oxidizing agent like bromine (see chapter 2.1.2).[1] Also other oxidizing solutions containing iodine or $KMnO_4$ lead to a Na content as low as x = 0.35, which is required for the superconducting host material to form $Na_{0.35}CoO_2 \cdot 1.3H_2O$. This type of deintercalation is always done *ex- situ* at ambient conditions and does often result in degraded crystallinity and morphological disordering of the films.[49] Krockenberger *et al.* showed that the sodium content of thin films grown by PLD can be controlled in a composition range of x = 0.46 to 0.65 using *in-situ* post deposition annealing at different temperatures in oxygen.[53] In this study, a detailed investigation of γ-Na_xCoO_2 thin films on STO (100) at different growth and post-annealing conditions was performed. A typical 2θ-θ XRD pattern for the deposited thin films is given in Fig. 4.30. The film stabilizes in its hexagonal γ-phase and grows (00l) oriented.

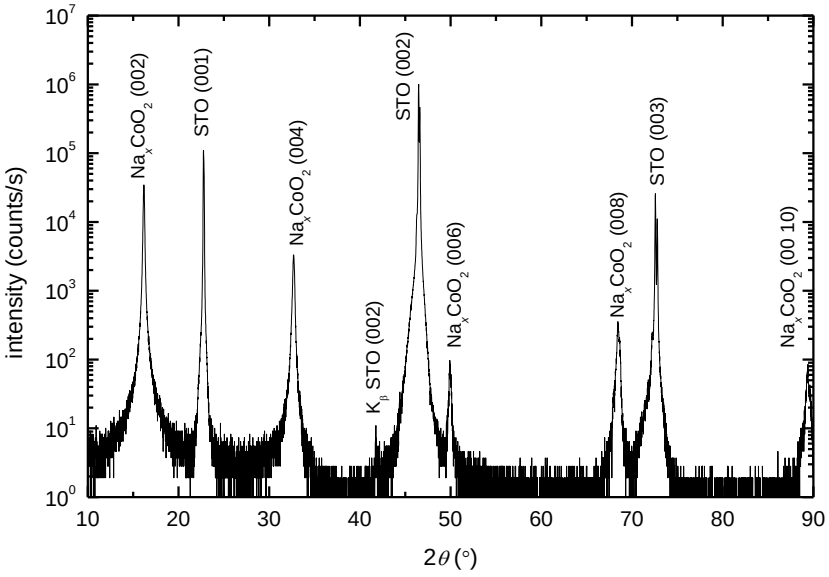

Fig. 4.30: 2θ–θ scan of a typical Na_xCoO_2 thin film. The reflections of the film and the STO substrate are denoted as (00l) and STO (00l), respectively. The film was grown at 550 °C, 1.2 J/cm^2 and an oxygen partial pressure of 0.25 mbar.

No reflections from other phases or impurities like Co_3O_4 are observable in the XRD pattern. This indicates *c*-axis oriented, single phase films within the measurement limits. The presence of higher orders of the (00l) reflections at higher 2θ angles and the high intensity of the (002) reflection indicate high crystallinity. The lattice constant c = 10.97 Å in this film has been calculated from the positions of all (00l) reflections using the *Nelson-Riley* function.

In addition, $c = c_0\text{-}kx$ (see chapter 4.1.1)was used to calculate the sodium content in the films. The calculated sodium contents as well as the *in-situ* annealing parameters are given in Table 4.2. In contrast to the strong dependence of c as function of the sodium content, no dependency of a on sodium content was found. For a Na_xCoO_2 film with $x = 0.64$, a was calculated from the (100) reflection (2.848 Å). The epitaxial growth of the films on (100) STO substrates is confirmed by XRD φ-scans of the (102) film reflection and the (103) STO substrate reflection. For these films a 12-fold symmetry is observed indicating two film domains, which are represented by even and odd sets of reflections (see Fig. 4.30).

Table 4.2: Sodium content and corresponding annealing parameters of the Na_xCoO_2 films.

#	$T_{Annealing}$ (°C)	$V_{annealing}$ (°C/min)	$t_{annealing}$ (min)	x (Na)
1	720	60	10	0.84
2	720	60	10	0.83
3	730	20	10	0.64
4	740	20	15	0.56
5	740	20	10	0.56
6	740	20	15	0.60
7	740	60	0	0.53
8	740	60	10	0.53
9	740	60	15	0.52
10	740	60	20	0.52
11	740	60	25	0.51
12	740	60	30	0.53
13	760	20	15	0.45
14	760	60	15	0.38

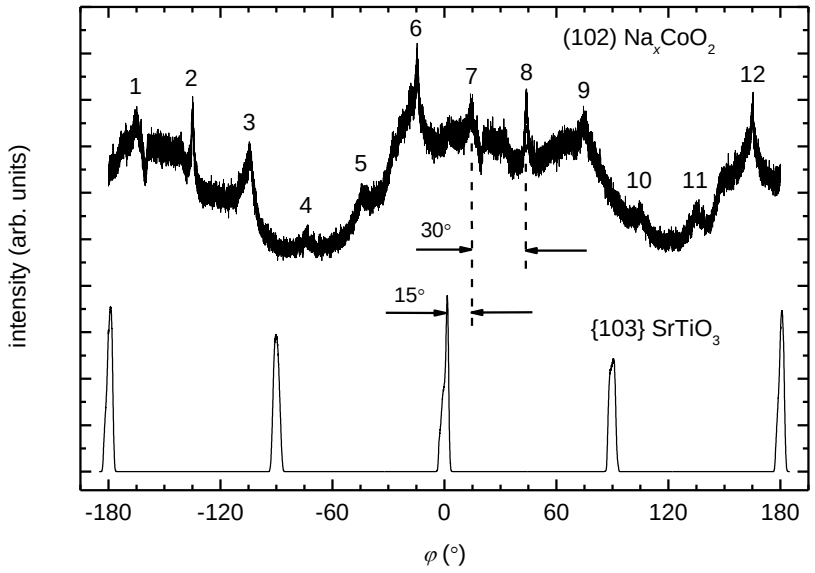

Fig. 4.31: XRD φ-scans of the (102) film and (103) STO reflections. For better clarity, the Na_xCoO_2 pattern is shifted vertically.

A angular shift of 30° between neighboring reflections is observed, which is due to in-plane rotation of the two domains by 30° with respect to each other. The six-fold symmetry for each of the two domains represents the hexagonal structure of γ–Na_xCoO_2. In contrast, on other substrates such as STO (111), *c*-cut Al_2O_3, and MgO (111) only six-fold symmetry was observered between (102) film and substrate reflections. This is corresponding with single hexagonal domains of the crystal lattice of these films.[56] In Fig. 4.31, the 12-fold symmetry is superimposed by a two-fold symmetrical pattern from the substrate, which can be attributed to thermal diffuse scattering from the substrate, e.g., scattering at non Bragg angles. A comparison of the φ-scans for the Na_xCoO_2 and the (103) STO substrate reveals 15° and 45° in-plane angular shifts between each of the four-fold symmetrical (103) reflection of STO and the odd and even neighbors of the 12-fold symmetrical (102) reflections of Na_xCoO_2. From this observation a growth model can be derived, which is visualized in Fig. 4.32.

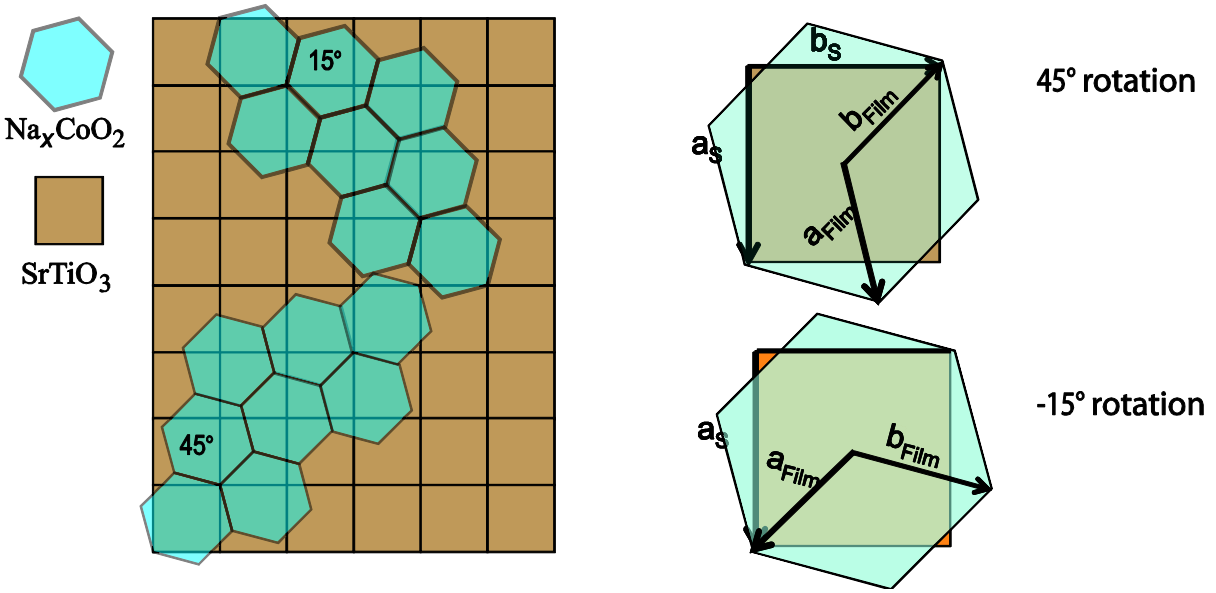

Fig. 4.32: Scheme of the in-plane arrangement of the hexagonal Na_xCoO_2 unit cells (blue hexagons) on cubic STO crystals (brown squares) following the epitaxial relation (001)Na_xCoO_2||(001) STO and [100]||<110>STO. The lengths of the squares and hexagons reflect relative dimensions of individual unit cells.

The diagonal of the STO lattice corresponds to two times the radius of the apothem of the Na_xCoO_2 hexagon. There are two possibilities for nucleation on the STO lattice, one domain is rotated 15° with respect to the underlying STO unit cell and another 45°. The epitaxial relation is given by (001)Na_xCoO_2||(100)STO and [100]Na_xCoO_2||<110>STO. The growth period for both domains is equal to five in-plane hexagonal cells of Na_xCoO_2, which fit four diagonals of the STO unit cells. The lattice mismatch between Na_xCoO_2 and STO in the epitaxial relation is calculated by $\delta=2^{1/2}a_{NaxCoO2}/(a_{STO}-1)=3.1\%$. Here, the lattice constants of STO (a = 3.905 Å) and of Na_xCoO_2 (a = 2.848 Å) are used for calculation. The positive value of the lattice mismatch indicates compressive stress in the *ab*-plane of the films, and, as a consequence of this, a tensile stress along *c* resulting in elongation of *c*. Another consideration of the growth mechanism would be the formation of a buffer layer. Usually buffer layers are formed to reduce stress/strain effects or to enhance film to substrate adhesion. In this case a Co_3O_4 layer is suggested with a thickness of one or two unit cells. This monolayer should have (111) orientation. The *a*-axis of cubic Co_3O_4 is 8.084 Å and the cobalt atoms sit on top of the positions of the strontium ions of the substrate. In the (111)-Co_3O_4 plane the distance

between two cobalt atoms is d = 5.717 Å. The epitaxial relationship with a buffer layer of Co_3O_4 would be (001)||(111)Co_3O_4||(001) STO. There is no experimental evidence for the formation of such a buffer layer. Sodium content in the deposited films and their crystallinity strongly depend on the annealing conditions after the deposition. The films annealed at lower temperatures ($T_{annealing}$ = 720 °C) have a relatively high sodium content of $x \geq 0.83$. Previously, films with a high sodium content were only deposited by sputtering with a lateral diffusion of Na into CoO thin film precursors at temperatures between 600 and 700 °C.[54] The sodium content in the films annealed at the lower temperature of 720 °C is inhomogeneous and the (002) reflection is splitted into two. These two reflections correspond to sodium contents of $x_1 \approx 0.84$ and $x_2 \approx 1.0$, as shown in Fig. 4.33. The inhomogeneous sodium content is accompanied by poor crystallinity of the films with high sodium content. The FWHM is larger than 1.2° in 2θ. The separation of the two phases can be an indication for a kinetically induced stabilization by the sodium diffusion process with an accumulation of Na near the surface. This process is prior to the formation of volatile Na_2O and gives rise to the x = 1.0 reflection. The annealing time of 10 min is too short (#1 and #2, see Table 4.2) to balance the oxidation potential of Na_xCoO_2 (at $T_{annealing}$ = 720 °C) and the diffusion time of sodium. Longer annealing at this temperature is necessary to produce a single phase films with high sodium content of x = 0.84. Other experiments with sodium cobaltate electrochemical cells showed that the oxidation potential is decreasing with increasing sodium content. As a consequence a lower annealing temperature ($T_{annealing}$ < 720 °C) is necessary for the stabilization of the x = 1 phase.[149, 150] When increasing the annealing temperature up to 760 °C, the sodium content can be controllably reduced from 0.83 down to 0.38. The temperature dependence is shown in Fig. 4.34.

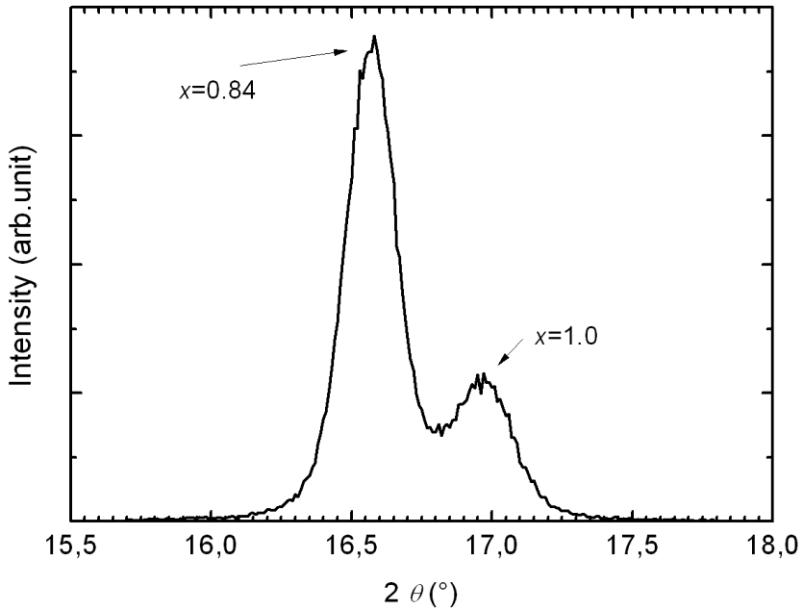

Fig. 4.33: XRD pattern of the (002) reflection for $Na_{0.84}CoO_2$ thin film. The splitting is a result of the formation of two phases with different sodium contents.

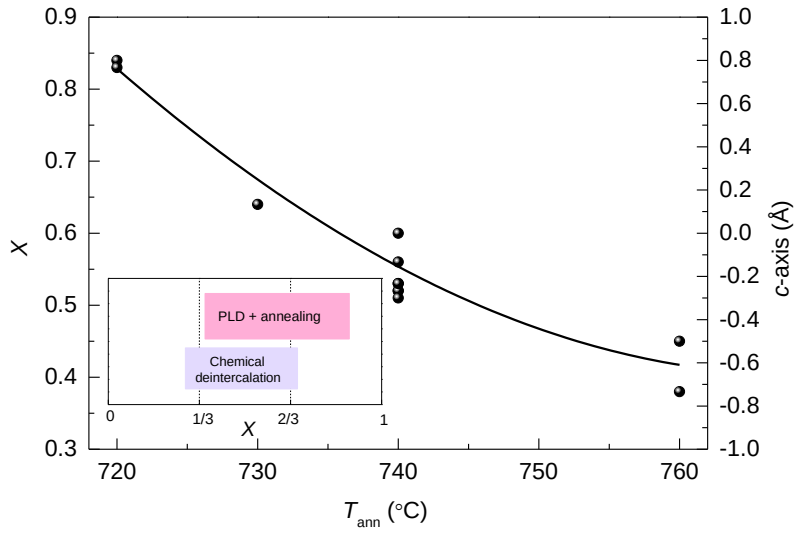

Fig. 4.34: Dependence of sodium content x and c of the Na_xCoO_2 films as a function of annealing temperature. The solid line is as a guide to the eye. The inset is visualizing accessable sodium contents by PLD and *in situ* annealing compared to the chemical deintercalation routes.

The γ–phase of Na_xCoO_2 with its hexagonal crystal structure persists in all these films despite of the major variation of the sodium content. Earlier such low sodium contents were only obtained by a chemical oxidation process (see inset of Fig. 4.34). The different sodium contents at $T_{annealing}$ = 740 °C shown in Fig. 4.34 can be explained by different annealing times (compare with Table 4.4). The films, which were annealed with a heating rate of 60 °C/min to 740 °C, have a decreased sodium content from $x = 0.6$ down to $x = 0.53$. This oxidation takes place in the first ten minutes during annealing time and is stable for the remaining 20 min. The first ten minutes of annealing at 740 °C is the characteristic for sodium diffusion out of the films. At this temperature the equilibrium sodium content is $x = 0.53$. The variation of the heating rate, $V_{annealing}$, between 20 °C/min and 60 °C/min results in minor changes of the sodium content of $x = 0.53$ to 0.56. The effect of a higher annealing rate is more distinct for higher annealing temperatures, at which the smallest sodium content was observed. The crystallinity of the Na_xCoO_2 thin films depends strongly on annealing time. The FWHM of the film annealed at 740 °C with a high heating rate of 60 °C/min yielded to values smaller than 0.2°, see Fig. 4.35.

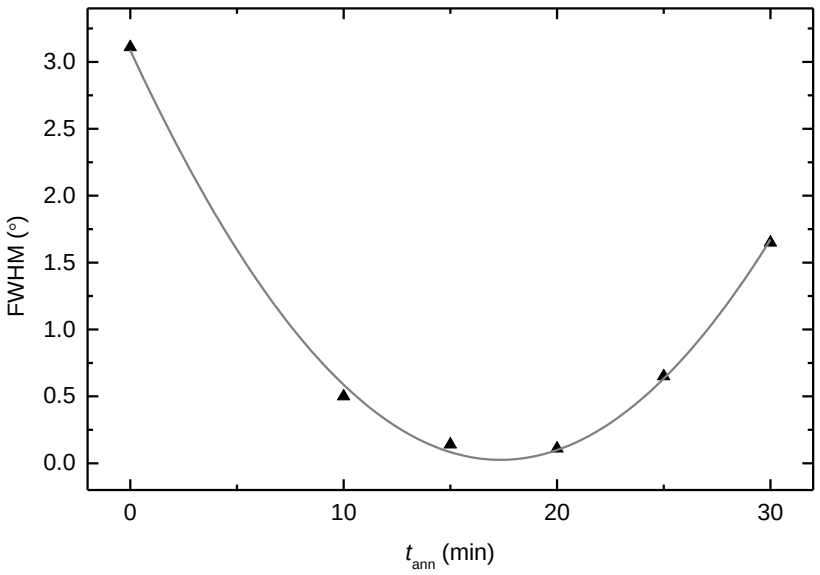

Fig. 4.35: Dependence of the FWHM of the (002) rocking curve as a function of annealing time for the Na_xCoO_2 thin films. Films were heated up to 740 °C at a heating rate of 60 °C/min. The solid line is as a guide for the eye.

Since the sodium content in the samples shown in Fig. 4.35 is stable at $x = 0.51$ to 0.53, the observed variation in crystallinity is not explainable by the diffusion gradient of the sodium ions. A longer annealing time leads to a larger FWHM of the rocking curve of the (002) reflection. The rocking curve of the sample which was annealed for 25 min is shown in Fig. 4.36. The curve is asymmetric, which can be fitted only by three Gaussian functions with different FWHM. Sharp and broad components are present, this is a well-known phenomenon explainable by classic diffraction theory.[171] The sharp component with a FWHM of 0.07 ° corresponds to the Bragg reflection, both broad reflections with FWHM's of 0.65° and 1.23° arise from diffuse scattering due to strain fields from dislocations. The dislocation density is a function of on annealing time. The coherence between neighboring grains is highest at an optimum annealing time, leading to the lowest dislocation density and resulting in less diffuse X-ray scattering.

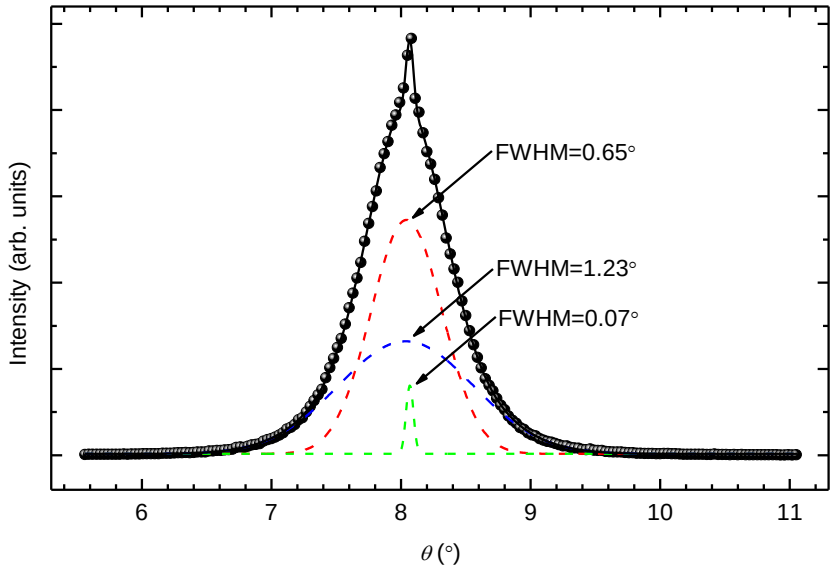

Fig. 4.36: Rocking curve of the (002) reflection of film #11. The rocking curve is fitted assuming three peaks with different FWHM (dashed line). The solid line shows a sum of the fitting peaks.

4.2.1.3 Buffer layer formation

To check for (111) Co_3O_4 buffer layer formation, a series of films were deposited with thicknesses of 3 to 8 monolayers. The results of the XRD-characterization of these films are given in Fig. 4.37. A mixture of Na_xCoO_2 (002) and (004) reflections and three orientations of Co_3O_4, the [(400) at 44°, the (440) at 65° and the (444) at 82°] could be observed. The postulated (111) reflection of Co_3O_4, which should appear at 19°, is missing in all eight patterns. The presence of Co_3O_4 reflections is an evidence for a mixture of Na_xCoO_2 and Co_3O_4. The growth of Co_3O_4 in (400) direction is favored since the lattice mismatch between STO and cubic Co_3O_4 (a = 8.08 Å) is small.[172] For Co_3O_4 (400)||STO (100) the lattice mismatch is 3.4%, which is relatively small. Reflections of Na_xCoO_2 are identifiable for 3 monolayers deposited on the substrate. This supports the growth model which has previously been described. After continuing deposition and subsequent annealing, the Co_3O_4 phase vanishes. No evidence for the formation of an (111) oriented Co_3O_4 buffer layer between substrate and Na_xCoO_2 films could be found. Even atomic layer deposition of 8 monolayers did not lead to the formation of a buffer layer.

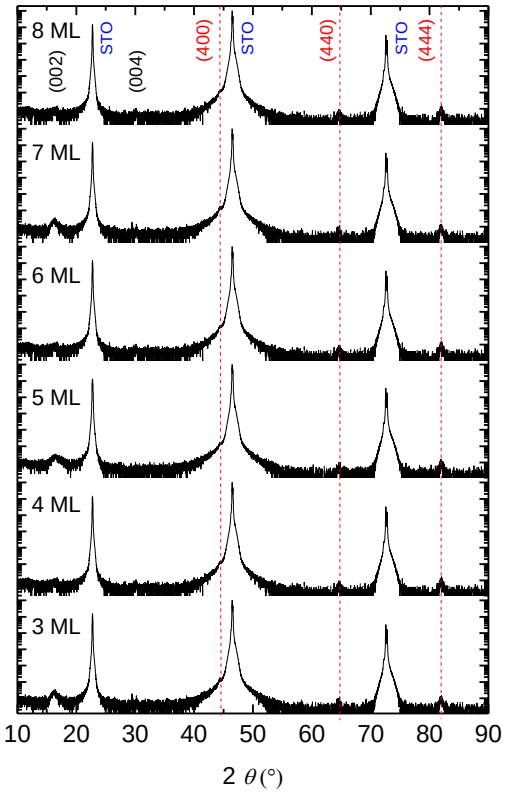

Fig. 4.37: XRD-patterns of the films with 3, 4, 5, 6, 7, and 8 monolayers (ML). The (002) and (004) reflections of Na_xCoO_2, substrate reflections, and (440), (400), and (444) reflections of Co_3O_4 are indexed in red. The dashed lines are guides to the eye.

4.2.2 Chemical deintercalation of sodium from Na_xCoO_2 thin films

Depending on the previously described annealing conditions, the thin films have different sodium content. To discuss the classical way of deintercalation of sodium films were chosen, which have a sodium content between $x = 0.45$ and 0.58. For all films c was calculated before and after deintercalation. The results of this experiment are given in Table 4.3. After deintercalation the sodium content in the films varied from $x = 0.34$ to 0.49. The sodium content is slightly above the value needed for the observation of superconductivity. The shift in 2θ of the (002) reflection due to sodium reduction is shown in detail for film #22. The intensity of the reflection decreases after deintercalation. A second effect of the deintercalation is an asymmetric broadening of the reflection, both can be attributed to a loss of crystallinity.

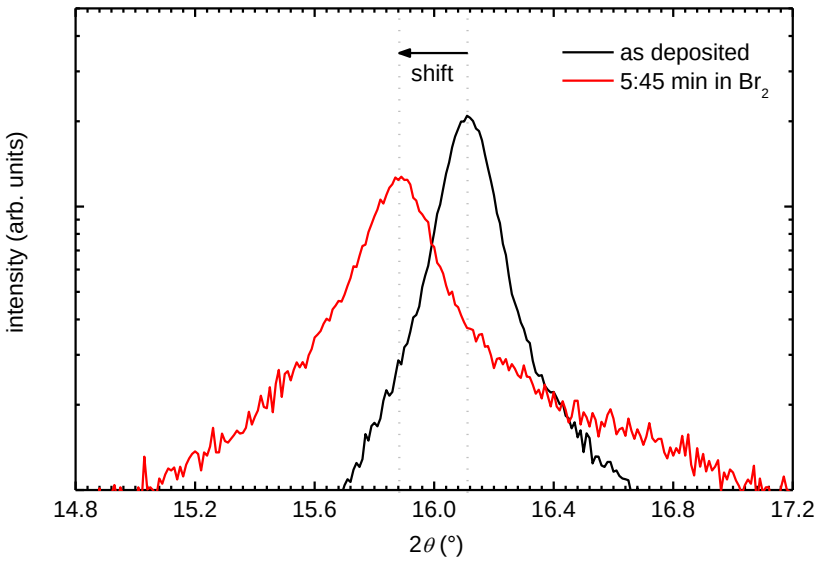

Fig. 4.38: XRD pattern of the (002) reflection of Na_xCoO_2 (film #22) before (black curve) and after (red curve) deintercalation using bromine solution.

Increasing of the deintercalation time showed no effect on the sodium content. Thin film #22 was deintercalated first for 5 min and 45 sec and second another 70 sec. It showed no change of sodium content even after two deintercalation steps. A possible explanation for this can be the deactivation of the films after treated once with bromine solution, a second oxidation process did not affect further sodium concentration in the films. Another explanation for this could be a too low bromine concentration in the solution. To rule out such effects, a higher bromine concentration in the solution was tested for sample#24. The film was treated with 3 mol Br_2 and afterwards neutralized in NaOH liquid solution. Interestingly the sample had the highest sodium content after deintercalation among all. The use of NaOH can have an opposite effect, it could higher the sodium content in the film by diffusion of Na into the crystal structure. This is supported by comparing of the sodium content of the film before and after treatment in NaOH liquid solution for 14 days. This sample remains to be the only one, in which the Na content is increased after a second deintercalation.

Table 4.3: *c*-axis length and sodium content of the thin films before and after sodium deintercalation treatment.

#	*c* as deposited (Å)	*x* (Na) as deposited	*c* after deint. (Å)	*x* (Na) after deint.
15	11.00	0.54	11.15	0.39
16	10.92	0.60	11.18	0.36
17	/	/	11.17	0.37
18	/	/	11.09	0.45
19	11.03	0.50	11.15	0.39
20	10.99	0.53	11.17	0.35
21	11.09	0.45	/	/
22	11.00	0.53	11.15	0.39
23	11.02	0.52	11.11	0.42
24	11.02	0.52	11.05	0.49
25	11.02	0.52	11.19	0.34
26	10.97	0.56	11.17	0.36
27	10.96	0.58	11.20	0.34

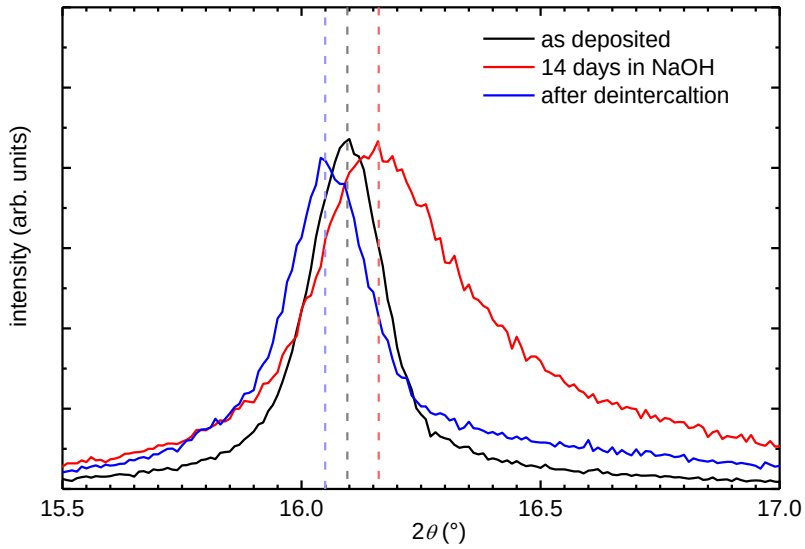

Fig. 4.39: XRD patterns of the (002) reflection shown for film #24 as deposited (black), after deintercalation (blue) and after 14 days in NaOH (red).The sodium content after deposition ($x = 0.52$) decreases after deintercalation to $x = 0.49$ and increases again after 14 days in NaOH liquid solution to $x = 0.61$.

In Fig. 4.39 the (002) reflection of this sample is shown for the, as deposited film, after deintercalation, and after 14 days in NaOH. The lowest sodium content in the films is achieved by using a higher bromine concentration and longer deintercalation time. Surprisingly, the sodium content of the film treated for 15 min is higher than the sodium content in the films treated for 14 and 12 min (#26, 25, 27). Finding a correlation of deintercalation parameters and the resulting sodium content in the films is not possible. Compared to classical use of bromine solution with bulk Na_xCoO_2, the deintercalation in thin films has obviously to be done more carefully. The reproducible deintercalation process of Na in thin films is still challenging.

4.2.3 Water intercalation in Na_xCoO_2 thin films

The first applied method to intercalate water into the structure of Na_xCoO_2 films with a sodium content between $x = 0.34$ and 0.42 was to bring the films in direct contact with water. The results of these experiments are similar to those of keeping the films in the green house chamber without N_2 flow. After the first days of intercalation, the XRD pattern does not change much, only a slight shoulder at higher 2θ values of the (002) reflection at an 2θ angle of 19° is observable. Visualizing this effect, the XRD patterns of sample cnc48-5d GC(RT) and cnc48-70 GC(RT) are given in Fig. 4.40. The XRD patterns of the films after 5 days in the green house chamber and after 70 days are very similar. The only change (after 70 days) is the formation of an impurity phase at an 2θ angle of 19°: This impurity phase is already formed after 5 days of intercalation, but for such short times only a broadening of the (002) reflection to higher 2θ values can be seen. Comparing with previous studies of Barnes *et al.*[43] and reference ICDD data (PDF 04-014-7502)[173] this reflection can be indexed as (100) $Co(OH)_2$. In the ideal structure $Co(OH)_2$ crystallizes in the *brucite*[1] type with $a = 3.186$ Å and $c = 4.653$ (space group $P\bar{3}m1$). The CoO_6 octahedron is compressed parallel to the threefold axis and is affected by the hydrogen bonds connecting the layers of the edge-sharing CoO_6 octahedra. Even after 70 days in humid atmosphere no evidence for the $Na_{0.3}CoO_2 \cdot 1.3 \cdot H_2O$ reflection is observable. The direct contact to water has a similar effect, even after a few days in water the water intercalated compound $Na_{0.35}CoO_2 \cdot 1.3\ H_2O$ did not form. Direct contact to water does seemingly not lead to the formation of the superconducting phase. The indirect way of water intercalation in high humidity at room temperature was also not successful.

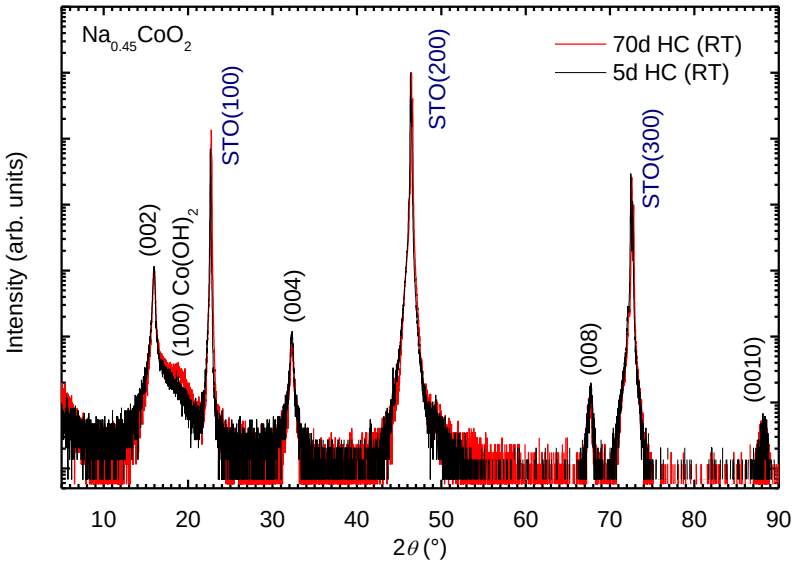

Fig. 4.40: XRD patterns of a $Na_{0.45}CoO_2$ film after 5 days (black curve) and after 70 days (red curve) in the green house chamber at room temperature. A shoulder is formed towards higher 2θ values, which can be indicated as the formation of the impurity phase $Co(OH)_2$.[43] The reflection corresponds to the (100) of $Co(OH)_2$.

[1] The *brucit* type is originally $Mg(OH)_2$, in which the Mg atom is octahedronally coordinated (MgO_6). The point symmetry is $\bar{3}2/m$, the crystal lattice is hexagonal.

Thermal energy has been provided to improve intercalation, therefore intercalation was performed for different durations at an elevated temperature of 85 °C. However, this experiment lead to similar results. First, the formation of a shoulder at higher 2θ values of the (002) reflection is visible and the longer the film is kept under humidity and warm atmosphere, the more pronounced this shoulder got. After 85 days in the green house chamber, all other film reflections vanished, only a very broad (001) reflection of $Co(OH)_2$ remains. The film is completely transformed into $Co(OH)_2$, see Fig. 4.41. Since the films seem to be more active right after the deintercalation step, a combined method was applied using NaOH liquid solution to stop deintercalation of Na and directly start intercalation of H_2O. The result of this attempt was the almost complete delamination of the film. The XRD pattern of the remaining film is given in Fig. 4.42.

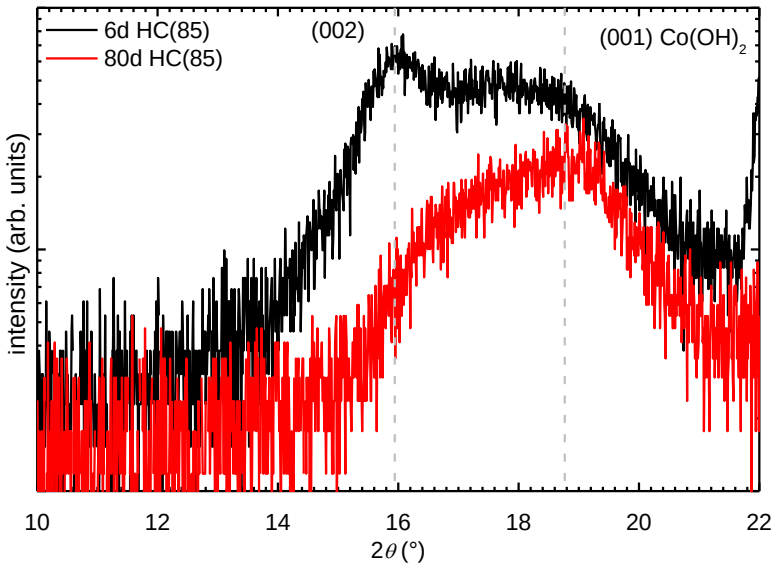

Fig. 4.41: XRD patterns of the thin film kept in the green house chamber for 5 and for 80 days at a temperature of 85 °C. The formation of $Co(OH)_2$ has already started after 5 days. After 80 days the (002) reflection of Na_xCoO_2 has vanished and only the (001) reflection of $Co(OH)_2$ remains.

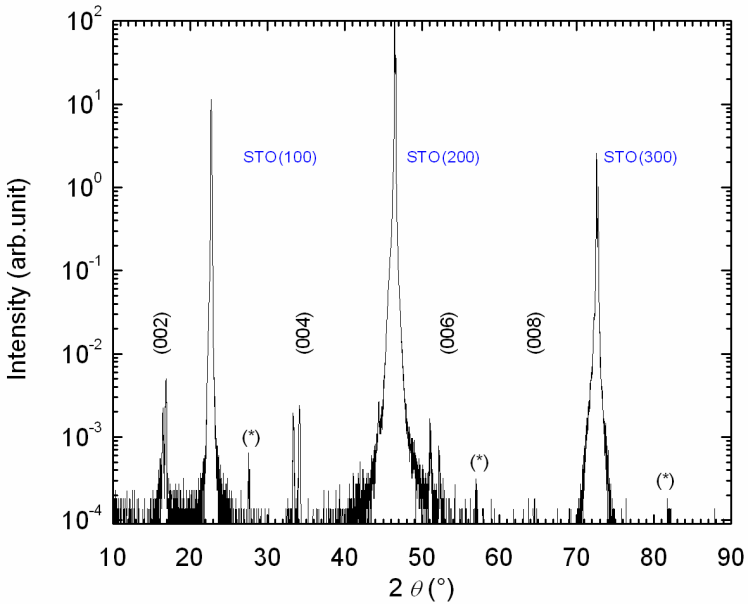

Fig. 4.42: XRD patterns of the film treated with a combined method of deintercalation and intercalation using NaOH liquid solution. The reflections split into doublets, which correspond to Na_xCoO_2 with $x \approx 0.8$ and $x \approx 1.0$, (*) marks reflections corresponding to the hydrated phases $y = 0.6$ and 1.3.

The XRD pattern of the remaining film shows two phases with $x \approx 0.8$ and 1.0 and an additional reflection, which can be attributed to be the hydrated analogon with $y \approx 0.6$ and 1.3. Film delamination is an indication for the formation of the hydrated phase, since the huge elongation of the *c*-axis due to the water molecules pushed into the unit cells causes high tension and stress in the film, which finally leads to the formation of cracks and delamination. The increased sodium content of the two phases (x= 0.8 and 1.0) compared to the pristine film compares with the observed effect of concentrated NaOH liquid solution on sodium content. Further investigations of the film surface and film cracks with SEM showed a "booklet"-like expansion of the films orthogonal to the surface, see Fig. 4.44. The effect of fanning out has been reported also for single crystals (Fig. 4.45).[42]

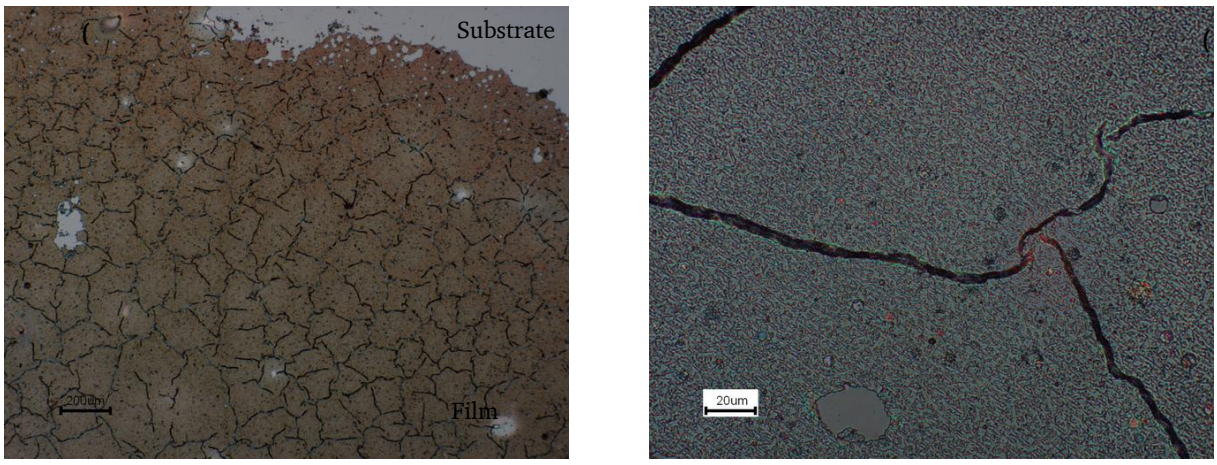

Fig. 4.43: (a) SEM image of the Na_xCoO_2 film surface after treatment with NaOH liquid solution combined deintercalation and intercalation. Many cracks can be identified visually. (b) Zoom-in of the sample surface showing cracks, which are opened by almost 1 μm.

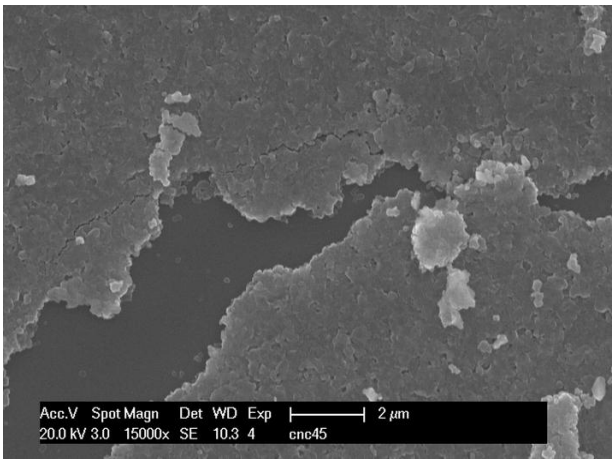

Fig. 4.44: SEM image of a crack for a Na_xCoO_2 film. The crack flanks of the film fan out due to incorporation of water molecules in the structure. Furthermore, small grains of the films can be identified, which leave the impression of a very rough and spongy film surface.

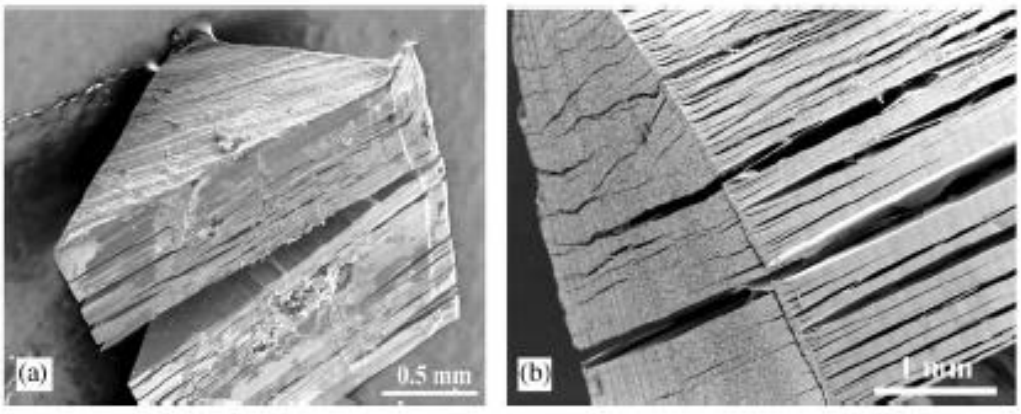

Fig. 4.45: Microscopic effect of water intercalation in Na_xCoO_2 single crystals, taken from Lin *et al.*[42]

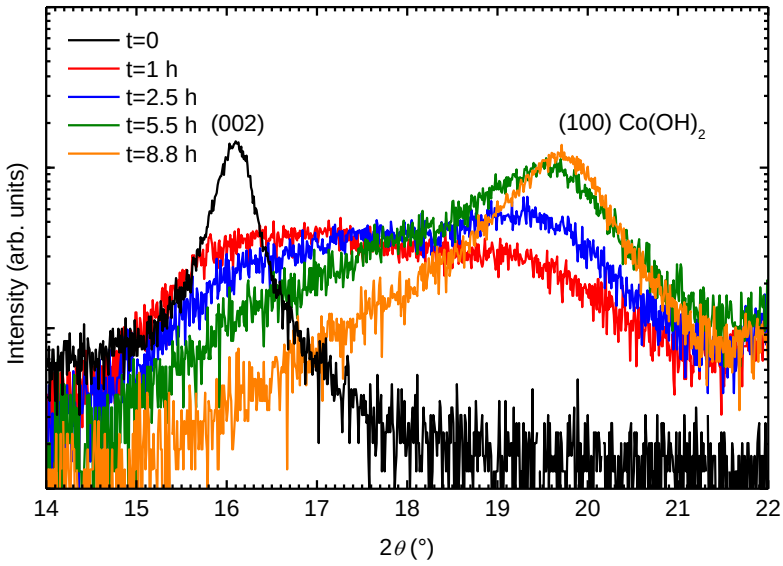

Fig. 4.46. XRD patterns of the (002) reflection of a Na_xCoO_2 film treated in the pressure cooker for 0, 1, 2.5, 5.5, and 8.8. The reflection of the "dry" phase vanishes with increasing time, whereas the intensity of the $Co(OH)_2$ reflection increases.

The usage of the pressure cooker pronounces the phase transformation of Na_xCoO_2 to the $Co(OH)_2$. The dependence of peak position and formation of $Co(OH)_2$, as a function of intercalation time is given in Fig. 4.46. Using pressurized hot water vapor, the formation of $Co(OH)_2$ is favoured. Unfortunately, the water-intercalated phase of NaxCoO2 could not be stabilized by this method. It has to be mentioned that all other film reflections vanished after film treatment and finally only the (100) $Co(OH)_2$ reflection remains. Since this reflection is very broad, crystallinity of the film is very poor. The poor crystallinity is connected with the ability of water intercalation into the unit cell. For that reason, the influence of film crystallinity on hydration was investigated. It was found that films with good crystallinity (FWHM (002) = 0.11°) tend to stay as such or completely transform to the $Co(OH)_2$ phase. Only for some films a hint of the existence of a hydrated phase can be identified (compare Fig. 4.47).

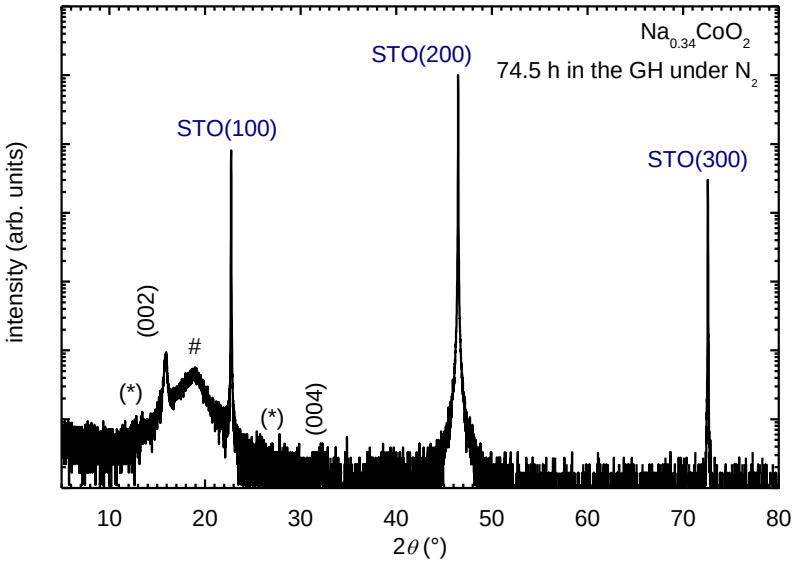

Fig. 4.47: XRD pattern of a Na_xCoO_2 film treated for 74.5 h in the green house chamber. The dry $Na_{0.34}CoO_2$ phase is still identifiable. Except of the (002) reflection all other film reflections are vanished. # indicates the $Co(OH)_2$ (001) reflection. (*) mark (002) and (004) reflections of the hydrated phase (y = 0.6).

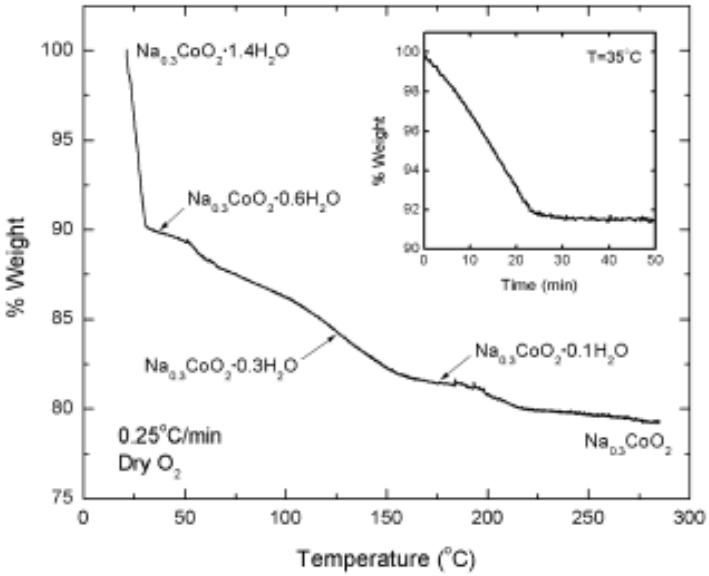

Fig. 4.48: Thermogravimetric analysis of hydrated Na_xCoO_2 heated in dry oxygen. The inset shows the loss of weight when heated very slowly (0.5°C/min) up to 35 °C. Taken from Foo *et al.*[174]

The $Na_xCoO_2{\cdot}1.3\ H_2O$ was unstable and decomposed into the $Na_xCoO_2{\cdot}\ 0.6\ H_2O$, after taking it out of the green house chamber or the pressure cooker. As soon as the warm sample was cooled down, the transformation of $Na_xCoO_2{\cdot}1.3\ H_2O$ to $Na_xCoO_2{\cdot}\ 0.6\ H_2O$ occurs. This is in good agreement with results of Foo *et al.*, which describe the chemical instability of Na_x-$CoO_2{\cdot}1.3\ H_2O$ under ambient conditions in dry environment.[174] It was shown that $Na_xCoO_2{\cdot}$ yH_2O is extremely sensitive to temperature and humidity, and easily dehydrates to the non-superconducting phase. The thermogravimetric analysis by Foo *et al.* is given in Fig. 4.48. The effect of dehydration is enhanced especially in thin films due to the small amount of material compared to bulk samples. Films crystallinity anyhow seems to play a crucial role for the stabilization of the superconducting phase. The first monolayers of the film are expected to grow coherent on the STO substrate. After a certain film thickness is reached, the film relaxes, compare to Fig. 4.36. The relaxed film has lower crystallinity but therefore, can be hydrated more easily.

4.2.4 Growth of Li_xCoO_2 thin films

The Li_xCoO_2 films were deposited on STO substrates with different orientations, (100), (111), and (110). For thin film battery applications of Li_xCoO_2 usually platinum,[84] quartz glass,[84] gold,[84] sapphire,[83] yttria stabilized zirconia,[175] and silicon[85, 176-178] are used as a substrate material, since the substrate has to be conductive. STO is an insulating material, but gets conducting by doping it with niobium, thus STO:Nb can be considered as a substrate for battery applications. The effect of different orientations of the STO substrate on the film growth is shown in Fig. 4.49. All films exhibit mixed orientation, (003) and (104), depending on substrate orientation the intensity ratio changes. In the case of STO (110), a third orientation of (110) is observed for Li_xCoO_2. All films have rhombohedral (SG 166) structure and compared to ICDD reference data (PDF 01-076-3172)[152] the film can be unambiguously identified to be Li_xCoO_2. Film thicknesses were 100 nm. Li_xCoO_2 has a layered rock-salt structure (α-$NaFeO_2$) with alternating layers of lithium and the transition metal, both occupying octa-

hedral sites. In the space group $R\bar{3}m$ the ions are located on the 3*a* and 3*b* sites. In contrast to this result, Ohnishi *et al.* observe a slight Li deficiency when using a $Li_{1.0}CoO$ target and suggest Li excess of around 0.1 to 0.2.[179] Another contradiction to the results of Ohnishi *et al.* is the absence of an impurity phase of Co_3O_4, which has been observed when using oxygen pressures higher than 0.1 Pa. In this study, the oxygen pressure was much higher during deposition and in all cases no Co_3O_4 was formed. Fig. 4.49 (a) shows a film, which has grown preferably in (104) direction. The integrated intensity ratios of $I_{(003)}/I_{(104)}$ are 0.015, (b) 0.98, and (c) 29,886. There is obviously a tremendous effect on film orientation as a function of STO orientation. On STO (100), see Fig. 4.49 (a), the film grows preferably (104) oriented, but significant fraction of the film has (003) orientation. No higher orders of both reflections are observable. In the case of STO (110) substrate, see Fig. 4.49 (b), both growth directions are observable with similar intensity. In contrast to these two films, the Li_xCoO_2film on STO (111), see Fig. 4.49 (c), is (003) oriented and the higher orders (006), (009), and (00 12) are observable as well. The intensity of the (104) reflection is very low, peak position is at 2θ = 44.49°. From literature it is known that film orientation is influenced by film thickness, which is a function of deposition time, independent on the deposition method.[83, 180] Thicker films grow preferably in (104) orientation due to the reduction of volume strain energy, whereas thinner films were (003) orientated due to minimized surface energy. All deposition parameters of the films were kept constant, so film orientation is only a function of substrate orientation, which is in good agreement with literature.[181] The difference of this work to previous results in literature are the different growth conditions. Almost all parameter, which are important for PLD growth differ from those used by Hirayama *et al.,* see Table 4.4. In addition, film thicknesses obtained by Hirayama *et al.* were thinner than film thicknesses measured during this study. This could be an explanation for the mixed film orientations present in all three films.[181]

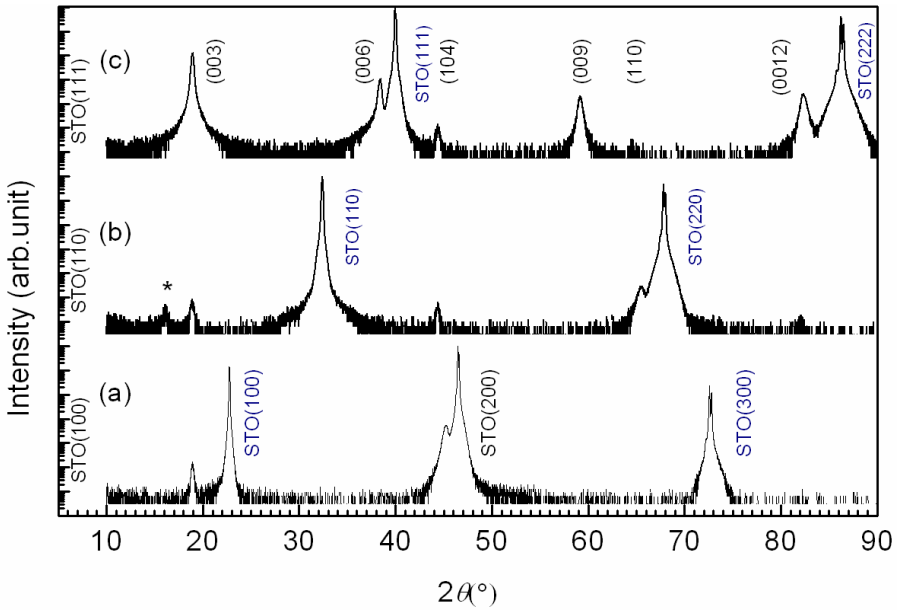

Fig. 4.49: X-ray diffraction patters of the Li_xCoO_2 films grown on $SrTiO_3$ substrates. (a) (100), (b) (110), and (c) (111) oriented.

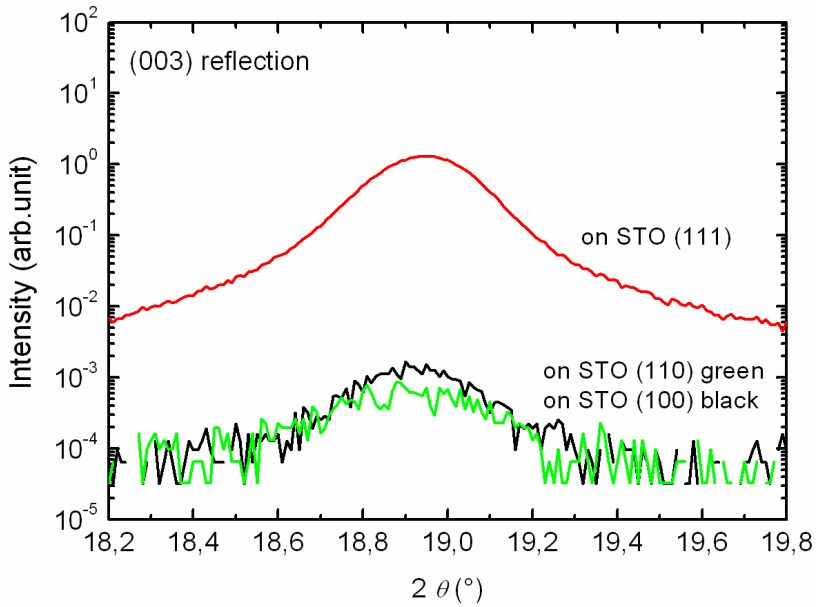

Fig. 4.50: (003) reflection of the Li_xCoO_2 films grown on STO (111) (red), STO (110) (green), and STO(100) black.

To further prove this result, a direct comparison of the (003) reflection of all Li_xCoO_2 films is given in Fig. 4.50. The (003) reflection is almost three orders of magnitude higher in intensity, for the STO (111) substrate. This was the only substrate for which higher orders of (003) orientation were indexable. For the STO (100) substrate, the *in-plane* epitaxial relation can be described as Li_xCoO_2 [1-20]||$SrTiO_3$ [011], resulting in a misfit between substrate and film of 1.87%, leading to a preferred (104) *out-of-plane* orientation. In the case of the STO (110) substrate, the epitaxial *in-plane* relation is Li_xCoO_2 [001]||$SrTiO_3$[111], which implies a misfit of 2.90% and results in preferred (110) growth of the film, see Fig. 4.49 (b). STO (111) substrates lead to preferred (00*l*) growth, since the lattice misfit between substrate and film (1.94%) is the smallest for all investigated substrates. Films had an *in-plane* relation of Li_xCoO_2 [110]||$SrTiO_3$ [1-10]. From previous work it is known that the (110) plane is parallel to the STO (2-20) plane.[181] For an application in thin film batteries as a cathode material, the (104) orientation is the preferable, since Li ions can diffuse easily in the direction of the applied voltage.

Table 4.4: Comparison of deposition parameters used by Ohnishi *et al.*, Hirayama *et al.*, and parameters used for this study.[179, 181]

Parameters	Ohnishi *et al*.	Hirayama *et al.*	This study
$T_{substrate}$ (°C)	800	650	550
f (Hz)	5	1	5
E_{laser} (mJ)	30	200	65
p_{O2} (Pa)	0.05-7.5	3.3	100
$d_{T\text{-}S}$ (mm)	45	45,75	38
D rate (nm/min)	0.18	0.3	8.1

4.2.5 Growth of $LiNi_{1/3}Mn_{1/3}Co_{1/3}O_2$ and $LiNi_{1/2}Co_{1/2}O_2$ thin films

After successful sol-gel preparation of the corresponding targets, thin films were grown by PLD on STO (100):Nb and characterized with X-ray diffraction. The 2θ-θ scans of the films are shown in Fig. 4.51 and Fig. 4.54.

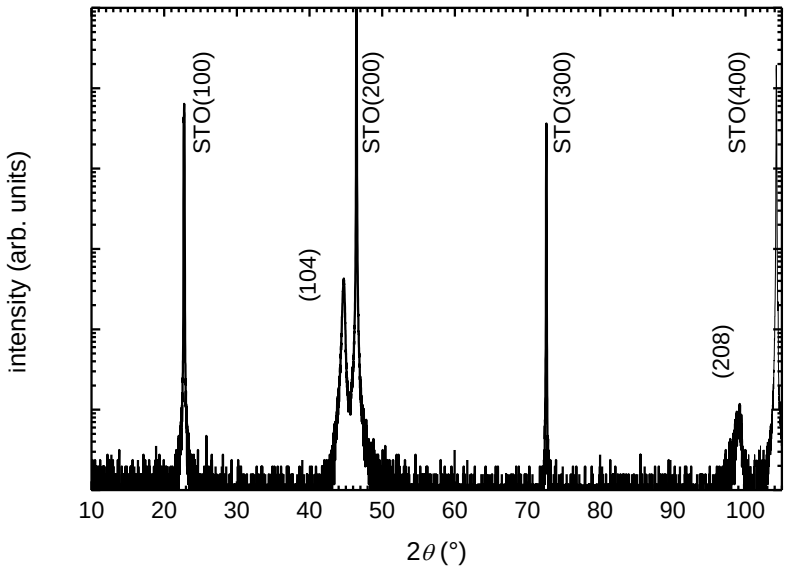

Fig. 4.51: 2θ–θ scan of a $LiNi_{1/2}Co_{1/2}O_2$ thin film on STO (100).

The $LiNi_{1/2}Co_{1/2}O_2$ film grows in (104) direction, the higher order is also observable in the X-ray pattern. No other phases or orientations can be determined. Compairing peak positions to ICDD reference data (PDF 04-013-4382), a loss of Li in the film is estimated. The rocking curve of the (104) reflection gives a FWHM of 1.45° after fitting with a Gaussian peak fit, see Fig. 4.52. From literature it is known that the (104) reflection tends to split into two due to the growth of (104) twin crystals.[181] A second peak fit based on two separate peaks was performed consequently, the results are given in Fig. 4.53. Both FWHM are 0.97° and 0.97. The mathematical expression for the peak intensity when fitted using a Gaussian function is given by Eq. 4.2.

Eq. 4.2

$$I^{Gaussian}(\alpha) = \frac{I_0}{1 + 4\left(\frac{\alpha - 2\theta}{\omega}\right)^2}$$

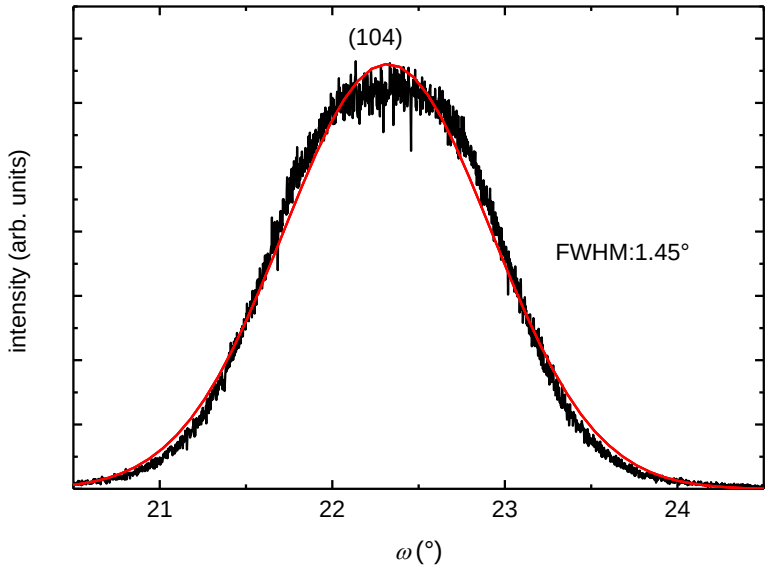

Fig. 4.52: Rocking curve of the (104) reflection of $LiNi_{1/2}Co_{1/2}O_2$ on STO (100) fitted with a Gaussian profile.

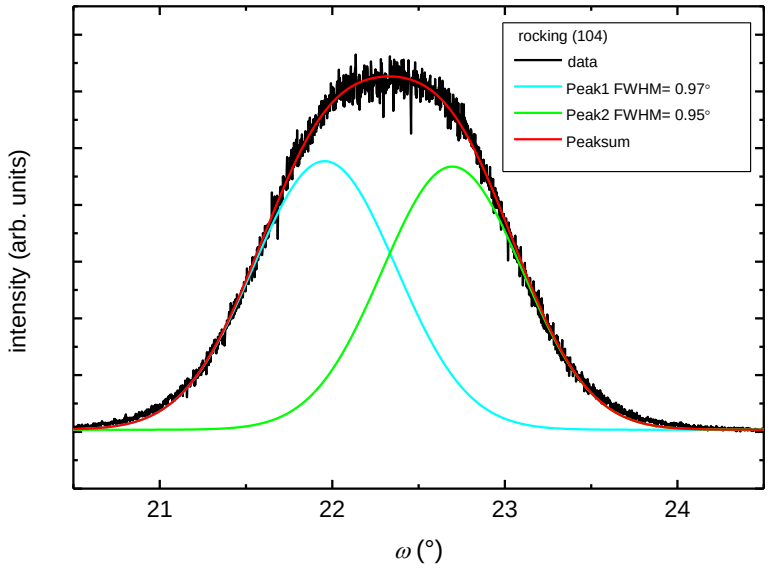

Fig. 4.53: Rocking curve of the (104) reflection of the $LiNi_{1/2}Co_{1/2}O_2$ on STO (100) fitted with two separate Gaussian profiles.

The FWHM of the reflections are related to crystal size or domains in the films. The smaller the FWHM, the higher the crystallinity of the film.

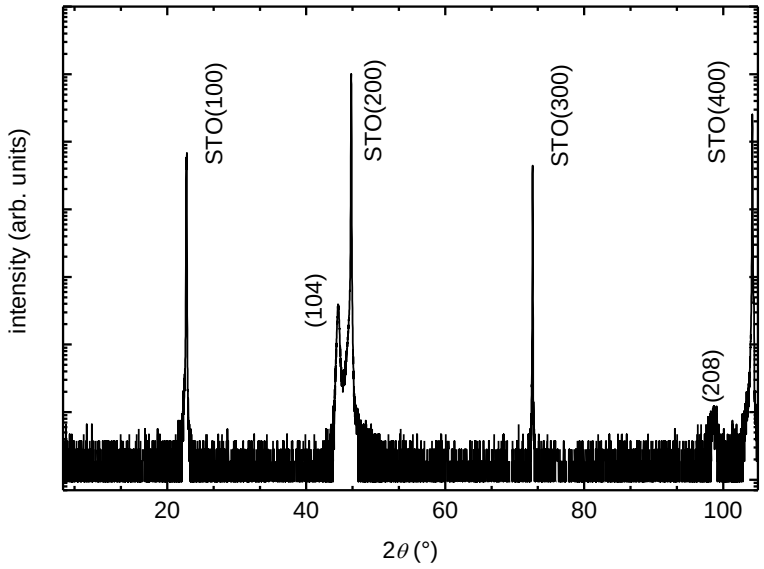

Fig. 4.54: 2θ-θ scan of a $LiNi_{1/3}Mn_{1/3}Co1_{/3}O_2$ thin film on STO (100) substrate.

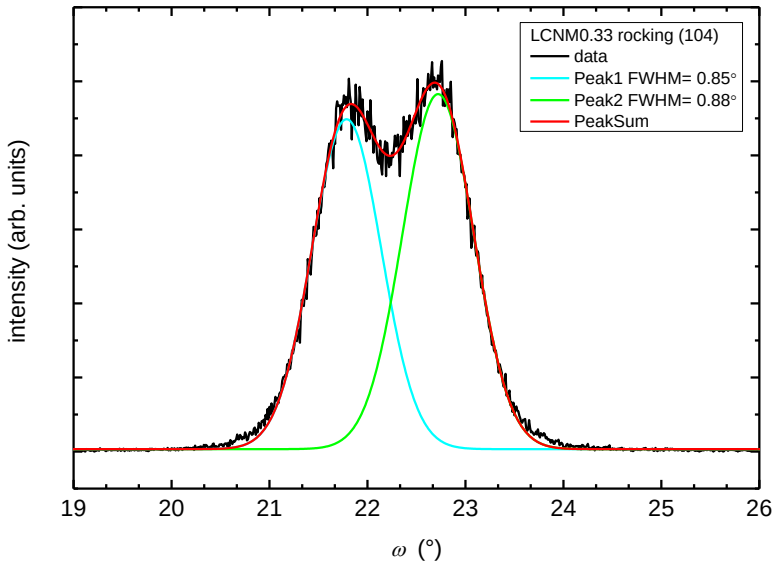

Fig. 4.55: Rocking curve of the (104) reflection of $LiNi_{1/3}Mn_{1/3}Co_{1/3}O_2$ on STO (100). The reflection is splitted into two indicating (104)oriented twin crystals.

The 2θ-θ scan of the $LiNi_{1/3}Mn_{1/3}Co1_{/3}O_2$ film is shown in Fig. 4.54. The film grows highly (104) oriented, no other orientations or reflections from impurity phases are identifiable, except of its higher orders. Comparison of peak position with ICDD reference data (PDF 00-056-0147) denotes to Li stoichiometry. The rocking curve of the (104) reflection is given in Fig. 4.55. It shows a clear splitting of the peak due to twinning, in accordance with observations by Hirayama *et al.*[181] The doublet can be fitted using two Gaussian functions and the FWHMs of both peaks are 0.85° and 0.88°. A FWHM value below 1° denotes to a good film crystallinity. The ϕ–scan of the *in-plane* (003) reflection, shown in Fig. 4.56, shows a four-fold symmetry, supporting the observation of crystal twinning. The domains are separated by an angle of 90°. The *in-plane* epitaxial relation is (003) LMNCO||<110>STO and the *out-of-plane* epitaxial relation is (104) LMNCO||<100>STO.

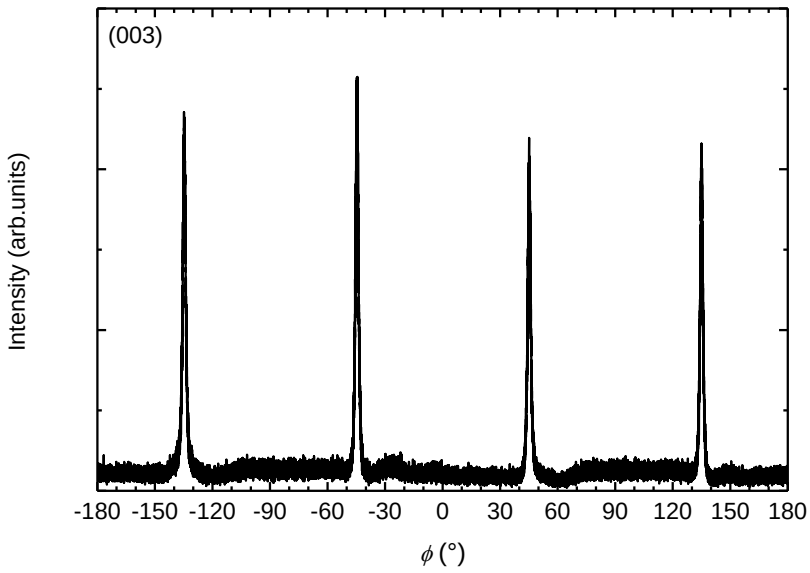

Fig. 4.56: ϕ-scan of the (003) reflection of a $LiNi_{1/3}Mn_{1/3}Co_{1/3}O_2$ thin film grown on STO (100).

Subsequent to structural characterization, the cation ratio of Ni:Mn:Co and Ni:Co were determined by EDS. The qualitative analysis is given in Table 4.5. In line with the measurement error of EDS, the ratio of Ni:Mn:Co in $LiNi_{1/3}Mn_{1/3}Co_{1/3}O_2$ equals 1:1:1 and for Ni:Co in $LiNi_{1/2}Co_{1/2}O_2$ equals 1:1.

Table 4.5: Results of quantitative EDS analyses of Ni, Co, and Mn for $LiNi_{1/3}Mn_{1/3}Co_{1/3}O_2$ and $LiNi_{1/2}Co_{1/2}O_2$ films.

Compound	$LiNi_{1/3}Mn_{1/3}Co_{1/3}O_2$ (wt%)	$LiNi_{1/2}Co_{1/2}O_2$ (wt%)
Ni	32.81	50.89
Mn	33.31	/
Co	33.88	49.02

5 Summary

In this work, PLD has been used for the investigation of Na_xCoO_2, $LiCoO_2$, $LiNi_{1/3}Mn_{1/3}Co_{1/3}O_2$ and $LiNi_{1/2}Co_{1/2}O_2$ thin films as well as the optimization of target fabrication. The main results are listed below:

- Na_xCoO_2, $LiNi_{1/3}Mn_{1/3}Co_{1/3}O_2$ and $LiNi_{1/2}Co_{1/2}O_2$ have been synthesized successfully by the sol-gel technique using acetate precursors. By using this method, lower synthesis temperatures were accessable, having a positive effect on the loss of Na or Li during high-temperature treatment in contrast to conventionally synthesized solid state material. The Li-based powders were of single phase, and cation stoichiometry corresponded to the initial acetate mixture. The sodium content in single phase Na_xCoO_2 was slightly reduced compared to the initial acetate mixture due to the high volatility of Na. The sodium content is in good agreement with observations of Na evaporation below 500 °C.[52, 149, 150] Due to the low sol-gel synthesis temperature, the powders had small grain sizes below 1 μm and later bulk target densities close to 60%, which is in good agreement to literature. This is very important for the use as battery materials, since smaller grain size enhance the ionic transport in the battery material.
- The growth mechanism of Na_xCoO_2 on $SrTiO_3$ substrates has been investigated in detail. The hexagonal unit cell of the Na_xCoO_2 grows 15° and 45° rotated with respect to the cubic substrate *ab*-plane. No formation of a buffer layer of Co_3O_4 (111) was found.
- The sodium content in and the crystallinity of the thin films has been investigated as a function of post-deposition annealing treatments. The sodium content in the films could be varied between 0.84 and 0.38 by changing annealing temperature and the deposited phase is stable as thin film. The γ–phase is preserved in all films despite of different sodium content. The *in-situ* variation of sodium stoichiometry, allows to tune the film properties in a wide range. This feature is an advantage compared to bulk Na_xCoO_2, in which only certain stoichiometries can be stabilized. No additional *ex-situ* de/intercalation process is necessary to change the sodium stoichiometry in the films.
- Fabrication of superconducting thin films by water intercalation is still challenging. Various attempts have been used to stabilize the superconducting phase, such as (a) direct contact with water, (b) green house chamber, and (c) pressured water vapor. All thin films degraded by the formation of $Co(OH)_2$ after deintercalation, regardless whether a green house chamber, water vapor or direct contact to water was applied. If a second phase to Na_xCoO_2 formed then only $Co(OH)_2$. Experiments with NaOH liquid solution have shown that fine tuning of sodium content during deintercalation is possible. All subsequent steps of film treatment caused a loss of crystallinity. The stabilization of the meta stable $Na_{0.3}CoO_2{\cdot}1.3H_2O$ phase for investigation of the superconducting pairing mechanism is not promising.
- The deposition parameters used for Na_xCoO_2 were transferred to the $LiCoO_2$. $LiCoO_2$ thin films on various orientations of $SrTiO_3$ substrates have been grown by PLD. By optimization of the growth parameters and substrate orientation, (003)-oriented or (104)-oriented films have been grown. The stoichiometry of is directly transferred from target to film.
- $LiNi_{1/3}Mn_{1/3}Co_{1/3}O_2$ and $LiNi_{1/2}Co_{1/2}O_2$ thin films have been grown by PLD. These thin film materials are promising candidates for the development of thin film batteries in the near future.

6 Future prospects

- Since the goal to fabricate superconducting Na_xCoO_2 thin films has not been achieved, the focus should be changed towards its very promising thermoelectric properties. The results of this thesis could be used to optimize the growth of thermoelectric thin films and help to established PLD as an advanced tool for thin film growth of thermoelectric materials. An *in-situ* fine-tuning of the sodium content at the lower side of the sodium content in the phase diagram, saves complex post treatment steps when targeting the formation of the superconducting phase. As films could be grown already with a sodium stoichiometry of $0.28 < x < 0.38$, the water intercalation step could perhaps be included into the deposition process by (for example) flushing the growth chamber with humid N_2.
- The establishment of the sol-gel technique applied on the fabrication of sodium and lithium-based cobaltates could be used for further investigations on the materials and its influence on thin film growth compared to the targets made by conventional solid-state synthesis. On the other hand this method is a very promising for fabrication of the battery materials, since the grain size is small compared to solid state synthesis.
- The successful growth of $LiNi_{1/3}Mn_{1/3}Co_{1/3}O_2$ and $LiNi_{1/2}Co_{1/2}O_2$ as thin films by PLD could be a starting basis for future activities regarding energy sustainability. Thin film battery cathodes of these materials will probably play an important role in future as they could replace state-of-the-art $LiCoO_2$ as a cathode material. The assembly of a test battery with this material grown by PLD could give first insights on device performance, and therefore film optimization should be prioritized first.
- Concerning performance optimization, safety and cost effectiveness a substitution of Li by Na would be favourable. Sodium is (compared to lithium) cheap, and world supply of sodium is huge.

List of Tables

List of Figures

References

[1] K. Takada, H. Sakura, E. Takayama-Muromachi, F. Izumi, R. Dilanian, and T. Sasaki, Nature **422**, 53 (2003).

[2] K. M. Shaju, G. V. Subba Rao, and B. V. R. Chowdari, Electrochimica Acta **48**, 145 (2002).

[3] J. G. Bednorz and K. A. Müller, Zeitschrift fuer Physik B: Condensed Matter **64**, 189 (1986).

[4] G. Woltersdorf, Zeitschrift für anorganische Chemie **252**, 126 (1943).

[5] C. Fouassier, G. Matejka, J.-M. Reau, and P. Hagenmuller, Journal of Solid State Chemistry **6**, 532 (1973).

[6] Q. Huang, M. L. Foo, R. A. Pascal, Jr., J. W. Lynn, B. H. Toby, T. He, H. W. Zandbergen, and R. J. Cava, Physical Review B **70**, 184110 (2004).

[7] M. L. Foo, Y. Wang, S. Watauchi, H. W. Zandbergen, T. He, R. J. Cava, and N. P. Ong, Physical Review Letters **92**, 247001 (2004).

[8] Y. Krockenberger, I. Fritsch, G. Christiani, H. U. Y. L. Habermeier, C. Bernhard, B. Keimer, and L. Alff, Applied Physics Letters **88**, 162501 (2006).

[9] M. Jansen and R. Hoppe, Zeitschrift anorganische allgemeine Chemie **408**, 104 (1974).

[10] J. Molenda, C. Delmas, P. Dordor, and A. Stoklosa, Solid State Ionics **12**, 473 (1989).

[11] I. Terasaki, Y. Sasago, and K. Uchinokura, Physical Review B **56**, 658 (1997).

[12] Y. Nakamura and S. Uchida, Physical Review B **47**, 8369 (1993).

[13] Y. Maeno, H. Hashimoto, K. Yoshida, S. Nishizaki, T. Fujita, J. G. Bednorz, and F. Lichtenberg, Nature **372**, 532 (1994).

[14] S. D. Obertelli, J. R. Cooper, and J. L. Tallon, Physical Review B **46**, 14928 (1992).

[15] H. Hänsel and W. Neumann, *Physik: Moleküle und Festkörper* (Spektrum Akademischer Verlag, Heidelberg, 1996).

[16] Y. Wang, N. S. Rogado, R. J. Cava, and N. P. Onhg, Nature **423**, 425 (2003).

[17] T. Motohashi, T. Karppinen, and H. Yamauchi, arXiv:cond-mat/0304479v1 (2003).

[18] W. D. Knight, Physical Review **76**, 1259 (1949).

[19] C. Domb, G. T. Rado, and H. Suhl, *Magnetism* (Acadamic Press Incoporated, New York, 1965).

[20] J. O. Haerter, M. R. Peterson, and B. S. Shastry, Physical Review Letters **97**, 226402 (2006).

[21] B. Kumar and B. S. Shastry, Physical Review B **68**, 104508 (2003).

[22] G. Baskaran, Physical Review Letters **91**, 097003 (2003).

[23] Q.-H. Wang, D.-H. Lee, and P. A. Lee, Physical Review B **69**, 092504 (2004).

[24] J. Hubbard, Proceedings of the Royal Society of London. Series A. Mathematical and Physical Sciences **276**, 238 (1963).

[25] T. Takeuchi, M. Matoba, T. Aharen, and M. Itoh, Physica B: Condensed Matter **312–313**, 719 (2002).

[26] T. Motohashi, R. Ueda, E. Naujalis, T. Tojo, I. Terasaki, T. Atake, M. Karppinen, and H. Yamauchi, Physical Review B **67**, 064406 (2003).

[27] J. Sugiyama, H. Itahara, J. H. Brewer, E. J. Ansaldo, T. Motohashi, M. Karppinen, and H. Yamauchi, Physical Review B **67**, 214420 (2003).

[28] H. Sakurai, S. Takenouchi, N. Tsujii, and E. Takayama-Muromachi, Journal of the Physical Society of Japan **73**, 2081 (2004).

[29] J. Sugiyama, J. H. Brewer, E. J. Ansaldo, B. Hitti, M. Mikami, Y. Mori, and T. Sasaki, Physical Review B **69**, 214423 (2004).

[30] J. Sugiyama, et al., Physical Review Letters **92**, 017602 (2004).

[31] J. Wooldridge, D. M. Paul, G. Balakrishnan, and M. R. Lees, J. Phys.-Condes. Matter **17**, 707 (2005).

[32] Q. Huang, M. L. Foo, and J. R. Cava, Journal of Physics: Condensed Matter **16**, 5803 (2004).
[33] H. X. Yang, C. J. Nie, Y. G. Shi, H. C. Yu, S. Ding, Y. L. Liu, D. Wu, N. L. Wang, and J. Q. Li, Solid State Communications **134**, 403 (2005).
[34] K. Y. Choi, K. D. Kim, and J. W. Yang, Journal of Materials Processing Technology **171**, 118 (2006).
[35] R. E. Schaak, T. Klimczuk, and M. L. Foo, Nature **424**, 527 (2003).
[36] D. J. Singh, Physical Review B **61**, 13397 (2000).
[37] K. Takada, K. Fukuda, M. Osada, N. Izumi, F. Izumi, and R. Dilanian, Journal of Materials Chemistry **14**, 1448 (2004).
[38] W. Li, W. R. McKinnon, and J. R. Dahn, Journal of The Electrochemical Society **141**, 2310 (1994).
[39] K. L. Nash, K. J. Sully, and A. B. Horn, The Journal of Physical Chemistry A **105**, 9422 (2001).
[40] R. W. T. Wilkins, A. Mateen, and G. W. West, American Mineralogist **59**, 811 (1974).
[41] C. J. Milne, D. N. Argyriou, A. Chemseddine, and N. Aliouane, Physical Review Letters **93**, 2470071 (2004).
[42] C. T. Lin, D. P. Chen, P. Lemmens, X. N. Zhang, A. Maljuk, and P. X. Zhang, Journal of Crystal Growth **275**, 606 (2005).
[43] P. W. Barnes, M. Avdeev, J. D. Jorgensen, D. G. Hinks, H. Claus, and S. Short, Physical Review B **72**, 134515 (2005).
[44] M. Deliens and H. Goethals, Mineralogical Magazine **39**, 152 (1973).
[45] F. Lichtenberg, Progress in Solid State Chemistry **30**, 103 (2002).
[46] C. Caroli, P. G. De Gennes, and J. Matricon, Physics Letters **9**, 307 (1964).
[47] K. Kuroki, S. Okubo, T. Nijima, and Y. Tanaka, Physica B **403**, 1151 (2007).
[48] I. I. Mazin and M. D. johannes, Nature letters **1**, 91 (2005).
[49] H. Zhou, X. P. Zhang, B. T. Xie, Y. S. Xiao, C. X. Yang, Y. J. He, and Y. G. Zhao, Thin Solid Films **497**, 338 (2006).
[50] X. P. Zhang, Y. S. Xiao, H. Zhou, B. T. Xie, C. X. Yang, Y. G. Zhao, and X. P. Zhang, Matererials Science Forum **3807**, 475 (2005).
[51] J. Y. Son, B. G. Kim, and J. H. Cho, Applied Physics Letters **86**, 221918 (2005).
[52] J. P. Kemp, D. J. Beal, P. A. Cox, and J. S. Foord, Vacuum **41**, 1739 (1990).
[53] Y. Krockenberger, I. Fritsch, G. Christiani, A. Matveev, H. U. Habermeier, B. Keimer, and L. Alff, Thin Solid Films **486**, 170 (2006).
[54] H. Ohta, S. im, S. Ohta, K. oumoto, M. Hirano, and H. Hosono, Crystal Growth & Design **5**, 25 (2005).
[55] C.-J. Liu, P. K. Nayak, and Y.-Z. Chen, Thin Solid Films **518**, 91 (2009).
[56] J. Y. Son, H.-B.-R. Lee, and J. H. Cho, Applied Surface Science **254**, 436 (2007).
[57] J. Y. Son and J. H. Cho, Journal of Crystal Growth **310**, 3093 (2008).
[58] L. Yu, Y. Krockenberger, I. Fritsch, and H. U. Habermeier, Progress in Solid State Chemistry **35**, 545 (2007).
[59] A. Karma and M. Plapp, Physical Review Letters **81**, 4444 (1998).
[60] J. Y. Son, Journal of Physics D:Applied Physics **41**, 095405 (2008).
[61] J. Y. Son, Y. H. Shin, and C. S. Park, Journal of Solid State Chemistry **181**, 2020 (2008).
[62] H. Okabe, M. Matoba, T. Kyomen, and M. Itoh, Journal of Applied Physics **95**, 6831 (2004).
[63] T. Haage, J. Zegenhagen, J. Q. Li, H. U. Habermeier, M. Cardona, C. Jooss, R. Warthmann, A. Forkl, and H. Kronmüller, Physical Review B **56**, 8404 (1997).
[64] K. Sugiura, H. Ohta, S.-i. Nakagawa, R. Huang, Y. Ikuhara, K. Nomura, H. Hosono, and K. Koumoto, Applied Physics Letters **94**, 152105 (2009).
[65] T. Valla, et al., Nature **417**, 627 (2002).

[66] T. F. Schulze, P. S. Häfliger, C. Niedermayer, K. Mattenberger, S. Bubenhofer, and B. Batlogg, Physical Review Letters **100**, 026407 (2008).
[67] T. Kanno, S. Yotsuhashi, and H. Adachi, Applied Physics Letters **85**, 739 (2004).
[68] A. Sakai, T. Kanno, S. Yotsuhashi, A. Odagawa, and H. Adachi, Japanese Journal of Applied Physics A **44**, L966 (2005).
[69] H. Kaibe, Y. Tanaka, M. Sakata, and I. Nishida, Journal of Physics and Chemistry of Solids **50**, 945 (1989).
[70] Y. Orikasa, N. Hayashi, and S. Muranaka, Journal of Applied Physics **103**, 113703 (2008).
[71] G. Nazri and G. Pistoia, *Lithium batteries : science and technology* (Kluwer Academic Publishers, Boston, 2004).
[72] M. Yoshio, R. J. Brodd, and A. Kozawa, *Lithium-ion batteries : science and technologies* (Springer, New York, 2009).
[73] A. Manthiram and J. Choi, Journal of Power Sources **159**, 249 (2006).
[74] T. Ohzuku and Y. Makimura, Chemistry Letters **30**, 642 (2001).
[75] Z. Lu, D. D. Macneil, and J. R. Dahn, Electrochemical and Solid-State Letters **4**, A191 (2001).
[76] H. Yoshizawa and T. Ohzuku, Journal of Power Sources **174**, 813 (2007).
[77] M. Guilmard, L. Croguennec, and C. Delmas, Chemistry of Materials **15**, 4484 (2003).
[78] M. Guilmard, L. Croguennec, D. Denux, and C. Delmas, Chemistry of Materials **15**, 4476 (2003).
[79] G. G. Amatucci, J. M. Tarascon, and L. C. Klein, Journal of Electrochemical Society **143**, 1114 (1996).
[80] J. M. Tarascon, G. Vaughan, C. Chabre, and L. Seguin, Journal of Solid State Chemistry **147**, 410 (1999).
[81] X. Q. Yang, X. Sun, and J. McBreen, Elelectrochemical Communications **2**, 100 (2000).
[82] B. Wang, J. B. Bates, F. X. Hart, B. C. Sales, R. A. Zuhr, and J. D. Robertson, Journal of The Electrochemical Society **143**, 3203 (1996).
[83] J. Xie, N. Imanishi, T. Matsumura, A. Hirano, Y. Takeda, and O. Yamamoto, Solid State Ionics **179**, 362 (2008).
[84] Y. Iriyama, M. Inaba, T. Abe, and Z. Ogumi, Journal of Power Sources **94**, 175 (2001).
[85] H. Xia, L. Lu, and G. Ceder, Journal of Power Sources **159**, 1422 (2006).
[86] Z. Chen and J. R. Dahn, Electrochimica Acta **49**, 1079 (2004).
[87] TU Freiberg, http://www.chem.tu-freiberg.de/~boehme/lehre/rksa/rksa01.html, 03.04.2012.
[88] Plasma Surface Technology, http://www.plasma.de/de/plasma_wissenswertes/part2.htm, 29.02.2012.
[89] W. K. Burton, N. Cabrera, and F. C. Frank, Philosophical Transactions of the Royal Society of London, Series A: Physical Sciences and Engineering **243**, 299 (1951).
[90] C. B. Carter and M. G. Norton, *Ceramic materials : science and engineering* (Springer, New York, 2007).
[91] K. L. Chopra, *Thin film phenomena* (R. E. Krieger Pub. Co., Huntington, N.Y., 1979).
[92] R. Eason, *Pulsed laser deposition of thin films : applications-led growth of functional materials* (Wiley-Interscience, Hoboken, N.J., 2007).
[93] D. Basting, *Excimer laser technology* (Springer, Berlin [u.a.], 2005).
[94] C. J. Knight, AIAA **17**, 519 (1979).
[95] A. Miotello and R. Kelly, Applied Physics A **69**, S67 (1999).
[96] M. N. R. Ashfold, F. Claeyssens, G. M. Fuge, and S. J. Henley, Chemical Society Reviews **33**, 23 (2004).
[97] F. Claeyssens, A. Cheesman, S. J. Henley, and M. N. R. Ashfold, Journal of Applied Physics **92**, 6886 (2002).
[98] P. R. Willmott and J. R. Huber, Reviews of Modern Physics **72**, 315 (2000).

[99] W. D. Kingery, H. K. Bowen, and D. R. Uhlmann, *Introduction to ceramics* (Wiley, New York, 1976).
[100] D. W. Richerson, *Modern ceramic engineering : properties, processing, and use in design* (CRC Taylor & Francis, Boca Raton, FL, 2006).
[101] M. N. Rahaman, *Ceramic processing and sintering* (M. Dekker, New York, 2003).
[102] D. Segal, *Chemical synthesis of advanced ceramic materials* (Cambridge University Press, Cambridge England ; New York, 1989).
[103] M. Pechini, edited by U. S. P. 3330697, U.S. Patent 3330697, 1967), Vol. 3330697.
[104] think ceramics: Technische Keramik, www.thinkceramics.org, 21.03.2012.
[105] C. H. Hsueh, A. G. Evans, and R. L. Coble, Acta Metallurgica **30**, 1269 (1982).
[106] M. A. Spears and A. G. Evans, Acta Metallurgica **30**, 1281 (1982).
[107] Institut für Arbeitsschutz der deutschen gesetzlichen Unfallversicherung, GESTIS substance database, 2012.
[108] N. V. Zubkova, D. Y. Pushcharovsky, G. Ivaldi, G. Ferraris, I. V. Pekov, and N. V. Chukanov, Neues Jahrbuch für Mineralogie - Monatshefte **2**, 85 (2002).
[109] J. Mu and D. D. Perlmutter, Thermochimica Acta **49**, 207 (1981).
[110] M. Mohamed, S. Halawy, and M. Ebrahim, Journal of Thermal Analysis and Calorimetry **41**, 387 (1994).
[111] K. A. Kemper and J. E. House Jr, Thermochimica Acta **170**, 253 (1990).
[112] M. D. Judd, B. A. Plunkett, and M. I. Pope, Journal of Thermal Analysis and Calorimetry **6**, 555 (1974).
[113] V. Amirthalingam and V. M. Padmanabhan, Acta Crystallographica **11**, 896 (1958).
[114] W. Krönig, Zeitschrift fuer angewandte Chemie **37**, 667 (1924).
[115] G. Hussein, A. Nohman, and K. Attyia, Journal of Thermal Analysis and Calorimetry **42**, 1155 (1994).
[116] M. A. Mohamed, S. A. Halawy, and M. M. Ebrahim, Journal of Analytical and Applied Pyrolysis **27**, 109 (1993).
[117] J. C. De Jesus, I. González, A. Quevedo, and T. Puerta, Journal of Molecular Catalysis A: Chemical **228**, 283 (2005).
[118] M. A. A. Elmasry, A. Gaber, and E. M. H. Khater, Journal of Thermal Analysis and Calorimetry **47**, 757 (1996).
[119] E. F. Bertaut, T. Q. Duc, P. Burlett, M. Thomas, and J. M. Moreau, Acta Crystallographica **B30**, 2234 (1974).
[120] A. E. Newkirk, Thermochimica Acta **2**, 1 (1971).
[121] A. K. H. Nohman, H. M. Ismail, and G. A. M. Hussein, Journal of Analytical and Applied Pyrolysis **34**, 265 (1995).
[122] J. M. Phillips, Journal of Applied Physics **79**, 1829 (1996).
[123] R. A. Cowley, Philosophical Transactions of the Royal Society of London. Series A: Mathematical, Physical and Engineering Sciences **354**, 2799 (1996).
[124] T. Riste, E. J. Samuelsen, K. Otnes, and J. Feder, Solid State Communications **9**, 1455 (1971).
[125] R. Loetzsch, A. Lubcke, I. Uschmann, E. Forster, V. Grosse, M. Thuerk, T. Koettig, F. Schmidl, and P. Seidel, Applied Physics Letters **96**, 071901 (2010).
[126] G. Shirane and Y. Yamada, Physical Review **177**, 858 (1969).
[127] D. P. Ostermann, K. Mohanty, and J. D. Axe, Journal of Physics C: Solid State Physics **21**, 2635 (1988).
[128] M. Afzal, P. K. Butt, and H. Ahmad, Journal of Thermal Analysis and Calorimetry **37**, 1015 (1991).
[129] E. Sawaguchi, A. Kikuchi, and Y. Kodera, Journal of the Physical Society of Japan **18**, 459 (1963).
[130] S. Doi and I. Takahashi, Philosophical Magazine A **80**, 1889 (2000).
[131] D. H. A. Blank, G. Koster, G. Rijnders, E. van Setten, P. Slycke, and H. Rogalla, Applied Physics A: Materials Science & Processing **69**, S17 (1999).

[132] Y. Krockenberger, TU Darmstadt, 2007.
[133] M. von Laue and I. Fränz-Gotthold, Annalen der Physik **425**, 249 (1938).
[134] M. De Graef and M. E. McHenry, *Structure of materials : an introduction to crystallography, diffraction, and symmetry* (Cambridge University Press, Cambridge [u.a], 2010).
[135] M. Eastmen, (Materials World Modules, http://www.materialsworldmodules.org/, 04.05.2012).
[136] P. Williams, Annual Review of Materials Science **15**, 517 (1985).
[137] H. M.Ortner, in *Methoden der Materialwissenschaft II*, 2000), Vol. 4.
[138] A. R. Bayly, A. R. Waugh, and K. Anderson, Nuclear Instruments and Methods in Physics Research **218**, 375 (1983).
[139] N. A. Burnham and R. J. Colton, Journal of Vacuum Science & Technology A: Vacuum, Surfaces, and Films **7**, 2906 (1989).
[140] J. N. Israelachvili, *Intermolecular and surface forces* (Academic Press, Burlington, MA, 2011).
[141] J. H. Hoh, J. P. Cleveland, C. B. Prater, J. P. Revel, and P. K. Hansma, Journal of the American Chemical Society **114**, 4917 (1992).
[142] H. A. Mizes, K. G. Loh, R. J. D. Miller, S. K. Ahuja, and E. F. Grabowski, Applied Physics Letters **59**, 2901 (1991).
[143] M. Steinberg and K. Schofield, The Journal of Chemical Physics **94**, 3901 (1991).
[144] H. Yamakawa, S. Lee, H. Takagi, and C. Randall, Journal of Materials Science **46**, 2064 (2011).
[145] A. R. Denton and N. W. Ashcroft, Physical Review A **43**, 3161 (1991).
[146] D. Igarashi, Y. Miyazaki, K. Yubuta, and T. Kajitani, Journal of Electronic Materials **39**, 1669 (2010).
[147] W. Borchardt-Ott, *Kristallographie : eine Einführung für Naturwissenschaftler* (Springer, Berlin [u.a.], 2002).
[148] Y. Ono, N. Kato, Y. Ishii, Y. Miyazaki, and T. Kajitani, Journal of the Japan Society of Powder and Powder Metallurgy **50**, 469 (2003).
[149] S. Miyazaki, S. Kikkawa, and M. Koizumi, Synthetic Metals **6**, 211 (1983).
[150] C. Delmas, J. J. Braconnier, C. Fouassier, and P. Hagenmuller, Solid State Ionics **3-4**, 165 (1981).
[151] S. P. Bayrakci, C. Bernhard, D. P. Chen, B. Keimer, R. K. Kremer, P. Lemmens, C. T. Lin, C. Niedermayer, and J. Strempfer, Physical Review B **69**, 100410 (2004).
[152] Y. Takahashi, N. Kijima, K. Dokko, M. Nishizawa, I. Uchida, and J. Akimoto, Journal of Solid State Chemistry **180**, 313 (2007).
[153] R. J. Gummow, M. M. Thackeray, W. I. F. David, and S. Hull, Materials Research Bulletin **27**, 327 (1992).
[154] Periodic table, www.periodictable.com, 24.05.2012.
[155] W. M. Haynes, *CRC handbook of chemistry and physics : a ready-reference book of chemical and physical data* (CRC Press, Boca Raton, Fla. [u.a.], 2011).
[156] L. Bergmann and C. Schaefer, *Lehrbuch der Experimentalphysik* (de Gruyter, Berlin
[157] web elements, www.webelements.de, 14.06.2012.
[158] E. Antolini and M. Ferretti, Journal of Solid State Chemistry **117**, 1 (1995).
[159] C.-y. Hu, J. Guo, Y. Du, H.-h. Xu, and Y.-h. He, Transactions of Nonferrous Metals Society of China **21**, 114 (2011).
[160] T. Ohzuku, A. Ueda, and M. Nagayama, Journal of The Electrochemical Society **140**, 1862 (1993).
[161] W. Krönig, Angewandte Chemie **37**, 667 (1924).
[162] D.-C. Li, T. Muta, L.-Q. Zhang, M. Yoshio, and H. Noguchi, Journal of Power Sources **132**, 150 (2004).
[163] J. Choi and A. Manthiram, Journal of Materials Chemistry **16**, 1726 (2006).

[164] Z. H. Lu, L. Y. Beaulieu, R. A. Donaberger, C. L. Thomas, and J. R. Dahn, Journal of The Electrochemical Society **149**, A778 (2002).
[165] L. Zhang, X. Wang, T. Muta, D. Li, H. Noguchi, M. Yoshio, R. Ma, K. Takada, and T. Sasaki, Journal of Power Sources **162**, 629 (2006).
[166] G. H. Kim, J. H. Kim, S. T. Myung, C. S. Yoon, and Y. K. Sun, Journal of The Electrochemical Society **152**, A1707 (2005).
[167] Z. R. Chang, Z. J. Chen, F. Wu, H. W. Tang, Z. H. Zhu, X. Z. Yuan, and H. J. Wang, Solid State Ionics **179**, 2274 (2008).
[168] H. W. Tang, Z. H. Zhu, Z. R. Chang, Z. J. Chen, X. Z. Yuan, and H. Wang, Electrochemical and Solid-State Letters **11**, A34 (2008).
[169] N. Yabuuchi and T. Ohzuku, Journal of Power Sources **119**, 171 (2003).
[170] A. Ueda and T. Ohzuku, Journal of The Electrochemical Society **141**, 2010 (1994).
[171] R. I. Barabash, W. Donner, and H. Dosch, Applied Physics Letters **78**, 443 (2001).
[172] K. Krezhov, K. Petrov, and T. Karamaneva, Journal of Solid State Chemistry **48**, 33 (1983).
[173] F. Pertlik, Monatshefte für Chemie / Chemical Monthly **130**, 1083 (1999).
[174] M. L. Foo, R. E. Schaak, V. L. Miller, T. Klimczuk, N. S. Rogado, and Y. Wang, Solid State Communication **127**, 33 (2003).
[175] Y. Ishida, A. Mizutani, K. Sugiura, H. Ohta, and K. Koumoto, Physical Review B **82** (2010).
[176] C. S. Nimisha, M. Ganapathi, N. Munichandraiah, and G. Mohan Rao, Vacuum **83**, 1001 (2009).
[177] H. Xia, Y. S. Meng, L.Lu, and G.Ceder, (2007).
[178] M. C. Rao and O. M. Hussain, Journal of Alloys and Compounds **491**, 503 (2010).
[179] T. Ohnishi and K. Takada, Applied Physics Express **5** 055502 (2012).
[180] J. B. Bates, N. J. Dudney, B. J. Neudecker, F. X. Hart, H. P. Jun, and S. A. Hackney, Journal of The Electrochemical Society **147**, 59 (2000).
[181] M. Hirayama, et al., Journal of Power Sources **168**, 493 (2007).